

INFORMATION TO USERS

This manuscript has been reproduced from the microfilm master. UMI films the text directly from the original or copy submitted. Thus, some thesis and dissertation copies are in typewriter face, while others may be from any type of computer printer.

The quality of this reproduction is dependent upon the quality of the copy submitted. Broken or indistinct print, colored or poor quality illustrations and photographs, print bleedthrough, substandard margins, and improper alignment can adversely affect reproduction.

In the unlikely event that the author did not send UMI a complete manuscript and there are missing pages, these will be noted. Also, if unauthorized copyright material had to be removed, a note will indicate the deletion.

Oversize materials (e.g., maps, drawings, charts) are reproduced by sectioning the original, beginning at the upper left-hand corner and continuing from left to right in equal sections with small overlaps.

**ProQuest Information and Learning
300 North Zeeb Road, Ann Arbor, MI 48106-1346 USA
800-521-0600**

UMI[®]

University of Alberta

Dynamics of the Substorm Expansive Phase

by

Erena Friedrich



A dissertation submitted to the Faculty of Graduate Studies and Research in partial fulfillment of the requirements for the degree of *Doctor of Philosophy*

Department of Physics

Edmonton, Alberta

Spring 2002



**National Library
of Canada**

**Acquisitions and
Bibliographic Services**

**395 Wellington Street
Ottawa ON K1A 0N4
Canada**

**Bibliothèque nationale
du Canada**

**Acquisitions et
services bibliographiques**

**395, rue Wellington
Ottawa ON K1A 0N4
Canada**

Your file Votre référence

Our file Notre référence

The author has granted a non-exclusive licence allowing the National Library of Canada to reproduce, loan, distribute or sell copies of this thesis in microform, paper or electronic formats.

The author retains ownership of the copyright in this thesis. Neither the thesis nor substantial extracts from it may be printed or otherwise reproduced without the author's permission.

L'auteur a accordé une licence non exclusive permettant à la Bibliothèque nationale du Canada de reproduire, prêter, distribuer ou vendre des copies de cette thèse sous la forme de microfiche/film, de reproduction sur papier ou sur format électronique.

L'auteur conserve la propriété du droit d'auteur qui protège cette thèse. Ni la thèse ni des extraits substantiels de celle-ci ne doivent être imprimés ou autrement reproduits sans son autorisation.

0-612-69832-7

Canada

University of Alberta
Library Release Form

Name of Author: *Erena Friedrich*

Title of Thesis: *Dynamics of the Substorm Expansive Phase*

Degree: *Doctor of Philosophy*

Year this Degree Granted: *2002*

Permission is hereby granted to the University of Alberta Library to reproduce single copies of this thesis and to lend or sell such copies for private, scholarly or scientific research purposes only.

The author reserves all other publication and other rights in association with the copyright in the thesis, and except as herein before provided, neither the thesis nor any substantial portion thereof may be printed or otherwise reproduced in any material form whatever without the author's prior written permission.

Erena Friedrich

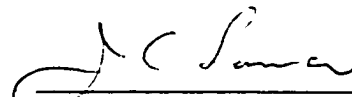
Department of Physics
University of Alberta
Edmonton, Alberta
T6G 2J1

Date: *January 2nd, 2002*

University of Alberta

Faculty of Graduate Studies and Research

The undersigned certify that they have read, and recommend to the Faculty of Graduate Studies and Research for acceptance, a thesis entitled *Dynamics of the Substorm Expansive Phase* submitted by *Erena Friedrich* in partial fulfillment of the requirements for the degree of *Doctor of Philosophy*.



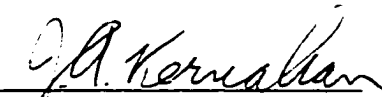
Dr. John C. Samson, Supervisor



Dr. Richard Marchand



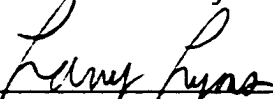
Dr. Robert Rankin



Dr. Tony Kernahan



Dr. Robert Fedosejevs



Dr. Larry Lyons

Date: July 4, 2001

To my family.

**.....A soft, frosty glow slowly covered the snow,
while the bright colors lit the dim night.
They'd all come to see a great mystery —
the phenomenon called "Northern Lights."**

**-- an excerpt from the children's book
"Arctic Fives Arrive" by Elinor J. Pinczes.**

Abstract

This thesis investigates the substorm expansive phase with particular emphasis on the dynamics associated with the initiation of expansive phase onset and the development of the substorm current wedge.

The first study in this thesis looks at the highly controversial question surrounding the sequence of events of the magnetospheric substorm. That is, does expansive phase onset occur prior to, or as a result of, near-Earth neutral line formation in the mid-tail? A new technique has been developed to analyze the CANOPUS meridian scanning photometer (MSP) data that fits a Gaussian distribution to the MSP data in order to determine the latitudinal location of the poleward and equatorward borders of the 557.7 nm and 630.0 nm emission regions, and the maximum peak of the 486.1 nm emissions. The new technique permits the study of the dynamics of the maximum peak, the poleward and the equatorward borders of the photometer emissions throughout the duration of the substorm. The relative motion of the borders of the emissions show that not only is the initial intensification of the expansive phase explosive, but the poleward border of the 557.7 nm emissions rapidly expands poleward past the maximum latitude of dipolarization (shown by the maximum of the H β emissions) to reach the poleward border of the 630.0 nm emissions in approximately 1 – 5 minutes. The rapid tailward expansion of the poleward border of the 557.7 nm emissions has been interpreted as the propagation of an instability anti-earthward down the tail, causing dipolarization of stretched field lines and perhaps initiating the reconnection of lobe flux. The results of this thesis show consistently that neutral line formation associated with the substorm expansive phase is a result, and not a cause, of expansive phase onset. That is, expansive

phase onset happens *prior to* lobe flux reconnection. The above-mentioned sequence of events and rapid timescale carry severe consequences for the other substorm models and theories that are currently published.

The second study in this thesis takes an indepth look at one of the main signatures of the expansive phase- the substorm current wedge. The presently accepted current wedge model creates the wedge by 'short-circuiting' the cross-tail current to the ionosphere, producing a pair of anti-parallel field-aligned current sheets flowing into and out of the ionosphere. The current circuit is closed by an ionospheric westward electrojet that is located in the same latitudinal region as the auroral emissions observed by the meridian scanning photometers. This current wedge is an equivalent current however, proposed to explain the magnetic signatures observed by satellite based and ground-based instruments at mid and low latitudes. The current wedge model is thus non-unique such that other model current systems can produce similar magnetic signatures. Therefore, the second objective of this thesis was to prove that another current configuration, based on the directly driven current system and variations in ionospheric electric fields and conductivities, can also produce the magnetic signatures of the substorm current wedge.

Acknowledgements

It is impossible to complete this thesis without thanking the people who were instrumental in the development and completion of my degree. First and foremost are my supervisors: Drs. Gordon Rostoker and John Samson. Gordon and John provided a very good environment from which to learn the field of space physics and they were always available for discussions of both a scientific and personal nature. Ironically, however, it was what they didn't try to teach directly that I learned the most from them. John provided an excellent example of how to apply the basic laws of physics to get to the heart of a physics problem. He asked the most probing questions and revealed the most insightful answers. Gordon is an excellent public speaker and representative for our field. He showed me how to give a good scientific presentation by engaging the audience and simplifying the content.

My degree program has not been a routine experience. Perhaps amazingly this thesis has been completed despite many extracurricular endeavours including being president of the GPSA, a public lecture at the Edmonton Space Science Center, a month long project with the Discovery Channel, and the birth of my second child. During a PhD. program that was far from ordinary, both Gordon and John were never less than supportive.

I would like to acknowledge the efforts of my examining committee who took the time to read and suggest changes for my thesis. Their critical comments were helpful and appreciated. I would also like to thank Larry Lyons, Bob McPherron, Wynne Calvert, Shin Ohtani, Goran Marklund, Tuija Pulkkinen, Jim Slavin, and Jesper Gjerlov for many helpful discussions during scientific meetings. I understand the nuances of this field much more clearly as a result of these entertaining and educational interactions.

Perhaps more is learned from day-to-day discussions with colleagues than from discussions with supervisors. My time at the University of Alberta was much enriched by the association of my "dungeon" colleagues: Frances Fenrich, Peter Damiano, Igor Voronkov, James Wanliss, Peter Dobias, Henry Sikkema, Sarah Derr, Martin Connors, and Susan Skone. A special acknowledgement goes to James Wanliss and Igor Voronkov. During the latter two years of my degree I have been fortunate enough to be involved in a few journal publications and conference presentations. The papers and

presentations were the result of fruitful collaborations with Igor and James. In particular, the work presented in Chapter 3 is an excerpt from a paper with James that utilized the new data analysis technique designed in this thesis and the new magnetic field model developed in James' thesis. I would also like to thank Karen Apps, an amazing computer programmer who makes programming in IDL seem effortless and porting code from Windows to Linux to VMS a trivial matter.

Not many students ask for maternity leave during the tenure of their degree programs. Lynn Chandler, the physics graduate secretary, was an amazing source of support during the latter 2 ½ years of my program and during my pregnancy. Apparently, she had a great time writing new regulations for graduate students needing maternity leave based on my experience and needs. I'm pleased to have been both a pioneer and a source of entertainment in this respect.

Our friends in Edmonton and in Hillsboro, Oregon provided a much needed reprieve from the rigors of the Ph D. program. Being able to commiserate about the challenges of raising a young family while trying to finish a degree was immensely helpful. Having to explain to our new U.S. neighbors exactly what the Northern Lights were and how they were produced was good practice for writing the Introductory Chapter to this thesis.

My family and my husband's family deserve a special acknowledgement. Both families have been very supportive during my degree and my husband's Ph D. Through the generosity of my parents we were able to live and raise a family in a house rather than student housing. My husband's family farm provided a wonderful haven from the bustle of city life.

Finally, I thank my husband and my children. My husband has been amazingly supportive during the past few years. I thank him for spending countless evenings discussing my work with me. The birth of my children helped to ground me in my thinking and prioritize my life properly. I completed this degree more for them than for myself.

Table of Contents

Chapter		Page
1	Introduction	1
	Prologue	1
	1.1 The Solar Wind	1
	1.2 The Magnetosphere	2
	1.3 The Ionosphere	5
	1.4 The Magnetospheric Substorm	12
	1.5 The Auroral Substorm	14
	1.5.1 Photometer Data	17
	1.6 Substorm Models	18
	1.7 Thesis Outline	19
	Bibliography	20
2	Instrumentation and Data Analysis	25
	2.1 CANOPUS	25
	2.1.1 Magnetometers	25
	2.1.1a Latitude Profiles	28
	2.1.2 Photometers	29
	2.1.2a Determining the borders of the auroral emissions	30
	2.2 SuperDARN	44
	2.2.1 The Merge Program	47
	2.3 GOES Satellites	48
	2.4 The Kisabeth Surge Program	50
	Bibliography	55
3	Dynamics of the Substorm Growth Phase	57
	3.1 Introduction	57

3.2	Particle Motion and Proton Precipitation in the Near-Earth Tail	59
3.3	Magnetic Field Model	62
3.4	Fitting the Photometer Data	68
3.5	Procedure	69
3.6	Results	71
3.7	Conclusion	75
	Bibliography	77
4	Dynamics of the Substorm Expansive Phase	81
4.1	Introduction	81
4.2	Procedure	85
4.3	Data and Observations	88
	4.3.1 February 9, 1995	88
	4.3.2 December 7, 1989	94
4.4	Discussion	97
4.5	Conclusions	108
	Bibliography	111
5	The Substorm Current Wedge	117
5.1	Introduction	117
5.2	The Model	123
5.3	Theory and Observations	132
	5.3.1 Magnetospheric Dynamics	138
	5.3.2 Geosynchronous Dynamics	141
5.4	Discussion and Conclusions	160
	Bibliography	165
6	Conclusions and Future Work	172
	Appendix I	178
	Bibliography	183

List of Tables

Table		Page
2.1	CANOPUS Instrument Sites (originally published in Rostoker [1995])	27
3.1	Range of energies of strong pitch-angle scattering (adapted from Lyons [1997])	62
3.2	Parameters for the Wanliss magnetic field model	65
4.1	Timing of Isolated Substorms	97
5.1	Current magnitudes for preonset model in Figure 5.3	123
5.2	Current magnitudes for the post-onset model in Figure 5.7	129
6.1	Pros and cons of substorm models based on observational constraints	173

List of Figures

Figure		Page
1.1	Schematic diagram of the magnetic field and plasma regimes in Earth's magnetosphere (modified from <i>Potemra</i> [1994]).....	3
1.2	Diagram showing the different layers of the ionosphere illustrating how temperature, ion density, and neutral density vary with height (from <i>Rees</i> [1989])	6
1.3	Schematic diagram showing the ionospheric electrojets, electric fields, and unbalanced upward and downward field-aligned (fac) in the auroral oval	8
1.4	Height-integrated isoconductivity contours (mhos) for the Northern Hemisphere in an invariant latitude and magnetic local time frame	9
1.5	Large-scale field-aligned currents during (a) quiet times ($AE < 100$ nT), and (b) disturbed times ($AE > 100$ nT)	11
1.6	The different phases of the auroral substorm as the polar cap responds to changes in the interplanetary magnetic field (from <i>Rostoker</i> [1996])	15
1.7	Meridian scanning photometer data from CANOPUS. The data from Gillam and Rankin have been merged to obtain the extended latitude range	17
2.1	Map of CANOPUS stations and instrumentation. Dark squares represent locations of meridian scanning photometers (MSP).....	26
2.2	Example of a latitude profile showing a westward electrojet centered on 65°N and 5° wide in latitudinal extent	29
2.3	An example of a step function fit of the 630.0 nm data for October 7, 1989 at 0433 UT	31
2.4	Meridian scanning photometer data for January 18, 1996	33
2.5	Cross-sections of the photometer data for January 18, 1996	35
2.6	Cross-sections of the photometer data for February 9, 1995	36
2.7	Comparison of the Gauss and Step fit for the February 9, 1995 event 630.0 nm data at $t=0433$ UT	39

2.8	The Gauss and Step fits for the March 9, 1995 event 630.0 nm data at T=0504 UT	39
2.9	A comparison of the Gauss and Step fits of the 630.0 nm data for January 18, 1996 at t=0518 UT	40
2.10	The Gauss and Step Function fits of the 630.0 nm data for October 7, 1989 at t=0425 UT	40
2.11	The poleward borders of the 557.7 nm and 630.0 nm emissions	41
2.12	An example of 557.7 nm photometer data with multiple peaks on January 18, 1996 at t=0458 UT	43
2.13	557.7 nm data for January 20, 1996 at 0609 UT showing the non-Gaussian structure of the data	43
2.14	The poleward border of the 557.7 nm data for the January 20, 1996 event using the Gauss fit procedure	44
2.15	Schematic of the SuperDARN radar sites in the Northern Hemisphere (courtesy of George Sofko, Principal Investigator of the Saskatoon radar).....	45
2.16	Illustration of how HF, VHF and UHF signals are scattered into space by nearly vertical magnetic field lines at high latitudes (adapted from Figure 4 in Greenwald et al., [1995])	46
2.17	The Saskatoon (T) – Kapuskasing (K) merge grid	47
2.18	Vectors for magnetic field calculations in spherical coordinates	49
2.19	A three-dimensional E-W current system with finite longitudinal and latitudinal extent	51
2.20	A north-south three-dimensional current system with finite latitudinal and longitudinal extent	52
3.1	The different aspects of the substorm growth phase (from <i>McPherron</i> [1972] ...	58
3.2	An example of Speiser motion as a proton travels near the neutral sheet with a weak normal magnetic field across the sheet and no electric fields	60
3.3	Magnetic streamlines from the Wanliss magnetic field model	66
3.4	Magnetic streamlines from the Wanliss magnetic field model for the latter growth phase	66

3.5	A comparison of the Wanliss magnetic field model to other models investigating the near-earth region	67
3.6	The equatorward border for the 486.1 nm emissions on March 9, 1995	69
3.7	Model prediction for the regions of proton precipitation in the ionosphere	71
3.8	CANOPUS data for the March 9, 1995 event. (a) Meridian scanning photometer data showing growth and expansive phase	72
3.9	Model statistics for the March 9, 1995 event	74
3.10	Position of the inner edge of the plasma sheet during the substorm growth phase	75
4.1	Meridian scanning photometer data for February 9, 1995	86
4.2	X-component magnetometer data from the CANOPUS Churchill line	90
4.3	Pi2 pulsations for February 9, 1995 from 04-05 UT	91
4.4	Poleward borders of the 557.7 nm (a) and 630.0 nm (b) data overlaid onto the meridian scanning photometer data for February 9, 1995.....	92
4.5	Variation (in time and latitude) of the poleward borders of the 557.7 nm (dashed line), 630.0 nm (solid line), and maximum emissions of the 486.1 nm (dotted line) for February 9, 1995	93
4.6	Meridian scanning photometer data for December 7, 1989	95
4.7	Poleward borders of the 557.7 nm (dashed line) and 630.0 nm (solid line), and maximum of the 486.1 nm (dotted line) emissions	96
4.8	Poleward borders of the 557.7 nm and 630.0 nm data, and maximum of the 486.1 nm emissions for (a). December 8, 1989, (b). February 26, 1995, and (c). December 16, 1996	98
4.9	Schematic of the sequence of events during a substorm as observed with the meridian scanning photometer data	99
4.10	Poleward and equatorward borders of the auroral electrojets for the February 9, 1995 event, overlaid onto the MSP data	100
4.10	Cont'd. Panel (c) shows the motion of the X-component peak of the substorm westward electrojet during the expansive phase overlaid onto 557.7 nm data	102

4.11	Schematic of a proposed substorm model based on the observations from the MSP and magnetometer data	109
5.1	Currently accepted model of the substorm current wedge illustrating the field-aligned currents, the closure current, and the ionospheric current of the wedge (from <i>McPherron et al.</i> , 1973)	118
5.2	Magnetic signatures observed at low latitudes from the field-aligned currents of the substorm current wedge	119
5.3	Schematic of the preonset ionospheric current system in the Northern Hemisphere	122
5.4	Latitude profile of the growth phase currents in the dusk sector	125
5.5	Latitude profile of the growth phase currents taken along the midnight meridian	126
5.6	Latitude profile of the growth phase currents in the morning sector.	127
5.7	Schematic of the expansive phase ionospheric current system in the Northern Hemisphere immediately after onset	128
5.8	Latitude profile of the post-onset current system showing an eastward electrojet in the dusk sector.....	131
5.9	Longitude profile of the perturbed directly-driven current system responsible for the substorm current wedge.....	132
5.10	A schematic equatorial plane cross-section of the tail illustrating the space charge associated with the Region I and Region II field-aligned currents (from <i>Rostoker</i> [1994])	133
5.11	One hour averages of meridional and azimuthal electric field components measured in a nonrotating frame of reference on 32 balloons flown in the auroral zone (from <i>Mozer and Lucht</i> [1974])	135
5.12	Electric field configurations for maximum and minimum electrojet current flow	136
5.13	An example of the electric field vectors for an event that occurred on January 11, 1994	137
5.14	Schematic of the closure currents of the preonset current system	142

5.15	Average magnetic field variations during substorms derived from GOES 5 and GOES 6 data	144
5.16	Magnetic signatures from a conjugate current wedge system that would be observed on the equatorial plane	145
5.17	Magnetic signatures due to a conjugate wedge current system observed +5° off the equatorial plane	146
5.18	Magnetic signatures calculated from the model closure currents in Figure 5.14 and the westward crosstail/ring current	147
5.19	Schematic of the closure currents for the post-onset system	149
5.20	Magnetic signatures calculated from the model closure currents in Figure 5.19 and the westward crosstail/ring current	150
5.21	A differential longitude profile illustrating the magnetic signatures due to the substorm current wedge	151
5.22	CANOPUS magnetometer data from the Churchill line for January 1, 1999.....	152
5.23	Magnetic H and D components from the station of Fredericksburg for January 1, 1999	153
5.24	Magnetic H and D component signatures from Newport station for January 1, 1999	155
5.25	CANOPUS magnetometer data for stations along and west of the Churchill line	156
5.26	Magnetic signatures from the station of Ottawa showing current wedge signatures for the 0502 UT intensification (courtesy of Larry Newitt at INTERMAGNET)	157
5.27	Magnetic signatures observed by the GOES 8 satellite for the event that occurred on January 1, 1999	159
5.28	Magnetic signatures observed by the GOES 10 satellite	160
5.29	POLAR UV images for the January 1, 1999 (data courtesy George Parks).....	161
5.30	Magnetic signatures observed by the station Poste-de-la-Baleine (data courtesy Larry Newitt at INTERMAGNET)	162
A.1	Electron and proton precipitation patterns over the Northern polar regions	

	of the Earth	179
A.2	Partial energy level diagrams for atomic oxygen showing excited and ground state configurations (from <i>Rees</i> [1989])	181
A.3	Proton (H^+) and H atom trajectories in the ionosphere (from <i>Rees</i> [1989])	182

List of Symbols and Abbreviations

a	radius of Earth
\AA	angstroms
AACGM	altitude adjusted corrected geomagnetic coordinates
ASI	all-sky imager
ACF	auto correlation function
\vec{B}	magnetic field vector
\vec{B}_i	ionospheric magnetic field vector
BLDM	boundary layer dynamic model
B_{lobe}	lobe magnetic field
B_n	component normal to magnetic field
B_p	WFR magnetic field
BPS	boundary plasma sheet
B_x, B_y, B_z	x, y, z component of magnetic field vector
c	speed of light
CANOPUS	Canadian Auroral Network for the OPEN program Unified Study
CCI	Cross-field Current Instability
CDAWeb	Coordinated Data Analysis Web
CPS	central plasma sheet
CRRES	Combined Release and Radiation Effects Satellite
D	magnetic perturbation component directed eastward
1D_2	momentum state of OI
DAN	data analysis network
DCS	data collection system
DMSP	Defence Meteorological Satellite Program
DP2	disturbance polar of the second type
DPY	disturbance polar regulated by IMF Y component
\vec{E}	electric field vector
\vec{E}_\perp	electric field vector directed normal to the magnetic field
e_p	primary electron
EPD	energetic particle detector
ϵ_0	dielectric constant in vacuum
e_s	secondary electron
eV	electron volts
F	Lorentz force
FAC	field-aligned current
GGG	global geospace science
GOES	Geostationary Operational Environment Satellite
GSM	geomagnetic solar magnetospheric
h	height of current system
h	Planck's constant
H	magnetic perturbation component directed northward

H⁺	proton
Hα	the first hydrogen Balmer line, Alpha
Hβ	hydrogen Balmer line
HBL	high latitude boundary layer
He	satellite magnetic field component pointing earthward
HF	high frequency
Hn	satellite magnetic field component perpendicular to Hp and He
Hp	satellite magnetic field component parallel to spin axis
Hz	Hertz
I	intensity
\bar{I}_i	ionospheric current
IMF	interplanetary magnetic field
Ipc	intensity of polar cap
ISTP	international solar terrestrial physics program
\bar{J}_\perp	current density normal to magnetic field
\bar{J}_\parallel	field-aligned current density
κ	Kappa parameter
k	wave vector
K	Kapuskasing
kHz	kiloHertz
km	kilometer
km/s	kilometer/second
keV	kilo electron volts
Kp	planetary geomagnetic disturbance index
Λ	latitude
L	length scale or radial distance measured in Earth radii
LLBL	low latitude boundary layer
L_y	WFR azimuthal length scale
L_z	cross-tail current sheet half-thickness
M	dipole moment
Mamps	mega amps
MHD	magnetohydrodynamic
MHz	megahertz
MIC	Magnetosphere Ionosphere Coupling model
MLT	magnetic local time
ms	millisecond
MSP	meridian scanning photometers
μ_0	magnetic permeability of free space
N	total number of samples
NASA	National Aeronautic and Space Administration
NECD	near-Earth current disruption
NENL	near-Earth neutral line
NEO	near Earth onset
nm	nanometer
nT	nanoTesla

OI	neutral oxygen species
OPEN	Origin of Plasmas in the Earth's Neighborhood
$^3P_{2,1}$	momentum state of OI
\bar{P}	pressure tensor
P_{\perp}	pressure normal to magnetic field
PACE	Polar Anglo-American conjugate experiment
Pi2	irregular pulsation
PSBL	plasma sheet boundary layer
q	elementary charge
r	coefficient of determination
r_o	position of observer
R	Rayleighs
kR	kiloRayleighs
RI	region I field-aligned current
RII	region II field-aligned current
R_E	1 Earth radius
R_{min}	minimum radius of curvature
ρ	charge density
ρ_{max}	maximum particle gyroradius
1S_0	momentum state of OI
SCW	substorm current wedge
SEM	space environment monitor
SFBI	shear flow ballooning instability
Sq	solar quiet current
STARE	Scandinavian Twin Auroral Radar Experiment
SuperDARN	Super Dual Auroral Radar Network
Σ_H	height-integrated Hall conductivity
Σ_P	height-integrated Pedersen conductivity
σ	ionospheric conductivity, standard deviation
σ_x	standard deviation of x data
σ_y	standard deviation of y data
σ_{xy}	covariance of xy data
t_0	time of beginning of growth phase
t_1	time of beginning of poleward expansion of H β
t_2	time of beginning of poleward expansion of 630.0 nm emissions
t_{A1}, t_{A2}	Alfvén travel time
T	Saskatoon radar station
T89, T96	Tsyganenko magnetic field models
TIGER	Tasman International Geospace Environment Radar
UHF	ultra high frequency
ULF	ultra low frequency
UT	universal time
UV	ultra-violet
ν	frequency
\bar{v}	plasma drift velocity
\bar{V}_i	ionospheric convection velocity

V_A	Alfvén velocity
V_{A1}	Alfvén speed from site of expansive phase onset
V_{A2}	Alfvén speed from site of reconnection
VHF	very high frequency
$\bar{\omega}_i (\bar{\Omega})$	vorticity of magnetospheric convection
ω	oscillation frequency
Ω	gyration frequency
WFR	weak field region
X	center of Gaussian distribution
Z	magnetic perturbation component directed downward

Chapter 1: Introduction

1 Prologue

The magnetospheric substorm is probably one of the most studied and most intensely debated topics in the field of space science. Despite the fact that for over half a century scientists have been diligently working towards understanding this phenomenon, we have yet to form a complete picture of the physics involved in this intense solar-terrestrial interaction. In this Introduction the basics of the Sun-Earth interaction will be described, beginning with some details of the solar wind and Earth's magnetosphere and ending with a detailed account of the magnetospheric and auroral substorms.

1.1 The Solar Wind

The driving force behind the substorm is the solar wind. The solar wind is an ever-present flow of charged particles (90% H^+ , 10% $^4He^{++}$) emanating from the sun and pervading the entire solar system. Its existence was first predicted by *Biermann* [1957] who studied observations of cometary tails. He noted that the tail of a comet pointed away from the sun regardless of the direction of travel and proposed that, in addition to electromagnetic energy, the sun also emitted particles possessing a significant amount of kinetic energy. Subsequently, *Parker* [1958] developed a dynamic model in which the solar wind was comprised of heated coronal plasma (the corona being the outer-most layer of the sun), which expanded outward throughout the solar system. The first satellite measurements confirmed Parker's solar wind theory and proved that the solar wind plays an important part in transporting plasma energy from the sun to the near-Earth space environment.

The reason the solar wind can transport plasma energy is due to the flow of plasma away from the sun and to the 'frozen-in-field' condition. The frozen-in-field condition essentially states that plasma elements lying on a magnetic field line remain on that same

field line, and the flux of a magnetic field through any closed contour moving with the plasma is constant. The frozen-in-field condition permits the solar wind to carry the sun's magnetic field throughout the interplanetary medium to the near-Earth space environment. Typical solar wind parameters at near-Earth orbit include interplanetary field strengths of $\sim 5\text{--}10$ nT, speeds varying from $300\text{--}700$ km/s (depending on solar activity), particle number densities from $1 - 10$ cm⁻³ ($10^6 - 10^7$ m⁻³), and kinetic energies of the solar wind flows from $1 - 5$ keV.

1.2 The Magnetosphere

The solar wind speeds stated above exceed both the sound speed (~ 50 km/s) and the Alfvén speed (~ 40 km/s). Thus, in the rest frame of the solar wind, the Earth's motion appears both supersonic and super-Alfvénic, resulting in a shock front called the bow shock, nominally $\sim 10 R_E$ in front of the Earth (Figure 1.1). At the sub-solar point on the bow shock the thermal, dynamic and magnetic pressures of the solar wind approximately equals those pressures exerted by the Earth's magnetic field. The bow shock acts to redirect the solar wind as it approaches the Earth, both slowing and heating the plasma as it passes inside the shock front. The shocked, slowed, and heated solar wind forms a region behind the bow shock called the magnetosheath.

The impact of the solar wind on the Earth's magnetic field deflects the solar wind around the Earth causing the magnetic field (which is intrinsically dipolar) to be distorted. Specifically, the magnetic field on the dayside is compressed and the field on the night side of the Earth is elongated, producing a geomagnetic tail. The magnetotail is sustained by a thin layer of current, centered on the midplane, called the cross-tail current. The cross-tail current is produced by the dawn-dusk (convection) electric field, which accelerates protons in the dawn-dusk direction and electrons in the opposite sense, producing a current that flows in the direction of the electric field. The current bifurcates at the flanks of the magnetotail and closes along the magnetopause.

The magnetopause is a boundary, which separates the solar magnetic field from the geomagnetic field. A discontinuity across this boundary, between the magnetic field and

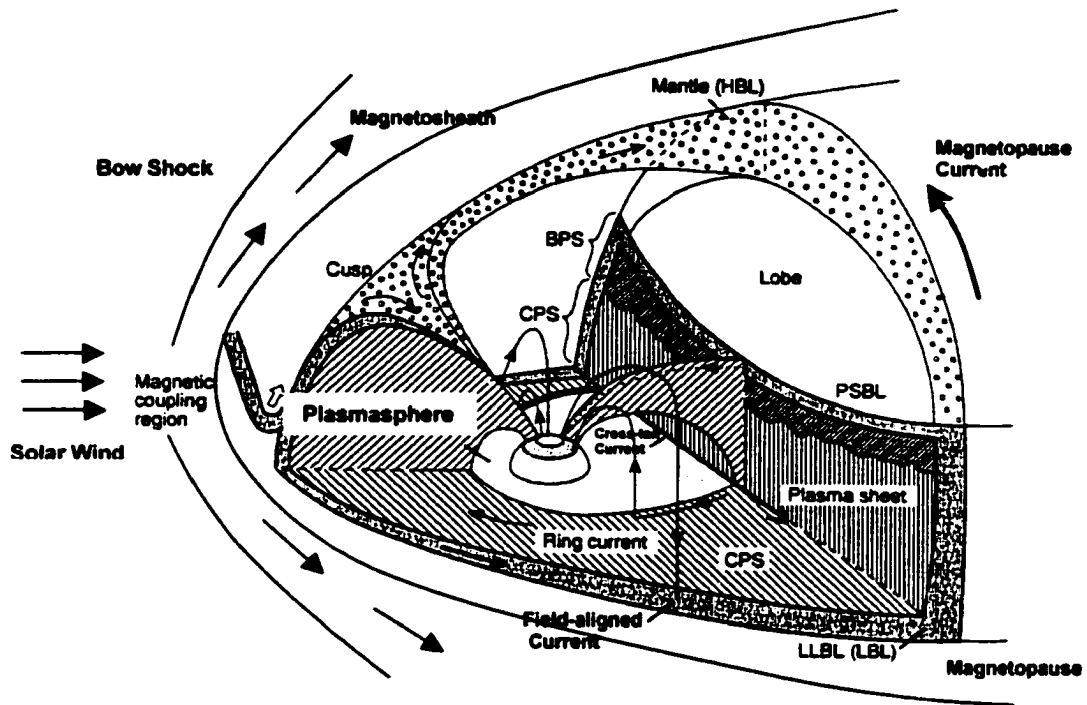


Figure 1.1: Schematic diagram of the magnetic field and plasma regimes in Earth's magnetosphere (modified from Potemra [1994]).

plasma pressure, causes a current to flow along the magnetopause. Consisting of two current loops flowing clockwise in the northern hemisphere (when viewed from the magnetotail toward the Earth) and counter-clockwise in the southern hemisphere, the magnetopause current arises from the differential gyromotions of protons and electrons at the magnetopause.

The deformation of the Earth's magnetic field, due to the passage of the solar wind, leads to the formation of a magnetic cavity called the magnetosphere in which the Earth resides. The magnetosphere is organized into different regimes based on magnetic field magnitudes and plasma properties. There are essentially six separate regions: the polar cusps, the plasma mantle and low latitude boundary layer, the tail lobes, the plasma sheet, the ring current (also known as the Van Allen Radiation Belts) and the plasmasphere (Figure 1.1).

On the dayside, the surface currents generated by the incidence of magnetosheath plasma on the Earth's dipolar field leads to the formation of two regions of weak field

known as the polar cusps. The cusps were first inferred by *Frank* [1971c] as a “funnel-like region” centered around two neutral points whereby magnetosheath plasma could enter the magnetosphere. *Frank* [1971c] associated the cusps with the neutral points inherent in the reconnection model of the solar-wind dipolar field interaction [*Dungey*, 1961]. Immediately adjacent to the magnetopause and the polar cusps is a boundary layer characterized by a streaming plasma of magnetosheath origin [*Akasofu et al.*, 1973]. This boundary layer is divided into two regions called the high latitude boundary layer and the low latitude boundary layer (LLBL), threaded by open and closed field lines, respectively [*Eastman et al.*, 1976]. The high latitude boundary layer is also known as the plasma mantle. Bounded above by the plasma mantle and at lower latitudes by the plasma sheet boundary layer (PSBL) are regions of open field lines called the ‘lobes’. These magnetic tubes stretch tailward and are populated by a cold, tenuous plasma ($<0.01 \text{ cm}^{-3}$ ($<10^4 \text{ m}^{-3}$)), consisting of ions from the cusp region and solar wind electrons. In comparison to other regions of the magnetosphere, the lobes also contain the largest magnetic field intensities tailward of $\sim 12 R_E$ (e.g. 25-30 nT at $25 R_E$).

As mentioned above, the lobes are bounded on their low latitude edge by the PSBL, a region characterized by large magnetic fields (as compared to the plasma sheet) and field-aligned beams of fast ions [*Lui et al.*, 1977]. Closed field lines thread the PSBL and as such, the interface between the tail lobe and the PSBL is considered a boundary between open and closed field lines that maps to the poleward border of the auroral oval in the ionosphere. Between the neutral sheet and the PSBL lies the central plasma sheet (CPS), a region of hot, isotropic plasma of solar wind and ionospheric origin. The CPS extends from $\sim 6.5 R_E$ [*Lui*, 1975] to $\sim 50 R_E$ [*Rostoker and Skone*, 1993], with the inner edge merging smoothly with the ring current region. The CPS contains only closed field lines inside $\sim 50 R_E$, and the magnetic field in this region is weakest in the neutral sheet (of the order of a few nT beyond $\sim 12 R_E$ [*Rostoker and Skone*, 1993]). The neutral sheet lies in the central plane of the CPS, separating the northern and southern magnetospheric hemispheres. It is a very thin region ($\sim 2 R_E$ thick), across which the magnetic field reverses direction from sunward to antisunward. This thesis will be concerned particularly with the magnetic field and particle dynamics of the CPS during the substorm.

Earthward of the CPS lies a large scale current, called the ring current, which is mainly carried by (5–500 keV), trapped ions. The ring current exists due to the motions of the particles under the influence of the Earth's dipole magnetic field. As electrons and ions are convected earthward by the convection electric field, the large-scale gradient in the magnetic field causes the particles to gradient and curvature drift. Since the electrons and ions drift in opposite directions (ions towards dusk, electrons towards dawn), a westward flowing current forms that can significantly alter the surface magnetic field during periods of intense auroral activity.

During magnetospheric substorms, plasma sheet electrons can be energized to tens of keV and injected into the trapping (ring current) region. Injected particles with larger pitch-angles will become trapped and intensify the ring current, reaching magnitudes up to a million amperes during a moderate substorm. Particles originating in the ionosphere can also populate the ring current as they can be injected into the magnetosphere during intense magnetic storms.

The plasmasphere is the region earthward of the CPS and is comprised mainly of cold (≤ 1 eV) ions and electrons, which escape from the ionosphere. The plasma is very dense in this region (ranging from 1 ion/cm³ ($\sim 10^6$ ions/m³) near the CPS to 100 ions/cm³ (10^8 ions/m³) at the plasmopause) and corotates with the Earth under the influence of the corotational electric field. The plasmasphere is bounded by the plasmopause nominally located at ~ 3 -5 R_E depending on magnetospheric activity and magnetic local time.

1.3 The Ionosphere

The ionosphere can be identified as a region of space roughly between 60 and 1000 km altitude where: 1. Energy input is dominated by solar ultra-violet (UV) radiation and auroral energetic particles, electric fields and electric currents; 2. The major neutral constituents are O, N₂, and O₂ and; 3. Neutral atmosphere dynamics are strongly influenced by plasma motions.

For the dayside ionosphere, the principal mechanism that produces the ionosphere is photoionization of the atmospheric constituents due to incident solar UV radiation. The ionosphere is maintained due to the slow recombination rate of the ions. It is divided into layers according to height and ion density. This thesis, in part, will concentrate on

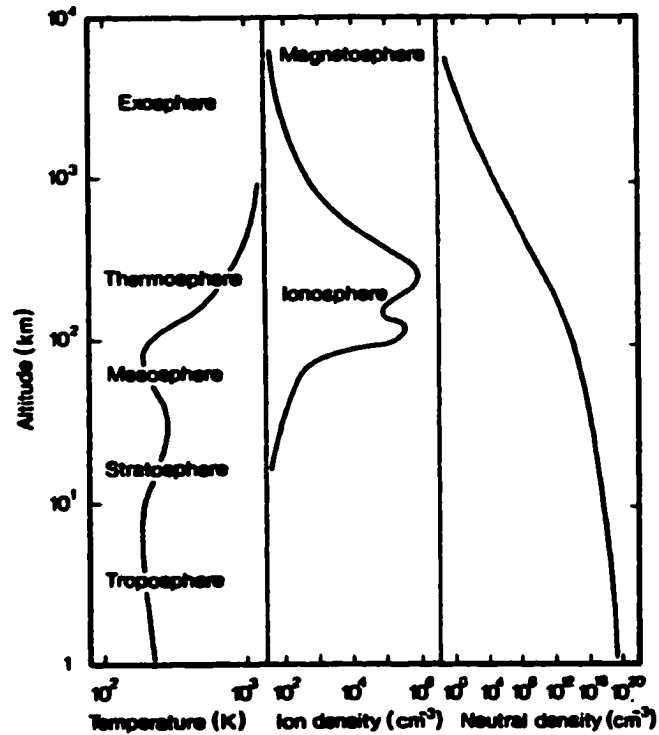


Figure 1.2: Diagram showing the different layers of the ionosphere illustrating how temperature, ion density, and neutral density vary with height (from Rees [1989]).

two layers: the E and F regions. As shown in Figure 1.2, the ion density of the ionosphere increases with altitude to approximately 300 km. Between 90 and 130 km there is a sharp increase in electron density to $\sim 10^5 \text{ cm}^{-3}$ ($\sim 10^{11} \text{ m}^{-3}$) indicating the E region where collisions between particles and atmospheric constituents (O_2^+ and NO^+) are prevalent. Above 130 km is the F region in which the electron density continues to increase until it reaches a maximum of $\sim 10^6 \text{ cm}^{-3}$ ($\sim 10^{12} \text{ m}^{-3}$) at roughly 300 km altitude.

Energetic electron precipitation through the ionosphere is most often observed along two oval shaped regions called the northern and southern auroral ovals. The term 'auroral oval' was first established by *Feldstein* [1973] on the basis of a statistical study of the International Geophysical Year all-sky photographic data in which he noted that auroral arcs preferentially aligned themselves along oval shaped bands. These oval bands are centered approximately 23° off the northern and southern geomagnetic poles. The

actual size and shape of the auroral ovals depends largely on the interplanetary magnetic field. During periods when the B_z component of the interplanetary magnetic field is northward, magnetospheric activity is low and the ovals can shrink to faint circles along 75° latitude. During periods of southward IMF B_z , strong magnetospheric activity can result in very dynamic ovals in which their midnight-regions reach far equatorward. The regions poleward of the ovals are called the polar caps.

The charged particle precipitation penetrates the ionosphere to altitudes of 100 – 150 km creating a ring of enhanced conductivity along the auroral ovals. Within these belts of conductivity flow large-scale horizontal currents between altitudes of 100-150 km. The complete list of currents will be mentioned here; however for brevity only those currents relevant to this thesis will be discussed in detail. The currents that are present at any one time are: the Sq (solar quiet) current system, the two cell circulation system known as “ionospheric convection” or DP2 (Disturbance Polar of the second type), the high latitude dayside current called DPY (Disturbance Polar regulated by the Y component of the IMF), Hall currents, Pedersen currents, and Cowling currents. The latter three currents are of importance to this thesis. The Cowling current will be discussed in Chapter 5. Discussions involving the former current systems can be found in introductory space physics textbooks (e.g. *Kivelson and Russell, 1995; Parks, 1991*).

The large-scale ionospheric electric field is shown in Figure 1.3 (solid thin arrow) to be directed poleward in the region of closed field lines in the evening sector, equatorward in the morning sector, and from dawn to dusk across the polar cap. At altitudes between 100 and 115 km ions undergo collisions with neutral atoms causing them to drift much slower than electrons. The electric field causes the electrons and ions to drift in a direction perpendicular to both \vec{E}_\perp and \vec{B} , producing a Hall current. The eastward and westward electrojets are primarily Hall currents that flow from noon towards midnight across the dusk and dawn sectors, respectively. Between altitudes of 120 and 150 km electrons and ions are accelerated between collisions and move differentially under the influence of \vec{E}_\perp . In this region the current, which flows north/south along the direction of the electric field, is a Pedersen current.

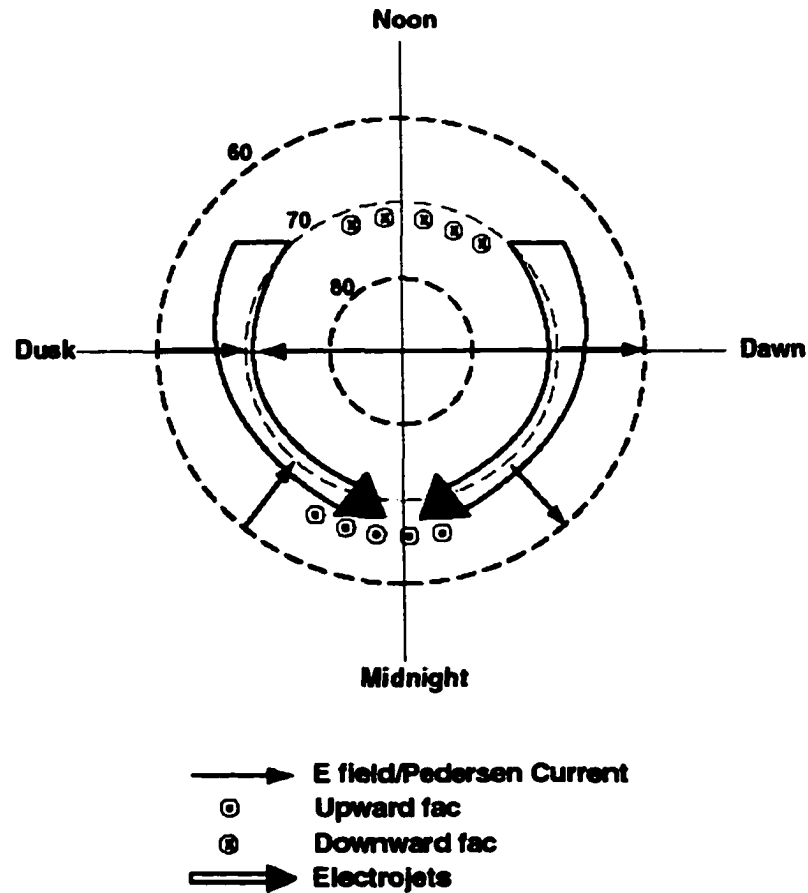


Figure 1.3: Schematic diagram showing the ionospheric electrojets, electric fields, and unbalanced upward and downward field-aligned current (fac) in the auroral oval. View is from above the North pole (modified after *Rostoker* [1987]).

The height-integrated Hall and Pedersen currents are most easily described using the ionospheric Ohm's Law:

$$\bar{J}_{\perp} = \Sigma_p \bar{E}_{\perp} + \Sigma_H (\bar{B} \times \bar{E}_{\perp}) / B \quad (1.1)$$

where \bar{J}_{\perp} is the linear ionospheric current density flowing perpendicular to the magnetic field, Σ_p and Σ_H are height-integrated conductivities associated with the Pedersen and Hall currents, respectively, \bar{E}_{\perp} represents the component of the ionospheric electric field directed perpendicular to the magnetic field, and \bar{B} is the ambient magnetic field.

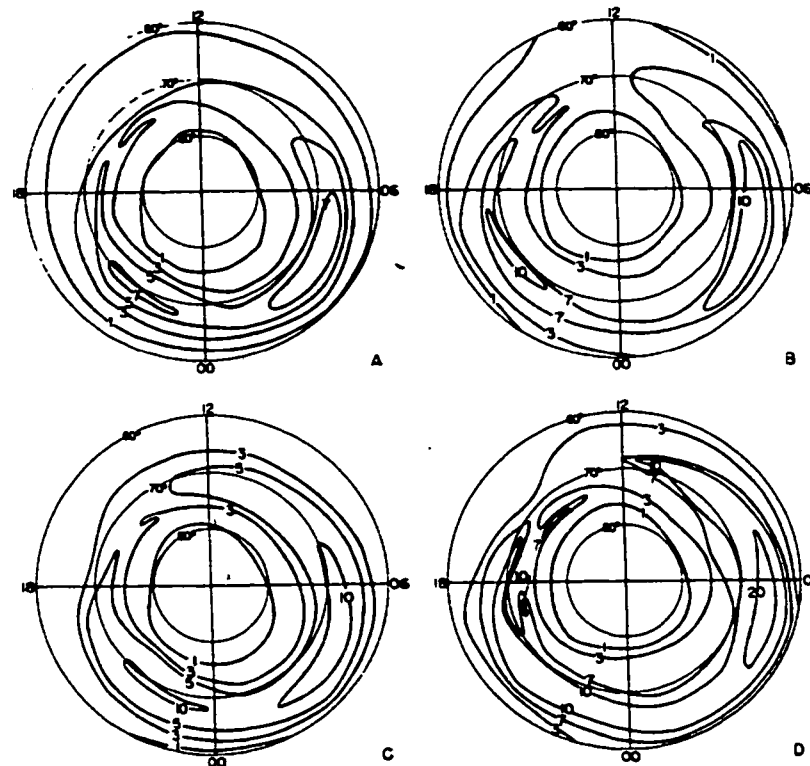


Figure 1.4: Height-integrated isoconductivity contours (mhos) for the Northern Hemisphere in an invariant latitude and magnetic local time frame. Figures A) and C) represent Pedersen and Hall conductivities for quiet times. Figures B) and D) represent Pedersen and Hall conductivities for disturbed times (from Wallis and Budzinski [1981]).

The Hall and Pedersen height-integrated conductivities are distributed throughout the auroral oval as shown in Figure 1.4 [Wallis and Budzinski, 1981]. The conductivities were determined using background ionization sources and average particle distributions observed by the energetic particle detector (EPD) on the polar orbiting satellite Isis 2. All plots are displayed for the Northern Hemisphere in an invariant latitude and magnetic local time frame. Figures 1.4a and 1.4c show the height-integrated Pedersen and Hall isoconductivity contours (mhos), respectively, for intervals of low activity ($0 \leq K_p \leq 3$); K_p being a measure of the planetary disturbance level on a logarithmic scale ranging from 0 to 9, with 9 indicating the most intense disturbance. The small 'o' is part of a sub-designation of -, o, + used as an indication of the intensity of the disturbance between

adjacent levels on the 0 to 9 scale (cf. *Parks* [pg. 512, 1991])). From these Figures it can be seen that the ratio between evening and morning sector conductivities is approximately 1:1. The ratio between Hall and Pedersen conductivity (Σ_H/Σ_P) is approximately 1.5:1.

Figures 1.4b and 1.4d are Pedersen and Hall isoconductivity contours for periods of disturbed activity ($3o < Kp \leq 9+$). The ratio of the evening to morning sector Pedersen conductivity is again approximately 1-2; however, the evening to morning ratio for the Hall conductivity has increased to 2. The ratio Σ_H/Σ_P is approximately 2.

The Pedersen and Hall currents flowing within the auroral oval are fed by currents flowing along magnetic field lines connecting the ionosphere with the magnetosphere. Field-aligned currents (FAC) were first suggested by the Norwegian physicist Kristian Birkeland as a means for maintaining the horizontal currents discussed above. His theory met with considerable debate, however, and it wasn't until the late 1960's that FACs were proven to exist. It was with a tri-axial magnetometer on board the polar orbiting satellite TRIAD (altitude ~800 km) that fluctuations in the east/west component of the magnetic field were observed during passes through the auroral zone. Surprisingly, the initial investigation of the data reported the magnetic disturbances to be hydromagnetic waves [*Zmuda et al.*, 1966; 1967]. It was the interpretation of the data by *Cummings and Dessler* [1967] that suggested the level shifts in the east/west component of the magnetic field were, in fact, produced by Birkeland's FACs [*Potemra*, 1994].

A number of studies in the 1970's solidified the existence of field-aligned currents [*Armstrong and Zmuda*, 1970; 1973] and began to create a statistical picture of the distribution of these currents [*Zmuda and Armstrong*, 1974b; *Iijima and Potemra*, 1976a; *Sugiura and Potemra*, 1976]. By the mid-1970's it was apparent that the FACs flow as sheets of current either into, or out of, the ionosphere throughout most of the region coincident with the auroral oval (Figure 1.5). In most local time zones two well defined regions of FAC are observed, denoted as Region I (RI) and Region II (RII). Region I currents flow into the ionosphere in the morning sector and out of the ionosphere in the dusk sector. In contrast, Region II currents flow equatorward of the Region I currents and in the opposite direction. The intensity of the current sheets differs greatly with local

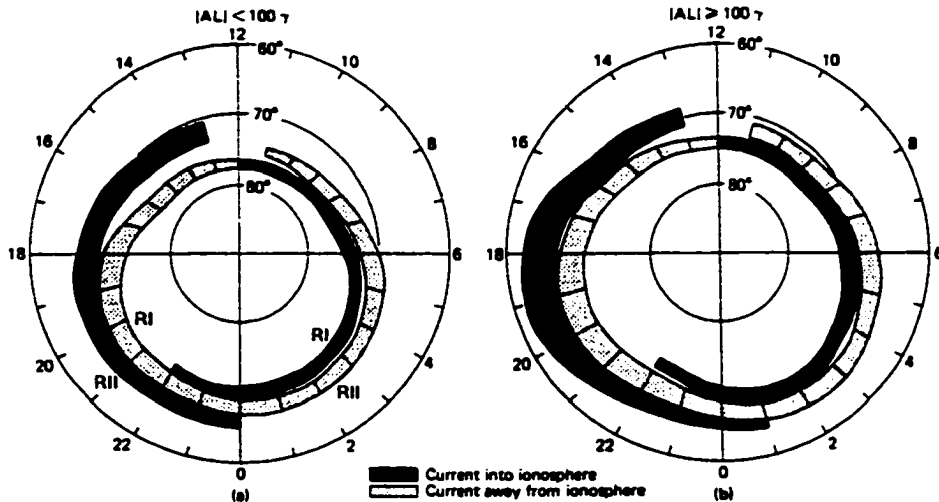


Figure 1.5: Large-scale field-aligned currents during (a) quiet times ($AE < 100$ nT), and (b) disturbed times ($AE > 100$ nT) (from Iijima and Potemra [1987]).

time. Generally it has been found that the RI currents are larger than the RII currents [Yasuhara *et al.*, 1975] except in the midnight region where the ratio of RI to RII is approximately equal [Iijima and Potemra, 1978]. Typical RI current magnitudes in the dawn and dusk Northern Hemisphere sectors are ~ 1.5 MA for quiet times and 2.5 MA for more active times. Typical current densities range from $0.5\text{--}1.0 \times 10^{-10}$ A/cm² ($0.5\text{--}1.0$ $\mu\text{A}/\text{m}^2$) [Iijima and Potemra, 1978].

Theoretical studies have shown the dominant sources of field-aligned current generation on the nightside to include vorticity of magnetospheric convection ($d/dt(\bar{\Omega}/\bar{B})$, where $\bar{\Omega} = \nabla \times \bar{v}$ and \bar{v} is the velocity of the flow), magnetic field and magnetospheric pressure gradients ($\bar{B} \times \bar{\nabla}P \cdot \bar{\nabla}B$), and inertial currents ($\frac{d\bar{v}}{dt} \times \bar{B} \cdot \bar{\nabla}\rho$) [Hasegawa and Sato, 1979; Vasyliunas, 1984; Kan, 1987]. On the basis of low altitude electric and magnetic field observations and particle precipitation measurements it is believed that Region I currents flow on closed field lines that map to the plasma sheet and low latitude boundary layer (LLBL) [Potemra, 1994]. The velocity shear across the interface between the central plasma sheet and the LLBL provides the vorticity that is the dominant term for Region I current generation.

There is compelling evidence, both from observations and field line mapping, that Region II FACs are generated in the near-Earth central plasma sheet and ring current regions [Iijima *et al.*, 1990]. In these regions, plasma pressure gradients in the presence of gradients in the magnetic field represent the dominant sources for current generation [Vasyliunas, 1984; Kan, 1987]. A secondary source for Region II currents could be velocity shear at the inner edge of the CPS between plasma convecting earthward (to a location where it becomes influenced by the corotation electric field) and plasma further earthward moving solely under the influence of the corotation electric field [Rostoker, 1987].

The source regions and dominant generators of field-aligned currents discussed above are valid for the pre-midnight and post-midnight sectors, but become more complicated in the midnight sector. The FACs near midnight are due almost entirely to processes internal to the magnetosphere that are associated with substorm activity, whether it's the creation of new currents associated with the substorm current wedge (discussed below) or the redistribution of field-aligned currents already present. The Region I and Region II nomenclature is no longer meaningful in the midnight sector due to the complex nature of these currents. Finally, the three-tiered current sheets in the midnight sector (Figure 1.5) vanish when geomagnetic activity is low [Potemra, 1994].

1.4 The Magnetospheric Substorm

The magnetospheric substorm can be defined generally as an interval of energy storage and release within the magnetosphere, caused by the interaction between the solar and terrestrial magnetic fields, that results in a large amount of energy dissipated in the ionosphere and large increases in ionospheric current intensities.

The substorm also can be characterized by two distinct processes known as *directly driven* and *storage-release* [Rostoker *et al.*, 1987a]. As the name suggests, the directly driven process involves solar wind energy being directly deposited in the auroral ionosphere and ring current, thereby driving the currents in these regions. The response of the ionosphere and ring current to the increase in energy input is almost immediate, less the propagation time (of the order of a few minutes) of information via the Alfvén

velocity. The directly driven activity is manifest as an increase in intensity of the auroral electrojets and their associated field-aligned currents. The time scale of this activity is of the order of tens of minutes to an hour.

As some of the solar wind energy is being dissipated directly into the ionosphere, energy is also being concurrently stored in the tail magnetosphere. This activity marks the first part of the *storage-release* process in which energy is stored in the tail magnetic field and plasma kinetic energy. More specifically, the energy is stored as gradients in the pressure of the magnetotail (∇P) and enhanced sheets of parallel current such as the cross-tail current (∇j_{\parallel}). The second part of this process involves the sudden release of the stored energy through the formation of the substorm current wedge (discussed in Chapter 5) and a series of auroral surge formations, which appear in quasi-periodic fashion throughout the expansive phase (see below) of the substorm.

In addition to being characterized by two processes, the magnetospheric substorm can be divided into three phases: growth, expansion, and recovery in which the magnetosphere stores energy, explosively releases it, and returns to a pre-substorm state. The growth and expansive phases are synonymous with the storage and release processes of the substorm, the directly-driven system being active throughout all phases of the substorm.

The growth phase [McPherron, 1970] begins when the interplanetary magnetic field (IMF) turns southward and merges with the terrestrial magnetic field on the dayside magnetopause. The merging process begins an interval of energy storage and momentum transfer into the magnetotail. During this time, the cross-tail electric field is enhanced, energizing particles in the plasma sheet as they convect earthward. An earthward pressure gradient is created along the inner edge of the plasma sheet [Kistler *et al.*, 1992] that, together with the cross-tail particle acceleration, increases the cross-tail current in the equatorial plane of the magnetosphere. The increasing cross-tail current causes the magnetic field lines to gradually stretch tailward.

Eventually the magnetic field line stretching and the energy loading in the magnetotail lead the magnetosphere into an enhanced energy state that it can no longer sustain. Through a process or mechanism that has yet to be determined, the stored energy is explosively released marking the beginning of the expansive phase. The intense cross-

tail current is suddenly decreased accompanied by dipolarization of the stretched magnetic field lines and large inductive electric fields. The sudden decrease in the cross-tail current also leads to the formation of a new equivalent current known as the substorm current wedge (SCW). It is commonly believed that the inductance of the magnetosphere, and the ability of the ionosphere to serve as a natural sink for magnetospheric energy, causes the disrupted current to form a three-dimensional current loop between the ionosphere and the magnetosphere. Two field-aligned currents flowing into and out of the ionosphere, closed by a westward electrojet in the ionosphere and an eastward equivalent current in the neutral sheet, form the substorm current wedge. This current system will be discussed in more detail in Chapter 5.

The expansive phase continues until the magnetotail reaches a new equilibrium state of lower energy and current wedge activation has ceased. At this point the recovery phase begins and the magnetosphere returns to its pre-substorm configuration. The storage and release process does not operate during this phase; the dominant feature is the decay of the driven system.

1.5 The Auroral Substorm

The auroral component of the magnetospheric substorm is the *auroral* substorm. In its original definition, *Akasofu* [1964] described the auroral substorm to begin with the intensification of a discrete arc within a myriad of parallel arc structures that stretched across a number of local time zones. The disturbance then evolved asymmetrically about midnight, evolving through the poleward and westward motion of discrete auroral arcs and the eastward drift of auroral patches on the dawn side of the disturbance region. The westward edge of the activity was termed the ‘westward traveling surge’ because it was observed to propagate westward at an average speed of ~ 1 km/s. There was no defined growth phase in the *Akasofu* [1964] presentation of the substorm.

The expansive phase of the substorm was defined in three stages [*Kisabeth*, 1972]: (1) The auroral arcs near midnight brighten suddenly, there is a sharp change in the magnetic field in the vicinity of the arc, and a Pi2 pulsation [*Olson*, 1999] is initiated; (2) The auroral arcs become distorted and move poleward and the magnetic field perturbations

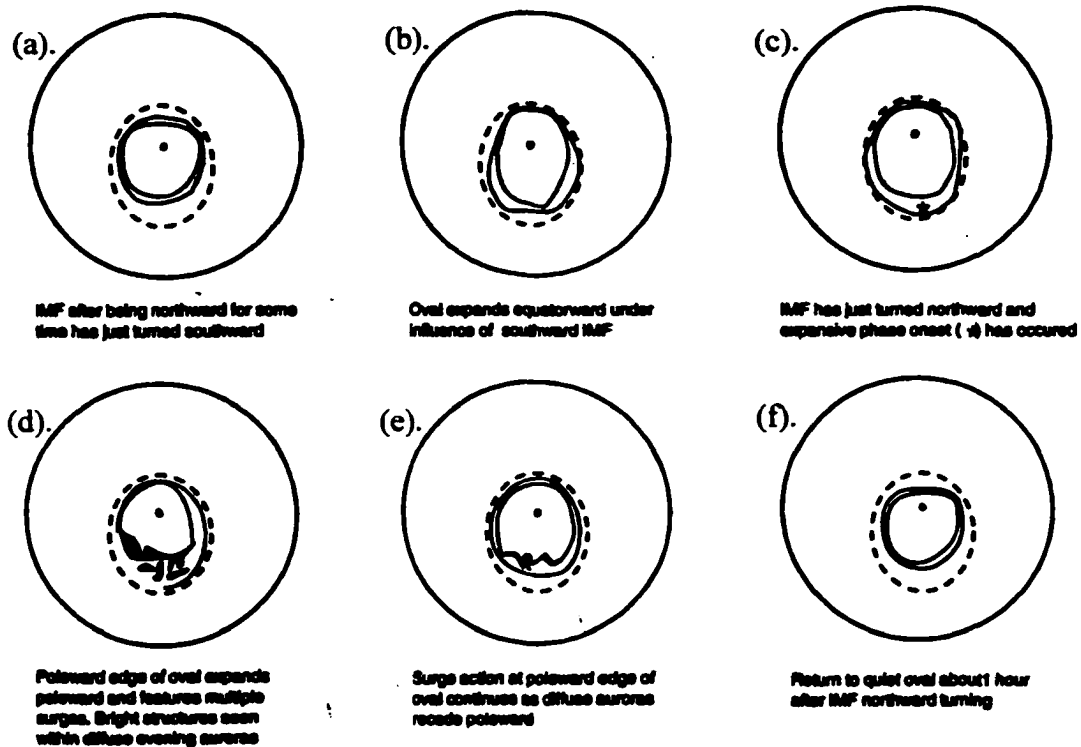


Figure 1.6: The different phases of the auroral substorm as the polar cap responds to changes in the interplanetary magnetic field. The dashed line represents the maximum extent of the auroral oval, the dot in the center of the oval represents the north pole. The region inbetween the North pole and the poleward border of the auroral oval is the polar cap (from Rostoker [1996]).

intensify; (3) The westward traveling surge and eastward drifting patches appear and the associated magnetic perturbations intensify strongly.

Similarly, the recovery phase was also divided into three stages: (1) the arcs reach their northernmost position and begin to recede southward, while surges and loops distort the northern border. The magnetic field perturbations remain large and irregular; (2) the arcs continue to drift equatorward, the drifting loops change into irregular bands, and the magnetic perturbations begin to decrease in intensity; (3) the arcs slowly complete their equatorward drift, and the magnetic activity ceases.

Later investigations of the substorm with improved observations and coordinated studies have produced a more detailed picture of the substorm phenomenon, including a growth phase. From the point of view of the auroral oval, the substorm growth phase is

manifest as a growth of the polar cap region (by an equatorward expansion of the auroral oval borders in the midnight sector), after a southward turning of the IMF (Figure 1.6b).

The equatorward expansion of the auroral oval borders is consistent with the stretching of magnetic field lines discussed above. Expansive phase onset is signaled by a brightening of the equatorward most auroral arc (Figure 1.6c) within the region of proton precipitation [Voronkov *et al.*, 1999]. This auroral arc evolves into a large-scale vortex or surge with energetic (5-10 keV) electrons at the surge front. As the energy stored in the magnetotail is released, discrete arcs successively brighten poleward and westward of previous arcs (Figure 1.6d) leading to a stepwise northwestward expansion of the substorm-disturbed region [Kisabeth and Rostoker, 1974; Wiens and Rostoker, 1975]. The energetic electrons at the surge front comprise an upward FAC, which is closed by a westward electrojet, forming a 'wedgelet'. The previously stored energy is dissipated through a series of such wedgelets, each with a scale size ranging from 100-500 km and a characteristic lifetime of ~15 minutes [Rostoker, 1991]. The ensemble of wedgelets is believed to form the substorm current wedge. As the energy is dissipated the equatorward border of the auroral oval begins to retreat poleward (Figure 1.6e). The poleward retreat of the oval is the beginning of the recovery phase when the oval will return to its pre-substorm configuration (Figure 1.6f).

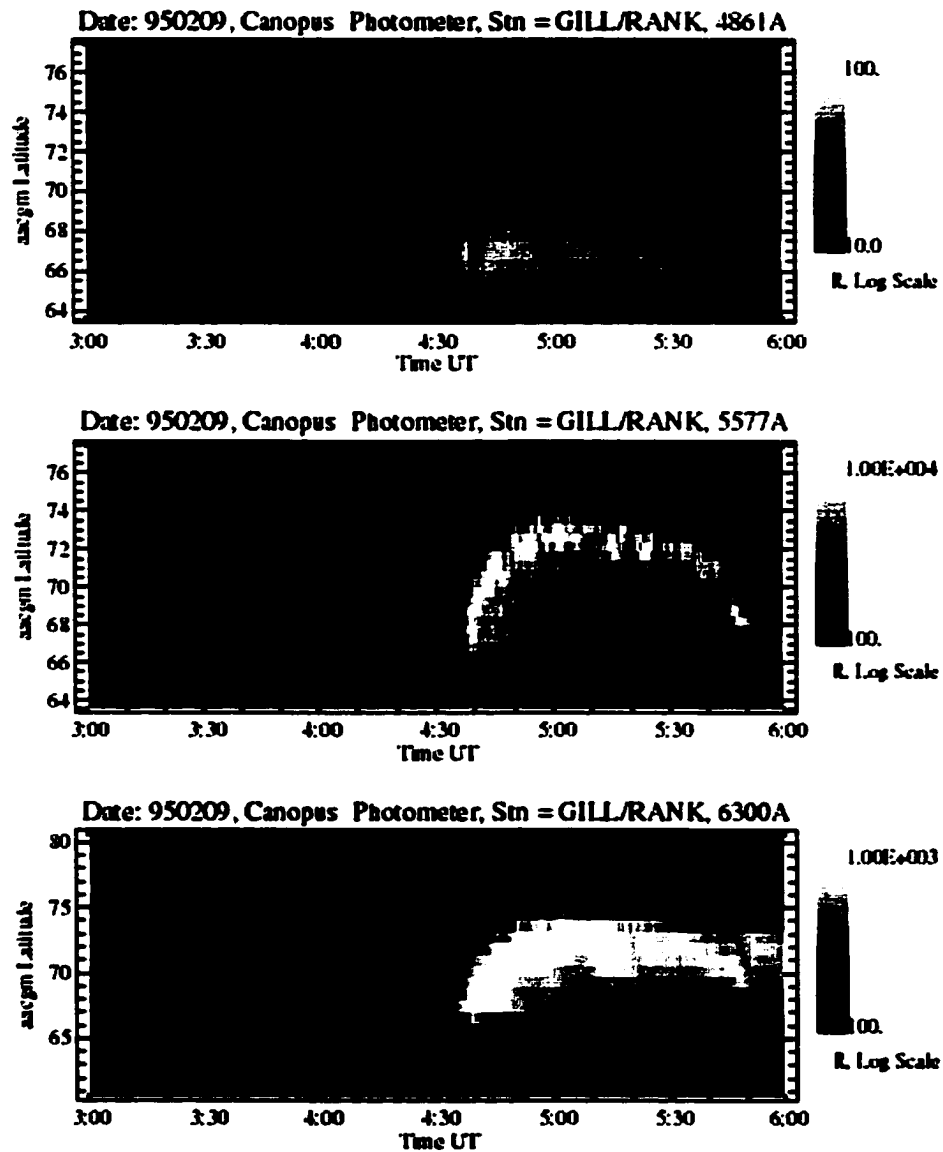


Figure 1.7: Meridian scanning photometer data from CANOPUS. The data from Gillam and Rankin have been merged to obtain the extended latitude range. From top to bottom panels show H β , 557.7 nm and 630.0 nm emissions (from Friedrich et al. [2001]).

1.5.1 Photometer Data

The growth and expansive phases of the substorm are seen quite clearly in meridian scanning photometer (MSP) data (Figure 1.7). The scale on the right side of the panels is a logarithmic scale in Rayleighs, a measure of surface brightness (the Rayleigh is defined

as a measure of the omnidirectional emission rate in a column of unit cross section along the line of sight: $1R = 10^6$ photons $\text{cm}^{-2} \text{s}^{-1}$). The top panel shows auroral emissions at a wavelength of 486.1 nm ($\text{H}\beta$) produced by energetic proton ($E > 20$ keV) precipitation. The $\text{H}\beta$ emissions are observed in a band on average between 64° and 68° latitude. They are not observed equatorward of this range due to the protons becoming trapped in the ring current region. They are not observed poleward of these latitudes because the protons, convecting from regions further down the magnetotail, do not possess sufficient energies. The middle panel exhibits 557.7 nm emissions produced by energetic proton precipitation during the growth phase and energetic electron interactions during the expansive phase. The bottom panel shows emissions produced at a wavelength of 630.0 nm by low energy (100's of eV) electrons. Appendix I gives a detailed description of the atmospheric chemistry producing these emissions.

The growth phase is observed as a gradual equatorward motion of the auroral emissions consistent with the stretching of dipolar magnetic field lines in the nightside magnetosphere [Wanliss *et al.*, 2000]. Expansive phase onset is characterized by a brightening of the $\text{H}\beta$ in the equatorward band of emissions (if more than one band is present) within which the auroral electron arc will brighten to initiate expansive phase onset. The emission region then begins to expand poleward as energy is released and dissipated during the expansive phase. The emission region continues to expand poleward in most cases reaching latitudes that are comparable to their pre-substorm levels.

1.6 Substorm Models

The nature of this field of science is such that dense sampling of fields and particles in the magnetosphere is very difficult due to the enormous amount of financial resources such measurements would require. While the situation is improving with greater numbers of satellites carrying instruments of higher sensitivity, the data available in the past have been scant in terms of multipoint observations. The result has been the creation of a multitude of substorm theories, based on observation or theory, which have

attempted to explain the phenomenon of the substorm either in whole or in part. Some of these theories include: Thermal Catastrophe Model [Goertz and Smith, 1989], Magnetosphere-Ionosphere Coupling Model [Kan, 1993], Boundary Layer Dynamic Model (BLDM) [Rostoker, 1996], Electric Field Model [Lyons, 1995], the Domino Theory [Calvert, 1998b], Near-Earth Current Disruption (NECD) [Lui, 1996], the Near-Earth Neutral Line Model (NENL) [Baker et al., 1996], and the flow braking model [Shiokawa et al., 1997; Birn et al., 1999]. There are a few models that deal solely with the mechanism for expansive phase onset. Some of these are: the Ballooning Instability [Roux et al., 1991; Bhattacharjee et al., 1998], the Shear Flow Ballooning Instability Model (SFBI) [Voronkov et al., 1997], and the Nonlinear Detonation Model [Hurricane et al., 1997, 1998]. Reviews of some of these models can be found in Lui [1991] and Elphinstone et al. [1996].

1.7 Thesis Outline

This thesis attempts to determine the most accurate substorm model out of those mentioned above by providing some robust observational constraints. Detailed analysis of the CANOPUS meridian scanning photometer data has been completed which has provided some clues to the substorm expansive phase process. In addition, a new model for the creation of the substorm current wedge has been developed which utilizes solely the directly driven current system, providing an alternative to the traditional current wedge concept. The data and instrumentation used in the research of this thesis will be discussed in Chapter 2. Chapter 3 will deal with some aspects of particle motion and magnetospheric dynamics during the growth phase of the substorm. The dynamics of the expansive phase established from observations of the magnetometer and photometer data will be discussed in Chapter 4. As mentioned earlier in this introduction, Chapter 5 will present a new substorm current wedge model. Finally, Chapter 6 will outline some conclusions and future directions.

Bibliography

- Akasofu, S. -I., The development of the auroral substorm, *Planet. Space Sci.*, 12(4), 273, 1964.
- Akasofu, S. -I., E.W. Hones Jr., S.J. Bame, J.R. Ashbridge, and A.T.Y. Lui, Magnetotail and boundary layers plasmas at a geocentric distance of ~ 18 RE: Vela 5 and 6 Observations, *J. Geophys. Res.*, 78, 7257, 1973.
- Armstrong, J. C., and A. J. Zmuda, Field-aligned current at 1100 km in the auroral region measured by satellite, *J. Geophys. Res.*, 75, 7122, 1970.
- Armstrong, J. C., and A. J. Zmuda, Triaxial magnetic measurements of field-aligned currents at 800 km in the auroral region: initial results, *J. Geophys. Res.*, 78, 6802, 1973.
- Baker, D. N., T. I. Pulkkinen, V. Angelopoulos, W. Baumjohann, and R. L. McPherron, Neutral line model of substorms: Past results and present view, *J. Geophys. Res.*, 101, 12975, 1996.
- Biermann, L., Solar corpuscular radiation and the interplanetary gas, *Observatory*, 77, 109, 1957.
- Calvert, W., The gotcha-kata-kata or “domino” theory of substorm expansion, in *Substorms-4*, edited by S. Kokubun and Y. Kamide, pp. 259-263, Terra Sci. Publ. Co., Tokyo, Japan, 1998b.
- Cummings, W.D., and A.J. Dessler, Field aligned currents in the magnetosphere, *J. Geophys. Res.*, 72, 1007, 1967.
- Davidson, G. T., Expected spatial distribution of low-energy protons precipitated in the auroral zones, *J. Geophys. Res.*, 70, 1061, 1965.
- Dungey, J.W., Interplanetary magnetic field and the auroral zones, *Phys. Rev. Lett.*, 6, 47, 1961.
- Eastman, T.E., E.W. Hones Jr., S.J. Bame and J.R. Ashbridge, The magnetospheric boundary layer: site of plasma, momentum and energy transfer from the magnetosheath into the magnetosphere, *Geophys. Res. Lett.*, 3, 685, 1976.
- Elphinstone, R. D., J. S. Murphree, and L. L. Cogger, What is a global auroral substorm?, *Rev. Geophys.*, 34, 169, 1996.
- Feldstein, Y. I., Auroral oval, *J. Geophys. Res.*, 78, 1210, 1973.

- Frank, L.A., Plasma in the Earth's polar magnetosphere, *J. Geophys. Res.*, 76, 5202, 1971c.
- Fukunishi, H., Dynamic relationship between proton and electron auroral substorms, *J. Geophys. Res.*, 80, 553, 1975.
- Goertz, C. K., and R. A. Smith, The thermal catastrophe model of substorms, *J. Geophys. Res.*, 94, 6581, 1989.
- Hasegawa, A. and T. Sato, Generation of field-aligned current during substorms, in *Dynamics of the Magnetosphere*, ed. S.-I. Akasofu, D. Reidel Publishing, New York, p. 529, 1979.
- Iijima, T. and T. A. Potemra, The amplitude distribution of field-aligned currents at northern high latitudes observed by TRIAD, *J. Geophys. Res.*, 81, 2165, 1976a.
- Iijima, T. and T. A. Potemra, Large-scale characteristics of field-aligned currents associated with substorms, *J. Geophys. Res.*, 83, 599, 1978.
- Iijima, T., T. A. Potemra, and L. J. Zanetti, Large-scale characteristics of magnetospheric equatorial currents, *J. Geophys. Res.*, 95, 991, 1990.
- Kan, J. R., Generation of field-aligned currents in magnetosphere-ionosphere coupling in an MHD plasma, *Planet. Space Sci.*, 35, (7), p. 903, 1987.
- Kan, J. R., A global magnetosphere-ionosphere coupling model of substorms, *J. Geophys. Res.*, 98, 17263, 1993.
- Kisabeth J. L. and G. Rostoker, The expansive phase of magnetospheric substorms 1. Development of the auroral electrojets and auroral arc configuration during a substorm, *J. Geophys. Res.*, 79, 972, 1974.
- Kistler, L.M., E. Möbius, W. Baumjohann, G. Paschmann, and D.C. Hamilton, Pressure changes in the plasma sheet during substorm injections, *J. Geophys. Res.*, 97, 2973, 1992.
- Kivelson, M. G. and C. T. Russell, *Introduction to Space Physics*, Cambridge University Press, New York, © 1995.
- Lui, A. T. Y., A synthesis of magnetospheric substorm models, *J. Geophys. Res.*, 96, 1849, 1991.
- Lui, A. T. Y., Current disruption in the Earth's magnetosphere: Observations and models, *J. Geophys. Res.*, 101, 13067, 1996.

- Lui, A.T.Y., C.D. Anger, and S.-I. Akasofu, The equatorward boundary of the diffuse aurora and auroral substorms as seen by the ISIS 2 auroral scanning photometer, *J. Geophys. Res.*, *80*, 3603, 1975.
- Lui, A.T.Y., E.W. Hones Jr., F. Yasuhara, S.-I. Akasofu, and S.J. Bame, Magnetotail plasma flow during plasma sheet expansions: Vela 5 and 6 and Imp 6 observations, *J. Geophys. Res.*, *82*, 1235, 1977.
- Lyons, L. R., A new theory for magnetospheric substorms, *J. Geophys. Res.*, *100*, 19069, 1995.
- McPherron, R.L., Growth phase of magnetospheric substorms, *J. Geophys. Res.*, *75*, 5592, 1970.
- Olson, J. V., Pi2 pulsations and substorm onsets: A review, *J. Geophys. Res.*, *104*, 17499, 1999.
- Parks, G. K., *Physics of Space Plasmas: An Introduction*, Addison-Wesley Publishing, New York, © 1991.
- Parker, E. N., Interaction of the solar wind with the geomagnetic field, *Phys. Fluids*, volume 1, 171, 1958.
- Potemra, T. A., Sources of large-scale Birkeland currents, in *Physical Signatures of Magnetospheric Boundary Layer Processes*, eds. J. A. Holtet and A. Egeland, Kluwer Academic Publishers, Netherlands, p. 3, 1994.
- Rees, M. H., *Physics and Chemistry of the Upper Atmosphere*, Cambridge University Press, New York , © 1989.
- Reme, H., and J. M. Bosqued, Evidence near the auroral ionosphere of a parallel electric field deduced from energy and angular distributions of low-energy particles, *J. Geophys. Res.*, *76*, 7683, 1971.
- Rostoker, G., The role of magnetospheric substorms in magnetosphere-ionosphere coupling, in *The Solar Wind and the Earth*, eds. S.-I. Akasofu and Y. Kamide, Terra Scientific Publishing Company, Tokyo, p. 163, 1987.
- Rostoker, G., Some observational constraints for substorm models, in *Magnetospheric Substorms*, ed. By J.R. Kan, T.A. Potemra, S. Kokubun, and T. Iijima, pp. 61-72, Geophys. Monograph 64, AGU, Washington, DC, 1991.
- Rostoker, G., Phenomenology and physics of magnetospheric substorms, *J. Geophys. Res.*, *101*, 12955, 1996.

- Rostoker, G. and S.H. Skone, Magnetic flux mapping considerations in the auroral oval and the Earth's magnetotail, *J. Geophys. Res.*, *98*, 1377, 1993.
- Rostoker, G., S.-I. Akasofu, W. Baumjohann, Y. Kamide, and R.L. McPherron, The roles of direct input of energy from the solar wind and unloading of stored magnetotail energy in driving magnetospheric substorms, *Space Sci. Rev.*, *46*, 93, 1987a.
- Roux, A., S. Perraut, P. Robert, A. Morane, A. Pedersen, A. Korth, G. Kremser, B. Aparicio, D. Rodgers, and R. Pellinen, Plasma sheet instability related to the westward traveling surge, *J. Geophys. Res.*, *96*, 17697, 1991.
- Samson, J. C., Mapping substorm intensifications from the ionosphere to the magnetosphere, in *Proceedings of the ICS-2 International Conference on Substorms*, eds. J. R. Kan, J. D. Craven, and S.-I. Akasofu, Fairbanks, Alaska, USA, p. 237, 1994.
- Sugiura, M. and T. A. Potemra, Net field-aligned currents observed by TRIAD, *J. Geophys. Res.*, *81*, 2155, 1976.
- Vasyliunas, V. M., Discussion of paper by Harold E. Taylor and Edward W. Hones, Jr.: Adiabatic motion of auroral particles in a model of the electric and magnetic fields surrounding the earth, *J. Geophys. Res.*, *73*, 5805, 1968.
- Vasyliunas, V. M., Fundamentals of current description, in *Magnetospheric Currents*, ed. T. A. Potemra, Geophys. Monograph 28, AGU, Washington, D.C., p. 63, 1984.
- Voronkov, I., R. Rankin, P. Frycz, V. T. Tikhonchuk, and J. C. Samson, Coupling of shear flow and pressure gradient instabilities, *J. Geophys. Res.*, *102*, 9639, 1997.
- Voronkov, I., E. Friedrich, and J.C. Samson, Dynamics of the substorm growth phase as observed using CANOPUS and SuperDARN instruments, *J. Geophys. Res.*, *104*, 28491, 1999.
- Wallis, D. D. and E. E. Budzinski, Empirical models of height integrated conductivities, *J. Geophys. Res.*, *86*, 125, 1981.
- Wanliss, J. A., J. C. Samson, and E. Friedrich, On the use of photometer data to map dynamics of the magnetotail current sheet during substorm growth phase, *J. Geophys. Res.*, in press, 2000.
- Wiens, R. G. and G. Rostoker, Characteristics of the development of the westward electrojet during the expansive phase of magnetospheric substorms, *J. Geophys. Res.*, *80*, 2109, 1975.
- Yasuhara, F., Y. Kamide, and S.-I. Akasofu, Field-aligned and ionospheric currents, *Planet. Space Sci.*, *23*, 1355, 1975.

Zmuda, A.J., J.H. Martin, and F.T. Heuring, Transverse magnetic disturbances at 1100 km in the auroral region, *J. Geophys. Res.*, 71, 5033, 1966.

Zmuda, A.J., F.T. Heuring, and J.H. Martin, Dayside magnetic disturbances at 1100 km in the auroral oval, *J. Geophys. Res.*, 72, 1115, 1967.

Zmuda, A. J. and J. C. Armstrong, The diurnal flow pattern of field-aligned currents, *J. Geophys. Res.*, 79, 4611, 1974b.

Chapter 2: Instrumentation and Data Analysis

The ground-based CANOPUS and SuperDARN arrays, and the GOES geostationary satellites provided the data used for this research. This chapter contains descriptions of the CANOPUS and SuperDARN arrays, the GOES satellites, the instruments provided by each of these sources, and the methods of data processing used in this thesis work.

2.1 CANOPUS

CANOPUS began in the early 1980's as a vehicle to allow Canadian scientists to participate in NASA's OPEN (Origin of Plasmas in the Earth's Neighborhood) program. In its entirety, the acronym stands for: Canadian Auroral Network for the OPEN Program Unified Study. A large-scale array of remote sensing instruments, CANOPUS monitors the high latitude ionosphere from the north-central to the northwest portion of North America. It comprises 13 magnetometers and riometers, four meridian scanning photometers, and a digital all sky camera. The instruments are linked by geostationary satellite to a central receiving node in Ottawa, where data are archived and made available to participating scientists through the data collection system (DCS) and data analysis network (DAN). Figure 2.1 shows the sites and various instruments of the CANOPUS array. The coordinates of each site are given in Table 2.1. In 1988 OPEN was renamed GGS (Global Geospace Science) and integrated into the International Solar Terrestrial Physics (ISTP) program.

2.1.1 Magnetometers

This thesis used data from a series of magnetometers running along a north/south line through Fort Churchill and Taloyoak. The Churchill line consists of seven sites, from Pinawa to Taloyoak (see Figure 2.1), extending from 61° to 80° North

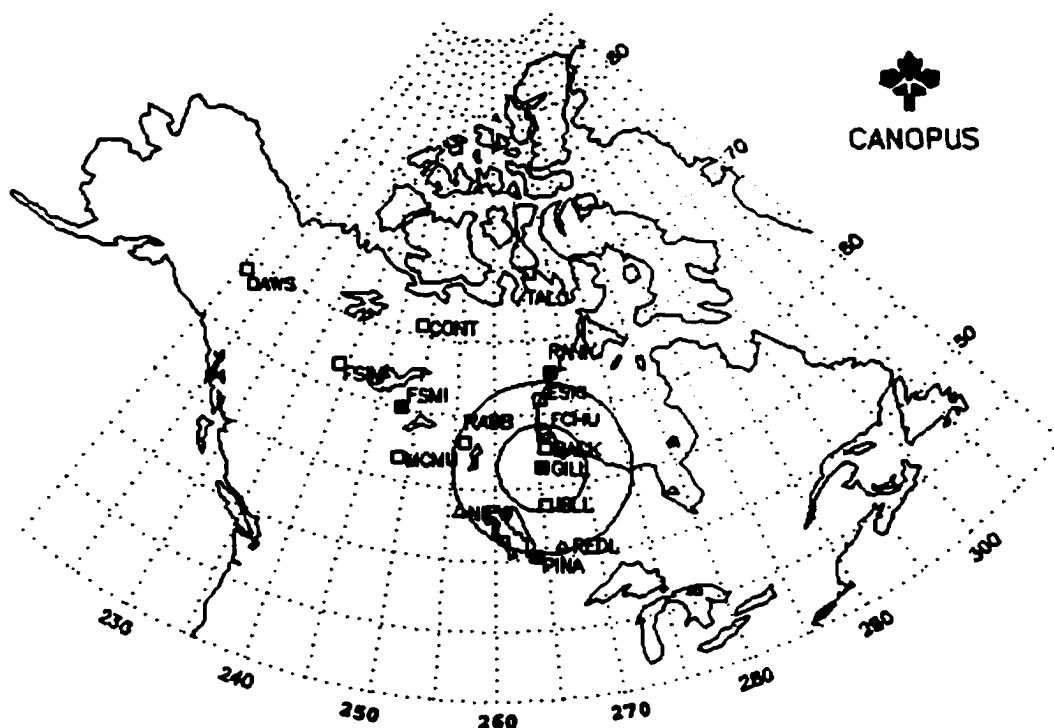


Figure 2.1: Map of CANOPUS stations and instrumentation. Dark squares represent locations of meridian scanning photometers (MSP). The circle centered on Gillam represents the field of view of the MSP. See Table 2.1 for details.

PACE (Polar Anglo-American Conjugate Experiment) latitude [Baker and Wing, 1989]. (Note that the Churchill line magnetometers are oriented in geodetic coordinates with the X-component set as geodetic north. The geomagnetic field declination along the Churchill line, except at TALO, is less than 3 degrees so that geographic north and geomagnetic north are essentially equivalent. The PACE coordinate system is a variation on the corrected geomagnetic coordinate system.) The magnetometers are 3-component ring-core fluxgate magnetometers operating over a dynamic range of 80,000 nT, with a resolution of 0.025 nT and an 8 Hz output sample rate. Along with the magnetometer, each site is equipped with a 30 MHz zenith riometer, including a 4-element antenna and a single 250 kHz broadband receiver. The riometers sample the ionosphere for variations in cosmic radio noise absorption over a region of ~100 km radius centered at the zenith. The noise absorption can be quantitatively related to the flux of energetic electrons

Table 2.1 CANOPUS Instrument Sites (originally published in Rostoker [1995])

Location	Station	Geographic		PACE ^b		L	Instr. ^a
		Acronym	Lat.	Long.	Lat.		
Back	BK	57.7	265.8	68.72	-30.58	7.5	M
ContwoytoLK	CL	65.8	248.8	73.43	-61.23	12.4	M
Dawson	DC	64.1	220.9	65.93	-90.08	5.9	M
EskimoPoint	EP	61.1	266.0	71.93	-31.75	10.2	M
FtChurchill	FC	58.8	265.9	69.72	-30.76	8.2	M
FtMcMurray	FM	56.7	248.8	64.81	-54.37	5.5	M
Ft Simpson	FS	61.7	238.8	67.62	-69.86	6.8	M
Ft Smith	SM	60.0	248.1	67.92	-57.29	7.1	M P
Gillam	GI	56.4	265.4	67.38	-30.93	6.7	M P I
IslandLake	IL	53.9	265.3	64.94	-30.33	5.5	M
Nipawin	NI	53.5	256.3	63.20	-43.10	4.9	R
Pinawa	PI	50.2	264.0	61.16	-31.58	4.3	M P
Rabbit Lake	RB	58.2	256.3	67.77	-45.04	6.9	M
Rankin Inlet	RI	62.8	267.9	73.72	-28.97	12.4	M P
Red Lake	RL	50.9	266.5	62.20	-28.00	4.5	R
Taloyoak	TA	69.5	266.5	79.65	-36.38	29.96	M

^a M = Magnetometer, riometers, tellurics (MARIA).

P = Meridian scanning photometer (MPA).

I = All-sky imager (ASI).

^b See Baker and Wing (1989) for a description of eccentric PACE invariant coordinates. L is the location that a field line, associated with a particular station, would cross the equatorial plane, i.e. the L value for that station.

precipitating overhead into the ionosphere. Therefore, the riometers can be considered as an instrument for detecting overhead particle precipitation.

The 8 Hz output data streams are subsequently merged and filtered using a 0.1 Hz lowpass digital filter before yielding one sample every 5 seconds. The data are transmitted to Ottawa on average every 2.5 minutes, with each transmission containing 30 samples of each measured component.

2.1.1a Latitude Profiles

Latitude profiles are a useful means by which to study the spatial and temporal development of three-dimensional current systems (i.e. current systems including large-scale ionospheric currents and vertical Birkeland currents), and their use as a technique to study magnetic disturbances has been discussed by several authors [e.g. *Walker*, 1964; *Bonnevier et al.*, 1970; *Kisabeth and Rostoker*, 1971]. A latitude profile is produced by plotting the X, Y, and Z components of magnetic perturbations observed along a chain of stations, as a function of latitude at a specific instant in time. (The X, Y and Z components are part of the local geodetic system in which the X axis is directed positive northward, the Y axis is defined positive eastward, and the Z axis completes the right-hand system and is defined vertically downward.) An example of a latitude profile is given in Figure 2.2. The latitude profile in this figure represents a westward electrojet centered at 67.5° N latitude. The peak in the negative X component provides a measure of the strength of the ionospheric currents. For example, a one MA current can produce a magnetic perturbation of ~ 750 nT, which is above average for the magnitude of a substorm perturbation. The width of the current system can be inferred from the latitudinal distance between the positive and negative Z-component peaks. The center of the current system (assuming that there is only one current flowing at the time of the observations) can be determined from the latitudinal position of the peak of the negative X-component and from the position where the Z-component crosses zero. The Y-component provides a measure of whether the central meridian of the observed perturbation pattern is east, west, or coincides with the line of observing stations.

In many cases, there is more than one current flowing in the ionosphere producing magnetic perturbations that cannot be attributed to a specific current system. In such cases a technique known as differential profiling [*Kisabeth and Rostoker*, 1973] can be used to filter out perturbations due to complex current structures. The technique involves using magnetic field values at a specific instant in time that is just prior to the time of interest, as baseline values from which new perturbation magnitudes could be measured. Producing a differential profile assumes that the current flowing at the time of baseline choice does not change much in the ensuing few minutes. As a result, this technique is

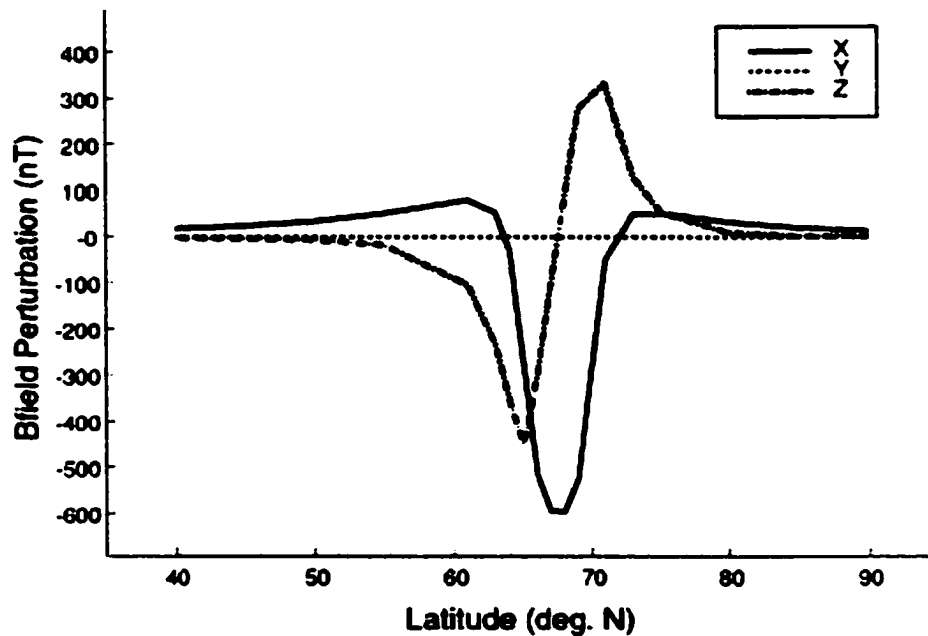


Figure 2.2: Example of a latitude profile showing a westward electrojet centered on 65°N and 5° wide in latitudinal extent.

only valid for a short interval of time (a few minutes) from the time chosen as the baseline value.

2.1.2 Photometers

Along with the magnetometers of the Churchill line, data from two of the four meridian scanning photometers (Rankin Inlet and Gillam) were also utilized in this thesis. Each photometer is equipped with an eight-channel filterwheel that permits it to measure auroral emissions at five wavelengths (630.0, 557.7, 470.9, and two at 486.1 nm) and background emissions at three wavelengths (625.0, 493.5, and 480.0 nm). The background intensities are provided to correct for contamination of the data caused by blended auroral emissions, and scattered light of solar and/or lunar origin.

The photometers scan the Churchill meridian twice each minute, once on the even minute and again 30 seconds later, providing an output of 510 samples per scan per channel. Each scan is corrected for nonlinearity and for dark count and then binned into

17 latitudinal bins. The scan starting at the even minute and the scan starting 30 seconds later are then averaged. As well, the data from the two 486.1 nm channels and the two corresponding background channels (480.0 and 493.5 nm) are averaged. Bin boundaries are computed assuming an altitude of 110 km (for 470.9, 486.1, and 557.7 nm emissions) with a 0.5° latitude in width. For 630.0 and 625.0 nm, the emission altitude is assumed to be 250 km with the resulting bins being 1.0° width in latitude.

Two scans in the resulting four auroral emissions, two background channels as well as housekeeping data are transmitted by each instrument every two minutes to the node at Ottawa. More detailed information about CANOPUS, its instruments and their description can be found in *Rostoker et al.* [1995].

2.1.2a Determining the borders of the auroral emissions

Chapters 3 and 4 will discuss the dynamics of the substorm growth and expansive phases from an in-depth look at the poleward and equatorward borders of the auroral emissions. In this section, the methods of calculating the borders of the auroral emissions will be discussed.

Blanchard et al. [1995] provided a means by which to determine the poleward border of the 630.0 nm emissions by fitting a step function to the photometer data. The step function represents an idealized emission profile: In the polar cap it is assumed that the emissions are low intensity (< 300 R) and uniform; while at the boundary of the auroral zone, it is assumed that the intensity (I) of emissions jumps by ΔI and remains uniform throughout the auroral zone. To calculate the boundary of the emissions, the authors begin at the most poleward latitudes of the data and, moving equatorward, create step functions at each latitude. For each step function created, the intensity in the polar cap (I_{pc}) and the difference in intensity between two adjacent latitudes (ΔI) are written to a file. A coefficient of determination is also calculated at each stage and stored. A fit to the data is found when certain criteria are met: if I_{pc} is equal to the polar cap intensity (i.e. low intensity emissions < 300 R), ΔI is an appreciable jump in intensity ($> 0.75 I_{pc}$), and the coefficient of determination is at a maximum. The poleward edge of the data is

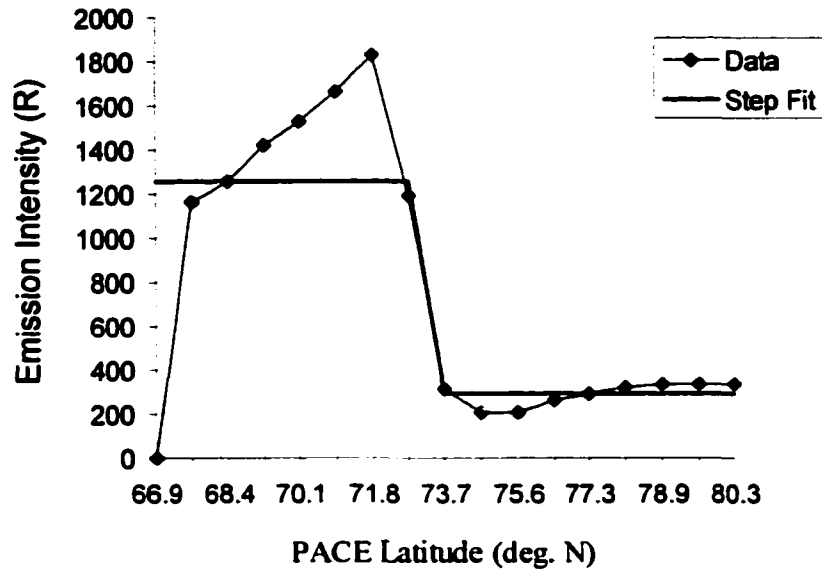


Figure 2.3: An example of a step function fit of the 630.0 nm data for October 7, 1989 at 0433 UT. The poleward edge is calculated to be $\Lambda = 73.2^\circ$.

calculated as the point halfway between the minimum and maximum level of the step (Figure 2.3).

The step function algorithm is designed for data that exhibits a stark contrast between the low intensities of background emissions and the higher intensities of the emissions due to energetic precipitating particles. In this respect it is well suited for the 630.0 nm emissions where the data changes quickly from the low intensity polar cap emissions to the much higher intensity of the emissions due to the precipitation of particles at auroral latitudes. Indeed, the events discussed by *Blanchard et al.* [1995] exhibit this characteristic strongly and the step function fits the data quite well. The data studied for this thesis, however, were of substorm intervals (the *Blanchard et al.* study was for predominantly non-substorm intervals) and as a result the background emissions, within latitudes close to the maximum of the emissions, are heightened in intensity. The contrast between the emissions, needed by the step function, is no longer as pronounced. This was especially true of the 557.7 nm data, which the step function had difficulty fitting.

Apart from the difficulty with the step function, repeated examination of the data showed that the emissions were not uniform throughout the auroral zone, as assumed by *Blanchard et al.* [1995], but rather exhibited a Gaussian profile (see, for example, Figures 2.5 and 2.6 below). It seemed natural, therefore, to fit the data using a Gaussian distribution. Using a Gaussian distribution provides the latitudinal location of the maximum of the emissions as well as the equatorward and poleward borders of the photometer data. The added value of the information gained by adopting the Gaussian algorithm, and the apparent structure of the data, supported the decision to fit the data using a Gaussian distribution as opposed to a step function.

There are two reasons why the data is observed to be Gaussian in shape: the natural form of the emissions themselves, and the fact that the data analyzed are from the separate Gillam and Rankin stations—not the merged data.

H β and 557.7 nm data are predominantly Gaussian in shape due to the latitudinal location of the enhanced emissions. This is especially true of the growth phase emissions, where the enhanced emissions are confined to a fairly narrow latitudinal band and are surrounded by emissions of lower intensity. Figure 2.4 shows an example of the 486.1 nm, 557.7 nm, and 630.0 nm data for an event that occurred on January 18, 1996. Examples of the latitudinal cross-sections of the data at specific universal times are shown in Figures 2.5 and 2.6. The ground-based observing station, Gillam, observes the ionosphere along a range of latitudes from 63° – 71° North. The H β and 557.7 nm emissions are clearly at a maximum within the latitudes covered by the Gillam photometer. Similarly, the photometer at Rankin Inlet scans a meridian from 67° – 81° North and the 630.0 nm emissions exhibit a maximum within this range.

A program (called Extract) was developed to create the theoretical Gaussian distribution and fit the data. Extract is written in C++ with object-oriented architecture and command line input control. Depending on the commands given by the user, Extract will obtain, process and analyze the photometer data and place the results in an output file.

An example of the command line input for the program is given below:

```
extract -b 270 -e 320 -g -s 40 -l 0 -sh 300 95020900_g_6300.dat g6300.dat
```

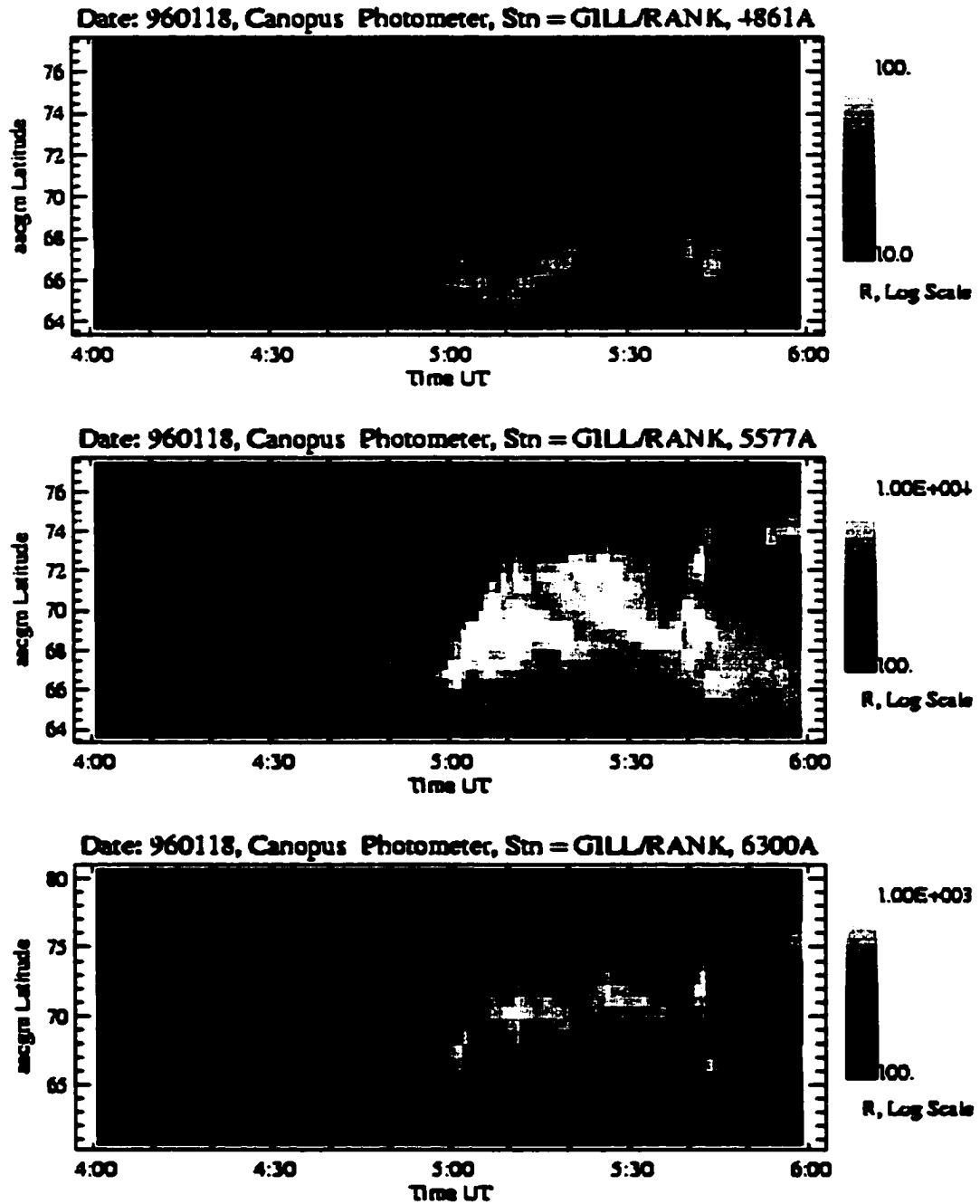


Figure 2.4: Meridian scanning photometer data for January 18, 1996. From top to bottom panels show 486.1 nm, 557.7 nm and 630.0 nm data.

The first field is the name of the program, the second field (-b 270) is the start time for the border calculation (the times are based on UT minutes rather than hours: 270 minutes = 0430 UT), -e 320 is the end time for the calculation, -g indicates fitting a Gaussian

profile to the data, the `-s 40` command determines where in the profile the edge of the emissions is found, the `-l` command indicates whether or not to interpolate the data where 0 indicates no interpolation and 5 indicates the maximum index for interpolation. The `-sh` command directs the program to write the emission data and the theoretical profile to an output file for a specified UT time, in this case $t=300$ UT minutes. This allows the user to inspect the detailed structure of the emission data and the fit to that data for a specific time. The next field is the name of the input data file and the final field is the name of the output file, chosen by the user. By typing `'extract -h'` a small help file is produced which lists these commands and their functions. A few of these commands will be discussed in more detail below.

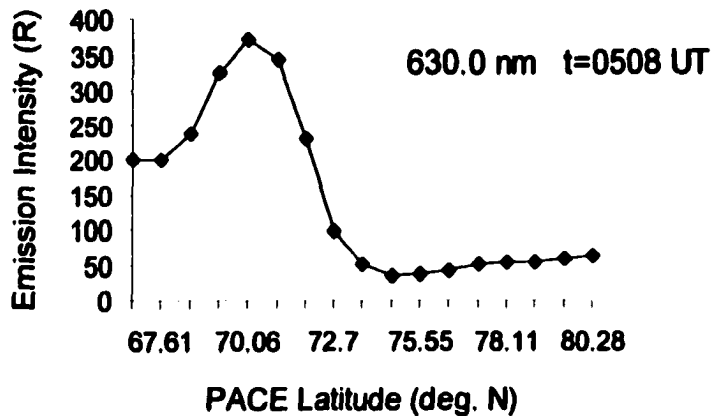
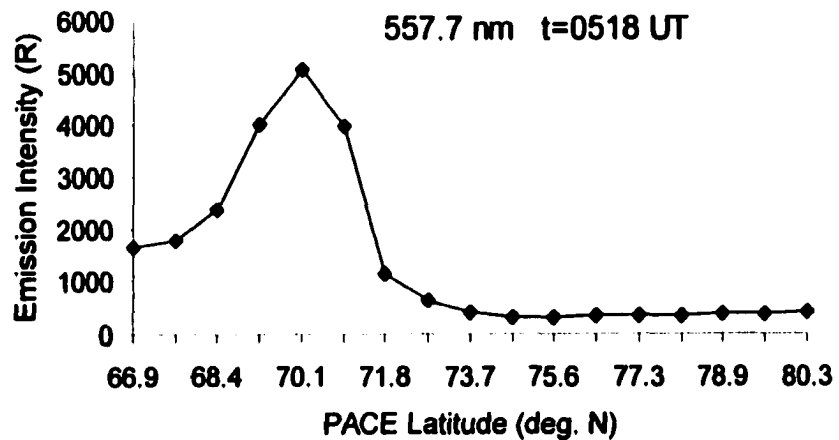
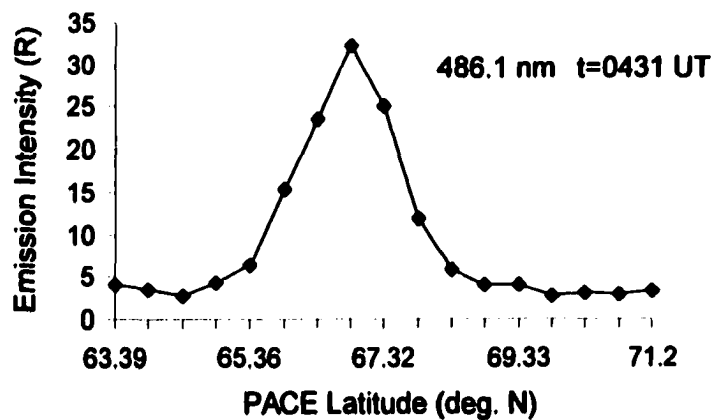


Figure 2.5: Cross-sections of the photometer data for January 18, 1996. Top left: H β data at 0431 UT, top right: 557.7 nm data at 0518 UT, bottom: 630.0 nm data at 0508 UT.

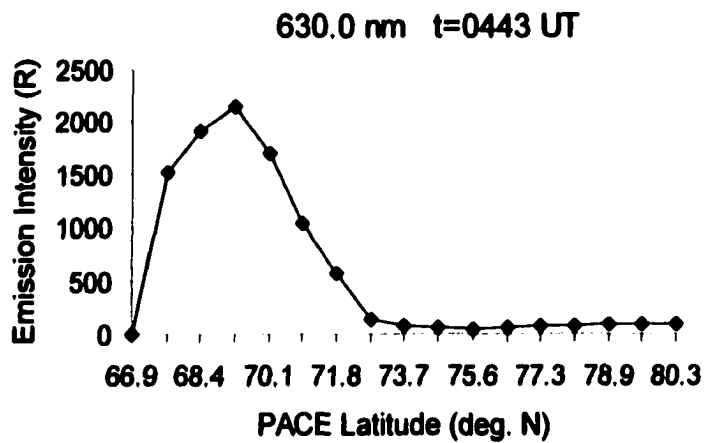
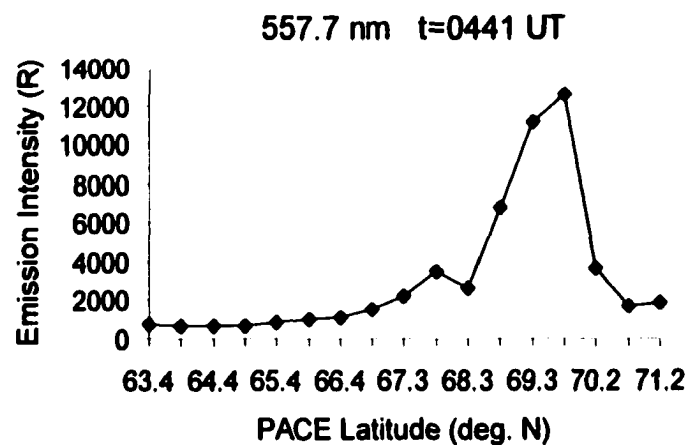
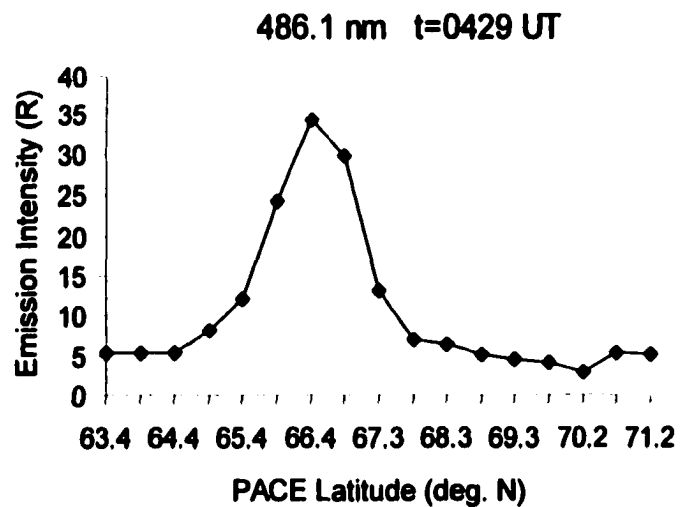


Figure 2.6: Cross-sections of the photometer data for February 9, 1995. Top left: H β data at 0429 UT, top right: 557.7 nm data at 0441 UT, bottom: 630.0 nm data at 0443 UT.

The Extract program has been written in a fairly general form so that the photometer data can be analyzed in many different ways. Aside from fitting a Gaussian profile to the data (-g command), the user can instead choose to fit a step function to the data (-sf) (based on the work by *Blanchard et al.* [1995, 1997]), or simply locate the maximum of the emissions (-m). The -m command is particularly useful for the H β data, which suffers from emission spreading [*Davidson*, 1965]. Finally, in addition to finding the poleward edge of the data, the equatorward border can also be determined by adding -eq to the command line inputs. This command was used extensively for the growth phase study discussed in Chapter 3.

The function used to create the theoretical Gaussian distribution used to fit the data is given by Equation 2.1:

$$f_{X,\sigma}(x) = \frac{1}{\sigma\sqrt{2\pi}} e^{-(x-X)^2/2\sigma^2} \quad 2.1$$

where X is the center, or mean, of the distribution and σ is the width [*Taylor*, 1982 pg. 112].

Thus, for the time range input by the user (-b and -e commands) the program locates the maximum of the emissions and treats the maximum as the mean of the distribution. Then the program creates a theoretical Gaussian profile with a narrow width ($\sigma = 0.2$) and systematically increases σ until the theoretical profile matches the distribution of the data. The fit between each theoretical profile and the data is monitored by calculating a coefficient of determination (also known as a correlation coefficient) [*Taylor*, 1982 pg. 180]:

$$r = \frac{\sigma_{xy}}{\sigma_x \sigma_y} \quad 2.2$$

where $\sigma_{xy} = \frac{1}{N} \sum (x_i - X)(y_i - Y)$ is the covariance between the data and the theoretical profile, and σ_x and σ_y are the standard deviations in each case. The fit is chosen when this coefficient is maximized; that is, when r approaches 1.

Once the appropriate Gaussian profile is found, the edge of the data must be determined. The -s command defines the edge of the emission data by utilizing the fact

that 34% of the area under a normal distribution (calculated from the mean) corresponds to one standard deviation and 47% corresponds to two standard deviations. It is assumed that the poleward edge, for example, of the photometer data would be located somewhere between these two limits. The choice of where to locate the poleward edge of the profile was constrained by comparing the Gaussian fits to the poleward edges identified by *Blanchard et al.*'s step function method. As mentioned above, *Blanchard et al.* [1995] used a step function to determine the poleward border of the 630.0 nm data. The authors verified their procedure and results by comparing with precipitating particle observations from the Defence Meteorological Satellite Program (DMSP) satellites. The results of their comparison showed that fitting a step function to the data accurately determined the poleward edge with an estimated precision of $\pm 0.9^\circ$ invariant latitude. We compared the latitudinal location of the poleward edge of the emissions determined by *Blanchard et al.* to our theoretical Gaussian fits to determine what standard deviation should be chosen as the poleward edge. The results of the comparison showed that the poleward edge was found on average for a $\sigma = 1.5$. A standard deviation of 1.5 corresponds to $\sim 40\%$ of the integrated area under the Gaussian distribution. Figures 2.7 to 2.10 illustrate the comparison between Blanchard's step function fit and our Gaussian fit to the data.

Latitudinal spreading of the emission data, noted primarily in the 486.1 nm data [*Davidson, 1965*], can extend up to 2° from its location of maximum intensity. As a result, the poleward edge of the 486.1 nm data gets obscured within the spreading and it becomes difficult to determine the exact latitudinal location of the edge of the emissions. For this reason, the latitude of the maximum intensity of the emissions was used, rather than the edge of the emissions, as the indicator of the dynamics of the H β data.

An example of the poleward borders of the 557.7 nm and 630.0 nm emissions and the latitude of the maximum intensity emissions of the 486.1 nm data are shown in Figure 2.11.

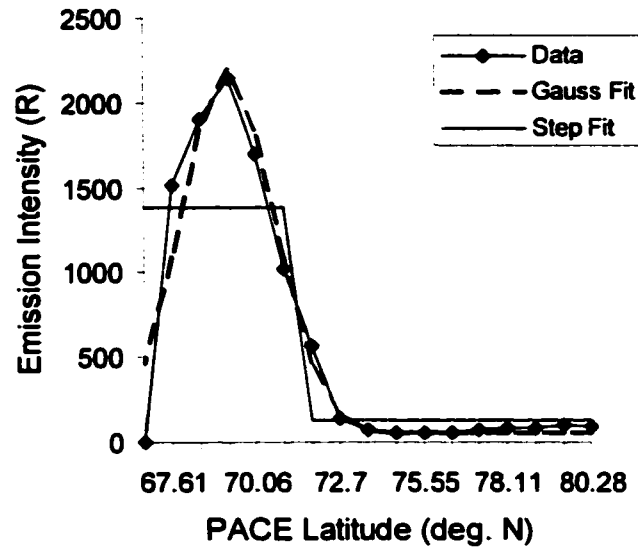


Figure 2.7: Comparison of the Gauss and Step fit for the February 9, 1995 event 630.0 nm data at $t=0443$ UT. The poleward edge of the emissions, calculated by the step function is $\Lambda=71.4^\circ$. This latitude corresponds to a standard deviation of ~ 1.5 .

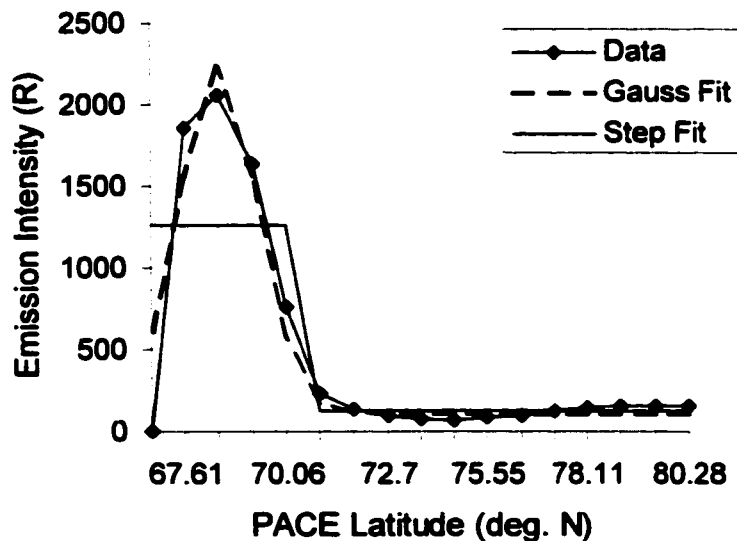


Figure 2.8: The Gauss and Step fits for the March 9, 1995 event 630.0 nm data at $t=0504$ UT. The poleward edge of the data, calculated by the step function is $\Lambda=70.5^\circ$. This latitude corresponds to a $\sigma = 2.0$.

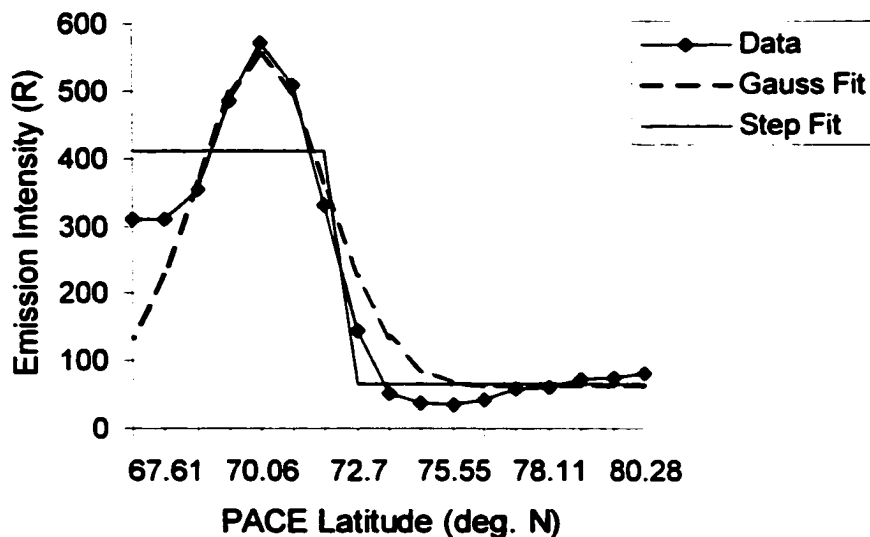


Figure 2.9: A comparison of the Gauss and Step fits of the 630.0 nm data for January 18, 1996 at $t=0518$ UT. The step fit calculates the poleward edge of the photometer data to be $\Lambda=72.3^\circ$ corresponding to a $\sigma=1.5$.

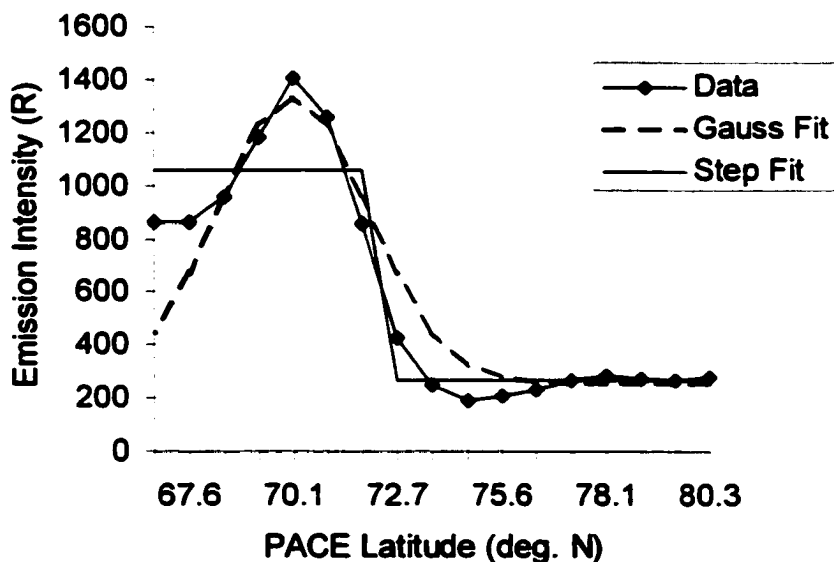


Figure 2.10: The Gauss and Step Function fits of the 630.0 nm data for Oct 7, 1989 at $t=0425$ UT. The step fit calculates the poleward edge of the data to be $\Lambda=72.3^\circ$ corresponding to a $\sigma=1.5$.

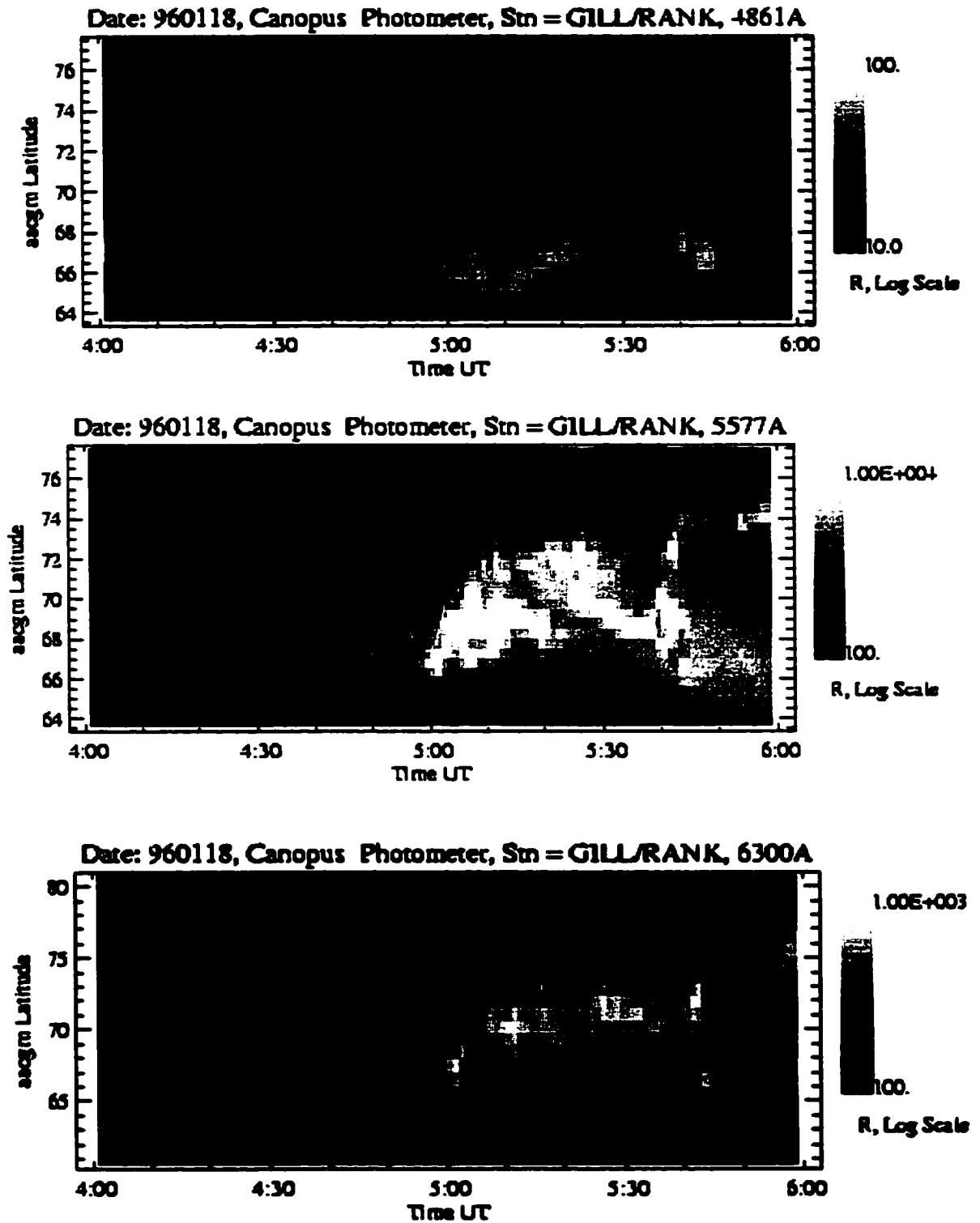


Figure 2.11 The poleward borders of the 557.7 nm and 630.0 nm photometer emissions and the latitude of the maximum intensity of the 486.1 nm data for January 18, 1996.

For a majority of the events the cross-sections of the data involve only one central peak of maximum intensity, which the program can easily discern as the mean of the Gaussian distribution. However, in some cases the data involves more structure and multiple peaks exist. An example of a cross-section involving multiple peaks is shown in Figure 2.12. For this example the maximum peak is clearly discernible and the Extract program easily chooses it as the mean of the data. A problem arises however when the size of the peaks are within 90% of each other, as the choice of which peak to use as the mean for the theoretical profile becomes unclear. The program attempts to solve this problem by checking if two adjacent peaks in the data are within 90% magnitude of each other. If so, the user can instruct the program to locate the poleward or equatorward peak and use that peak as the mean of the Gaussian distribution.

While most of the data examined in this thesis is well represented by a Gaussian distribution, there were some instances of the 557.7 nm and 630.0 nm data during the expansive phase of the substorms where the data was clearly not Gaussian in shape and obviously would be fit better by the step function algorithm. For example, Figure 2.13 shows a cross-section of the 630.0 nm data for the January 20, 1996 event at 0609 UT that is non-Gaussian in shape.

The border calculated from data that is non-Gaussian in shape will clearly stand out as being incorrect (Figure 2.14 $t=0609$ UT). Once the time of the incorrect border point is identified, it can be analyzed using the `-sh` (show) command to determine its shape. The latitude of the poleward border, in these cases, can be found using a step function fit.

It should be noted that the frequency of occurrence of the non-Gaussian shaped data ranged from $< 2\%$ for events such as February 9, 1995 to $\sim 20\%$ of the 630.0 nm data for the January 20, 1996 event. Anyone analyzing photometer data with the intent of calculating emission borders should be aware that the possibility exists that the data might be non-Gaussian in structure and that these data should be analyzed separately on a case-by-case basis.

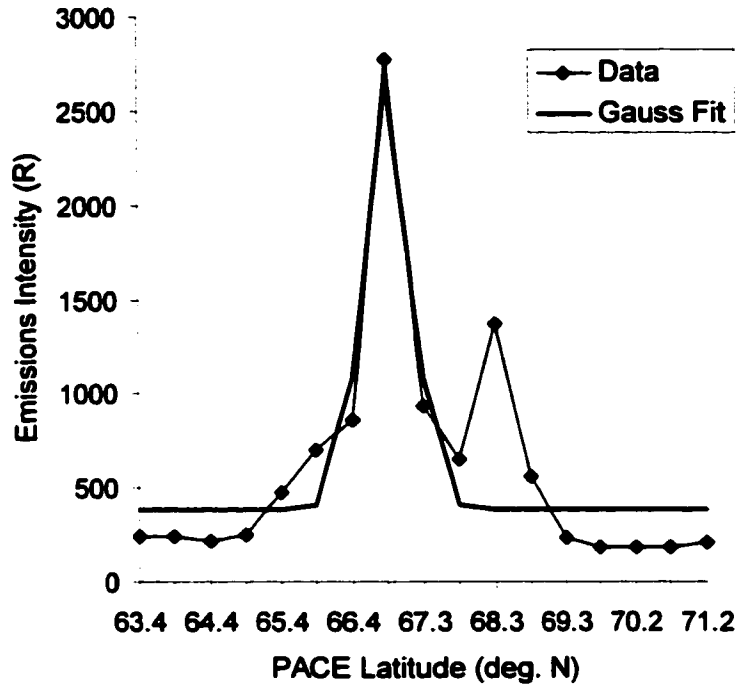


Figure 2.12: An example of 557.7 nm photometer data with multiple peaks on January 18, 1996 at $t=0458$ UT.

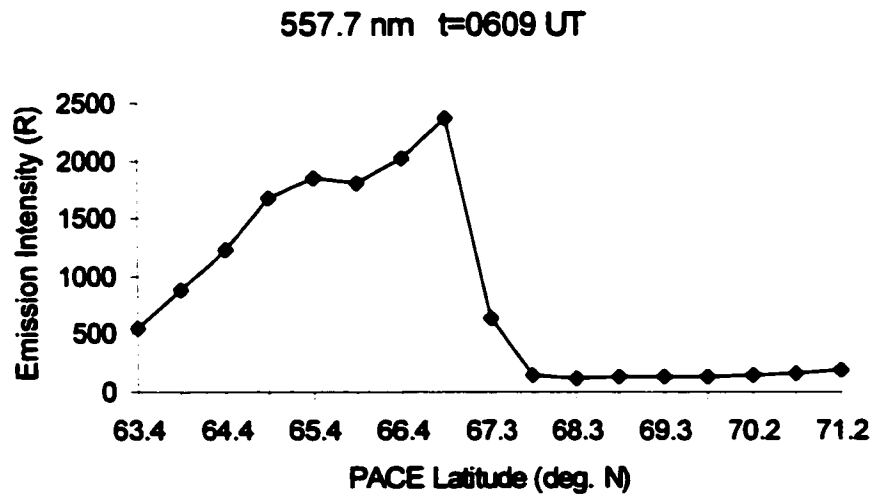


Figure 2.13: 557.7 nm photometer data for January 20, 1996 at 0609 UT showing the non-Gaussian structure of the data that sometimes exists.

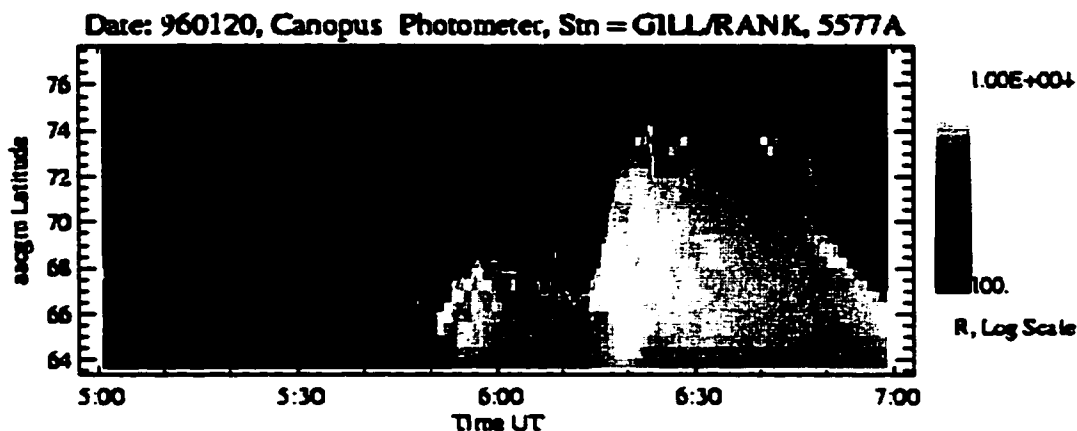


Figure 2.14: The poleward border of the 557.7 nm data for the January 20, 1996 event using the Gauss fit procedure. The border calculated at 0609 UT is clearly incorrect and will be fit more accurately using the step function procedure.

2.2 SuperDARN

The Super Dual Auroral Radar network (SuperDARN) [Greenwald *et al.*, 1995] is a global scale network of high frequency (HF) and very high frequency (VHF) radars for the purpose of scientific investigation of the upper atmosphere, ionosphere, and magnetosphere. SuperDARN is an international collaboration of immense proportions consisting of the STARE (Scandinavian Twin Auroral Radar Experiment in northern Scandinavia) VHF radar system, a Northern Hemisphere chain extending along a latitudinal ring from Kodiak, Alaska to Hankasalmi, Finland (Figure 2.15), and a Southern Hemisphere chain along a line of $\sim 42^\circ$ E AACGM (Altitude Adjusted Corrected Geomagnetic Coordinates) longitude from Halley Station to Kerguelen, Antarctica. A recent addition to the collaboration has been the TIGER (Tasman International Geospace Environment Radar) array, officially commissioned in Tasmania last year.

The main antenna array at each radar site comprises 16 log-periodic antennas, which, at any instant, can form a single radar beam. The beam is electronically steered in 16 directions by means of a phasing matrix, covering an azimuthal sector of 52° and a latitudinal range of 3000 km. The beams of the radar are numbered 0 to 15, from

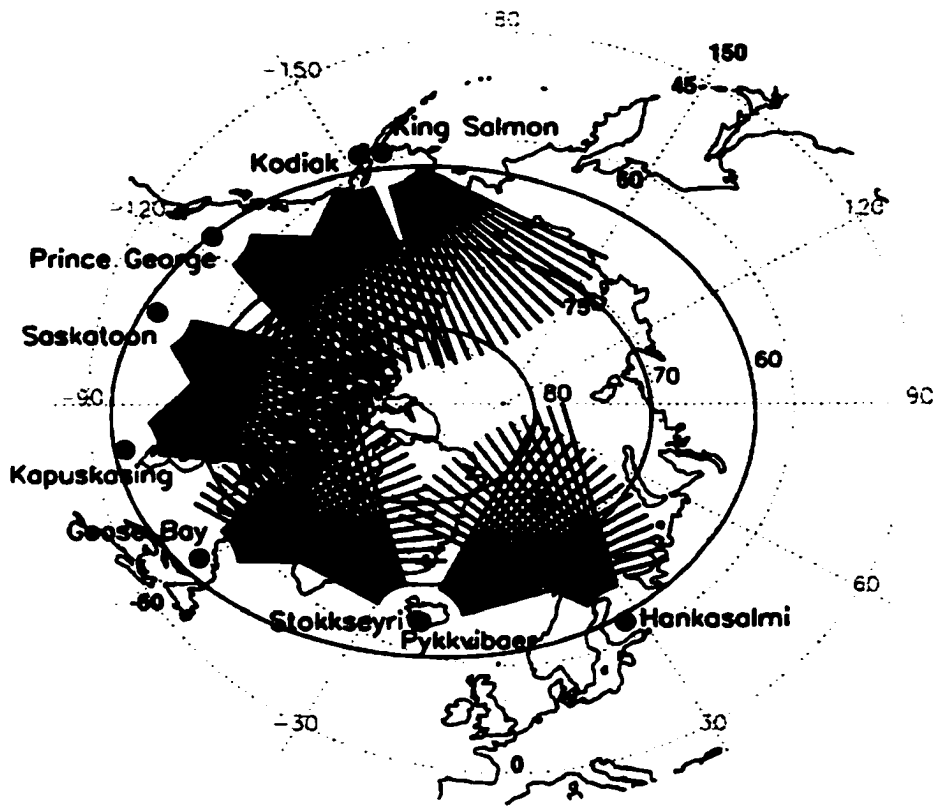


Figure 2.15: Schematic of the SuperDARN radar sites in the Northern Hemisphere (courtesy of George Sofko, Principal Investigator of the Saskatoon radar).

westernmost to easternmost beam. When sampling the near-space regions each beam has an integration time of 6.25 seconds, resulting in a sampling interval of approximately 100 seconds per complete 16 beam scan. The radars operate in a frequency band from 8-20 MHz with an azimuthal resolution of measurements from 6° at 8 MHz to 2.5° at 20 MHz, respectively. At each beam azimuth, the SuperDARN radars emit a multipulse transmission sequence of 5 to 7 pulses over a time period of 100 ms. The backscatter returns from these pulses are sampled and processed to produce multi-lag autocorrelation functions (ACFs) as a function of range.

The ACFs are fit to determine the backscatter power, mean Doppler velocity, and the width of the Doppler power spectrum for each range of significant backscatter returns.

The SuperDARN radars are coherent radars sensitive to Bragg scattering from small-scale electron density irregularities in the ionosphere. Ionospheric irregularities are

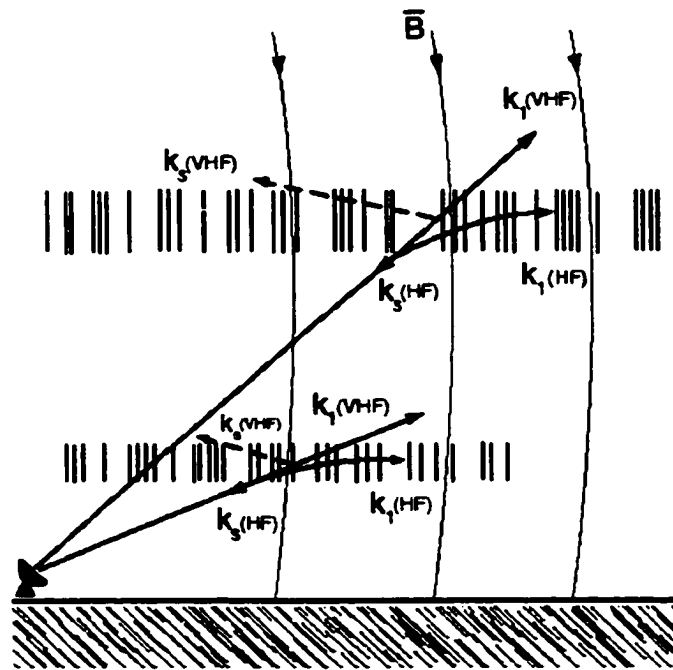


Figure 2.16: Illustration of how HF, VHF and UHF signals are scattered into space by nearly vertical magnetic field lines at high latitudes (adapted from Figure 4 in Greenwald et al., [1995]).

field-aligned in structure with their wavenumber vector directed orthogonal to the magnetic field. As a result, the incident radar signal must also be orthogonal to the magnetic field in order for a backscattered signal to return to the radar.

During the past decade, HF radars have been used to study F region irregularities. The radars use ionospheric refraction to achieve the orthogonality condition in both the E and F regions, although the F region electron density is generally much greater than that in the E region, resulting in refraction occurring predominately in the F layer over a broad range of altitude. Figure 2.16 shows how VHF and UHF signals are scattered into space by the nearly vertical magnetic field lines at high latitudes while the HF signals are refracted.

The technique of using ionospheric refraction to achieve orthogonality works very well during non-substorm and substorm growth phase conditions. During the expansive phase, however, the enhanced particle precipitation into the ionosphere saturates the E region. As a result, the radar beam cannot penetrate into the F region and the number of

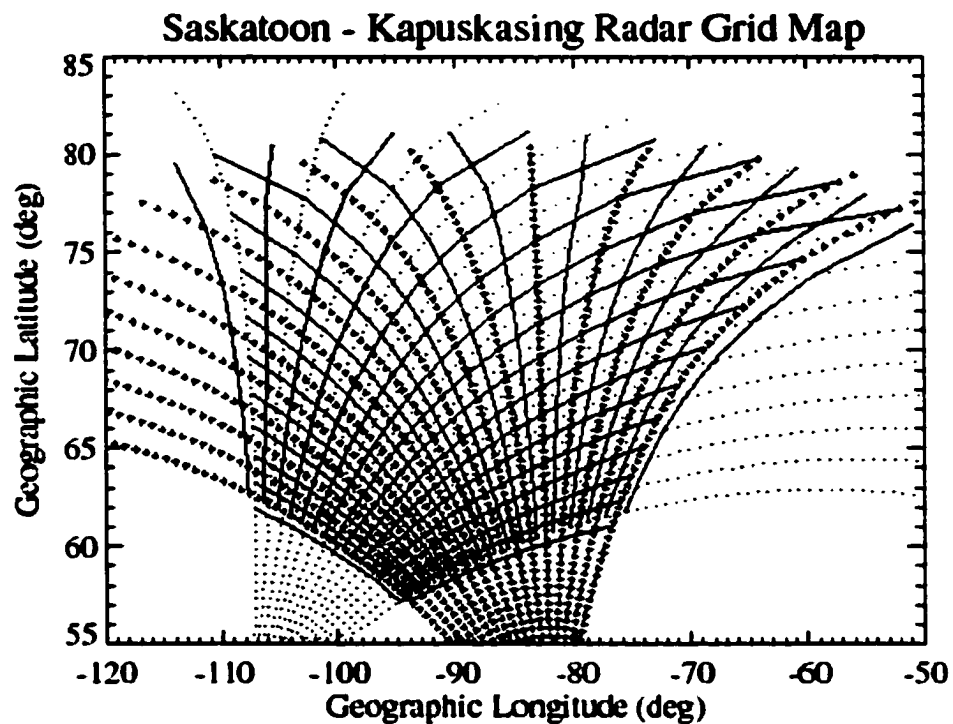


Figure 2.17: The Saskatoon (T) - Kapuskasing (K) merge grid. The Saskatoon radar (dots) shares a common field of view with Kapuskasing (crosses) northward of 58° latitude (from Fenrich [1997]).

backscattered signals is severely reduced. Since this thesis concentrates on the expansive phase of the substorm, the amount of data available for investigation was limited.

2.2.1 The Merge Program

The radars operate in pairs and have been strategically located so that the common field of view of the radars will cover $15\text{-}20^\circ$ invariant latitude and ~ 3 hours magnetic local time. Doppler information contained in the backscattered signals of the paired arrays is combined (merged) to yield maps of high-latitude (auroral zone and polar cap) plasma convection and the convection electric field. When possible, this thesis has utilized SuperDARN's ability to produce data of merged velocity vectors in order to study the instantaneous magnitude and direction of the ionospheric electric field in the auroral zone.

The Saskatoon and Kapuskasing radar pair share a common field of view (Figure 2.17) directly over the CANOPUS Churchill line of magnetometers ($\sim 95^\circ$ longitude). The line of sight velocity vectors from each radar can be merged using a technique developed by *Hamise et al.*, [1993], producing a two-dimensional map of convection velocity in the high-latitude ionosphere. The velocity vectors are rotated by 90° clockwise and multiplied by the magnitude of the ionospheric magnetic field to produce equivalent electric field vectors.

2.3 GOES Satellites

The Geostationary Operational Environment Satellites operate in the Earth's geographic equatorial plane at a radial distance of $6.6 R_E$. Usually two satellites are in operation at all times: one at approximately $75^\circ W$ geographic longitude, the other at approximately $135^\circ W$ longitude and both situated at the equatorial plane. For this thesis data from the GOES 8 and GOES 10 satellites were studied to determine the configuration of the field-aligned currents at geostationary orbit during the course of a substorm.

The GOES monitor spaceweather via the onboard Space Environment Monitor (SEM) system. The SEM consists of three components that monitor: soft x-rays, energetic particles, and the near-Earth magnetic field. Twin-fluxgate magnetometers are used to sample the local magnetic field, describing the field by three mutually perpendicular components: H_p , H_n and H_e . The H_p component is directed parallel to the satellite's spin axis, which itself is perpendicular to the satellite's orbital plane. The component H_e lies parallel to the satellite-Earth centerline, pointing earthward, and H_n is perpendicular to both H_p and H_e . For the GOES satellites used in this study, the H_n component was directed eastward.

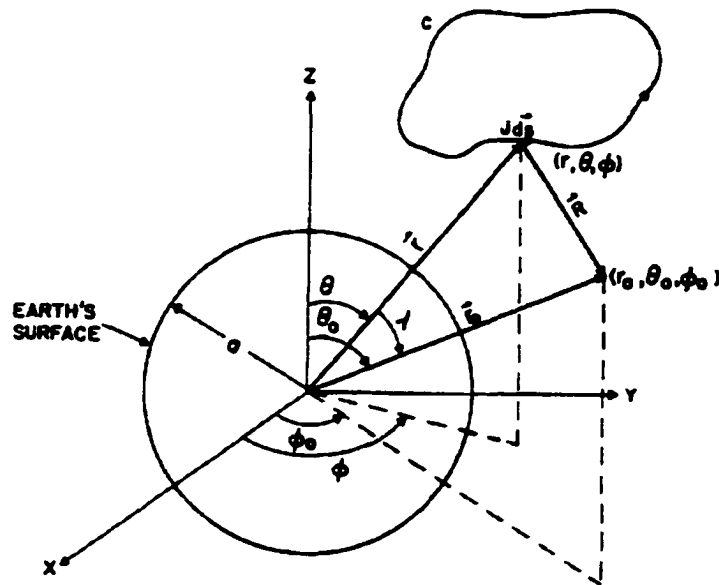


Figure 2.18: Vectors for magnetic field calculations in spherical coordinates. The Earth's surface is at radius 'a' and the coordinates of the observer (r_o, θ_o, ϕ_o) and current source (r, θ, ϕ) are defined with respect to the center of the Earth (from *Kisabeth and Rostoker [1977]*).

The onboard magnetometer samples the magnetic field every 0.75 seconds with a sensitivity of 0.2 nT. In a 3 second measurement, four consecutive samples are recorded, constituting a "frame", and sent to a ground station. For the GOES used in this thesis, the high and low values in the frame are discarded and the remaining two values are averaged. The averaged value is recorded as the magnetic field for that 3-second measurement.

The GOES magnetic field data studied in this thesis are one-minute averages, made available in GSM (geomagnetic solar magnetospheric) coordinates by the Coordinated Data Analysis Web (CDAWeb).

2.4 The Kisabeth 'Surge' Program

Since the work of *Bostrom* [1964], it has become accepted that the current flow at high latitudes associated with magnetospheric substorms is three-dimensional in nature, being composed of both the ionospheric (horizontal) Hall and Pedersen currents and the vertical Birkeland currents. From the point of view of the ground observer, measurements generally reflect the magnetic perturbations of the horizontal currents with some contribution from the Birkeland current system.

The 'Surge' program was written by Jerry Kisabeth in the early 1970's as a means to calculate the magnetic field perturbations due to the currents mentioned above. It is an example of 'forward modeling' in which a set of parameters, chosen by the modeler, defines a current system that produces the observed magnetic perturbations. The basic component of the program is the Biot-Savart law defined in a spherical coordinate system,

$$\vec{B}(r_o) = \frac{\mu_o}{4\pi c} \int \frac{\vec{J}(\vec{r}) \times (\vec{r}_o - \vec{r}) d^3 r}{|\vec{r}_o - \vec{r}|^3} \quad (2.3)$$

where $\vec{J}(\vec{r})$ is the current density vector, $d^3 r$ is the differential volume element in spherical coordinates, \vec{r}_o is the position of the observer, \vec{r} is the position of the currents, and c is an arbitrary current loop external to the Earth's surface (Figure 2.18).

Expressing the cross product $\vec{J}(\vec{r}) \times (\vec{r}_o - \vec{r})$ in terms of the observation coordinates (r_o, θ_o, ϕ_o) , Equation 2.3 was derived in matrix form in spherical coordinates,

$$B(\vec{r}_o) = \frac{\mu_o}{4\pi c} \int K(\vec{r}_o, \vec{r}) J(\vec{r}) d^3 r \quad (2.4)$$

where $B = (B_1 \hat{r}_o \ B_2 \hat{\theta}_o \ B_3 \hat{\phi}_o)$, $J = (J_1 \hat{r} \ J_2 \hat{\theta} \ J_3 \hat{\phi})$ and $K(\vec{r}_o, \vec{r})$ is a 3 x 3 orthogonal transformation matrix. At the time the matrix form was useful because it required small amounts of computer time; but the matrix form also allows the Biot-Savart law to be easily applied to complex current systems. For details of the matrix formulation see *Kisabeth and Rostoker* [1977].

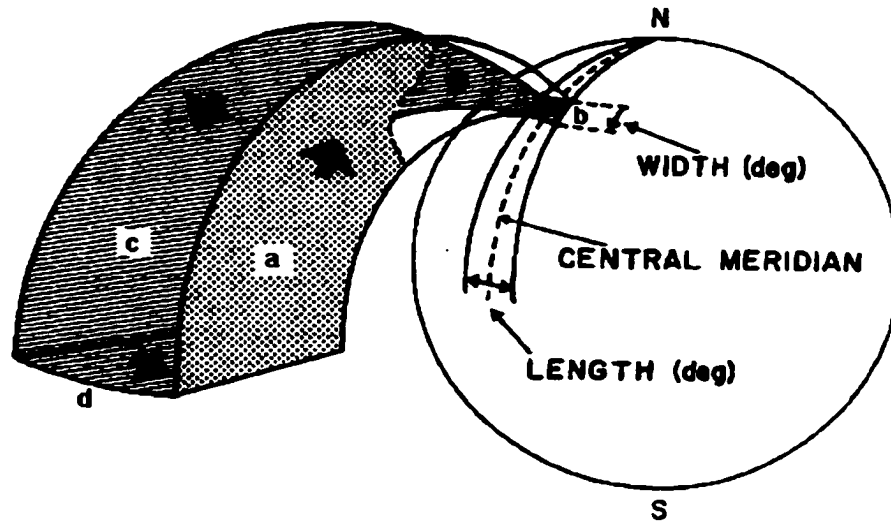


Figure 2.19: A three-dimensional E-W current system with finite longitudinal and latitudinal extent. The elements a,b,c,d represent the different parts of the current path (modified from Figure 3 in *Kisabeth and Rostoker* [1977]).

Equation 2.4 can be applied to three-dimensional current systems flowing east-west and north-south with respect to the ionosphere. An example of an east-west system is shown in Figure 2.19 in which field-aligned (Birkeland) currents flow from the magnetospheric equatorial plane down field lines to the eastern edge of the ionospheric westward electrojet, westward along the electrojet, and then return to the magnetospheric equatorial plane via field lines. The path of the current flow is completed by an eastward-directed current in the equatorial plane. From a modeling point of view, the equivalent eastward current is analogous to decreasing the intensity of the ring current or cross-tail current in that particular sector of the equatorial plane. To portray a system comprising an eastward electrojet (i.e. eastward directed current in the ionosphere) one merely reverses the direction of current flow.

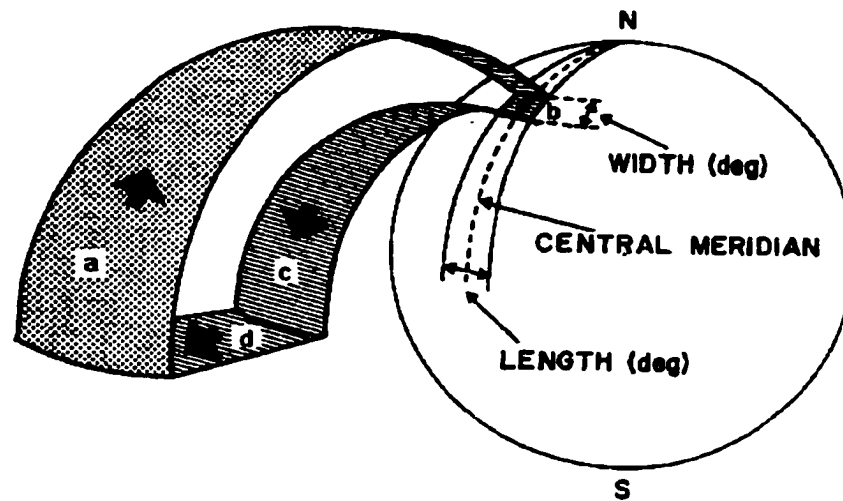


Figure 2.20 A north-south three-dimensional current system with finite latitudinal and longitudinal extent (modified from Figure 7 of *Kisabeth and Rostoker [1977]*).

In a similar manner the north-south current system can be modeled as shown in Figure 2.20. The path of current flow begins with a Birkeland current flowing from the magnetospheric equatorial plane to the northern edge of a southward-directed ionospheric current. The current then flows southward in the ionosphere and out along a field line at the southern edge to the equatorial plane. The current path is completed with a tailward directed current in the equatorial plane. A northward directed ionospheric current flow would be obtained by reversing the direction of the currents.

Since the Surge program was developed for a dipolar field geometry, the configuration of the total current system is controlled by the configuration of the magnetic dipole field and thus the physical parameters of the total system can be represented by those of the ionospheric segment alone. For ground-based observations this is very useful since the ionospheric segment provides the largest contribution to the magnetic perturbations.

For purposes of the calculations it is assumed that the height-integrated ionospheric segment can be approximated by a horizontal sheet current at a height h above the surface of the Earth. In this case, the radial position, \bar{r} , of the source current is given as $a + h$ (the radius of the earth plus the height of the current sheet).

The Surge program also takes into account variations of the Earth's magnetic field due to currents induced in the Earth. A very simple model of the Earth's conductivity structure was assumed as a spherical shell of an infinitely conducting medium of radius b ($b < a$, the radius of the Earth). Through trial and error, the most effective depth for the super-conducting spherical shell was found to be ~250 km.

Thus the input parameters to the Surge program are the coordinates for the ionospheric current segment (latitude and longitude in degrees), the height of the ionospheric current segment (usually assumed to be 115 km), the depth of the super-conducting shell (usually assumed to be 250 km), the coordinates of the observing stations (latitude, longitude and radial distance from the Earth. Observing stations on the Earth's surface have a radius = 1.0), and the total current flowing in the system in megamps.

In order to calculate the magnetic field due to the east-west or north-south current systems, the current path is divided into four parts a, b, c, d flowing along lines of constant latitude and longitude, respectively. Therefore, an additional input to the program is necessary that states which current path, a,b,c or d, (or all four) to evaluate.

Altogether the input file to the Surge program looks as follows:

```

stal
  45.0
 210.0
   1.0

 250.0
 115.0
   65.0
 200.0
   65.0
 220.0
   70.0
 200.0
   70.0
 220.0
   1.0
alllatmedclose*
```

The final line in the input file tells the program to calculate the magnetic perturbation due to all current paths a,b,c and d, (hence the keyword 'all' at the beginning of the line),

to calculate the magnetic field across lines of constant latitude (keyword 'lat'), to perform the Gaussian integration with medium precision (keyword 'med'), and to include a closure current in the equatorial plane (keyword 'close').

Each current path element specified in the input is evaluated separately using the matrix formulation of the Biot-Savart law and the resultant magnetic perturbations are added together to form the final magnetic field perturbation due to that current system. The output from the Surge program is the magnetic perturbation field in H, D, and Z geomagnetic components for each observing location. In this case the H, D, and Z components are the magnetic induction components (also referred to as X_m , Y_m , and Z_m) with H defined positive northward, D defined positive eastward, and Z defined as in the local geodetic system, positive downward.

Bibliography

- Baker, K.B., and S. Wing, A new magnetic coordinate system for conjugate studies of high latitudes, *J. Geophys. Res.*, *94*, 9139, 1989.
- Blanchard, G. T., L. R. Lyons, and J. C. Samson, Locating the polar cap boundary from observations of 6300A auroral emissions, *J. Geophys. Res.*, *100*, 7855, 1995.
- Blanchard, G.T., L.R. Lyons, and J.C. Samson, Accuracy of using 6300A auroral emissions to identify the magnetic separatrix on the nightside of Earth, *J. Geophys. Res.*, *102*, 9697, 1997.
- Bonnevier, B., R. Boström, and G. Rostoker, A three-dimensional model current system for polar magnetic substorms, *J. Geophys. Res.*, *75*, 107, 1970.
- Boström, R., A model of the auroral electrojets, *J. Geophys. Res.*, *69*, 4983, 1964.
- Fenrich, F.R., The field line resonance: Observation and theory, Ph.D. Thesis, University of Alberta, 1997.
- Greenwald, R.A., K.B. Baker, J.R. Dudeney, M. Pinnock, T.B. Jones, E.C. Thomas, J.-P. Villain, J.-C. Cerisier, C. Senior, C. Hanuise, R.D. Hunsucker, G. Sofko, J. Koehler, E. Nielsen, R. Pellinen, A.D.M. Walker, N. Sato, and H. Yamagishi, DARN/SUPERDARN, in *Global Geospace Mission*, edited by C.T. Russell, pp.761-796, Kluwer Acad., Norwell, Mass., 1995.
- Hanuise, C., C. Senior, J.-C. Cerisier, J.-P. Villain, R.A. Greenwald, J.M. Ruohoniemi, and K.B. Baker, Instantaneous mapping of high-latitude convection with coherent HF radars, *J. Geophys. Res.*, *98*, 17387, 1993.
- Kisabeth, J.L., and G. Rostoker, Development of the polar electrojet during polar magnetic substorms, *J. Geophys. Res.*, *76*, 6815, 1971.
- Kisabeth, J.L., and G. Rostoker, Current flow in auroral loops and surges inferred from ground-based magnetic observations, *J. Geophys. Res.*, *78*, 5573, 1973.
- Nakamura, S., *Applied numerical methods in C*, Chapter 2, pp. 24-34, Prentice-Hall Inc., New Jersey, USA, © 1993.
- Rostoker, G., J.C. Samson, F. Creutzberg, T.J. Hughes, D.R. McDiarmid, A.G. McNamara, A. Vallance Jones, D.D. Wallis, and L.L. Cogger, CANOPUS- A ground-based instrument array for remote sensing the high latitude ionosphere during the ISTP/GGS program, in *Global Geospace Mission*, edited by C.T. Russell, pp. 743-760, Kluwer Acad., Norwell, Mass., 1995.

Walker, J.K., Space-time associations of the aurora and magnetic disturbance, *J. Atmospheric Terrest. Phys.*, 26, 951, 1964.

¹Chapter 3: Dynamics of the Substorm Growth Phase

3.1 Introduction

Before discussing the dynamics of the substorm expansive phase it is useful to study the state of the magnetosphere prior to expansive phase onset, i.e. during the substorm growth phase. The existence of a growth phase of the substorm was discussed as early as the late 1960's as an interval of time during which the magnetosphere could extract energy from the solar wind and store it for later release [McPherron, 1970; McPherron, 1972]. The growth phase is a direct consequence of the interplanetary magnetic field B_z component becoming negative (i.e. turning southward). The negative field merges with the dipolar field on the dayside magnetopause and energy begins to be transferred from the solar wind to the magnetosphere through a process of reconnection and merging of magnetic fields (Figure 3.1). Energy transferred to the tail causes the tail lobe field to increase in magnitude, the associated convection electric field causing the lobe field lines to drift towards the neutral sheet. Consequently the plasma sheet starts to thin and the magnetic flux crossing the neutral sheet near the inner edge of the current sheet begins to decrease.

The enhanced convection electric field initiates particle energization in the plasma sheet. Protons are accelerated duskward across the magnetotail as they convect earthward, increasing the cross-tail current strength [Kaufmann, 1987] and generating an earthward pressure gradient at the inner edge of the plasma sheet [Kistler *et al.*, 1992]. The increase in the cross-tail current magnitude and the earthward penetration of the tail current system (via the convecting protons) causes the dipolar magnetic field lines to stretch tailward, thinning the plasma sheet. During intervals of extreme energy storage, the field line stretching can be severe, causing the near-earth cross-tail current sheet to thin to fractions of an R_E [Sergeev *et al.*, 1993].

¹ A version of this chapter has been published. Wanliss, J.A., J.C. Samson and E. Friedrich, On the use of photometer data to map dynamics of the magnetotail current sheet during substorm growth phase, *J. Geophys. Res.*, 105, 27673, 2000.

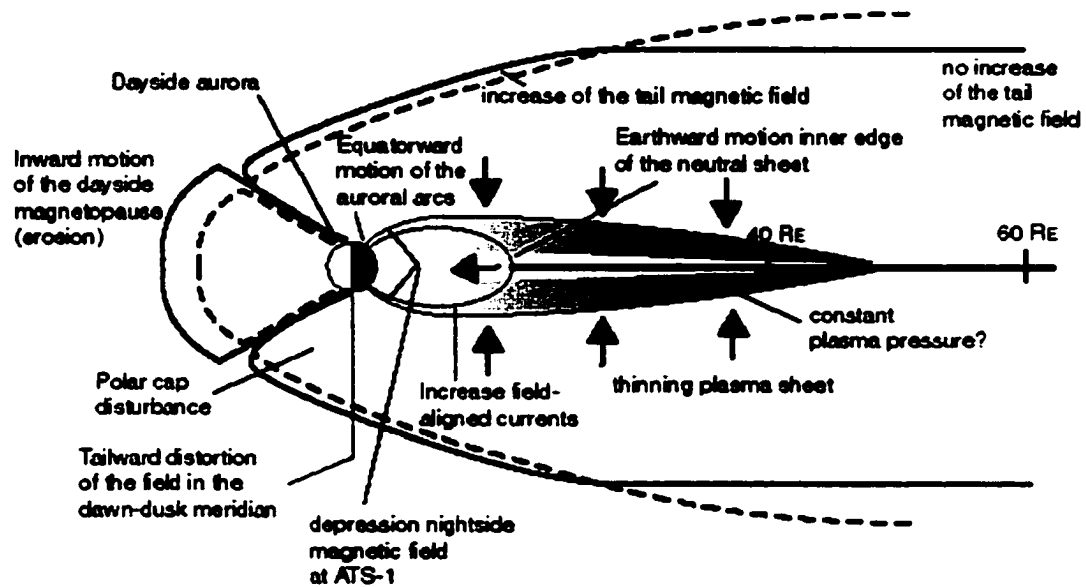


Figure 3.1: The different aspects of the substorm growth phase (reproduced from McPherron [1972]).

In the previous chapter the CANOPUS network was discussed. Part of CANOPUS comprises an array of four meridian scanning photometers (MSP). The MSP, being able to monitor auroral emissions produced by precipitating particles, is useful for identifying the growth phase and delineating the different regions of the magnetosphere where the sources of these particles are found. Mapping of the magnetosphere has traditionally been done using the magnetic field and particle populations of its different regions from data acquired during multiple satellite traversals. The knowledge that the ionosphere and magnetosphere are connected via magnetic field lines, and that information about dynamic events in the magnetosphere is carried to the ionosphere along these field lines, makes remote sensing the ionosphere a useful method of studying the magnetosphere. As mentioned in Chapter 2, the MSPs observe the $H\beta$ 486.1, and the O 557.7 and 630.0 nm emissions, which are a product of precipitating particles. *Samson* [1994] offered a plausible model of the plasma regimes in the magnetotail, which are the sources of these precipitating particles. From an ionospheric point of view, the growth phase is observed as an equatorward movement of these emissions, in particular, a region of relatively strong $H\beta$ emissions. The $H\beta$ emissions, being the product of precipitating heated

protons, relates the particle population to the earthward edge of the plasma sheet and the outer edges of the ring current [Samson, 1994]. Thus, the MSPs provide a useful tool for mapping the magnetosphere.

The stretching of the magnetotail field lines is thought to be consistent with the equatorward motion of the region of ionospheric disturbance. For example, on the dayside the polar cusps move equatorward during the growth phase [Pulkkinen, 1991] while on the nightside pre-existing auroral arcs also move equatorward marking the footpoints of the stretching auroral field lines [Pulkkinen *et al.*, 1992]. Lewis *et al.* [1998] showed that the backscatter of coherent radar waves from the ionosphere moved equatorward due to expansion of the polar cap and tailward stretching of magnetic field lines. As well, Voronkov *et al.* [1999] showed that the maximum of the proton aurora and the maximum of the ionospheric convection velocity as observed by the SuperDARN radars moved equatorward during the growth phase. With respect to the work by Lewis *et al.* [1998], this implies that the equatorward motion of the photometer emissions was due to the stretching of the tail field lines, although no efforts were made to quantify this idea at the time. Thus, it seemed natural to pose the question of whether the equatorward motion of the photometer emissions were due in any way to the stretching of the tail field lines and, further, whether the emissions could provide some indication of when the orbits of the particles in the plasma sheet might become chaotic and the plasma sheet particle distribution isotropize. This chapter investigates these questions.

3.2 Particle motion and proton precipitation in the near-Earth tail

Particles trapped on closed field lines precipitate via processes that cause violation of the first adiabatic invariant and move particles into the loss cone. The primary causes of such scattering are non-guiding center motion in weak magnetic field regions, scattering by plasma waves, and field-aligned acceleration by electric fields parallel to the magnetic field lines [Lyons, 1997]. This chapter will be concerned only with scattering due to non-guiding center motion. Particles follow guiding center trajectories until they reach the current sheet. Within the current sheet, their motion can be divided into two components

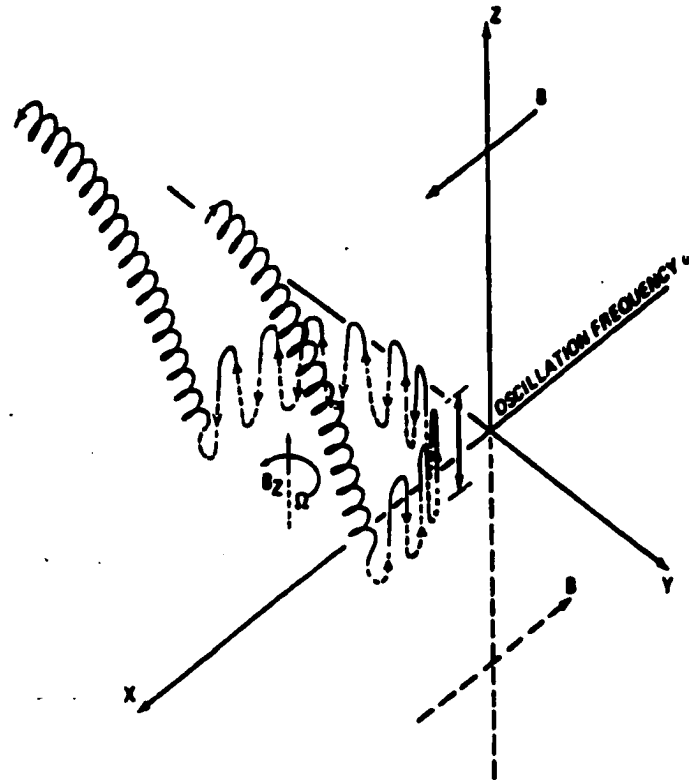


Figure 3.2: An example of Speiser motion as a particle travels near the neutral sheet with a weak normal magnetic field across the sheet and no electric fields. Direction shown is appropriate for negatively charged particles (from Lyons [1997]).

(Figure 3.2): an oscillation about the plane of the current sheet with frequency ω that is due to the reversal of B_x across the current sheet, and a gyration about B_n (a weak normal component of the magnetic field) with frequency Ω [Lyons, 1997].

Within the current sheet, particle motion violates the guiding center approximation leading to pitch angle scattering. The character of particle motion within the current sheet depends upon the ratio of the minimum radius of curvature of field lines to the maximum particle gyroradius (referred to as the Kappa parameter) [Sergeev *et al.*, 1983; Büchner and Zelenyi, 1989]:

$$\kappa^2 = R_{\min}/\rho_{\max} \quad (3.1)$$

where R_{\min} is the minimum magnetic field line radius of curvature, and ρ_{\max} is the maximum particle gyroradius measured in the current sheet. Equation 3.1 illustrates that adiabatic and chaotic particle motion is dependent upon both the magnetic field geometry

and particle energy. During the latter part of the growth phase, the intense cross-tail current produces strongly curved field lines across the neutral sheet, and the magnetic field component normal to the current sheet can become very small. When the radius of curvature of the magnetic field at the current sheet becomes comparable to the particle Larmor radius, the particle motion becomes nonadiabatic, i.e. the particle is pitch angle scattered.

The Kappa parameter changes in different regions of the magnetosphere. In the distant tail particles travel in a meandering motion that could lead to the formation of a thin current sheet [Ashour-Abdalla *et al.*, 1994]. In this regime $\kappa \ll 1$. Closer to the Earth the dipole field is stronger and $\kappa \gg 1$. In this region the particle motion is adiabatic. In between, at the transition between tail-like and dipole-like field configurations, κ can be particularly variable for plasma sheet ions. Zelenyi *et al.* [1990] demonstrated that for $1 \leq \kappa \leq 3$ near-Earth plasma sheet ions might become untrapped. Delcourt *et al.* [1996] recently showed that it is these ions, corresponding to κ values between 1 and 3, that can be pitch angle scattered out of the current sheet, a fraction of which may enter the loss cone and precipitate into the ionosphere. If the magnetic field is very stretched, the fraction entering the loss cone can be quite significant [Lyons and Speiser, 1982]. Liu *et al.* [1998] quantified this effect using theoretical models of a stretched near-Earth current sheet.

The particle energy corresponding to a given value of κ is proportional to $1/B_n^4$, the component normal to the magnetic field. B_n increases with decreasing radial distance in the tail so that the range of energies of the convecting particles subject to strong scattering within the current sheet increases strongly closer to the Earth. Plasma sheet protons are subject to strong pitch angle scattering throughout most of the tail plasma sheet. Therefore, isotropic proton precipitation is expected to occur throughout the entire nightside plasma sheet. Table 3.1 illustrates the range of energies for which strong pitch-angle scattering is expected for different regions of the nightside magnetosphere.

Table 3.1 Range of energies of strong pitch-angle scattering (adapted from Lyons [1997]).

Region	Protons
Distant tail ($B_n \sim 1$ nT, $B_{lobe} \sim 10$ nT, $L \sim 10^3$ km)	0.008 eV – 50 eV
Mid-tail ($B_n \sim 5$ nT, $B_{lobe} \sim 20$ nT, $L \sim 5 \times 10^3$ km)	0.030 – 190 keV
Near-tail ($B_n \sim 30$ nT, $B_{lobe} \sim 60$ nT, $L \sim 10^4$ km)	0.017 – 110 MeV
Synchronous orbit (quiet times) (based on Sergeev et al., 1983)	~ 0.15 – 960 MeV

3.3 Magnetic Field Model

Changes in the configuration of the geomagnetic tail magnetic field are known to play a fundamental role in magnetospheric substorms. However, adequate sampling of the geomagnetic tail is hampered by the paucity of multipoint measurements by satellites. As a result, scientists turn to magnetic field models to provide some of the details of the magnetic field dynamics. The most widely used models to date are the set of time-independent models developed by *Tsyganenko* [1987, 1989, 1995, 1996]. These models are global in extent, based on statistical analysis of years of satellite observations. Unfortunately, the statistical nature of *Tsyganenko's* models makes them inadequate to represent the current sheet during the growth phase of magnetospheric substorms, as they tend to reflect a thicker current sheet than is realistically present in the magnetotail. The problem lies in the fact that the *Tsyganenko* models calculate a statistical cross-tail current that represents an average over all configurations of the magnetosphere: the stretched configuration observed during the growth phase and the more dipolar configuration that is representative of the expansive phase. The result is a model that cannot resolve thin current sheets or other sharp magnetic field gradients and therefore cannot be expected to properly portray the substorm growth phase. The fact that the near-Earth cross-tail current is intensified and the tail field lines extremely stretched during the growth phase has motivated some modification of *Tsyganenko's* global models. For example, in order to achieve a reasonable picture of the near-Earth magnetic

field stretching, *Pulkkinen et al.* [1998] modified T89 (*Tsyganenko* 1989) to include a localized thin cross-tail current. A similar modification was applied to T96 by *Lu et al.* [1999].

The magnetotail magnetic field model used in this investigation attempts to simulate the extreme conditions of the substorm growth phase magnetotail, which the models discussed above have difficulty representing. Accordingly, established aspects of the growth phase were used to define the model such as the enhancement of the near-Earth cross-tail current [*Kaufmann*, 1987], thinning of this current to fractions of an R_E , and limiting the radial and azimuthal extent of the current intensification to within a few hours around magnetic midnight [*Baker and McPherron*, 1990; *Iijima et al.*, 1993]. The magnetic field becomes very weak and tail-like in the midplane [*Kokubun and McPherron*, 1981; *Pulkkinen et al.*, 1992; *Nakai et al.*, 1997] as a consequence of the above changes in the cross-tail current, and localized regions of weak magnetic field near the neutral sheet are produced. These changes in current sheet structure are also expected to lead to particle chaotization and enhanced ionospheric precipitation.

Highly non-adiabatic ion motion in the magnetotail can occur when the tail field is significantly stretched. Since this ion motion cannot be described by the guiding center approximation [*Parks*, 1991 Ch.4], the complete Lorentz equation ($F = q(E + v \times B)$) must be used to trace the particles in the model. Many calculations are needed in this endeavour and with the issue of the global models being inadequate to model the latter growth phase of the substorm, a simpler model was devised; one that minimized computing time while being as realistic as possible. The model used in this study comprises a dipole field, an equilibrium tail component, and an azimuthally and radially confined weak magnetic field region (WFR) [*Wanliss*, 2000]. All three modular components, expressed in dipole coordinates, are used to build up the final model configuration:

$$\bar{B}(\bar{r}) = \bar{B}^{Dipole}(\bar{r}) + \bar{B}^{Tail}(\bar{r}) + \bar{B}^{WFR}(\bar{r}) \quad (3.2)$$

The components in Equation 3.2 are divergence free making the entire model divergence free also.

The coordinate system is centered on the Earth, with the X-axis positive sunward, the Z-axis anti-parallel to the dipole moment (which itself is directed southward along the dipole axis), and the Y-axis perpendicular to the other two axes, positive eastward.

The dipole component of the model is given by,

$$\bar{B}^{dipole}(\vec{r}) = -\frac{3Mxz}{r^5}\hat{x} - \frac{3Myz}{r^5}\hat{y} - \frac{M(3z^2 - r^2)}{r^5}\hat{z} \quad (3.3)$$

where M is the dipole moment and $r^2 = x^2 + y^2 + z^2$ is the radius from the center of the Earth.

The tail component of the model is the *Zwingmann* [1983] two-dimensional equilibrium tail field model, which includes equilibria with spatial oscillations in the tail. The equilibrium tail field model has $B_y^{Tail} = 0$, and the B_x^{Tail} and B_z^{Tail} components as combinations of a hyperbolic tangent function and a function, $F(x)$, that describes how fast the lobe field falls off with distance downtail. The B_x^{Tail} and B_z^{Tail} components are dependent on the magnetotail current sheet half-thickness, L_z . This parameter will play an important role in modeling the current sheet dynamics in Section 3.5 as it has the strongest influence on the model topology. A detailed description of the parameters involved in these components can be found in *Zwingmann* [1983].

Various theoretical models predict a region of small B_z will form in the intermediate region between dipole-like and tail-like magnetic fields under the action of a dawn-to-dusk electric field [e.g. *Erickson*, 1984; *Hau et al.*, 1989]. Thus, the final component to the model is a three-dimensional magnetic structure that creates a depression, or weak magnetic field region (WFR), near the Earth. The magnetic field in the WFR is given by [*Wanliss*, 2000]

$$B_x^{WFR} = 0 \quad (3.4)$$

$$B_y^{WFR} = B_p L_y \sec h\left(\frac{x+10}{L_y}\right) \tanh\left(\frac{y}{L_y}\right) \partial_z G(z) \quad (3.5)$$

$$B_z^{WFR} = B_n - B_p \sec h\left(\frac{x+10}{L_y}\right) \sec h^2\left(\frac{y}{L_y}\right) G(z) \quad (3.6)$$

where the background normal field in the distant current sheet is $B_n = 1$ nT, the parameter $B_p = 28.45$ nT regulates the magnitude of the depressed magnetic field near the current

sheet region, and $L_y = 3^{1/2} R_E$ determines the width, in azimuthal extent, of the depression in the current sheet region. Finally, the function $G(z)$, given by

$$G(z) = \left(1 + \frac{z^2}{L_y^2}\right)^{-1/3} \quad (3.7)$$

constrains the depression of the magnetic field to be confined primarily to the current sheet region around $Z=0$.

The electric current system given by the weak field region model flows in an oval pattern (see Figure 4.2 in *Wanliss* [2000]) in agreement with the work of *Iijima et al.* [1993]. The majority of the current flows between $|Z| \leq 1 R_E$ and the current is divergence free, i.e. $\nabla \cdot \vec{J}^{WFR} = 0$.

Kaufmann [1987] showed that a requirement of the growth phase was enhanced stretching of field lines, particularly in the near-tail region. Thus, the weak field region is constructed to simulate the observation that the growth phase current sheet is enhanced in a radially and azimuthally confined region (Figures 3.3 and 3.4). Equations 3.4 to 3.7 describe a depression, or weak, magnetic field around $X = -10 R_E$, reflecting an enhanced stretching of magnetic field lines in the near-Earth region.

The parameters for the Wanliss magnetic field model are summarized in Table 2.

Table 3.2: Parameters for the Wanliss magnetic field model (modified from Table 1 in *Wanliss* [2000]).

Field Component	Parameter name	Value
Dipole	M (nt/ R_E^3)	31100
Tail	B_o (nT)	50
Tail	L_z (R_E)	1 - 0.05
WFR	B_p (nT)	28.45
WFR	B_n (nT)	1
WFR	L_y (R_E)	$3^{1/2}$

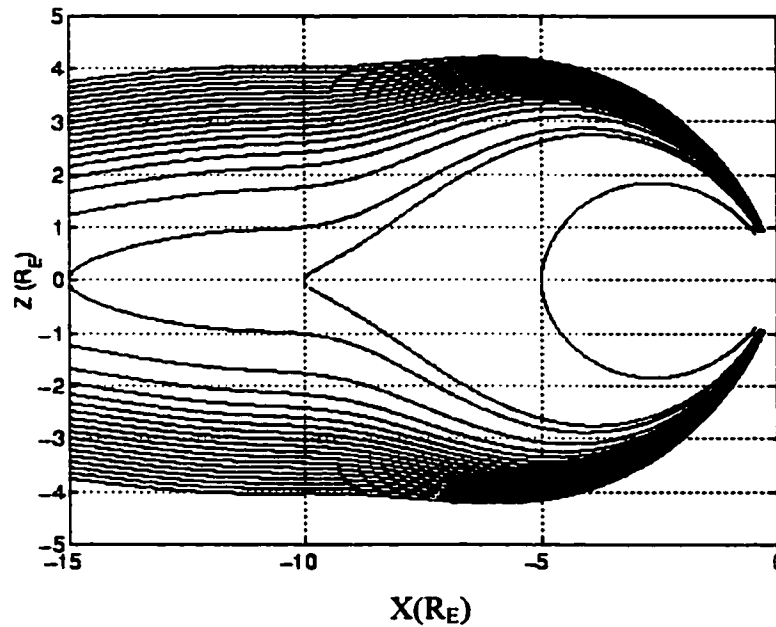


Figure 3.3: Magnetic streamlines from the Wanliss magnetic field model at the beginning of the growth phase. Profile is taken in the noon-midnight meridian plane for current sheet half-thickness $L_z = 1 R_E$ (modified from *Wanliss et al. [2000]*).

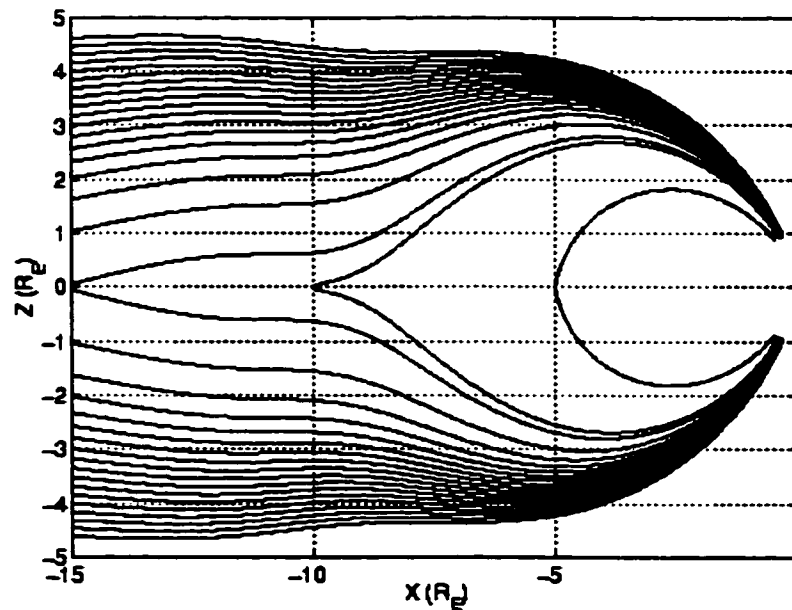


Figure 3.4: Magnetic streamlines from the Wanliss magnetic field model for the latter growth phase. Current sheet thickness is $L_z = 0.05 R_E$. The thinner current sheet is shown by the decreased radius of curvature of the magnetic field line (modified from *Wanliss et al. [2000]*).

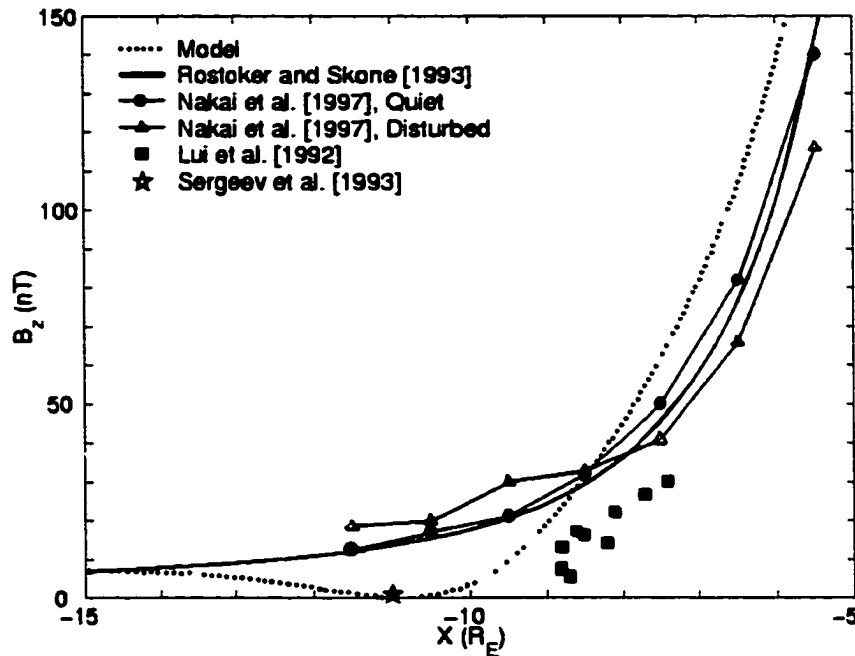


Figure 3.5: A comparison of the Wanliss magnetic field model to other models investigating the near-earth region. The Wanliss model successfully simulates the weak magnetic field between 10-11 R_E (modified from Figure 1 in *Wanliss et al.* [2000]).

The magnetic field model was constrained using statistical data and results of observational studies (see *Wanliss* [2000] Ch. 4 for details). The two parameters that most strongly affect particle motion in the magnetotail are the current sheet half-thickness, L_z , and the location (width and depth) of the WFR. The position of the WFR was constrained using the results of observational studies, which report a minimum in the B_z component at midnight near the transition region of dipole-like and tail-like magnetic fields. The position of the WFR chosen for this study is $X = -10 R_E$ and is justified by comparison to the observational data (Figure 3.5). The model is a good fit to the *Rostoker and Skone* [1993] study tailward of $X = -14 R_E$ and agrees very well with the *Sergeev et al.* [1993] data. The current sheet half-thickness, L_z , will be discussed in Section 3.5.

3.4 Fitting the Photometer Data

The usefulness of the CANOPUS photometer data lies in its complete view of the substorm, the ease to which one can determine the substorm's different phases, and its ability to order the regimes in the magnetosphere. For this study, we wanted to learn more about the current sheet dynamics and plasma sheet particle dynamics during the growth phase by comparing model calculations with actual data. This was done by least squares fitting the results from the Wanliss magnetic field model with the data from the meridian scanning photometers.

In order to fit the model data to the MSP emissions, a time series of the poleward and equatorward borders of the region of H β luminosity was required. Using the Gaussian fit method described in Chapter 2, the poleward and equatorward borders of the H β emissions were calculated. The method of determining the poleward border of the data has already been discussed in detail and will not be repeated here; instead the procedure used to calculate the equatorward border of the emissions will be discussed.

As was mentioned in Section 2.1.2, the Extract program runs under command line input control. The equatorward border of the photometer data was determined by adding the command `-eq` (for equatorward border) to the command line inputs. The Extract program follows essentially the same procedure as if it were searching for the poleward border of the emissions- locating the maximum of the emissions and finding the correct Gaussian profile fit to the data- however, instead of determining the poleward latitude associated with a standard deviation of 1.5, the program calculates the equatorward latitude associated with this standard deviation. Recall that the poleward edge of the emissions was determined to be between the limits of +1 standard deviation (~34% of the integrated area under the Gaussian distribution) and +2 σ (~ 47% of the integrated area). For this study, it was assumed that the equatorward edge would be located within the limits of -1 and -2 standard deviations of the data. An example of the equatorward border of the 486.1 nm emissions for March 9, 1995 is shown in Figure 3.6. Two of the forty (5%) of the poleward border fits were unable to be determined using a Gaussian function; for these cases a step function was used [Blanchard *et al.*, 1995]. Once the borders were determined, they were compared to the borders calculated by the magnetic

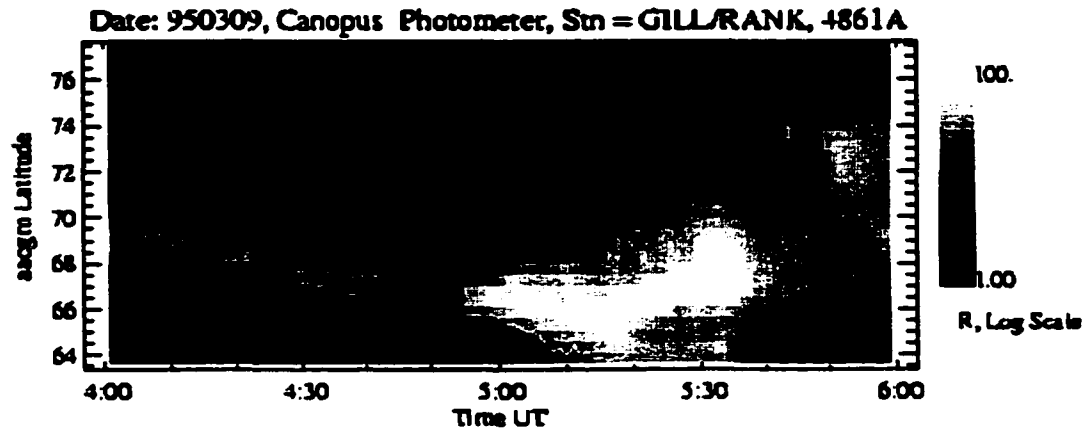


Figure 3.6: The equatorward border for the 486.1 nm emissions on March 9, 1995.

field model, in order to determine how well the model predicted the observed locations of the auroral regions of luminosity.

3.5 Procedure

The magnetic field model may be used to predict where in the ionosphere regions of auroral proton precipitation will occur. In a manner similar to that of *Pulkinnen et al.* [1992], the regions of pitch-angle scattering of the high energy protons in the near-Earth magnetotail were magnetically mapped to the ionosphere. Using the simple model outlined above, the near-earth current sheet of the substorm growth phase was simulated by varying only the parameter L_2 , the cross-tail current sheet half-thickness. In this way it was possible to study the evolution and dynamics of the current sheet as it was affected by this one parameter.

For this study, the current sheet half-thickness was constrained using the H β meridian scanning photometer data. The 486.1 nm (H β) auroral emissions are caused by protons with energies of several to several tens of keV, with an average of about 20 keV [Samson et al., 1992]. These energies (10 – 30 keV) were used to calculate the κ -parameter in the cross-tail current sheet, which restricted the modeling to an energy range close to the average of these energies.

Most models investigating the dynamics of the growth phase vary the location of the inner edge of the plasma sheet in order to affect magnetic field line stretching. For this study, however, the κ -parameter was used to indicate the topology of the magnetotail magnetic field. The κ -parameter is sensitive to current sheet thickness and particle energy. Monitoring the κ -parameter can determine how sensitively the proton precipitation depends on the current sheet thickness during the course of the growth phase. Near the Earth the κ -parameter is largest, and it decreases with distance downtail. The boundary between adiabatic and non-adiabatic particle motion is defined by the $\kappa = 3$ separatrix in the near-earth neutral sheet. As the current sheet thins, the location of the equatorward border of the proton precipitation, which is defined by the $\kappa = 3$ separatrix, moves earthward. *Samson et al.* [1992] found that the onset of the substorm intensification occurs in the region of proton precipitation that maps to the inner edge of the plasma sheet and the $\kappa = 3$ separatrix. As mentioned previously, scattering out of the current sheet occurs for $1 \leq \kappa \leq 3$. Thus, rather than varying the inner edge of the plasma sheet to simulate dynamics of the growth phase, the κ -parameter was used.

During this investigation, the parameter L_z was varied and the κ -parameter was calculated as a function of L_z and the allowed proton energy ranges (viz. 10-30 keV). The position and depth of the magnetic WFR was not varied during the fitting procedure. Using the method discussed in Section 3.4, the poleward and equatorward borders of the 486.1 nm emissions were calculated. In order to determine what values of L_z resulted in the best fit of the auroral luminosity regions, least squares fitting of the $H\beta$ proton data to the model predicted borders was completed. In the least-squares fitting procedure it was assumed that the $\kappa = 1$ boundary, defined from the 10-30 keV protons, corresponded to the poleward border of $H\beta$ emissions, although this may not always be true.

It should be mentioned that the lobe field strength, B_0 , is fixed in this model so the question of how the variation of the lobe field would affect the results cannot be answered. This is not an issue for the present study, however, as this study does not address the dynamics of the poleward border of the auroral oval (nor the outer edge of the plasma sheet), instead dealing solely with the inner edge of the current sheet from 6-15 R_E . For studies that would investigate the dynamics of the outer edge of the plasma sheet

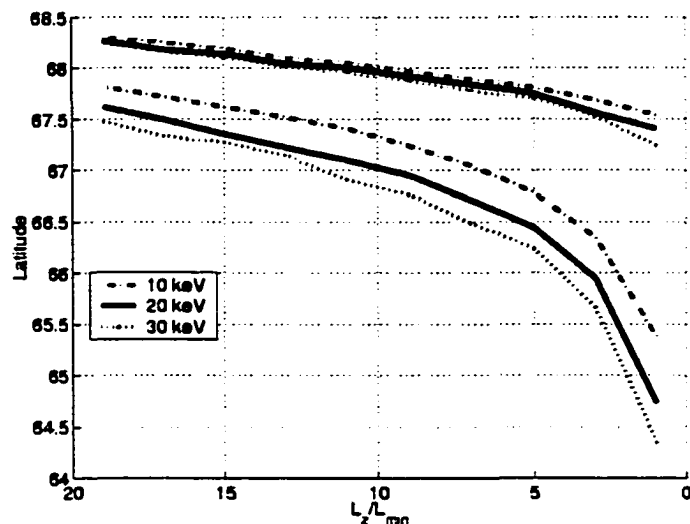


Figure 3.7: Model prediction for the regions of proton precipitation in the ionosphere. Precipitation occurs in the region between the high- and low latitude borders. The x-axis is the model current sheet half-thickness, normalized to $L_{\min}=0.05 R_E$ (from *Wanliss et al.*, 2000).

during the substorm the affects of varying the lobe field strength would be important and should be included in any modeling investigation. Figure 3.7 shows the model predicted latitudes of auroral H β emissions, plotted against the current sheet thickness parameter, L_z . The borders for the 10 keV protons are shown as dot-dashed lines, 20 keV are solid, and 30 keV are dotted. Precipitation is assumed to occur in the region between the high and low latitude borders. In all cases it is clear that as the current sheet thins the precipitation region moves equatorward. As well, the equatorward border of the precipitation region moves equatorward at a faster rate for small current sheet thicknesses.

3.6 Results

As discussed above, the magnetic field model can be used to connect the field and current variations in the magnetotail to the changes in the precipitation pattern seen in the auroral regions. Several events have been studied for which the growth phase is very clear and has no evidence of disturbance activity (i.e. Pi2 pulsations) before expansive phase onset. In this section, data from one representative substorm event is presented.

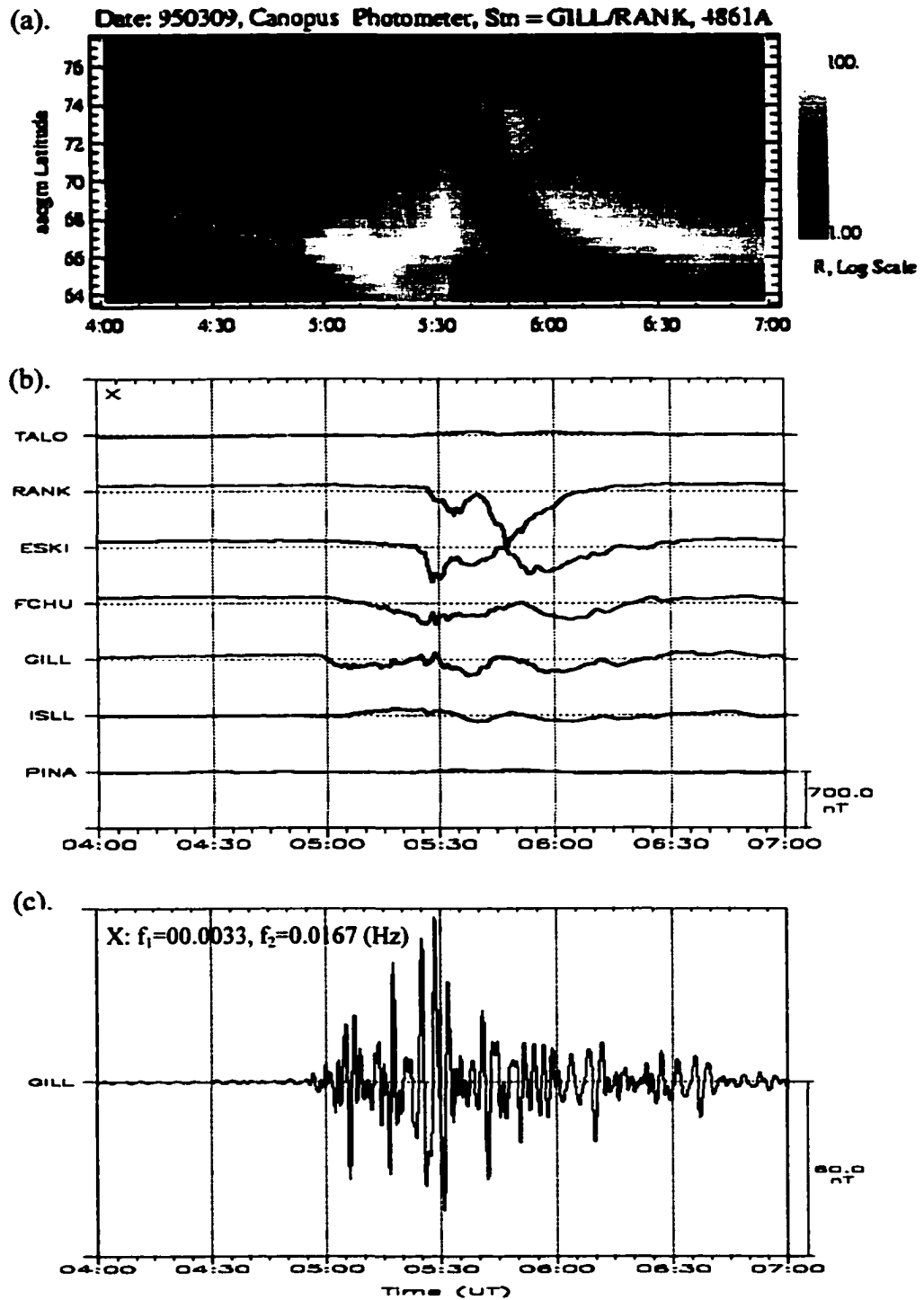


Figure 3.8: CANOPUS data for March 9, 1995. (a) MSP data showing growth and expansive phase. Data from Gillam and Rankin Inlet have been merged. AACGM is similar to PACE coordinates [Baker and Wing, 1989]. (b) X-component magnetometer data from the Churchill line of magnetometers. (c) Pi2 pulsations observed at Gillam (modified after Wanliss *et al.* [2000]).

The substorm occurred on March 9, 1995 with a growth phase that began between 0325-0335 UT [Voronkov *et al.*, 1999]. Figure 3.8 shows the H β (486.1 nm) emissions, the CANOPUS Churchill line magnetometer data, and the Pi2 activity at Gillam between 0400-0700 UT. The H β emissions in Figure 3.8a are in the form AACGM invariant latitude versus time, and have a 1 minute temporal resolution. At 0400 UT preexisting proton aurora are moving slowly equatorward ($\sim 0.5^\circ/10$ min), and the equatorward motion increases rapidly after ~ 0430 UT ($\sim 1^\circ/10$ min). Figure 3.8b presents the simultaneous magnetometer data from the Churchill line of magnetometer stations. Only the geomagnetic north-south (X) component is shown. A positive perturbation of the magnetic X -component appears after ~ 0400 UT, which indicates an enhancement in the eastward electrojet. This positive perturbation is present until 0459 UT when Gillam observes expansive phase onset. Figure 3.8c shows the impulsive Pi2 pulsations and it is noted that no Pi2 pulsations are present prior to expansive phase onset at 0459 UT, indicating a "quiet" growth phase.

Figures 3.9a and 3.9b show the poleward and equatorward borders of the auroral emissions and the variation in the current sheet thickness during the late growth phase and early expansive phase (0430-0510 UT). Error bars are included in Figure 3.9a, as well as the model best-fit predictions, which are shown as circles. From these fits to the luminosity borders estimates for the model current sheet thickness (calculated at $X = -8 R_E$) were obtained during the late growth and early expansive phases. The line marked with circles in Figure 3.9b is the best-fit current sheet thickness, calculated at $8 R_E$. At the start of the modeling interval, the current sheet was almost $2 R_E$ thick, but its thickness rapidly decreased to $0.2 R_E$ within 20 minutes. This is consistent with prior satellite measurements [Fairfield, 1984; Mitchell *et al.*, 1990; Sergeev *et al.*, 1993].

It is noteworthy that there is a high degree of correlation between the thinning of the current sheet, corresponding to magnetic field line stretching, and the equatorward motion of the proton aurora. Within the framework of our model, this implies that the equatorward motion of auroral precipitation is directly related to the stretching of the magnetic field lines in the magnetotail.

As mentioned earlier, the inner edge of the plasma sheet was not an input to this model; instead it was a product. Samson *et al.* [1992] showed that the 486.1 nm

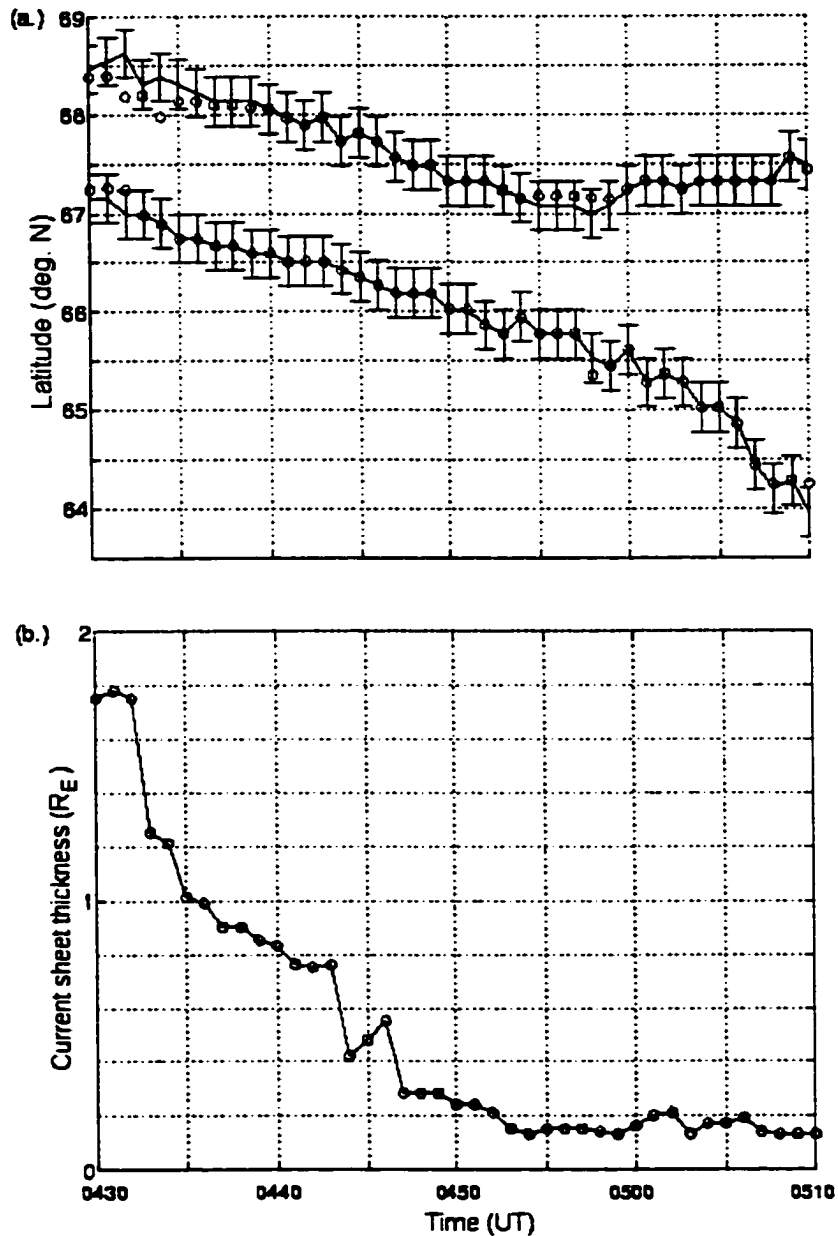


Figure 3.9: Model statistics for the March 9, 1995 event. (a) Emission borders (solid line with error bars) and best-fit values (circles) calculated from the magnetic model predicted precipitation regions. (b) Model predictions for current sheet thickness at $8 R_E$ (modified after Wanliss et al. [2000]).

emissions could be used to delineate the earthward edge of the plasma sheet. Thus, using the equatorward border of the $H\beta$ emissions, the position of the inner edge of the plasma

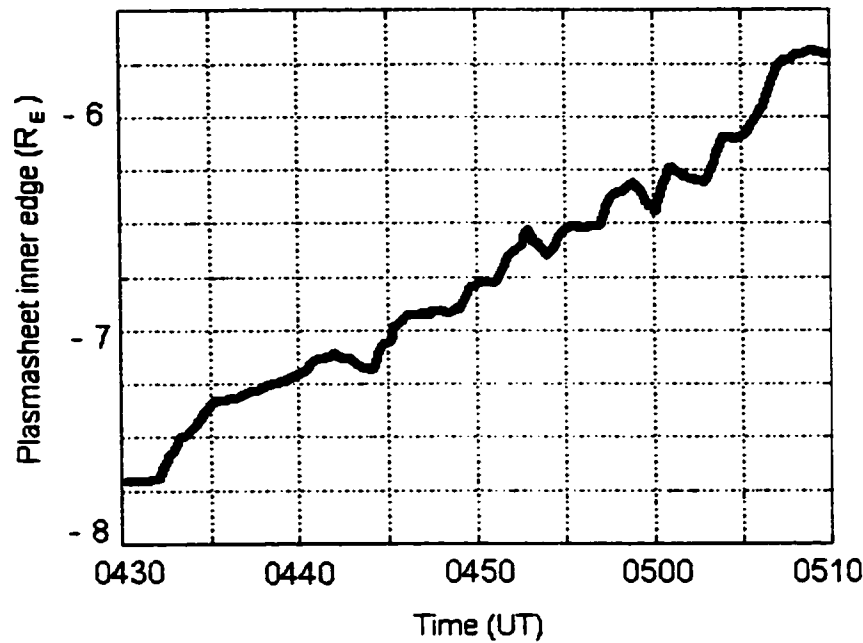


Figure 3.10: Position of the inner edge of the plasma sheet during the substorm growth phase on March 9, 1995 (modified from Figure 4 in *Wanliss et al.* [2000]).

sheet was derived. The position of the inner edge for March 9, 1995 is shown in Figure 3.10.

3.7 Conclusion

This study has demonstrated how the new technique of fitting a Gaussian profile to the photometer data can be very useful. By fitting a Gaussian distribution rather than a Step Function to the data, it was possible to determine the equatorward border of the H β auroral emissions. The ability to determine the equatorward border directly resulted in the calculation of the current sheet thickness and the calculation of the location of the inner edge of the plasma sheet.

It was found that the cross-tail current sheet could thin to as little as $0.2 R_E$, which has also been observed in satellite measurements [*Mitchell et al.*, 1990; *Sergeev et al.*, 1993]. The inner edge of the plasma sheet moved earthward to $6 R_E$ in the case presented here,

supportive of the study by *Korth et al.* [1999] who found that during moderate substorm activity the particle population of the plasma sheet could reach geosynchronous altitudes. A similar conclusion was reached by *Lyons* [1997] from the point of view of particle isotropy. *Lyons* [1997] observed that isotropy could extend to lower latitudes with increasing particle energy for both electrons and ions.

Finally, it has been proposed that the H β auroral emissions, due to the precipitation of energetic protons in the ionosphere, are associated with the thinning of the equatorial current sheet. Two length scales are important in this study: the magnetic field radius of curvature in the equatorial plane, and the proton gyroradius. At the start of the substorm the current sheet thickness is typically larger than the proton gyroradius and ions behave adiabatically. As the current sheet thins and becomes of the order of the proton gyroradius they become nonadiabatic and may be scattered into the ionosphere [*Zelenyi et al.*, 1990]. As shown by *Liu et al.* [1998], strong nonadiabatic behaviour can lead to enhanced proton precipitation leading to H β . By using the ionospheric data as a proxy for precipitation it was possible to map the changing topology of the magnetotail current sheet during substorm growth phase. Together with the Gaussian fit technique and the Wanliss magnetic field model it has been shown that the growth phase H β emissions can be at least partially explained by the precipitation of protons out of the thinning cross-tail current sheet. Furthermore, it has been shown that the magnetic field line stretching in the magnetotail (i.e. thinning of the current sheet) is correlated with the equatorward motion of the H β .

Bibliography

- Ashour-Abdalla, M., L.M. Zelenyi, V. Perroomian, and L.R. Richard, Consequences of magnetotail ion dynamics, *J. Geophys. Res.*, *99*, 14891-14916, 1994.
- Baker, K.B. and S. Wing. A new magnetic coordinate system for conjugate studies at high latitudes, *J. Geophys. Res.*, *94*, 9139-9143, 1989.
- Baker, D.N. and R.L. McPherron, Extreme energetic particle decreases near geostationary orbit: A manifestation of current diversion within the inner plasma sheet, *J. Geophys. Res.*, *95*, 6591, 1990.
- Blanchard, G.T., L.R. Lyons, J.C. Samson, F.J. Rich, Locating the polar cap boundary from observations of 6300 A auroral emissions, *Geophys. Res. Lett.*, *100*, 7855-7862, 1995.
- Büchner, J. and L.M. Zelenyi, Chaotization of the electron motion as the cause of an internal magnetotail instability and substorm onset, *J. Geophys. Res.*, *92*, 13456, 1987.
- Delcourt, D.C., J.-A. Sauvaud, R.F. Martin and T.E. Moore, On the nonadiabatic precipitation of ions from the near-Earth plasma sheet, *J. Geophys. Res.*, *101*, 17409, 1996.
- Erickson, G.M., On the cause of X-line formation in the near-earth plasma sheet: Results of adiabatic convection of plasma sheet plasma, in *Magnetic Reconnection, Geophys. Monogr. Ser.*, *30*, ed. E.W. Hones Jr., pp. 296-302, American Geophysical Union, Washington, D.C., 1984.
- Fairfield, D.H., Magnetotail energy storage and the variability of the magnetotail current sheet, in *Magnetic reconnection in Space and Laboratory Plasmas, Geophys. Monogr. Ser.*, *vol. 30*, ed. E.W. Hones Jr., pp. 168-177, AGU, Washington, D.C., 1984.
- Hau, L.N., R.A. Wolf, G.-H. Voight, and C.C. Wu, Steady state magnetic field configurations for the Earth's magnetotail, *J. Geophys. Res.*, *94*, 1303, 1989.
- Kaufmann, R.L., Substorm currents: growth phase and onset, *J. Geophys. Res.*, *92*, 7471, 1987.
- Kistler, L.M., E. Mobius, W. Baumjohann, G. Paschmann, and D.C. Hamilton, Pressure changes in the plasma sheet during substorm injections, *J. Geophys. Res.*, *97*, 2973, 1992.

- Kokubun, S., and R.L. McPherron, Substorm signatures at synchronous altitude, *J. Geophys. Res.*, *86*, 11265, 1981.
- Korth, H., M.F. Thomsen, J.E. Borovsky, and D.J. McComas, Plasma sheet access to geosynchronous orbit, *J. Geophys. Res.*, *104*, 25,047, 1999.
- Lewis R.V., M.P. Freeman, and G.D. Reeves, The relationship of HF radar backscatter to the accumulation of open magnetic flux prior to substorm onset, *J. Geophys. Res.*, *103*, 26613, 1998.
- Liu, W.W., G. Rostoker, and J.C. Samson, Precipitation of hot protons from a stretched near-earth current sheet, *COSPAR Colloquia Series, V.9*, 165, Elsevier, 1998.
- Lu, G., N.A. Tsyganenko, A.T.Y. Lui, H.J. Singer, T. Nagai, S. Kokubun, Modeling of time-evolving magnetic fields during substorms, *J. Geophys. Res.*, *104*, 12327-12337, 1999.
- Lui A.T.Y. et al, Multipoint study of a substorm on February 9, 1995, *J. Geophys. Res.*, *103*, 17333, 1998.
- Lyons, L.R. and T.W. Speiser, Evidence for current sheet acceleration in the geomagnetic tail, *J. Geophys. Res.*, *87*, 2276, 1982.
- Lyons, L.R., Magnetospheric processes leading to precipitation, *Space Science Rev.*, *80*, 109, 1997.
- McPherron, R.L., Substorm related changes in the geomagnetic tail: The growth phase, *Planet. Space. Sci.*, *20*, 1521, 1972.
- Mitchell, D.G., D.J. Williams, C.Y. Huang, L.A. Frank, and C.T. Russell, Current carriers in the near-Earth cross-tail current sheet during substorm growth phase, *Geophys. Res. Lett.*, *17*, 583, 1990.
- Nakai, H., Y. Kamide, C.T. Russell, Statistical nature of the magnetotail current in the near-earth region, *J. Geophys. Res.*, *102*, 9573-9586, 1997.
- Pulkkinen, T.I., D.N. Baker, R.J. Pellinen, J. Buchner, H.E.J. Koskinen, R.E. Lopez, R.L. Dyson, L.A. Frank, Particle scattering and current sheet stability in the geomagnetic tail during the substorm growth phase, *J. Geophys. Res.*, *97*, 19283, 1992.
- Pulkkinen, T.I., D.N. Baker, D.G. Mitchell, R.L. McPherron, C.Y. Huang, and L.A. Frank, Thin current sheets in the magnetotail during substorms: CDAW 6 revisited, *J. Geophys. Res.*, *99*, 5793, 1994.

- Pulkkinen, T.I., D.N. Baker, L.L. Cogger, T. Mukai, and H.J. Singer, Coupling of inner tail and midtail processes, in *Substorms-4: International Conference on Substorms 4, Lake Hamana, Japan, March 9-13, 1998*, edited by S. Kokubun and Y. Kamide, pp.749-754, Terra Sci., Tokyo, 1998.
- Samson, J.C., L.R. Lyons, P. T. Newell, F. Creutzberg, B. Xu, Proton aurora and substorm intensifications, *Geophys. Res. Lett.*, *19*, 2167, 1992.
- Samson, J.C., Mapping substorm intensifications from the ionosphere to the magnetosphere, in *Proceedings of the International Conference on Substorms 2*, ed. J.R. Kan, J.D. Craven, S.-I. Akasofu, p.189, Univ. Alaska, 1994.
- Sergeev, V.A., Sazhina, E.M., Tsyganenko, N.A., Lundblad, J.A., and Soraas, F., Pitch-angle scattering of energetic protons in the magnetotail current sheet a the dominant source of their isotropic precipitation into the nightside ionosphere, *Planet. Space Sci.*, *31*, 1147.
- Sergeev, V.A., D.G. Mitchell, C.T. Russell, D.J. Williams, Structure of the tail plasma/current sheet at 11 R_E and its changes in the course of a substorm, *J. Geophys. Res.*, *98*, 17345, 1993.
- Tsyganenko, N.A., Global quantitative models of the geomagnetic field in the cislunar magnetosphere for different disturbance levels, *Planetary and Space Science*, *35*, 1347-1358, 1987.
- Tsyganenko, N.A., A magnetospheric magnetic field model with a warped tail current sheet, *Planetary and Space Science*, *37*, 5-20, 1989.
- Tsyganenko, N.A, Modeling the earth's magnetospheric magnetic field confined within a realistic magnetopause, *J. Geophys. Res.*, *100*, 5599-5612, 1995.
- Tsyganenko, N.A, Effects of the solar wind conditions on the global magnetospheric configuration as deduced from data-based models, in *Proceedings of ICS-3 Conference on Substorms, Versailles, France, ESA SP-389*, pp.181-185, 1996.
- Voronkov, I., E. Friedrich and J.C. Samson, Dynamics of the substorm growth phase as observed using CANOPUS and SuperDARN instruments, *J. Geophys. Res.*, *104*, 28491, 1999.
- Wanliss, J.A., Fast ion flows in the Earth's magnetotail, *PhD. Thesis*, University of Alberta, Edmonton, Alberta, Canada, 2000.
- Wanliss, J.A., J.C. Samson, and E. Friedrich, On the use of photometer data to map dynamics of the magnetotail current sheet during substorm growth phase, *J. Geophys. Res.*, *105*, 27673, 2000.

Zelenyi, L., A. Galeev, C.F. Kennel, Ion precipitation from the inner plasma sheet due to stochastic diffusion, *J. Geophys. Res.*, 95, 3871, 1990.

Zwingmann, W., Self-consistent magnetotail theory: equilibrium structures including arbitrary variation along the tail axis, *J. Geophys. Res.*, 88, 9101-9108, 1983.

²Chapter 4: Dynamics of the substorm expansive phase

4.1 Introduction

As was discussed in the Introduction, the magnetosphere cannot sustain the stretched topology associated with energy storage of the growth phase indefinitely. To release the stress in the system, the magnetosphere undergoes a rapid reconfiguration during the next phase of the substorm- the expansive phase.

The past 4 years have seen considerable controversy grow over the sequence of events during a magnetospheric substorm. The controversy centers around exactly where expansive phase onset occurs. On the one hand, there is the Near-Earth Onset (NEO), or Near-Geosynchronous Onset, model championed, for example, by *Lui* [1991], *Ohtani et al.* [1992a], and *Samson* [1998]. In this model the substorm expansive phase is believed to begin close to the Earth, near geosynchronous orbit, followed by the tailward expansion of a rarefaction wave, or current disruption region, toward the site of near-Earth neutral line formation in the midtail. On the other hand, recent Near Earth Neutral Line (NENL) models postulate that a NENL is formed in the midtail region, prior to expansive phase onset [*Baker and McPherron*, 1990], ejecting plasma and magnetic flux earthward [*Angelopoulos et al.*, 1994]. This flux ‘piles up’ along the inner edge of the plasma sheet, causing the divergence of the cross-tail current and formation of the substorm current wedge [*Birn and Hesse*, 1996]. Observational and theoretical support has been provided for both models [*Nagai et al.*, 1998; *Shiokawa et al.*, 1997; *Vasyliunas*, 1998; *Samson et al.*, 1992b; *Lui*, 1996], yet there still is no consensus as to whether the near-Earth onset or the NENL begins the process of the substorm expansive phase.

The idea that expansive phase onset is located at the inner edge of the plasma sheet was suggested ~30 years ago on the basis of ionospheric observation [*Atkinson*, 1967; *Kisabeth and Rostoker*, 1971]; however, it was not until the early 1990s that

² A version of this chapter has already been published. Friedrich, E., J.C. Samson, and I. Voronkov, Dynamics of the substorm expansive phase onset, *J. Geophys. Res.*, 106, 13145, [2001].

observational evidence from geostationary and inner plasma sheet satellites lent support to the idea [Lopez and Lui, 1990; Sergeev *et al.*, 1993] and initiated the series of near-Earth onset substorm models. A review of the observations and models is given by Lui [1996]. The concept of the NEO model was substantiated by the observations of Lopez *et al.* [1990] and Samson *et al.* [1992a], who used photometer data to suggest that the substorm expansive phase onset was initiated in the region of the near-Earth plasma sheet, characterized by the transition from stretched to dipolar field lines. By correlating Defence Meteorological Satellite Program (DMSP) particle data and meridian-scanning photometer (MSP) data, Samson *et al.* [1992b] showed that the electron arc that brightens at the onset of expansive phase is embedded in a region of intense H β emissions. The 'brightening' of the arc consistently occurred 4° - 6° equatorward of the region of open field lines, which are determined by the poleward border of the 630.0 nm emission region. This region is associated with auroral electron precipitation from the plasma sheet. These facts, along with the observation that brightening arcs can be associated with field line resonances that occur on quasi-dipolar field lines, suggested that expansive phase onset occurs in the near-Earth plasma sheet between 6 and 10 R_E. Recent observations using the CRRES [Erickson *et al.*, 2000] and Polar [Frank and Sigwarth, 2000] spacecrafts have also revealed near-Earth onsets, in some cases as far earthward as ring current distances (4-7 R_E).

With the launch of the Geotail spacecraft in 1992 the scientific community was afforded an opportunity to study the magnetotail (from radial distances of $-210 < x < -8$ R_E) in an effort to interpret the physical processes taking place in this region both during and apart from magnetospheric substorms. A controversial result produced from the Geotail data is the observation that fast plasma flows in the magnetotail precede ground Pi2 onset and may directly trigger expansive phase onset. This observation was first published by Sergeev *et al.* [1995] but has been followed by numerous findings [Nagai and Machida, 1998; Nagai *et al.*, 1998; Shiokawa *et al.*, 1998]. The latest study by Machida *et al.* [1999] applied a superposed epoch analysis to 263 substorm events observed by Geotail. Their results showed that tailward flows associated with plasmoids began about 2 or 3 min before the ground-based Pi2 onset.

These results are not definitive, however, as recent studies incorporating methods other than ground-based Pi2 signatures to determine expansive phase onset have produced conflicting results. *Lui et al.* [1998] used auroral breakups as observed using global images from Polar to determine expansive phase onset. Correlating the auroral breakups with plasma and magnetic field measurements from Geotail, *Lui et al.* [1998] found that strong plasma flows preceding, or at the time of, expansive phase onset were not always observed, even when Geotail was well within the central plasma sheet in the midnight sector. Second, their results showed that plasma sheet activity associated with auroral breakups is spatially limited and transient in nature, consistent with the model of current disruption. *Ohtani et al.* [1999] performed a detailed study of substorm onset timing and the cause-and-effect relationship between NENL formation and the trigger of tail current disruption. Comparing ground-based and satellite-based data for one event, *Ohtani et al.* [1999] found that the signature of reconnection did, in fact, precede the near-Earth onset. However, there were additional observations that were difficult to explain in terms of the NENL model, leading *Ohtani et al.* [1999,p.22,713] to assert that ‘tail current disruption is a unique process rather than a direct consequence of NENL formation.’ *Ohtani et al.* [1999] also suggested that tail current disruption can play a dominant role compared to near-Earth reconnection with respect to substorm dynamics.

Obviously, the substorm problem is complex and difficult, but the problem is a tractable one given the increasing remote-sensing abilities of the ground-based networks and the growing number of spacecraft in the magnetosphere. *Samson et al.* [1992b] provided evidence for two substorm events using DMSP and MSP data and showed that after expansive phase onset on near-Earth closed field lines (as inferred from the 486.1 nm emissions), the enhanced 557.7 nm emission region expanded poleward to reach the edge of the open field line region in approximately 4 to 5 min. A recent paper by *Frank and Sigwarth* [2000] has reported similar observations on comparable timescales using high-resolution global images from Polar. *Samson* [1998] expanded on this timing to include all aspects of the substorm from growth to recovery and provided a model framework from which to test the time intervals for each process. The model’s ‘intensification’ phase and expansive phase have a duration of the order of tens of seconds to minutes,

respectively. The rapid timescale of these phases points to an intrinsically explosive process (with respect to the initial intensification of expansive phase onset) and can be characterized only by high growth rate or nonlinear instabilities in the equatorial plane of the near-Earth magnetotail [Samson *et al.*, 1996].

Among other candidate mechanisms, some recent work has suggested that some form of the ballooning instability may provide high growth rates in this region. These models utilized the MHD ballooning instability [Lee, 1998; Bhattacharjee *et al.*, 1998], nonlinear ballooning detonation [Hurricane *et al.*, 1997, 1998], kinetic ballooning instability [Cheng and Lui, 1998], and the ballooning and tearing mode coupling model [Sundaram and Fairfield, 1997].

Samson *et al.* [1992b] discussed the value of the photometer data with respect to qualitatively delineating plasma regimes and the phases of the substorm. In this paper we have used photometer and magnetometer data from the Canadian Auroral Network for the OPEN Program Unified Study (CANOPUS) array to quantitatively determine the chronology of the processes centered around the expansive phase (i.e., explosive growth, dipolarization, lobe flux reconnection). Determining the chronological order of ground-based signatures of the expansive phase processes may help to determine which physical process, or processes, governs the onset of the expansive phase. The photometer data were used to determine the poleward border of the 557.7 and 630.0 nm emissions and the latitudinal maximum of the 486.1 nm emissions. The magnetometer data were used to determine the borders of the substorm auroral electrojets and were correlated with the photometer data in order to determine the location of the electrojets during the substorm process. Evidence is presented that substantiates the claim that the onset of the expansive phase (that is, the first intensification of the most equatorward auroral arc and the beginning of dipolarization) begins first in the near-Earth region and is followed by reconnection within periods of tens of seconds to a few minutes. Magnetometer and photometer data for two isolated events will be highlighted: February 9, 1995, and December 7, 1989.

4.2 Procedure

The criteria used to choose the events for this study were the following: First, the events must be isolated with extended periods of quiescence before the beginning of the growth phase. In this way one is assured that the magnetosphere is as close to a 'ground,' or quiet, state as is likely to occur before the advent of a substorm. Second, the growth phase must be 'clean' with no significant activity such as pseudobreakups prior to the initial intensification of the expansive phase. Third, the entire event must be observed in both the Gillam and Rankin photometers in all three of the wavelengths: 486.1, 557.7, and 630.0 nm. All substorms were chosen so that they occurred close to or directly over the Churchill line of magnetometers (by visual inspection of magnetometer data) so that data from these magnetometers could be correlated with data from the meridian scanning photometers at Gillam and Rankin.

A detailed description of the CANOPUS instruments is given by *Rostoker et al.* [1995].

Many studies have been carried out in the past describing the nature of particle precipitation in the ionosphere [*Winningham and Heikkila*, 1974; *Winningham et al.*, 1975; *Parks et al.*, 1992]. In one such study, *Galperin and Feldstein* [1991] described 630.0 nm luminosity poleward of the auroral oval as being related to precipitation from the outer boundaries of the plasma sheet. In a similar vein, *Samson et al.* [1992] noted that the poleward boundary of the 630.0 nm emissions occurred quite close to the transition region from closed to open field lines and that its equatorward motion may indicate the expansion of the region of open field lines, i.e. the polar cap. To substantiate this hypothesis, *Blanchard et al.* [1995] used DMSP and meridian scanning photometer data to show that the poleward border of the 630.0 nm emissions could indeed be used as a continuous monitor of the boundary of the polar cap, marking the ionospheric separatrix between open and closed field lines. The results of their study indicated that the equatorward expansion of the 630.0 nm emissions is consistent with the growth of the polar cap. Similarly, the poleward recovery of the emissions is consistent with the shrinking of the polar cap. In this study the results of *Blanchard et al.* [1995] have been adopted with the interpretation that when the emissions move equatorward the region of open field lines is expanding, whereas the subsequent poleward movement indicates the

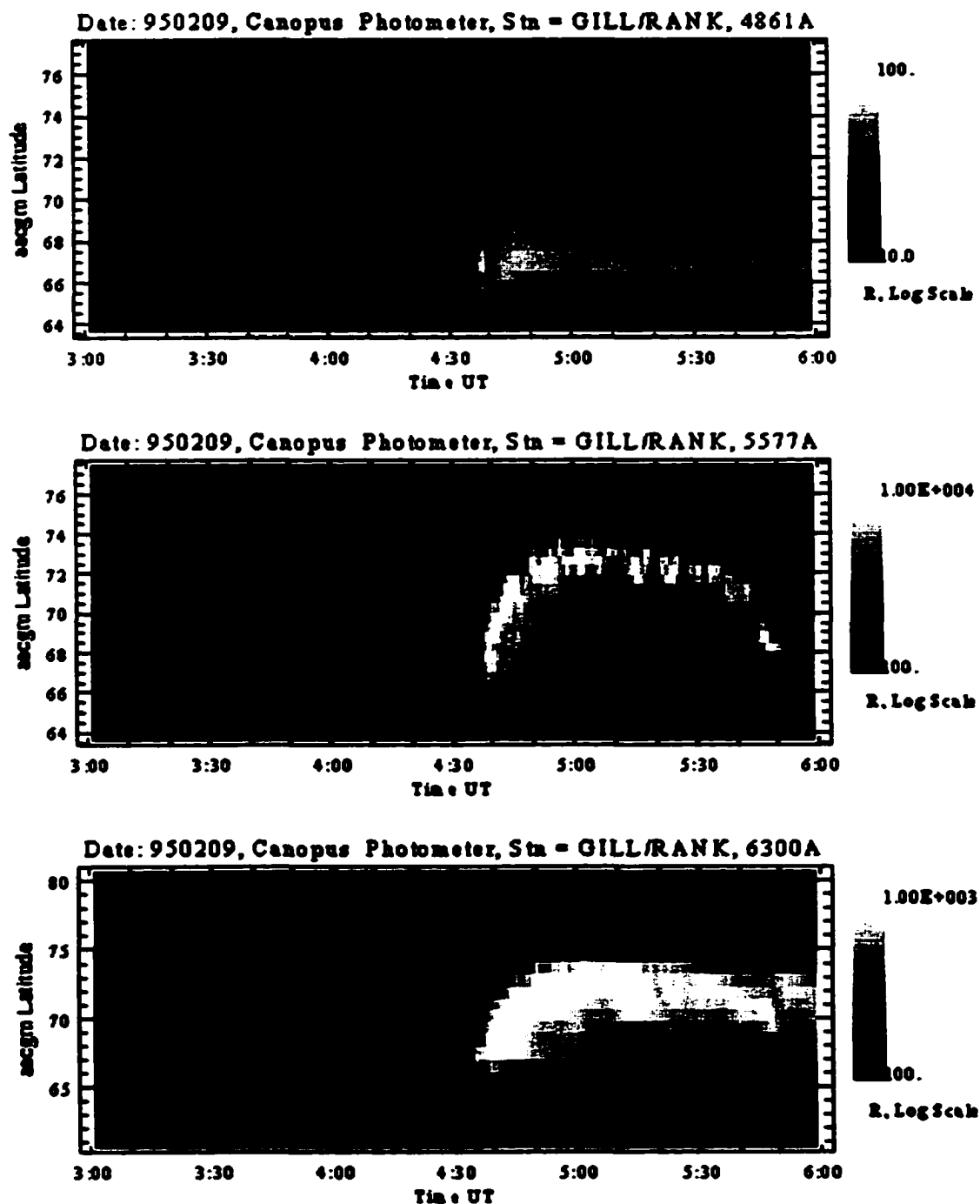


Figure 4.1: Meridian scanning photometer data for February 9, 1995. From top to bottom panels show 486.1 nm, 557.7 nm and 630.0 nm emissions, respectively. Emission intensity is measured in Rayleighs by the logarithmic bar scale to the right of each panel.

reconnection of those open field lines and the closure of lobe flux. The primary goal of this study was to determine whether the relative poleward motion of the poleward edge of the electron emissions, as obtained using the 557.7 and 630.0 nm lines, was a repeatable phenomenon. If so, it could be indicative of some generic physical process occurring during the substorm. An example of MSP data plotted in an altitude adjusted corrected geomagnetic (AACGM) latitude versus time format is shown in Figure 4.1. The goal is to follow the poleward border of the 557.7 and 630.0 nm emissions to determine when the borders expand poleward in relation to each other.

Using the process outlined in Chapter 2, the poleward borders of the emissions were determined by fitting a Gaussian profile to the data and finding the edge at a specified standard deviation. The borders of the electrojets were chosen by determining the positive and negative peaks in the Z component of the magnetic perturbations in a series of latitude profiles. Following the description outlined by *Kisabeth and Rostoker [1971]*, the width of a current system can be determined quite accurately by the distance between the positive and negative extrema in the Z component profile as long as the line of stations sampling the currents crosses the ionospheric electrojet. To ensure that the CANOPUS photometers were close to the ionospheric activity, we chose events where the substorm onset occurs either at the location of, or near, the Churchill line of magnetometer stations. The positive and negative peaks in the ΔZ profile gave the poleward and equatorward borders of the electrojet, respectively.

For an accurate determination of the electrojet borders the choice of baseline is crucial. The latitude profiles that are produced by magnetometer data are complicated profiles composed, in most cases, of more than one current system. For some events it is possible to find a reference point that is magnetically quiet (as compared to the magnetic perturbations associated with the substorm) in the few hours preceding the onset of the substorm. In these cases this point can be used as a baseline for the data [e.g., *Voronkov et al., 1999, Figure 3*]. There are instances, however, when high-frequency pulsations contaminate the data throughout the duration of the substorm, making it impossible to find a quiet reference point. Such was the case for the February 9, 1995, and February 23, 1995 events. For these events, differential profiles [*Kisabeth and Rostoker, 1973*] were also used to determine the borders of the electrojets.

While there are many ways to identify expansive phase onset, timing the onset correctly is a complex problem. Traditionally, the identification of ground-based Pi2 signatures has been used to determine the onset. Indeed, there are recent papers [*Nagai et al.*, 1998; *Miyashita et al.*, 1999] that rely solely on ground-based Pi2 signatures. However, as more studies are completed, it is becoming increasingly obvious that the Pi2 signature may not be an accurate parameter for the precise timing that is required [*Ohtani et al.*, 1999; *Liou et al.*, 1999]. This fact has led scientists to other data sets, alone and in combination with Pi2 signatures, to time expansive phase onset [*Lui et al.*, 1998].

In this study we have used a combination of ground-based Pi2 signatures, current wedge signatures observed in latitude profiles, and the onset of dipolarization as observed in the H β emissions to time the onset of our events. The H β and 557.7 nm emissions from the MSP are an excellent visual source for timing the onset [*Samson et al.*, 1992b] with a resolution of ~ 1 min between data points. The time when the H β emission begins to expand poleward marks the time of dipolarization of near-Earth, stretched, tail field lines and therefore the time of expansive phase onset (less the ~ 2 minute propagation time between the site of onset and the ionosphere [*Samson*, 1992b; *Samson*, 1994]). The 557.7 nm emission region expands poleward at the same time as the H β , marking the time of energization of plasma sheet electrons. However, it is the magnetometer data, with a resolution of up to 5 sec, that gives the precise timing that is required. For our study we determined the onset to within 1 min resolution using the MSP data. A series of latitude profiles was then produced every 10 sec for a 2 min interval centered around the time determined from the optical data. The profiles were visually inspected for the localized westward electrojet associated with the substorm intensification. When that signature was found, the time of onset was noted.

4.3 Data and Observations

4.3.1 February 9, 1995

We begin our study with an event that took place on February 9, 1995. The February 9, 1995 event is unique in that it afforded our scientific community with one of those rare

instances when all conditions for a 'perfect' substorm are met. Owing to an unusually long interval of northward interplanetary magnetic field (IMF), the magnetosphere was as close to a low-energy, or 'quiet,' state as is likely to be possible before the advent of a substorm. In addition, the number of satellites that were not only within the magnetotail, but in strategic locations for observing substorm processes was unprecedented. The amount of useful data available for this event was a veritable 'gold mine' for magnetospheric scientists [*Lui et al.*, 1998].

The IMF, observed by the Wind satellite at ~ 193 RE upstream from the Earth, was northward for ~ 12 hours before turning southward from 0200-0400 UT on February 9. This brief southward turning led to a substorm growth phase beginning at ~ 0335 UT, as seen by the enhanced $H\beta$ emissions in the photometer data shown in Figure 4.1 and in the magnetometer data (not shown). The growth phase is also manifest in the 630.0 nm emissions with a region of intense precipitation which begins to move equatorward slightly before 0335 UT, starting at a latitude of $\sim 74^\circ$.

The ionospheric footprint of the plasma sheet can be reasonably approximated by the latitudinal extent of the 630.0 nm emission region [*Samson*, 1994]. From the 630.0 nm data in Figure 4.1, the latitudinal width of the emissions has narrowed to $\sim 5^\circ$ just prior to expansive phase onset, indicating that the plasma sheet has thinned prior to expansive phase onset.

The thinning of the region of electron precipitation was also seen in the events studied by *Voronkov et al.* [1999], where they noted the electron precipitation narrowing during the course of the growth phase, reaching latitudinal widths of $\sim 2^\circ - 5^\circ$ just prior to substorm intensification. Their study also noted that the main dynamics of the growth and expansive phase took place within or very close to the proton aurora region. Correlation of radar data from the Super Dual Auroral Radar Network (SuperDARN) Kapuskasing and Saskatoon radars showed that at the beginning of the growth phase, ionospheric convection was enhanced near the proton auroral band, resulting in a flow with a large westward component of velocity. This region of flow moves equatorward following the proton aurora band and develops significant latitudinal gradients prior to substorm intensification.

Start Time 1995/02/08(040) 04:00:00 UT
 BASELINE: MEAN 09-04:00:00 TO 09-06:00:00

X

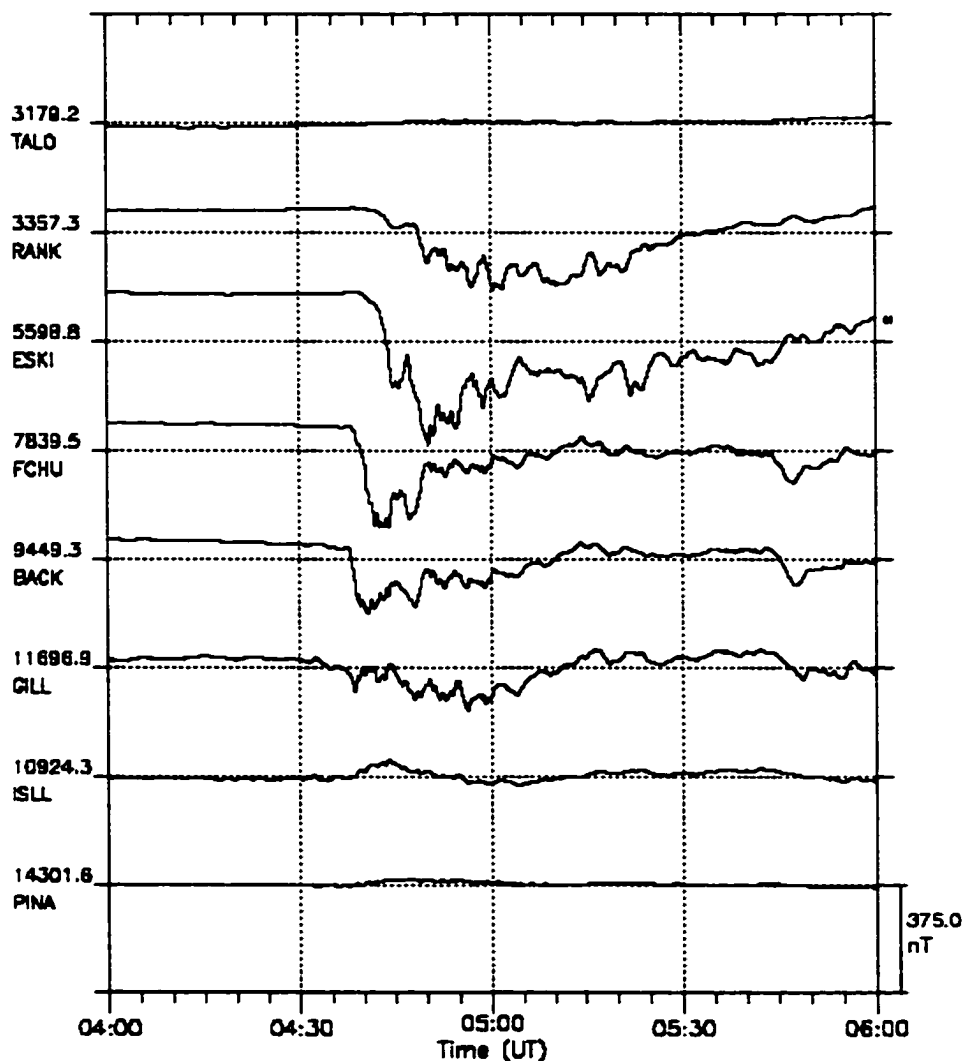


Figure 4.2: X-component magnetometer data from the CANOPUS Churchill line. The westward electrojet associated with expansive phase onset appears at ~ 0437 UT.

The equatorward edge of the 630.0 nm emission and the poleward edge of the 557.7 nm emission data of the February 9 event show an intensification at ~ 0431 UT. The 0431 UT timing was described by *Lui et al.* [1998] to be the onset of the expansive phase on the basis of Pi2 signatures and auroral kilometric radiation index signatures. However, we believe that this is not the onset of the expansive phase proper for the following reasons: *Akasofu* [1964] originally defined the expansive phase as that period of the substorm

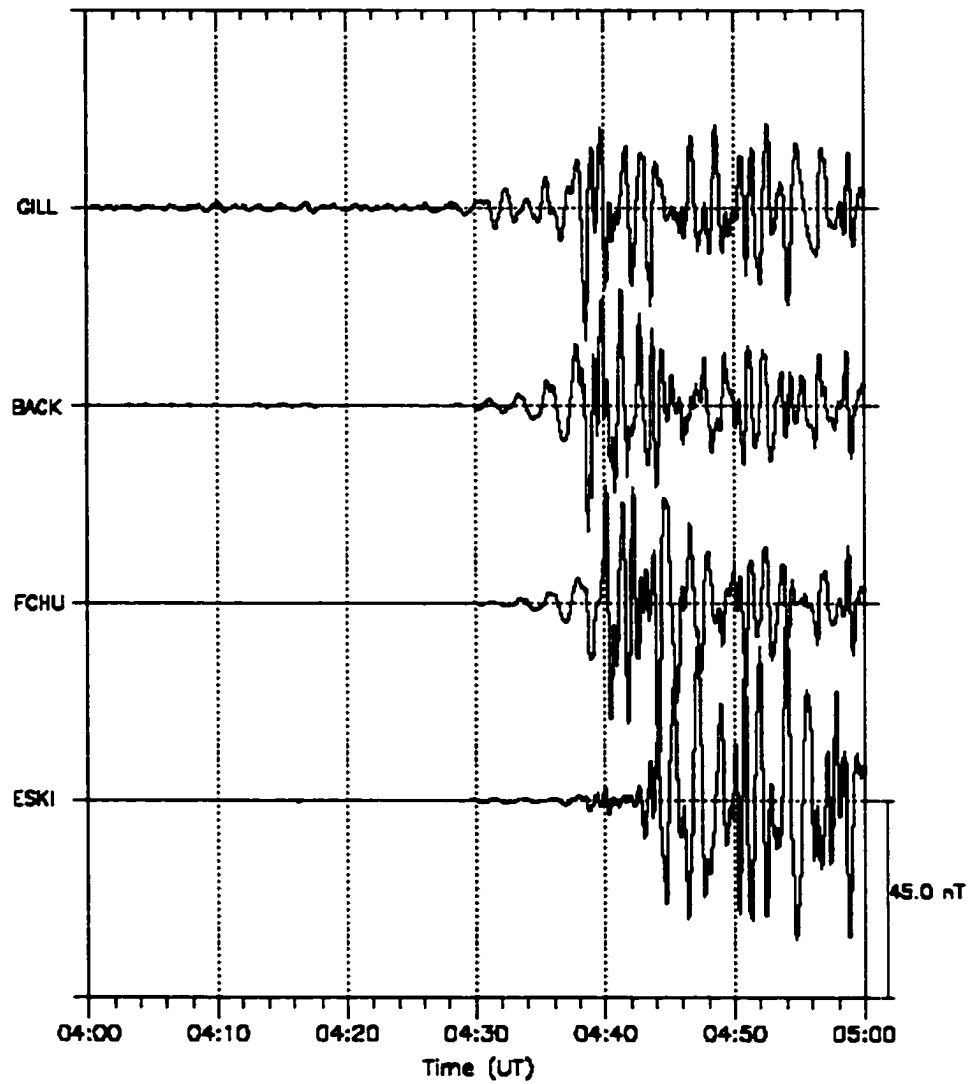


Figure 4.3: Pi2 pulsations for February 9, 1995 from 04-05 UT. The smaller oscillations due to the precursor at ~0430 UT are evident, followed by the larger pulsations associated with expansive phase onset at 0437 UT.

when the poleward border of the auroral oval in the midnight sector moved poleward. This definition has been used by *Lyons* [1997, p.27,039] in his definition of a classical substorm as 'one that has auroral brightening and electrojet formation at onset, followed by poleward expansion of the region of bright aurora.' As can be seen from the H β and oxygen green line emissions, there is no poleward movement of the precipitation at 0431 UT (see Figure 4.1). Also, Figure 4.2 illustrates the X component magnetic data from the

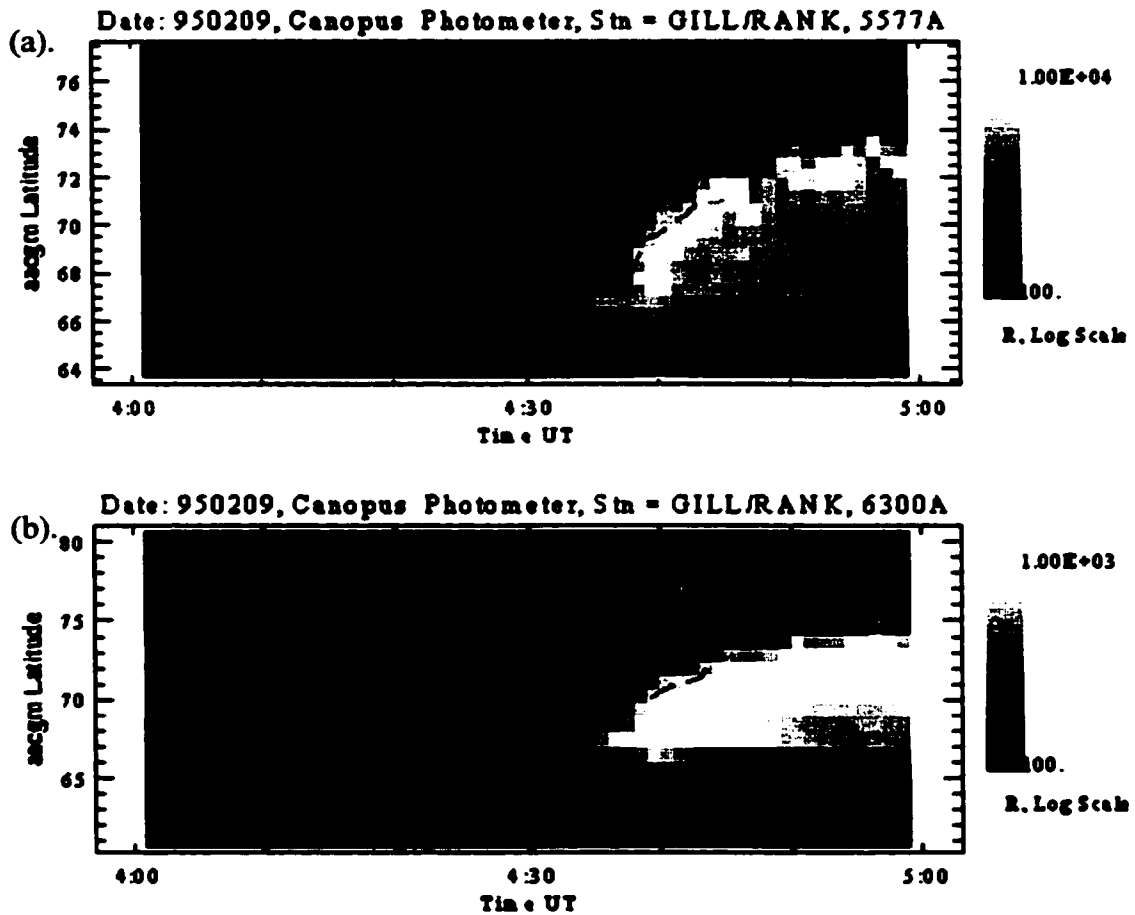


Figure 4.4: Poleward borders of the 557.7 nm (a) and 630.0 nm (b) data overlaid onto the meridian scanning photometer data for February 9, 1995.

Churchill magnetometer line, and it is clear that the negative bay associated with expansive phase onset takes place after 0435 UT. Therefore we propose the following terminology: The small Pi2 signature and the intensification seen in the red and green line emissions is what we call a 'precursor' to the poleward expansion of the emissions (Figure 4.3). Following the precursor, the 557.7 nm and H β emission regions begin to expand poleward at 0436 and 0437 UT, respectively. The onset of poleward expansion of the 486.1 nm emissions marks the beginning of dipolarization and of a process that may accelerate (energize) high-energy electrons in the central plasma sheet. If one believes that poleward expansion of the precipitation is an ionospheric signature of the beginning of the expansive phase, then the actual onset of the expansive phase for this event occurs ~6 min later at 0437 UT. Thus we define expansive phase onset at the ionospheric level

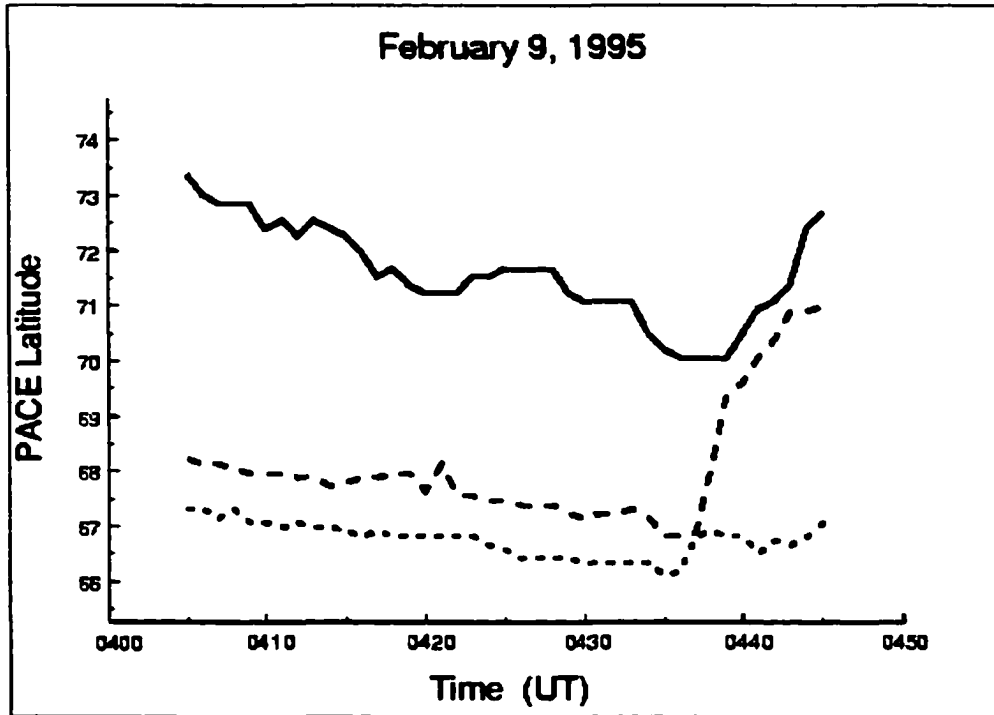


Figure 4.5: Variation (in time and latitude) of the poleward borders of the 557.7 nm (dashed line), 630.0 nm (solid line), and maximum emissions of the 486.1 nm (dotted line) for February 9, 1995. Expansive phase onset is 0437 UT and the beginning of lobe flux reconnection is 0439 UT.

by the beginning of the poleward expansion of the H β and 557.7 nm emissions and by the beginning of the poleward movement of the substorm westward electrojet, as seen in the latitude profiles of the magnetometer data (see Section 4.4). In the case of the February 9 event the 557.7 nm emissions begin to move poleward from 67° at 0437 UT and continue to expand poleward to 72.5° by 0444 UT. Within this time interval the 630.0 nm emissions begin to expand poleward, reaching a maximum latitude of 74°. As was mentioned earlier, the poleward border of the red line emissions delineates the boundary between open and closed field lines [Samson *et al.*, 1992a; Blanchard *et al.*, 1997]. In Figure 4.1 we see this boundary expanding equatorward from 74° to 71° during the growth phase and returning poleward to 74° during the expansive phase. The expansion and subsequent shrinking of the open-closed field line boundary give an indication of the dynamic changes of the polar cap area during the substorm [Brittnacher *et al.*, 1999].

Using the Gaussian fit program described in Chapter 2, we determined the latitudinal location of the poleward borders of the green line and red line emissions. The fit to the data is shown in Figures 4.4a and 4.4b. As described in Chapter 2, the borders follow the latitudinal motion of the maximum intensity of the data. Figure 4.5 shows the temporal development of the borders of the emissions as a function of AACGM latitude. The green line emissions begin to move poleward at 0437 UT. At 0439 UT the 630.0 nm border begins to expand poleward from 70° to 73° . The time delay between the beginning of the poleward expansion of the green line emissions and the beginning of the poleward expansion of the red line border is 2 min. It is interesting that the poleward border of the 557.7 nm emissions continues to expand poleward past the region of dipolarization (the dipolarization causes $H\beta$ to expand poleward to a maximum latitude of 68.5°). The rapid poleward motion of the emissions is suggestive of an unstable region that is expanding rapidly tailward in the central plasma sheet, an instability that not only expands at high speeds, but may energize (accelerate) plasma sheet electrons as it propagates. It is further noteworthy that the border of the 630.0 nm emissions does not exhibit any significant movement until the 557.7 nm emissions have reached it. The data suggests that the region of the magnetosphere associated with the 630.0 nm emissions is not active at expansive phase onset, but becomes active a few minutes later. This is consistent with the observations of Frank and Sigwarth [2000].

4.3.2 December 7, 1989

An event similar in detail to the February 9, 1995, substorm occurred on December 7, 1989. Although there were no Wind data available for this event, the equatorward motion of the $H\beta$ emissions [Samson *et al.*, 1992b] indicates that the growth phase began at 0420 UT (Figure 4.6). This emission moved equatorward from 69° to 65° until expansive phase onset at 0609 UT. The growth phase 557.7 nm emissions follow the same equatorward motion as the $H\beta$ until 0608 UT, when there is a rapid equatorward excursion to 66° . This rapid excursion takes place ~ 1 min before expansive phase onset, consistent with the observations of the explosive growth phase by Ohtani *et al.* [1992b].

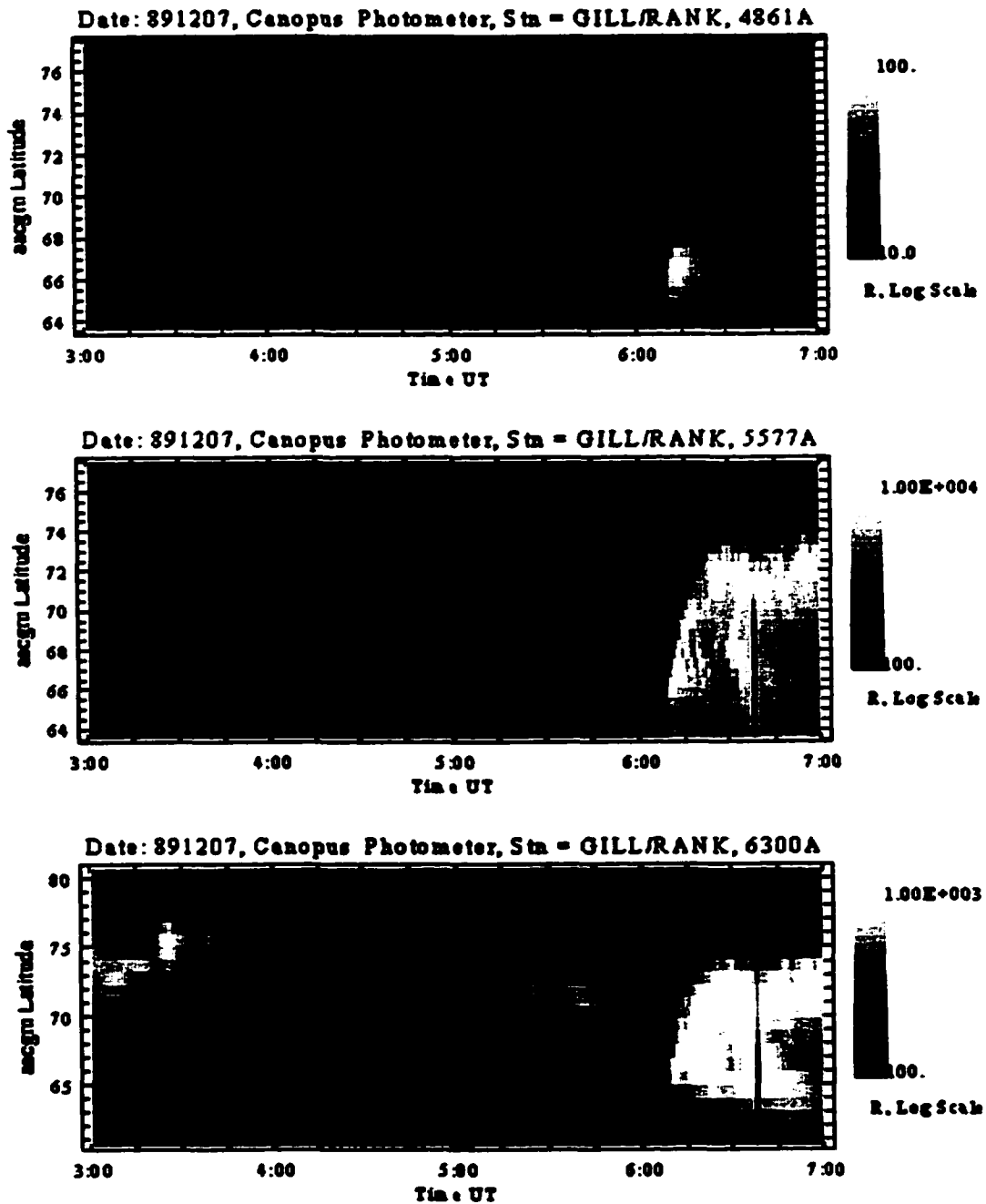


Figure 4.6: Meridian scanning photometer data for December 7, 1989.

At ~0609 UT the H β and 557.7 nm data begin to expand poleward, marking the time of expansive phase onset. The green line emissions expand rapidly poleward, reaching the poleward border of the 630.0 nm emissions at ~0614 UT. At this time the poleward

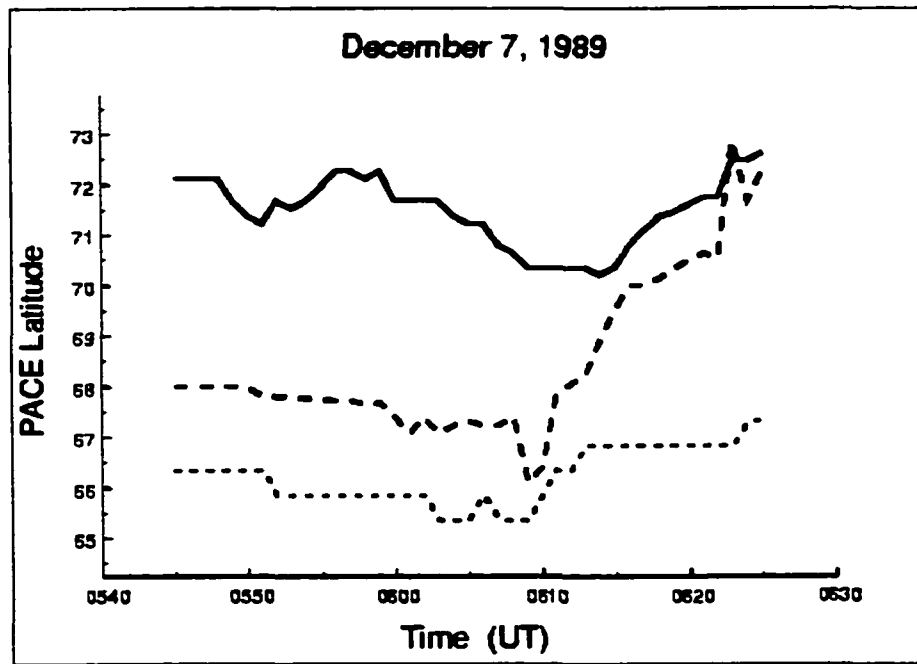


Figure 4.7: Poleward borders of the 557.7 nm (dashed line) and 630.0 nm (solid line), and maximum of the 486.1 nm (dotted line) emissions. Expansive phase onset begins at 0609 UT followed five minutes later by the beginning of lobe flux reconnection.

border of the red line emissions begin moving poleward from 70.5° back to presubstorm latitudes of $\sim 74^\circ$. *Samson et al.* [1992b] correlated optical data for this event with precipitating particle data from the DMSP satellites and found that the latitudes of the 630.0 nm emissions are consistent with the transition region from closed to open field lines. A comparison of the poleward borders of the red and green line emissions is shown in Figure 4.7. The time delay between onset and the beginning of lobe flux reconnection is 5 min.

The details described above are consistently reproduced in other substorms of this study. Figure 4.8 illustrates the poleward borders of the green line and red line data and the maximum of the H β data for December 8, 1989 (Figure 4.8a), February 26, 1995 (Figure 4.8b), and December 16, 1996 (Figure 4.8c). Table 4.1 summarizes the delay times determined in this study. In Table 4.1 Δt_2 represents the time interval between onset and the beginning of lobe flux reconnection.

Table 4.1 Timing of Isolated Substorms

Event ^a	Onset of poleward expansion of 486.1 nm and 557.7 nm Emissions (UT)	Δt_2 (min)
891207	0609	5
891208	0647	3
950209	0437	2
950223	0551	1
950226	0526	4
950306	0411	3
960118	0459	2
961216	0514	2

^a 891207 to be read as December 7, 1989.

4.4 Discussion

The events presented in the previous section all exhibit similar characteristics. The initial intensification of a preexisting auroral arc that is seen at expansive phase onset starts within the proton aurora region. The average latitude of the intensification is $\sim 67^\circ$, which presumably maps to the near-Earth plasma sheet at distances of $\sim 8 R_E$. The intensification region expands poleward with a timescale of the order of a few minutes toward the poleward border of the 630.0 nm emissions. After approximately 1-5 minutes, and possibly owing to plasma processes connected with the expanding intensification region, the poleward border of the red line emissions begins to move poleward. The beginning of the poleward movement is interpreted as the signature of the beginning of lobe flux reconnection as seen in the ionosphere.

The data suggest that expansive phase onset happens prior to reconnection of lobe field lines with an instability expanding rapidly downtail toward the site of reconnection. Thus there is some evidence that the process of lobe flux reconnection is influenced, if not initiated, by this mechanism. Figure 4.9 demonstrates this morphology, highlighting the time at which each detail would take place. The time t_0 represents the beginning of

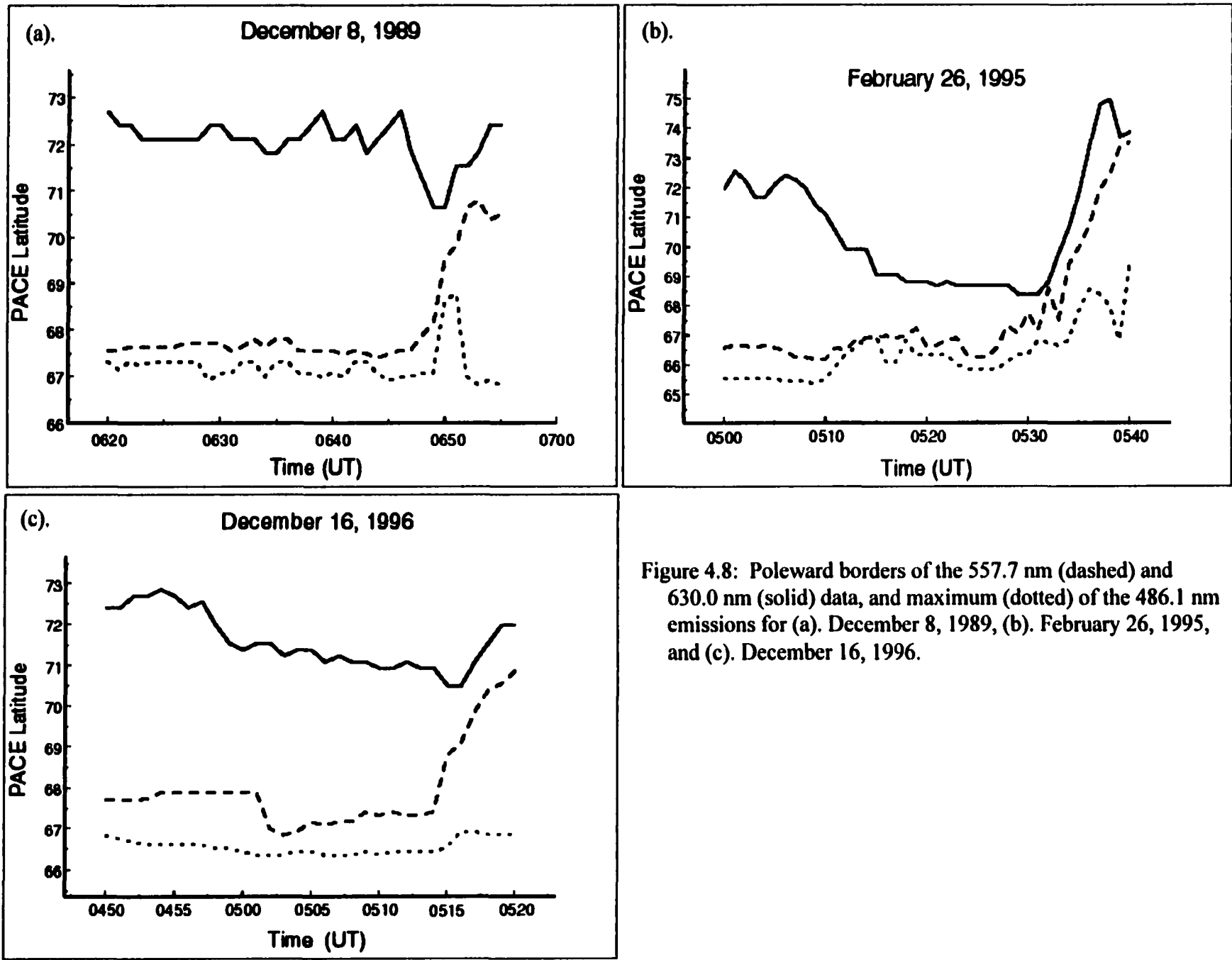


Figure 4.8: Poleward borders of the 557.7 nm (dashed) and 630.0 nm (solid) data, and maximum (dotted) of the 486.1 nm emissions for (a). December 8, 1989, (b). February 26, 1995, and (c). December 16, 1996.

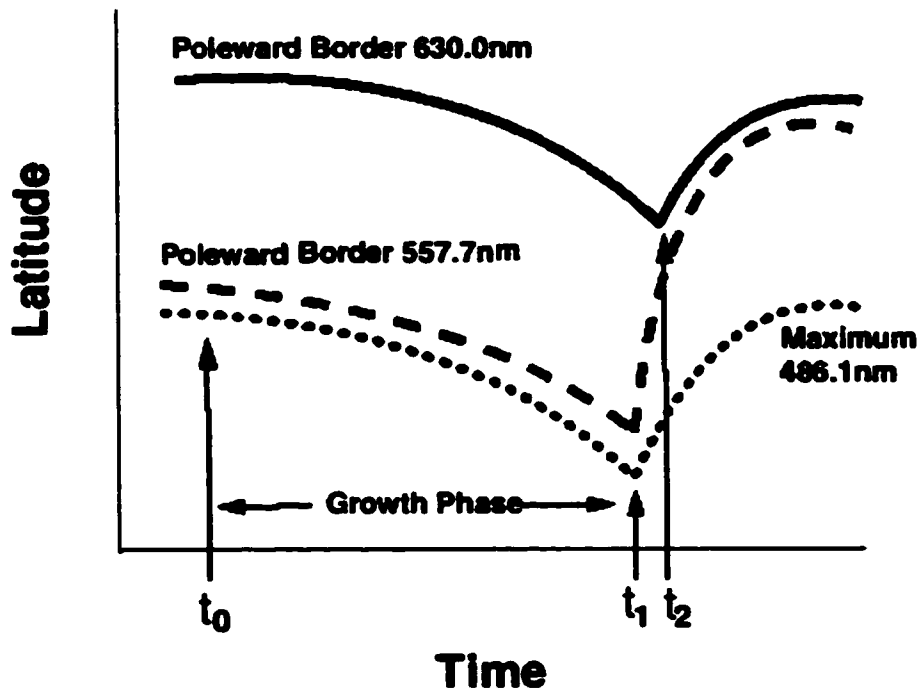


Figure 4.9: Schematic of the sequence of events during a substorm as observed with the meridian scanning photometer data.

timescale of this growth is of the order of tens of minutes. The time t_1 is the time for the beginning of the poleward expansion of the H β and green line emissions, which we identify as expansive phase onset. The 557.7 nm emission region moves rapidly poleward until time t_2 , which is the beginning of the poleward expansion of the electron aurora region, indicating the start of the closure of open flux.

The 557.7 nm emission activity shows that some physical process may be energizing the electrons in the near-Earth plasma sheet and continuing this energization down the tail toward the site of reconnection. It is possible that this acceleration may work in concert with processes that accelerate electrons into the ionosphere from altitudes of a few thousand kilometers, although the details of such a physical process are outside the scope of this study. In the February 9, 1995, event the time delay for the green line emissions to reach the open-closed field line boundary was ~ 2 min.

We define $\Delta t_2 = t_2 - t_1$ as the maximum time it takes for the near-Earth activation to propagate downtail to the site of lobe flux reconnection. The time Δt_2 is of the order of 1-

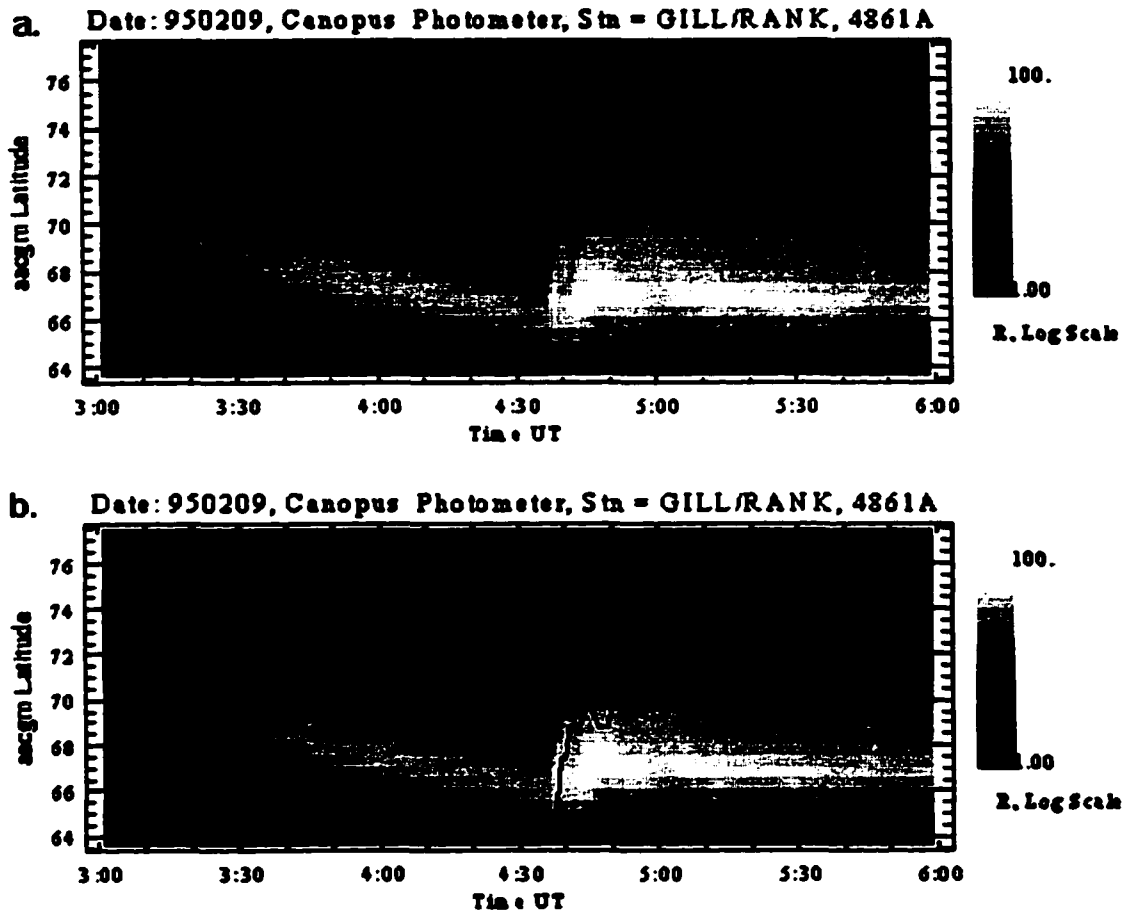


Figure 4.10: Poleward and equatorward borders of the auroral electrojets for the February 9, 1995 event, overlaid onto the MSP data. Panel (a) shows the borders for a growth phase eastward electrojet overlaid onto the 486.1 nm data. Panel (b) shows the equatorward border of a weak growth phase westward electrojet and the equatorward border of the expansive phase westward electrojet associated with the substorm current wedge.

5 min. This time should actually be shorter if we take into account the propagation time from the magnetospheric sources to the ionosphere. However, here we take, as a rough estimate, 2 min for Δt_2 . If we assume that lobe field line reconnection occurs at $\sim 25 R_E$ (an arbitrary value chosen between the 20 and 30 R_E stated by *Nagai et al.* [1998]) and that expansive phase onset occurs at an average distance of $\sim 10 R_E$, then a maximum propagation time of 2 min would produce a propagation speed of ~ 800 km/s for the instability, which is roughly comparable to the Alfvénic speed in the inner plasma sheet.

In an effort to understand the dynamics of the expansive phase more completely, the substorm electrojets were studied using the CANOPUS magnetometer data. Signatures of the growth phase and of dipolarization, obtained using the photometer data, can be compared with the higher time resolution magnetic data, showing dynamics of the electrojets. Figure 4.10 shows the MSP data for the February 9, 1995 event overlaid with the borders of the electrojets. The H β data with the poleward and equatorward borders of a growth phase eastward electrojet are presented in Figure 4.10a. The electrojet follows the gradual equatorward motion of the H β emission, which was expected since this electrojet was situated on field lines that are being stretched owing to energy input to the magnetosphere. Figure 4.10b shows the equatorward border of a weak westward electrojet that is situated slightly poleward of the eastward electrojet during the growth phase and the equatorward border of the westward electrojet associated with the substorm current wedge after 0437 UT. A comparison of Figures 4.10a and 4.10b shows that the growth phase electrojets, observed locally along the Churchill meridian line, disappear shortly before expansive phase onset and are replaced by the much stronger substorm westward electrojet at a lower latitude of $\sim 65^\circ$. Initially, the current wedge westward electrojet is embedded in the region of hot proton precipitation, providing further evidence that the onset of dipolarization occurs close to the Earth and not in the region of lobe field lines, as has recently been published [Baker *et al.*, 1999]. It would be interesting to determine where the discrete arc that brightens to begin expansive phase onset is located with respect to the electrojets. Voronkov *et al.* [1999] noted that the electron arc was situated within the region of the maximum of the 486.1 nm emissions. Unfortunately, there was no allsky imager data available for this event so the question of where the arc was located with respect to the electrojets cannot be conclusively answered. However, if one were to conjecture that the arc for the February 9, 1995 would also be located within the maximum of the H β emissions, then that arc would be collocated within the borders of the growth phase eastward electrojet.

Once dipolarization has begun, the equatorward border of the westward electrojet moves rapidly poleward along with the 486.1 nm emissions (Figure 4.10b). Figure 4.10c

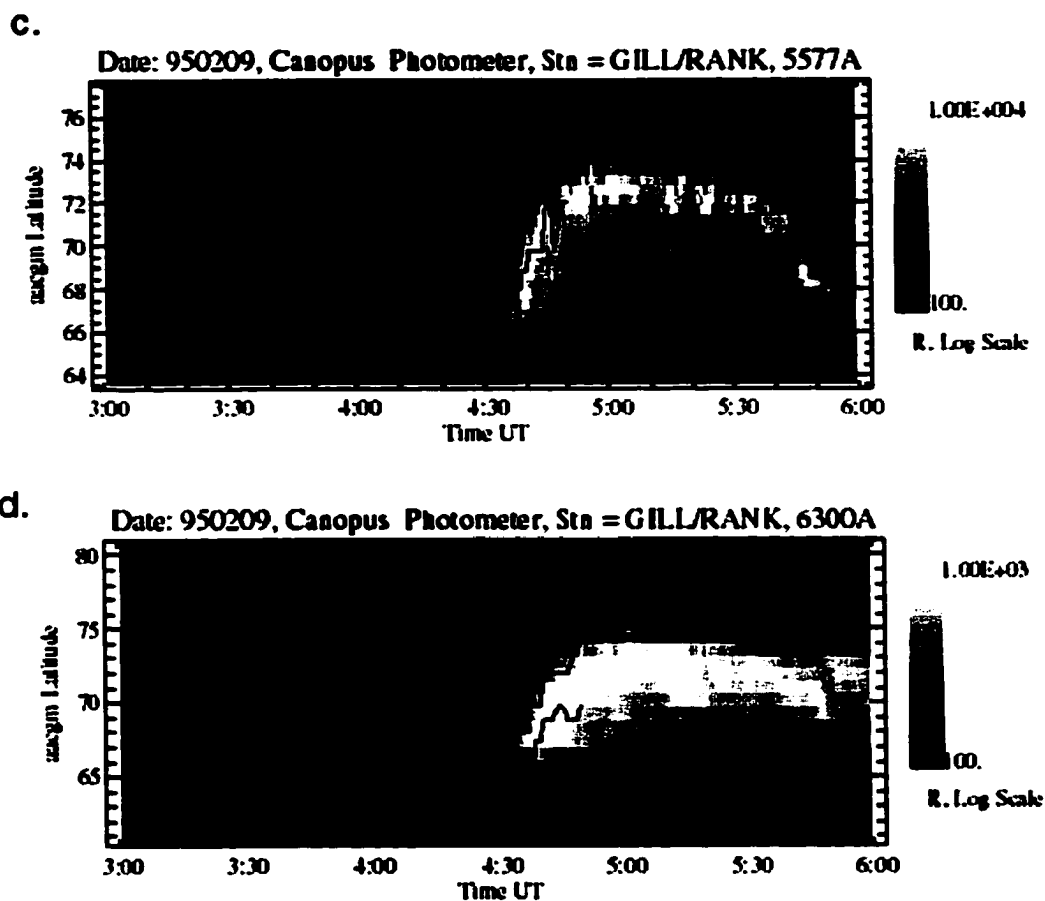


Figure 4.10: Cont'd. Panel (c) shows the motion of the X-component peak of the substorm westward electrojet during the expansive phase overlaid onto 557.7 nm data. Panel (d) shows the poleward and equatorward borders of the substorm westward electrojet overlaid onto the 630.0 nm data.

shows the 557.7 nm data with the center (maximum of the X component) of the substorm westward electrojet. The correlation between the poleward expansion of the center of the electrojet with the rapid poleward expansion of the photometer data is clear. A comparison of the equatorward and poleward borders of the expansive phase westward electrojet with the 630.0 nm emissions is displayed in Figure 4.10d. Closer inspection of Figure 4.10d suggests that the poleward border of the westward electrojet does not begin its sudden and rapid poleward retreat until the equatorward border reaches it at ~0440 UT. This is the same sequence of events as discussed earlier in Figures 4.5 and 4.7. It is obvious from Figure 4.10 that the borders of the electrojet are sensitive to what is happening to magnetic field lines in the magnetotail. The issue of how convection

changes during the course of the expansive phase needs further study, but the sensitivity of the electrojets and their possible correlation with magnetotail dynamics is intriguing.

It was thought that the higher time resolution of the magnetometer data may provide an observational signature of the closed field line reconnection proposed in the NENL model. The physical process of reconnection carries with it a reconfiguration of the reconnected magnetic field lines (dipolarization) and a restructuring of the plasma in the reconnection region. The NENL model predicts that reconnection takes place in the midtail region on closed, stretched field lines prior to expansive phase onset, the result of which would eject plasma earthward. While we cannot detect such high-speed ion flows in the photometer or magnetometer data, we can detect signatures of dipolarization, which would occur upon reconnection of stretched field lines. Dipolarization signatures, associated with expansive phase onset, are clearly seen in the photometer data as the poleward motion of the 486.1 and 557.7 nm emissions and in the motions of the borders of the electrojets. What we hoped to observe were signatures of dipolarization (for example, poleward motion of the electrojets, as discussed above) at latitudes consistent with closed plasma sheet field lines in the midtail region, prior to expansive phase onset. Despite the dynamics of the electrojets, however, Figures 4.10a and 4.10b show no indication of magnetic field line restructuring, consistent with dipolarization, on closed field lines prior to expansive phase onset.

To summarize thus far, there are two main observational criteria which we believe are essential to incorporate into any substorm model when discussing isolated substorms: expansive phase onset occurs prior to lobe flux reconnection in the midtail region, and the time delay between onset and reconnection of tail lobe field lines is of the order of a few minutes. In addition to these observational constraints, data presented by *Voronkov et al.* [1999] suggest that expansive phase onset occurs in a region of high plasma pressure and strong shear flow. Taken together, these observations suggest that the expansive phase of the substorm occurs in three stages: (1) the initial intensification of an electron arc within a region of enhanced proton aurora, (2) the dipolarization of closed, stretched field lines whose footpoints map initially into the region of proton aurora, and (3) closure of lobe flux and further dipolarization of the tail magnetic field. This is consistent with the original definition of the expansive phase by *Akasofu* [1964], which involved

poleward expansion of the midnight sector auroral oval. With the knowledge of these criteria we can now look at some current substorm theories in detail.

Most of the substorm models proposed to date can be grouped into three categories: those that advocate a near-geosynchronous onset, those that support a NENL-initiated onset, and those that believe that the ionosphere plays a critical role at expansive phase onset. The results presented here support a near-Earth onset model and the magnetosphere as the initiator of substorm dynamics. While it is possible that the ionosphere plays an important role during the expansive phase, it is difficult to envision it directing substorm dynamics since the Alfvénic travel time between the ionosphere and the near-Earth magnetosphere is roughly 2 min [Samson *et al.*, 1992b; Samson, 1994]. The data in the present study show the first two stages of the expansive phase to be completed, on average, within 2 min.

The models which advocate a near-Earth onset and tailward propagating instability are the near-Earth current disruption (NECD) model [Lui, 1996] and the boundary layer dynamic model (BLDM) [Rostoker, 1996]. Lui [1994] stated that magnetic field fluctuation is high during current disruption (CD) with a fluctuation timescale between 1 and 5 min (with an average of 2.5 min), consistent with the time intervals determined in the present study. There is evidence that current disruption begins close to geosynchronous orbit at $\sim 6-7 R_E$ [Lui, 1978] and can expand radially outward and azimuthally into the tail via a rarefaction wave that induces plasma sheet thinning and B_z reductions [Ohtani *et al.*, 1992a; Lopez and Lui, 1990; Jacquy *et al.*, 1991, 1993]. However, the tailward expansion speeds of the papers mentioned above are slightly lower ($\sim 200-400$ km/s) than the characteristic Alfvén speed for the central plasma sheet (~ 500 km/s) and a factor of 2 lower than what has been suggested in this study. Nevertheless, thinning of the plasma sheet and weak normal (to the neutral sheet) magnetic fields can be unstable with respect to tearing modes or other instabilities that may form X lines and plasmoids. Thus the NECD model puts magnetic reconnection as a consequence rather than a cause of substorm expansion. This sentiment has also been advocated by Kan *et al.* [1991] and Cowley [1992] and is consistent with the results found here.

The BLDM locates the initial intensification of the expansive phase in the region of intense cross-tail current along the earthward edge of the plasma sheet. In a similar

fashion as was described by *Lui* [1991], a rarefaction wave emanates from the region of dipolarization and propagates downtail, allowing the current sheet disruption region to expand out to a neutral line at $\sim 30 R_E$, where enhanced reconnection would be triggered. The enhanced reconnection would be responsible for high-latitude substorm surge activity, as it results in enhanced velocity shear along the interface between the low-latitude boundary layer (LLBL) and the central plasma sheet (CPS). *Rostoker* [1996] postulates the time delay between near-Earth onset and initiation of high-latitude activity to be between 7 and 24 min, depending on where the neutral line is located down the tail (the location being dependent on activity level). The minimum time delay of 7 min, while slightly longer, is of the order of the time delays found in this study.

One model which continues to go in and out of favor is the ballooning instability model by *Roux et al.* [1991]. This model locates expansive phase onset in the interface region between dipolar and tail field lines where a Raleigh-Taylor type of instability is excited. In the early 1990s the ballooning instability fell out of favor when it was shown that the neutral sheet region was stable to some types of ballooning modes [*Lee and Wolf*, 1992; *Ohtani and Tamao*, 1993]. However, *Liu* [1997] showed that for a high beta plasma, the ballooning instability can be excited easily by an earthward pressure gradient of any magnitude, thus bringing ballooning back into favor. A variation on the ballooning model which incorporates velocity shear flow along the inner edge of the plasma sheet was studied by *Voronkov et al.* [1997]. The authors showed that the ballooning instability, coupled with shear flow, could produce the intensification of the auroral arc at expansive phase onset with rapid growth rates on a timescale of seconds. The shear flow ballooning instability (SFBI) requires both an earthward pressure gradient and a region of shear flow in a direction perpendicular to the pressure gradient in order for mode coupling to occur. The existence of large earthward pressure gradients along the near-Earth plasma sheet has been shown previously [e.g., *Samson et al.*, 1992b; *Kistler et al.*, 1992]. *Voronkov et al.* [1999] presented observational evidence of shear flows with a large-amplitude westward component, colocated within the proton aurora region (i.e., in the region of large pressure gradients). The directions and magnitudes of the pressure gradient and shear flow were input into the shear flow ballooning instability model, and

the results were published by *Voronkov et al.* [2000]. The resulting vortex evolution images produced by the SFBI bear a striking resemblance to the vortices and surges observed by the all-sky imagers (ASI). A recent statistical study of the ASI data and large-scale auroral vortex formation suggests that the substorm expansive phase onset comprises three stages: brightening of the arc within the proton aurora region; the development of perturbations, or ripples, along the length of the arc; and poleward expansion of the breakup vortices evolved from this arc. This chronology is similar to what has been suggested in the present study on the basis of the MSP data.

Further evidence for the ballooning instability as the mechanism for expansive phase onset was provided by *Erickson et al.* [2000], who studied 20 events observed by the CRRES satellite, where the satellite traversed the local time sector occupied by the substorm current wedge. They derived Poynting vectors for the low-frequency waves and found that 19 of the 20 events were clearly inconsistent with the notion that the substorm current wedge results from braking of earthward bulk flows emanating from a near-Earth neutral line. Instead, they found that the data were consistent with drift-Alfvén ballooning in the near-geosynchronous plasma sheet as a mechanism for initiation of expansive phase onset and the substorm current wedge.

With respect to an instability traveling rapidly downtail toward the site of reconnection, a similar interpretation was also proffered by *Roux et al.* [1991] as a result of their study relating the ballooning instability to the westward traveling surge. They suggested that the general expansion of the auroral arcs to the north, and their azimuthal expansion, are the consequences of a ballooning instability, which starts developing in the inner plasma sheet and later expands until it covers a large fraction of the plasma sheet.

Magnetic reconnection, or more basically the merging of magnetic field lines, takes place when the plasma becomes non-ideal and the magnetic field starts diffusing across the plasma. From a physical point of view, any process that causes violation of the ideal conditions in a plasma leading to collisional effects will result in diffusion of magnetic fields and thus reconnection and a rearranged magnetic field topology. If one accepts the interpretation of the data presented here and by *Roux et al.* [1991], then as the ballooning

or shear flow ballooning instability reaches the region where field lines are merging, it may aid in decoupling the plasma from the field and allow for reconnection to take place.

Perhaps the model most contradictory to the results presented in this paper is the Near-Earth Neutral Line Model [Baker *et al.*, 1996]. In its most developed form the model has expansive phase onset occurring as a result of, and not prior to, substorm reconnection $\sim 25\text{-}30 R_E$ downtail. Shiokawa *et al.* [1997] have discussed a possible physical framework that explains how onset could occur after reconnection. Upon reconnection of closed field lines in the midtail region, high-speed ion flows travel earthward toward the inner edge of the plasma sheet carrying a substantial amount of northward magnetic flux [Angelopoulos *et al.*, 1994]. Shiokawa *et al.* [1997] asserts that the ion flows can be stopped at a boundary at the inner edge of the neutral sheet, between dipolar and tail-like magnetic fields. At this boundary, there is an earthward pressure gradient, the force of which would suddenly ‘brake’ the high-speed flows. The model calls on the ‘auroral avalanche’ theory by Haerendel [1992], which states that the substorm current wedge (and subsequent dipolarization of stretched tail magnetic field lines) will be caused by a dawnward inertia current created by the sudden deceleration of the high-speed flows. While there has yet to be any direct observational evidence of the flow braking and cross-tail current diversion process, there has been much observational evidence of reconnection in the midtail and of fast earthward flows [Nagai *et al.*, 1998; Shiokawa *et al.*, 1997; Machida *et al.*, 1999]. Håland *et al.* [1999] discussed multipoint observations of two substorms that occurred on December 10, 1996. They observed signatures of reconnection in the midtail region that were sporadic and burstlike and occurred prior to ground onset by ~ 10 min. Håland *et al.* [1999] noted that the events were reminiscent of the NENL model; however, they also noted that the model could not account for the explosive nature of the onset and the close relation between the solar wind interplanetary magnetic field signatures and onset. There is also the question of why the high-speed flows should build up along the inner edge of the plasma sheet when the particles have tens of minutes to convect, drift, or otherwise travel around the Earth. What has also not been adequately explained is how dipolarization (which would presumably occur at the instant of reconnection of the closed field lines and decrease the energy state of the magnetosphere) and increased energy input into the near-Earth

magnetosphere from the earthward transport of northward magnetic flux (which would serve to increase the energy state of the magnetosphere) can occur at the same time.

4.5 Conclusions

In this chapter we have presented the results of our study of eight isolated substorm events, two of which were discussed in detail. For all events the initial intensification of the expansive phase begins close to the Earth, prior to lobe flux reconnection in the midtail. Our observations suggest that the expansive phase is composed of three distinct stages that include (1) an electron arc brightening within the proton aurora, (2) rapid poleward expansion of the 557.7 nm emissions and dipolarization of near-Earth magnetic field lines, and (3) poleward expansion of 630.0 nm emissions, which we assert is a result of reconnection of lobe field lines. Of importance is the observation that the poleward border of the 630.0 nm emissions does not begin to expand poleward until after the 557.7 nm emissions have reached it, leading to the assertion that the instability expanding down the tail is causing, or creating favorable conditions for, lobe flux reconnection in the midtail. Second, the time delay between the onset of the expansive phase and the onset of lobe flux reconnection is of the order of 1-5 min. Since we must account for travel time of information between the ionosphere and the magnetosphere, the process of lobe flux reconnection in the magnetosphere must begin sometime within the 1-5 min time delay.

The rapid timescales observed in this study have also been seen in a separate study by *Frank and Sigwarth [2000]*. Using high-resolution global images of the visible emissions of 557.7 nm, they determined that the brightenings associated with the expansive phase initial intensification propagated rapidly in local time toward polar latitudes from the position of onset. This rapid poleward expansion was noted in three isolated substorms and occurred over a time interval of 4 min. *Frank and Sigwarth [2000]* also noted that the behavior of the polar arcs during onset and early expansive phase seemed to be unaffected by the explosive brightening and expansion of the onset arc. Inspection of Figures 4.7a-4.7c reveals the same behavior. The poleward borders of the 630.0 nm emissions do not begin to display any significant activity until the 557.7 nm emissions have reached them, after expansive phase onset.

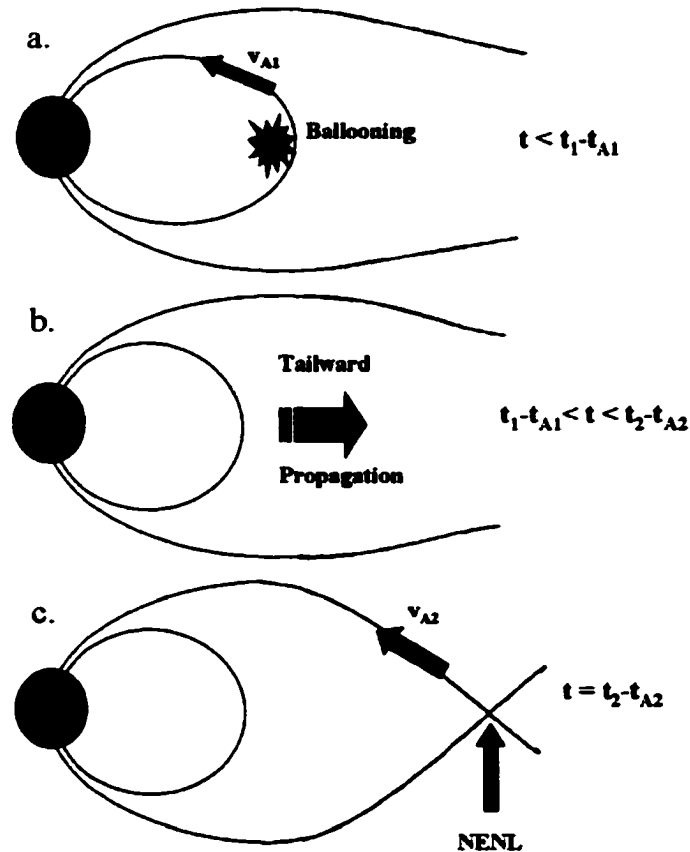


Figure 4.11: Schematic of a proposed substorm model based on the observations from the MSP and magnetometer data. The variables V_{A1} and t_{A1} represent the Alfvén speed and travel time with which the information of onset will travel from the magnetospheric source region to the ionosphere. The variables V_{A2} and t_{A2} represent the Alfvén speed and travel time with which the information of reconnection activity will travel from the magnetotail to the ionosphere.

The two major components of the substorm (growth, expansion) are clearly observed in the photometer and magnetometer data. What was not seen, however, was a signature of reconnection on closed field lines prior to expansive phase onset. The most recent NENL model incorporates closed field line reconnection in the plasma sheet up to a few minutes prior to expansive phase onset, as noted by ground-based data. Using the higher resolution of the CANOPUS magnetometer data, we looked for signatures of

dipolarization (which, we assumed, would naturally follow from reconnection of highly stretched field lines of the latter growth phase). However, we did not observe any signatures apart from enhancement of the growth phase electrojets.

We envision the substorm process, from beginning of growth to the beginning of recovery, to proceed as follows (see Figure 4.11): The beginning of the growth phase is described as the time when energy is input into the magnetotail (via merging on the dayside magnetosphere). An auroral arc forms on field lines threading the earthward edge of the plasma sheet. Vortex structures then form on this arc that are likely the result of the hybrid shear flow ballooning instability [Voronkov *et al.*, 1997, 2000]. Nearing the onset of the expansive phase, the field lines become extremely stretched, and the plasma sheet becomes very thin. An instability utilizing the large pressure gradient and shear flow along the inner edge of the plasma sheet (possibly a type of ballooning mechanism) appears, and dipolarization begins (Figure 4.11a). The variables V_{A1} and t_{A1} are the Alfvén speed with which the information of onset will travel to the ionosphere and the Alfvén travel time, respectively. On the basis of measurements using field line resonances [Samson, 1994], the time for information to travel along field lines from the initial instability near the earthward edge of the plasma sheet to the ionosphere is ~ 2 min. As the information travels to the ionosphere, the instability which initiated expansive phase onset develops farther downtail, possibly accelerating plasma sheet electrons as it propagates (Figure 4.11b). Eventually, the unstable region expands until it reaches the region of open flux and either initiates or influences lobe flux reconnection (Figure 4.11c). The variables V_{A2} and t_{A2} are respectively the Alfvén speed and Alfvén travel time of the information on reconnection activity propagating to the ionosphere. At this point, velocity shear between the LLBL and the CPS may excite the Kelvin-Helmholtz instability and produce vortex structures along the LLBL-CPS interface. These vortices map to the ionosphere as the poleward and westward motion of the region of auroral surge activations. Finally, the recovery phase is complete when reconnection of lobe flux ends and the magnetosphere reaches a lower energy equilibrium.

Bibliography

- Akasofu, S.-I., The development of the auroral substorm, *Planet. Space Sci.*, 12, 273, 1964.
- Angelopoulos, V., C. F. Kennel, F. V. Coroniti, R. Pellat, M. G. Kivelson, R. J. Walker, C. T. Russell, W. Baumjohann, W. C. Feldman, and J. T. Gosling, Statistical characteristics of bursty bulk flow events, *J. Geophys. Res.*, 99, 21,257, 1994.
- Atkinson, G., The current system of geomagnetic bays, *J. Geophys. Res.*, 72, 6063, 1967.
- Baker, D. N., and R. L. McPherron, Extreme energetic particle decreases near geostationary orbit: A manifestation of current diversion and energy conversion within the inner plasma sheet, *Adv. Space. Res.*, 10(9), 131, 1990.
- Baker, D. N., T. I. Pulkkinen, V. Angelopoulos, W. Baumjohann, and R. L. McPherron, Neutral line model of substorms: Past results and present view, *J. Geophys. Res.*, 101, 12,975, 1996.
- Baker, D. N., T. I. Pulkkinen, J. Buchner, and A. J. Klimas, Substorms: A global instability of the magnetosphere-ionosphere system, *J. Geophys. Res.*, 104, 14,601, 1999.
- Bhattacharjee, A., Z. W. Ma, and X. Wang, Ballooning instability of a thin current sheet in the high-Lundquist-number magnetotail, *Geophys. Res. Lett.*, 25, 861, 1998.
- Birn, J., and M. Hesse, Details of current disruption and diversion in simulations of magnetotail dynamics, *J. Geophys. Res.*, 101, 15,345, 1996.
- Blanchard, G. T., L. Lyons, and J. C. Samson, Locating the polar cap boundary from observations of 6300Å auroral emission, *J. Geophys. Res.*, 100, 7855, 1995.
- Blanchard, G. T., L. R. Lyons, and J. C. Samson, Accuracy of using 6300Å auroral emission to identify the magnetic separatrix on the nightside of Earth, *J. Geophys. Res.*, 102, 9697, 1997.
- Brittnacher, M., M. Fillingim, G. Parks, G. Germany, and J. Spann, Polar cap area and boundary motion during substorms, *J. Geophys. Res.*, 104, 12,251, 1999.
- Cheng, C. Z., and A. T. Y. Lui, Kinetic ballooning instability for substorm onset and current disruption observed by AMPTE/CCE, *Geophys. Res. Lett.*, 25, 4091, 1998.
- Cowley, S. W. H., The role and location of magnetic reconnection in the geomagnetic tail during substorms, in *Proceedings of the First International Conference on Substorms*, Eur. Space Agency Publ., ESA SP-335, 401, 1992.

- Davidson, G. T., Expected spatial distribution of low-energy protons precipitated in the auroral zones, *J. Geophys. Res.*, 70, 1061, 1965.
- Erickson, G. M., N. C. Maynard, W. J. Burke, G. R. Wilson, and M. A. Heinemann, Electromagnetics of substorm onsets in the near-geosynchronous plasma sheet, *J. Geophys. Res.*, in press, 2000.
- Frank, L. A., and J. B. Sigwarth, Findings concerning the positions of substorm onsets with auroral images from the Polar spacecraft, *J. Geophys. Res.*, 105, 12,747, 2000.
- Haerendel, G., Disruption, ballooning or auroral avalanche on the cause of substorms, in Proceedings of the First International Conference on Substorms, Eur. Space Agency Publ., ESA SP-335, 417, 1992. Håland, S., et al., Magnetospheric and ionospheric response to a substorm: Geotail HEP-LD and Polar PIXIE observations, *J. Geophys. Res.*, 104, 28,459, 1999.
- Hurricane, O. A., B. H. Fong, and S. C. Cowley, Nonlinear magnetohydrodynamic detonation: part 1, *Phys. Plasmas*, 4(10), 3565, 1997.
- Hurricane, O. A., B. H. Fong, S. C. Cowley, F. V. Coroniti, C. F. Kennel, and R. Pellat, Substorm detonation-the unification of substorm trigger mechanisms, in *Substorms-4: International Conference on Substorms-4*, Lake Hamana, Japan, March 9-13, 1998, Kluwer Acad., pp.373-378, Norwell, Mass., 1998.
- Jacquey, C., J. A. Sauvaud, and J. Dandouras, Location and propagation of the magnetotail current disruption during substorm expansion: Analysis and simulation of an ISEE multi-onset event, *Geophys. Res. Lett.*, 18, 389, 1991.
- Jacquey, C., J. A. Sauvaud, J. Dandouras, and A. Korth, Tailward propagating crosstail current disruption and dynamics of near-Earth tail: A multi-point measurement analysis, *Geophys. Res. Lett.*, 20, 983, 1993.
- Kan, J. R., L. Zhu, A. T. Y. Lui, and S.-I. Akasofu, A magnetosphere-ionosphere coupling theory of substorms including magnetotail dynamics, in *Auroral Physics*, edited by C.-I. Meng, M. J. Rycroft, and L. A. Frank, p.311, Cambridge Univ. Press, New York, 1991.
- Kisabeth, J. L., and G. Rostoker, Development of the polar electrojet during polar magnetic substorms, *J. Geophys. Res.*, 76, 6815, 1971.
- Kisabeth, J. L., and G. Rostoker, Current flow in auroral loops and surges inferred from ground-based magnetic observations, *J. Geophys. Res.*, 78, 5573, 1973.

- Kistler, L. M., E. Möbius, W. Baumjohann, G. Paschmann, and D. C. Hamilton, Pressure changes in the plasma sheet during substorm injections, *J. Geophys. Res.*, *97*, 2973, 1992.
- Lee, D.-Y., Ballooning instability in the tail plasma sheet, *Geophys. Res. Lett.*, *25*, 4095, 1998.
- Lee, D.-Y., and R. A. Wolf, Is the Earth's magnetotail balloon unstable?, *J. Geophys. Res.*, *97*, 19,251, 1992.
- Liou, K., C.-I. Ment, A. T. Y. Lui, and P. T. Newell, On relative timing in substorm onset signatures, *J. Geophys. Res.*, *104*, 22,807, 1999.
- Liu, W. W., Physics of the explosive growth phase: Ballooning instability revisited, *J. Geophys. Res.*, *102*, 4927, 1997.
- Lopez, R. E., and A. T. Y. Lui, A multisatellite case study of the expansion of a substorm current wedge in the near-Earth magnetotail, *J. Geophys. Res.*, *95*, 8009, 1990.
- Lopez, R. E., H. Luhr, B. J. Anderson, P. T. Newell, and R. W. McEntire, Multipoint observations of a small substorm, *J. Geophys. Res.*, *95*, 18,897, 1990.
- Lui, A. T. Y., Estimates of current changes in the geomagnetotail associated with a substorm, *Geophys. Res. Lett.*, *5*, 853, 1978.
- Lui, A. T. Y., A synthesis of magnetospheric substorm models, *J. Geophys. Res.*, *96*, 1849, 1991.
- Lui, A. T. Y., Mechanisms for the substorm current wedge, in *Proceedings of the ICS-2 International Conference on Substorms*, edited by J. R. Kan, J. D. Craven, and S.-I. Akasofu, p.195, University of Alaska, Fairbanks, 1994.
- Lui, A. T. Y., Current disruption in the Earth's magnetosphere: Observations and models, *J. Geophys. Res.*, *101*, 13,067, 1996.
- Lui, A. T. Y., et al., Multi-point study of a substorm on February 9, 1995, *J. Geophys. Res.*, *103*, 17,333, 1998.
- Lyons, L. R., Coordinated observations demonstrating external substorm triggering, *J. Geophys. Res.*, *102*, 27,039, 1997.
- Machida, S., Y. Mayashita, A. Ieda, A. Nishida, T. Mukai, Y. Saito, and S. Kokubun, GEOTAIL observations of flow velocity and north-south magnetic field variations in the near and mid-distant tail associated with substorm onsets, *Geophys. Res. Lett.*, *26*, 635, 1999.

- Miyashita, Y., S. Machida, A. Nishida, T. Mukai, Y. Saito, and S. Kokubun, GEOTAIL observations of total pressure and electric field variations in the near and mid-distant tail associated with substorm onsets, *Geophys. Res. Lett.*, 26, 639, 1999.
- Nagai, T., and S. Machida, Magnetic reconnection in the near-Earth magnetotail, in *New Perspectives on the Earth's Magnetotail, Geophys. Monogr. Ser.*, vol. 105, edited by A. Nishida et al., pp. 211-224, AGU, Washington, D. C., 1998.
- Nagai, T., M. Fujimoto, Y. Saito, S. Machida, T. Terasawa, R. Nakamura, T. Yamamoto, T. Mukai, A. Nishida, and S. Kokubun, Structure and dynamics of magnetic reconnection for substorm onsets with GEOTAIL observations, *J. Geophys. Res.*, 103, 4419, 1998.
- Ohtani, S., and T. Tamao, Does the ballooning instability trigger substorms in the near-Earth magnetotail?, *J. Geophys. Res.*, 98, 19,369, 1993.
- Ohtani, S., S. Kokubun, and C. T. Russell, Radial expansion of the tail current disruption during substorms: A new approach to the substorm onset region, *J. Geophys. Res.*, 97, 3129, 1992a.
- Ohtani, S., K. Takahashi, L.J. Zanetti, T.A. Potemra and R.W. McEntire, Initial signatures of magnetic field and energetic particle fluxes at tail reconfiguration: Explosive growth phase, *J. Geophys. Res.*, 97, 19,311, 1992b.
- Ohtani, S., F. Creutzberg, T. Mukai, H. Singer, A. T. Y. Lui, M. Nakamura, P. Prikryl, K. Yumoto, and G. Rostoker, Substorm onset timing: The December 31, 1995 event, *J. Geophys. Res.*, 104, 22,713, 1999.
- Parks, G. K., et al., Low-energy particle layer outside of the plasma sheet boundary, *J. Geophys. Res.*, 97, 2943, 1992.
- Rostoker, G., Phenomenology and physics of magnetospheric substorms, *J. Geophys. Res.*, 101, 12,955, 1996.
- Rostoker, G., J. C. Samson, F. Creutzberg, T. J. Hughes, D. R. McDiarmid, A. G. McNamara, A. Vallance Jones, D. D. Wallis, and L. L. Cogger, Canopus-A ground based instrument array for remote sensing the high latitude ionosphere during the ISTEP/GGS program, in *The Global Geospace Mission*, edited by C. T. Russell, pp.743-760, Kluwer Acad., Norwell, Mass., 1995.
- Roux, A., S. Perraut, P. Robert, A. Morane, A. Pedersen, A. Korth, G. Kremser, B. Aparicio, D. Rodgers, and R. Pellinen, Plasma sheet instability related to the westward traveling surge, *J. Geophys. Res.*, 96, 17,697, 1991.
- Samson, J. C., Mapping substorm intensifications from the ionosphere to the magnetosphere, in *Proceedings of the ICS-2 International Conference on Substorms*,

edited by J. R. Kan, J. D. Craven, and S.-I. Akasofu, p.237, University of Alaska, Fairbanks, 1994.

- Samson, J. C., Nonlinear, hybrid, magnetohydrodynamic instabilities associated with substorm intensifications near the Earth, in *Substorms-4: International Conference on Substorms-4*, Lake Hamana, Japan, March 9-13, 1998, edited by S. Kokubun and Y. Kamide, pp. 505-509, Kluwer Acad., Norwell, Mass., 1998.
- Samson, J. C., D. D. Wallis, T. J. Hughes, F. Creutzberg, J. M. Ruohoniemi, and R. A. Greenwald, Substorm intensifications and field line resonances in the nightside magnetosphere, *J. Geophys. Res.*, **97**, 8495, 1992a.
- Samson, J. C., L. R. Lyons, P. T. Newell, F. Creutzberg, and B. Xu, Proton aurora and substorm intensifications, *Geophys. Res. Lett.*, **19**, 2167, 1992b.
- Samson, J. C., A. K. MacAulay, R. Rankin, P. Frycz, I. Voronkov, and L. L. Cogger, Substorm intensifications and resistive shear ow ballooning instabilities in the nightside magnetosphere, in *Third International Conference on Substorms (ICS-3)*, Versailles, France, 12-17 May 1996, Eur. Space Agency Spec. Publ., ESA SP-389, 399, 1996.
- Sergeev, V. A., D. G. Mitchell, C. T. Russell, and D. J. Williams, Structure of the tail plasma/current sheet at ~11 RE and its changes in the course of a substorm, *J. Geophys. Res.*, **98**, 17,345, 1993.
- Sergeev, V. A., V. Angelopoulos, D. G. Mitchell, and C. T. Russell, In situ observations of magnetotail reconnection prior to onset of a small substorm, *J. Geophys. Res.*, **100**, 19,121, 1995.
- Shiokawa, K., W. Baumjohann, and G. Haerendel, Braking of high-speed flows in the near-Earth tail, *Geophys. Res. Lett.*, **24**, 1179, 1997.
- Shiokawa, K., G. Haerendel, and W. Baumjohann, Azimuthal pressure gradient as driving force of substorm currents, *Geophys. Res. Lett.*, **25**, 959, 1998.
- Sundaram, A. K., and D. H. Fairfield, Stability of resistive MHD tearing and ballooning modes in the tail current sheet, *J. Geophys. Res.*, **102**, 19,913, 1997.
- Taylor, J. R., An introduction to error analysis: The study of uncertainties in physical measurements, Chap. 9, pp.173-184, Oxford Univ. Press, New York, 1982.
- Vasyliunas, V. M., Theoretical considerations on where a substorm begins, in *Substorms-4: International Conference on Substorms-4*, Lake Hamana, Japan, March 9-13, 1998, edited by S. Kokubun and Y. Kamide, pp.9-14, Kluwer Acad., Norwell, Mass., 1998.

- Voronkov, I., R. Rankin, P. Frycz, V. T. Tikhonchuk, and J. C. Samson, Coupling of shear flow and pressure gradient instabilities, *J. Geophys. Res.*, *102*, 9639, 1997.
- Voronkov, I., E. Friedrich, and J. C. Samson, Dynamics of the substorm growth phase as observed using CANOPUS and SuperDARN instruments, *J. Geophys. Res.*, *104*, 28,491, 1999.
- Voronkov, I., E. F. Donovan, B. J. Jackel, and J. C. Samson, Large-scale vortex dynamics in the evening and midnight auroral zone: Observations and simulations, *J. Geophys. Res.*, *105*, 18,505, 2000.
- Winningham, J. D. and W. J. Heikkila, Polar cap auroral electron fluxes observed with Isis 1, *J. Geophys. Res.*, *79*, 949, 1974.
- Winningham, J. D., F. Yasuhara, S.-I. Akasofu, and W. J. Heikkila, The latitudinal morphology of 10-eV to 10-keV electron fluxes during magnetically quiet and disturbed times in the 2100-0300 MLT sector, *J. Geophys. Res.*, *80*, 3148, 1975.

³Chapter 5: The Substorm Current Wedge

5.1 Introduction

One of the more recognized signatures of the substorm expansive phase is the substorm current wedge. In the previous chapters, the dynamics of the growth and expansive phases were described with respect to the optical data as a gradual equatorward motion of the auroral emissions, followed by a sudden brightening in the H β and 557.7 nm emissions, which indicated the beginning of expansive phase onset from the point of view of the ionosphere. It is believed that the onset occurs in a localized region in the near-Earth plasma sheet, expanding rapidly tailward and azimuthally, which is reflected by the poleward expansion of the optical emissions. Chapter 4 showed that the timescale for the initial onset and expansion of the 557.7 nm emissions to regions of lobe field lines is of the order of 2 - 3 minutes.

As mentioned in the Introduction, as well as being characterized by three phases, the substorm consists of two processes: directly-driven and storage-release (also known as loading-unloading). The substorm current wedge occurs during the 'release' part of the storage-release process and has long been thought to be a current system separate and distinct from those occurring during the growth and recovery phases of the substorm. The presently accepted current wedge model calls for a disruption of the cross-tail current, by some physical means that is currently debated, which creates two regions of field-aligned current: downward (with respect to the ionosphere) on the eastern side of the disrupted region and upward on the western side. The field-aligned currents are closed via an eastward equivalent current in the equatorial plane of the magnetotail, and through the substorm westward electrojet in the ionosphere (cf. Figure 5.1). The instant of disruption of the cross-tail current occurs at expansive phase onset and is associated

³ A portion of this chapter has already been published. Friedrich, E. and G. Rostoker, Reconfiguration of the directly driven currents during a substorm expansive phase: Implications for the substorm current wedge, in *Substorms-4*, eds. S. Kokubun and Y. Kamide, Kluwer Academic Publishers, Boston, USA, pp. 83-86, 1998.

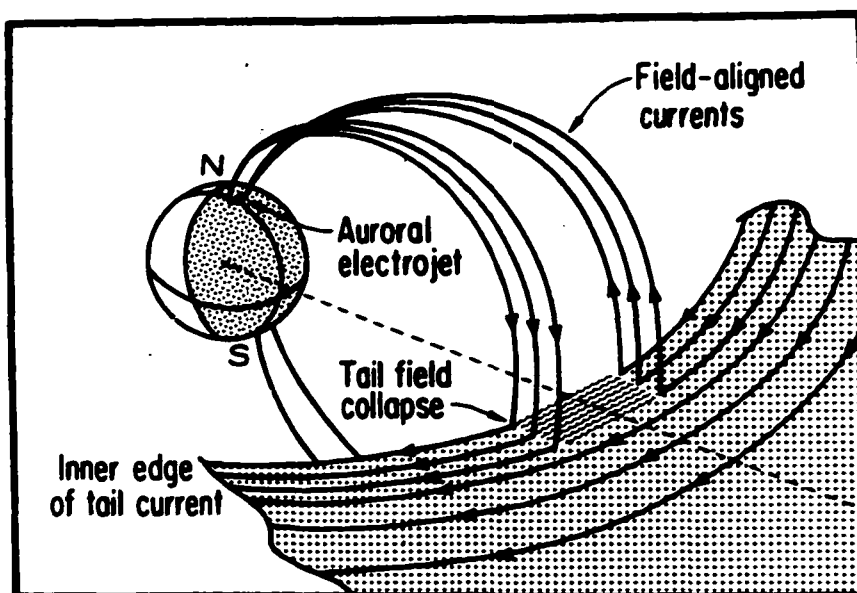


Figure 5.1: Currently accepted model of the substorm current wedge illustrating the field-aligned currents, the closure current, and the ionospheric current of the wedge (from *McPherron et al.*, 1973).

with the dipolarization of stretched field lines. The tailward expansion of the dipolarization region is consistent with the poleward motion of the H β emissions.

The low latitude magnetic signature produced from such a current system was described by *Clauer and McPherron* [1974]. Magnetic signatures from low latitude stations are usually displayed in local geomagnetic coordinates with components H, D, and Z. In this coordinate system H is the horizontal intensity in nanoteslas (nT) ($=\sqrt{X^2 + Y^2}$), Z is the vertical intensity, and D is the declination between the horizontal components (X and Y) and the geodetic X-axis. The declination is often given as an angle in minutes of arc and is converted to nT for analysis. Figure 5.2 illustrates the H and D components of the substorm current wedge. The H-component (positive northward) is symmetric across the midnight meridian of the wedge, the D-component (positive eastward) is antisymmetric across the midnight meridian (positive on the dusk side and negative on the morning side). The H and D magnetic perturbations are due to the field-aligned currents associated with the current wedge. The downward current on the eastern side of the wedge produces a positive H signature and a negative D signature (with respect to the midnight meridian), while the upward current on the western edge

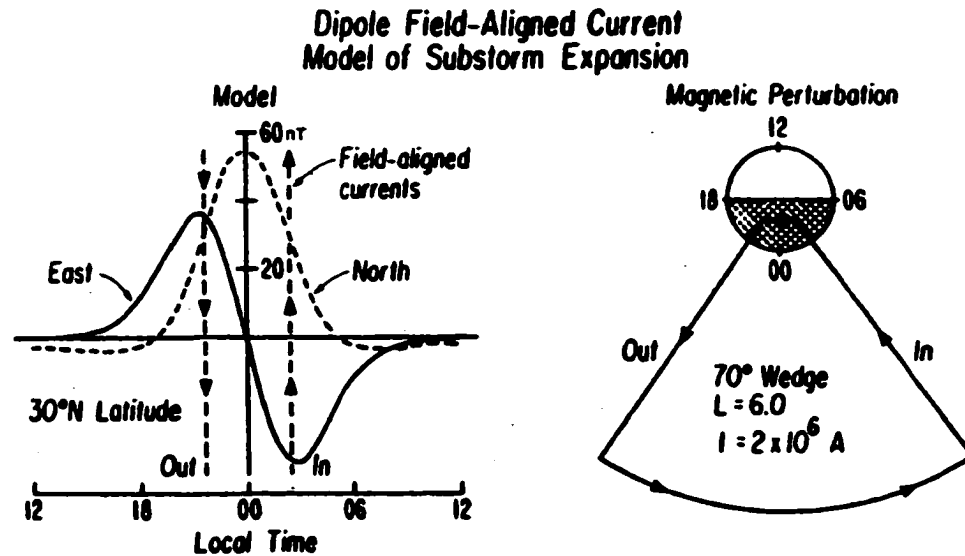


Figure 5.2: Magnetic signatures observed at low latitudes from the field-aligned currents of the substorm current wedge. (Left) Magnetic perturbations across the central meridian of the wedge. (Right) An ionospheric projection of the equivalent current system (from *McPherron et al.*, 1973).

produces a positive H signature and a positive D signature. The Z-component is not shown in this Figure as it is associated with the horizontal currents (i.e. the electrojets), which are seldom sensed at mid-low latitudes unless the magnetic activity is large.

The concept of the current wedge model originated with the Norwegian physicist Kristian Birkeland [*Birkeland*, 1908], but it was *Atkinson* [1967] who first considered the physics behind the model when he proposed that the neutral sheet current near the Earth would be diverted into the ionosphere in an azimuthally confined sector with the western edge of this sector subsequently expanding westward. Following this, *Akasofu and Meng* [1969] and *Akasofu and Chapman* [1972] proposed a “short-circuiting” (i.e. a sudden disruption of current flow) of the ring current into the ionosphere thereby producing the upward and downward field-aligned currents of the wedge. In an attempt to explain the differing magnetic signatures between the evening and midnight low latitude H-component, *Kamide and Fukushima* [1972] proposed a model current system for the substorm that included variations in the flow of the asymmetric partial ring current, and the diversion of the cross-tail current in a latitudinally and longitudinally localized

region. *McPherron et al.* [1973] summarized these models into the three-dimensional current system shown in Figure 5.1 as a means for explaining the magnetic signatures observed by the OGO 5 satellite (in the tail lobe) and by ground observing stations.

The schematic in Figure 5.1 shows the upward and downward field-aligned currents as localized regions of current flow. The localized upward field-aligned current is generally well accepted since the westward edge of the westward electrojet is the site of a localized region of intense electron precipitation associated with the auroral surge [*Baumjohann et al.*, 1981; *Opgenoorth et al.*, 1983]. However, physically resolving a localized region of downward field-aligned current is somewhat more difficult, especially in light of the fact that the downward field-aligned current has been considered to be less intense and more widespread longitudinally [*Baumjohann et al.* 1981; *Untiedt and Baumjohann* 1993]. In fact, there is presently no model of the substorm current wedge that includes a region of localized downward field-aligned current, or explains the physics behind such a region.

Despite the lack of explanations for the downward current however, a substantial amount of energy has been directed towards determining the physical nature of the current disruption itself. Several reviews of the observations and models regarding current disruption have been published [*Lui*, 1991; 1994; 1996]. There are four different theories proposed to produce the instability that begins near-Earth current disruption: the magnetosphere-ionosphere coupling (MIC) model [*Kan et al.*, 1988; *Rothwell et al.*, 1988], the ballooning instability model [*Roux et al.*, 1991; *Bhattacharjee et al.*, 1998], the cross-field current instability (CCI) model [*Lui et al.*, 1991, 1993], and the flow-braking model [*Shiokawa et al.*, 1997; *Birn et al.*, 1999]. All models advocate an instability that occurs in the near-Earth plasma sheet as the catalyst for current disruption. The physics involved in each instability however differs, despite the fact that they all stem from observations in the plasma sheet. The MIC model depends heavily on feedback from the ionosphere. Disruption of the cross-tail current is achieved due to the current in a propagating Alfvén wave and is maintained via induced electric fields, fast time changes in ionospheric conductivities and the creation of field-aligned current. The ballooning instability model is driven by the interactions of an ion pressure gradient with a local region of suitable magnetic curvature in the transition region between dipolar and tail-like

field geometry. The CCI model advocates that the cross-tail current will disrupt when the cross-tail current density intensifies to an instability threshold. A key requirement for this model centers around the ion drift speed in the neutral sheet, which must be a substantial fraction of the ion thermal speed. The relatively new flow-braking model proposed by *Haerendel* [1992] and *Shiokawa* [1997,1998] produces cross-tail current disruption and the substorm current wedge through the development of an inertia current at the inner edge of the neutral sheet. The inertia current is created when earthward high-speed ion flows are suddenly stopped by a substantial magnetic field gradient at a boundary between the dipolar and tail-like magnetic fields.

Although a majority of the effort in the past has been devoted to determining the exact nature of the instability that precipitates the onset of the expansive phase, within the past 10 years there has been a resurgence of the opinion that the directly driven system has an equally important role in the substorm process [*Rostoker et al.*, 1987; *Goertz et al.*, 1993; *Baker et al.*, 1997]. As mentioned in Chapter 1, the directly-driven system is composed of the ionospheric electrojets, the ionospheric Pedersen currents, and their associated Birkeland (field-aligned) currents which connect them to the magnetosphere. The directly-driven currents are always present in the magnetosphere and aid in dispensing energy input from the solar wind by directly transferring this energy to the high-latitude ionosphere and ring current via the Birkeland and ionospheric currents. To highlight the role this current system could have in the substorm process, *Rostoker* [1974] proposed a new model current system describing changes in real current flow in the magnetosphere associated with substorm activity. The model involved solely the directly-driven current system in which changes in the magnetic perturbation pattern at expansive phase onset were reproduced by the step-like motion (to the north and west) of the region of current outflow at the western edge of the westward electrojet (the auroral surge).

The substorm current wedge is only an equivalent current system. The currents comprising the wedge are never actually measured, they are inferred by the structure of the magnetic field perturbations. In addition, the lack of appropriate measurements in space allows for any number of real current systems that can explain the observations. In this chapter an alternative explanation for the observed magnetic signatures at low

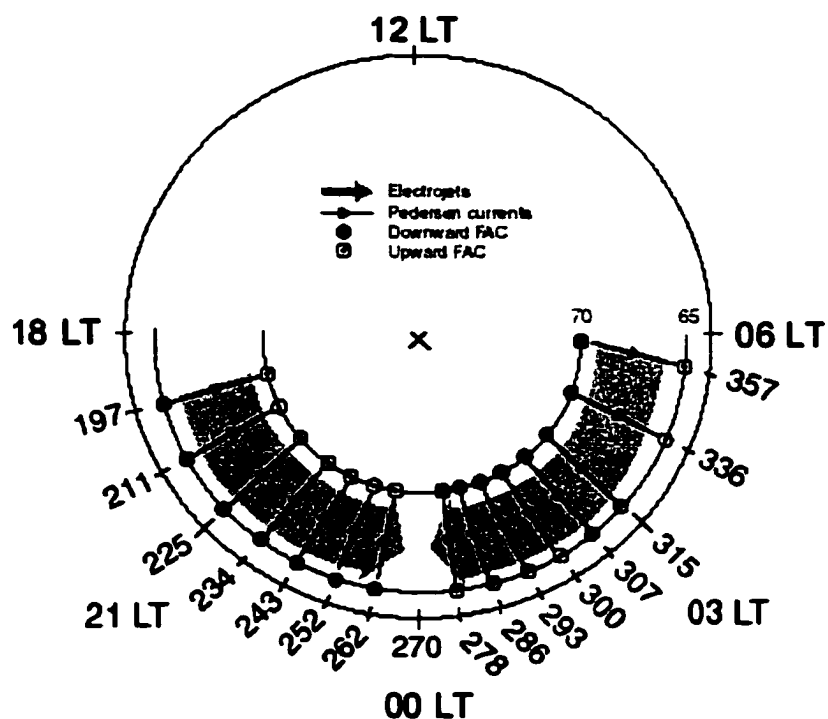


Figure 5.3: Schematic of the preonset ionospheric current system in the Northern Hemisphere. The currents shown are part of the directly-driven current system including the east and west large scale electrojets, the north/south Pedersen currents, and the associated Birkeland currents. LT=Local Time.

latitudes at expansive phase onset is proposed based on a refinement of the current model of *Rostoker* [1974]. This new model involves a perturbation of the directly-driven current system near midnight and a shift in the geometry of the Region II field aligned current system in the morning sector. By reconfiguring the Region II currents, the longitudinally extended downward field-aligned current associated with the current wedge is naturally produced. This new model current wedge is a real current system (as opposed to the equivalent current system producing the low latitude magnetic signatures in *Clauer and McPherron* [1974]) and produces qualitatively and quantitatively the magnetic signatures commonly attributed to the more conventional current wedge model.

5.2 The Model

The main thrust of this project was to explore the physics of creating the substorm current wedge. As such, a model of the growth phase and expansive phase current systems was needed to simulate changes occurring around expansive phase onset. The growth phase and expansive phase current systems were simulated by combining 52 current “elements” (26 elements each for the evening and morning sector currents, respectively) of differing size and current magnitude, which together reproduced realistic growth and expansive phase conditions.

Table 5.1 Current magnitudes for preonset model in Figure 5.3

Evening Sector	Longitude (° East)	Hall Current (MA)	Pedersen Current (MA)
	197-211	0.036	0.018
	211-225	0.035	0.0175
	225-234	0.034	0.017
	234-243	0.033	0.0165
	243-252	0.032	0.016
	252-262	0.031	0.0155
Morning Sector	278-286	0.0459	0.0228
	286-293	0.046	0.023
	293-300	0.047	0.0235
	300-307	0.048	0.024
	307-315	0.060	0.030
	315-336	0.070	0.035
	336-357	0.080	0.040

All currents flow between latitudes 65° and 70°.

Figure 5.3 shows the current systems that were used to simulate growth phase conditions ~1 minute prior to expansive phase onset. With respect to substorm dynamics, one can envision the inner edge of the cross-tail current being quite enhanced with large pressure gradients both radially and azimuthally. In Figure 5.3, 270° E is the local

magnetic midnight meridian. The large gray-shaded arrows are the eastward and westward electrojets, respectively. The thin black arrows represent the north-south Pedersen currents, and the \otimes and \odot are the downward and upward field-aligned currents, respectively. Looking at the dawn side as an example, the Hall and Pedersen currents extend from 357° to 278° E longitude and from 65° to 70° N latitude, although for clarity the electrojets have not been drawn to the full 5° width. The electrojets and Pedersen currents gradually weaken in magnitude as they approach midnight, simulating the idea that an increasing amount of current is transported out of the ionosphere via field-aligned currents, i.e. the electrojets “bleed” up the field lines. Approximately one half time zone directly east and west of midnight there is no current flowing, simulating a region characterized by a weak electric field [Kamide and Vickrey, 1983] and low conductivity. The relative magnitudes of the Hall and Pedersen currents were chosen based on reported ionospheric conductivity ratios (Σ_H/Σ_P) [Brekke et al., 1974; Wallis and Budzinski, 1981]. During the growth phase, the Σ_H/Σ_P ratio is typically 1 – 2 and the ratio of morning to evening sector currents is approximately 2:1. The relative magnitudes of the Hall and Pedersen currents are given in Table 5.1.

The current elements were designed to be input into the Kisabeth Surge program described in Chapter 2, Section 2.4, where the magnetic perturbations produced by the current systems can be calculated using the Biot-Savart law in a dipolar field geometry (cf. Kisabeth and Rostoker [1977]). Each element is described by a set of latitude and longitude coordinates. For example, the coordinates (70, 300; 70, 307), (65, 300; 65, 307) describe a Pedersen current 7° in longitudinal extent and 5° wide. The coordinates, input in this way to the Surge program, describe a current that is fed by a downward field-aligned current at 70° latitude, flows equatorward, and flows out along a field-aligned current at 65° . The electrojets are treated in a similar fashion, being divided up into current elements along their length.

Each of the current elements that comprise the growth phase (preonset) system is connected to the equatorial plane via the field-aligned currents. The current circuits make separate closed current loops that connect the ionosphere to the magnetosphere. For each current loop $\nabla \cdot J = 0$.

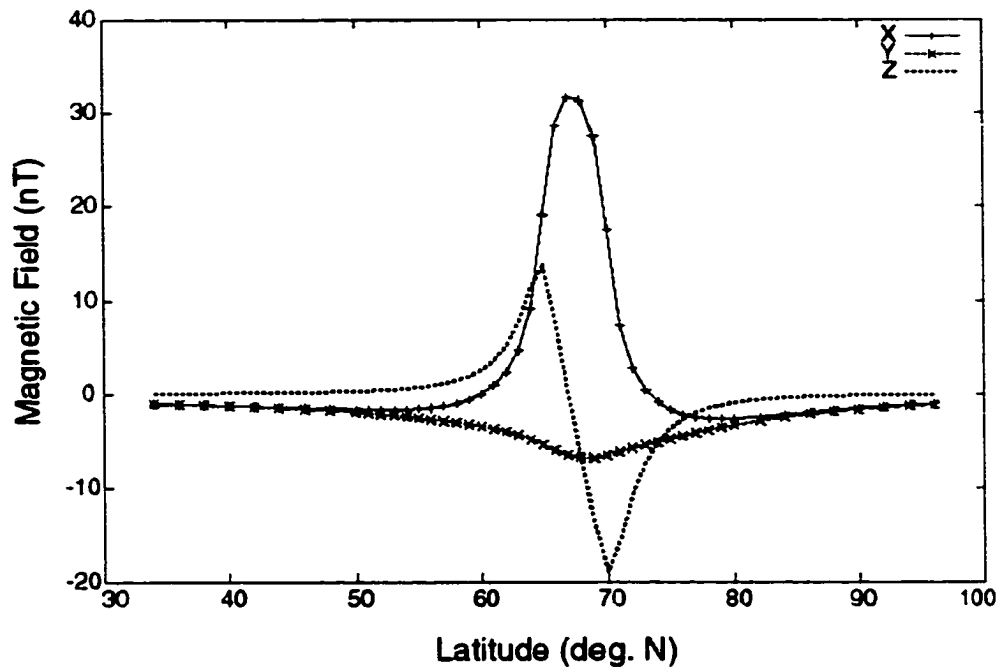


Figure 5.4: Latitude profile of the growth phase currents in the dusk sector. This profile was taken along a meridian at 229° E and illustrates the signatures of an eastward electrojet.

To ensure that our growth phase model was realistic (that is, produced acceptable magnetic perturbation magnitudes), three latitude profiles were plotted along the dusk, midnight, and dawn sectors, respectively. Figure 5.4 shows the latitude profile along the dusk sector, taken along the meridian 229° E. The profile is indicative of an eastward electrojet with a positive X-component peak at the center of the electrojet and an antisymmetric Z-component, which crosses zero at the latitude of the X-component peak. The slightly negative Y-component is a result of edge effects of the downward field-aligned currents at the equatorward edge of the electrojet. The latitude profile taken along a meridian at midnight is shown in Figure 5.5. The polarity transition of the Y-component across 65°N is due to the edge effect of the net upward FAC of the eastward and westward ionospheric electrojets as their current “bleeds” up the field lines. The X-component represents the combined effects of the ionospheric westward electrojet (which dominates its eastward counterpart) and the edge effects of the anti-parallel Birkeland currents. The positive Z-component is due to the edge effect of the meridional ionospheric closure currents linking the Birkeland current sheets.

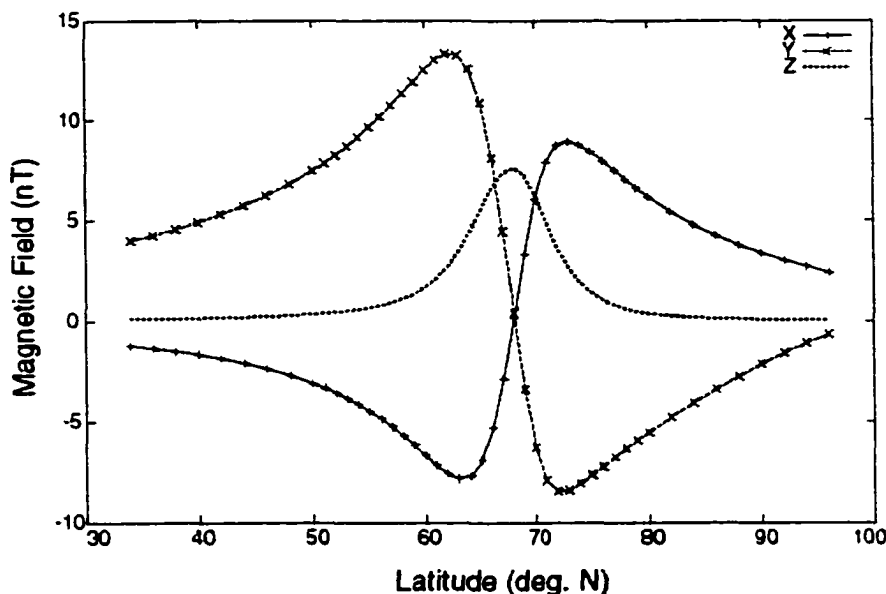


Figure 5.5: Latitude profile of the growth phase currents taken along the midnight meridian.

Figure 5.6 shows the latitude profile taken in the morning sector along the meridian 318° E. The signature of a westward electrojet is clearly observed with the antisymmetric Z-component that is reversed in polarity from its eastward electrojet counterpart. The negative 'dip' in the Y-component is due to edge effects of the field-aligned currents.

Figure 5.7 shows the model current system immediately (≤ 1 min) after expansive phase onset. The evening sector equatorward meridional currents and eastward electrojet have been retracted one time zone to the west (one time zone equals 15° East longitude). The westward electrojet has been extended one time zone to the west, intruding into the evening sector as a Cowling channel. A section of the Region II upward FAC in the post-midnight sector has also been shifted westward one time zone into the midnight sector in response to changes in the electric field and conductivity in the auroral ionosphere at expansive phase onset.

In terms of the substorm model, the substorm current wedge has formed and the magnetosphere is now returning to a lower energy state by unloading its stored energy. From the point of view of the previous chapters, one would now envision the beginning of the dipolarization of inner plasma sheet magnetic field lines and the beginning of the poleward motion of the H β emissions. The discrete arc that brightens to begin the expansive phase would be located along the equatorward portion of the electrojets, with

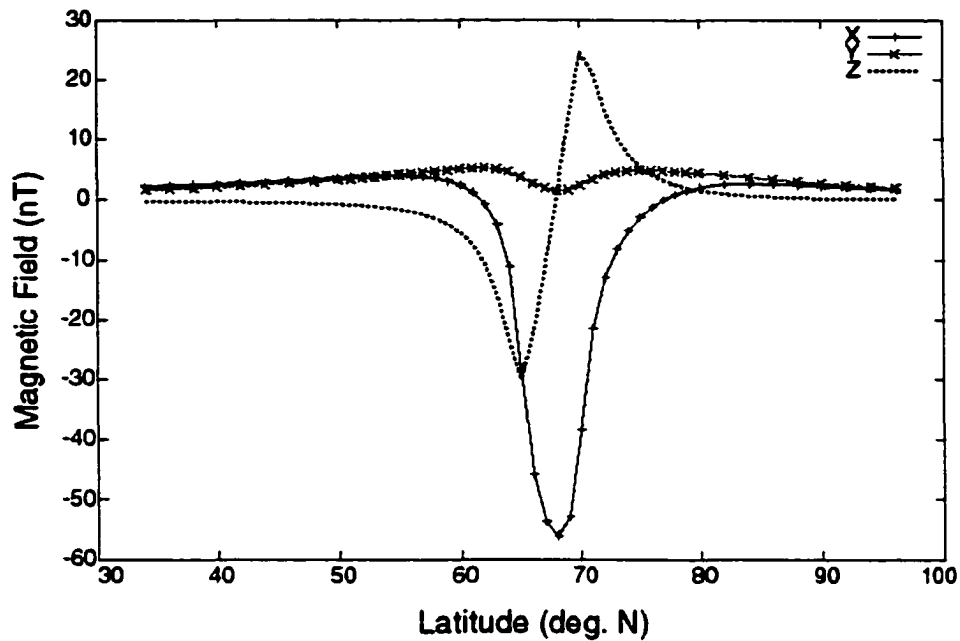


Figure 5.6: Latitude profile of the growth phase currents in the morning sector. The profile is taken along a meridian of 318° and illustrates the signature of a westward electrojet.

the H β emissions located within the electrojets. However, instead of the current wedge being produced by the disruption of the cross-tail current, it is suggested here that the directly-driven system becomes enhanced to dissipate the energy into the ionosphere and the current wedge is formed by the reconfiguration of the directly-driven system as described above. The timescales involved in such a reconfiguration will be discussed later in this chapter.

It should be noted at this point that this new current wedge model is not intended to be a full-scale substorm model that explains all aspects of each phase of the substorm. This model deals only with the physics needed to create the substorm current wedge, and the simple question being asked is whether or not the current wedge signatures can be produced using a current system different from one related to the diversion of the cross-tail current.

The interplay between the conductivity and the electric field in ionospheric currents is highly variable in both longitude and latitude [Kamide and Vickrey, 1983; Robinson *et al.*, 1985; Lewis *et al.*, 1998]. Kamide and Vickrey [1983] suggest that the eastward electrojet is electric field dominant and that the westward electrojet is divided into two

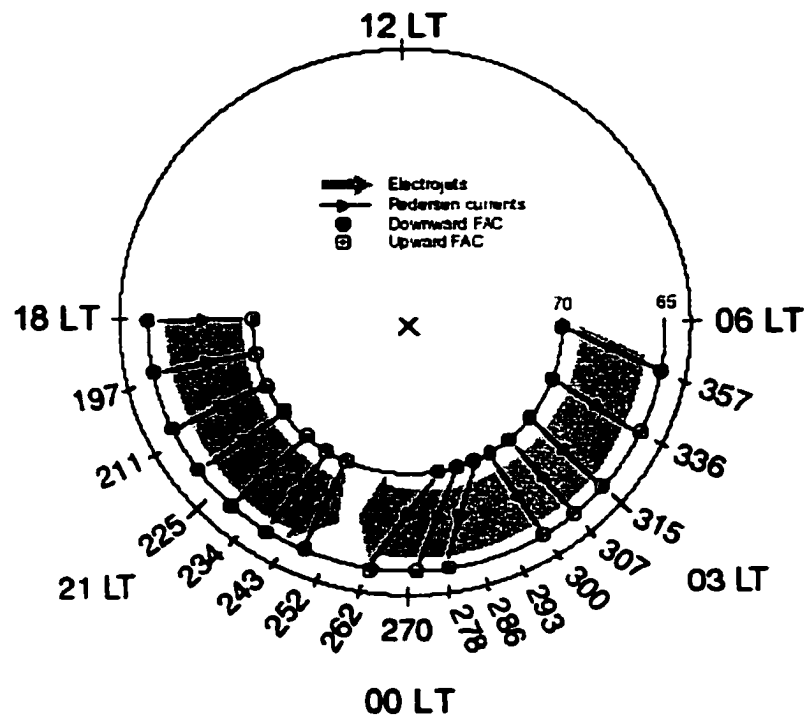


Figure 5.7: Schematic of the expansive phase ionospheric current system in the Northern Hemisphere immediately after onset. The evening sector currents have been retracted one time zone westward. The westward electrojet has been extended one time zone into the pre-midnight sector and the Region II field-aligned currents have been shifted westward in association.

distinct components: conductivity dominant in the midnight and early morning sectors; and electric field dominant in the late morning region. In contrast, *Lester et al.* [1996] argue that the westward electrojet in the midnight sector is electric field dominant, saying more detailed spatial structure exists in the currents than was originally observed by *Kamide and Vickrey* [1983]. The ratio of Σ_H to Σ_P in the auroral zone has been reported to increase to ~ 4 during periods of high magnetic activity [*Brekke et al.*, 1974]. In addition, estimates of the Σ_H/Σ_P ratio in the western edge of the auroral surge have been reported to vary between 3.0 and 5.4 [*Opgenoorth et al.*, 1994]. Therefore, in accordance with these findings, the Hall and Pedersen currents have been increased so that their ratio is 3:1 in the dawn and dusk sectors, and the current element magnitudes have been varied in longitude to simulate the electric field versus conductivity dominant regions. The evening to morning sector ratio has been kept at 1:2. The relevant current magnitudes can be found in Table 2.

Latitude profiles along meridians in the dusk, midnight and dawn sectors are shown in Figures 5.8 a-c. The dusk sector profile shown in Figure 5.8a was taken along the meridian 232°E, three degrees East of the original preonset meridian. The retraction of the eastern current system to 180°E caused our observation meridian at 229° to pass close to the ends of field-aligned currents causing edge effects in the results. Therefore, to keep the observation points away from the ends of the currents, the observation meridian was shifted slightly. Figure 5.8a shows an eastward electrojet that has been enhanced due to increase energy input to the directly-driven system during the growth phase. That

Table 5.2 Current magnitudes for the post-onset model in Figure 5.7

Evening Sector	Longitude (° East)	Hall Current (MA)	Pedersen Current (MA)
	180-195	0.093	0.031
	195-210	0.087	0.029
	210-219	0.081	0.027
	219-228	0.078	0.026
	228-237	0.060	0.020
	237-246	0.045	0.015
Morning Sector	263-271	0.090 (263-286)	0.030
	271-278		0.045
	278-286		0.049 (278-300)
	286-293	0.135	
	293-300	0.147	
	300-307	0.159	0.053
	307-315	0.090	0.035
	315-336	0.100	0.040
	336-357	0.080	0.040

All currents flow between latitudes 65° and 70° N.

the currents are increasing in magnitude can be seen by the polarity shift in the Y-component, which is due to field-aligned currents (compare with the Y-component in Figure 5.4).

The latitude profile along the midnight meridian is shown in Figure 5.8b. This profile reflects the existence of an intense westward electrojet that has intruded into the midnight sector and is enhanced due to intense particle precipitation associated with the auroral surge. Figure 5.8c illustrates the latitude profile along the meridian 318°E in the morning sector. As in the preonset case, the structure of the westward electrojet is clear.

A differential longitude profile for this model was produced by subtracting the pre-onset magnetic perturbations from the post-onset perturbations for a series of observing stations along a constant latitude of 45°N. The longitude profile shown in Figure 5.9 exhibits the essential features of the expansive phase substorm current wedge signature complete with the symmetric H component peak and the antisymmetric D component profile across the central meridian. The similarity between Figure 5.9 and Figure 5.2 by *Clauer and McPherron* [1974] proves that reconfiguration of the directly-driven current system can successfully reproduce wedge-like perturbation signatures at expansive phase onset.

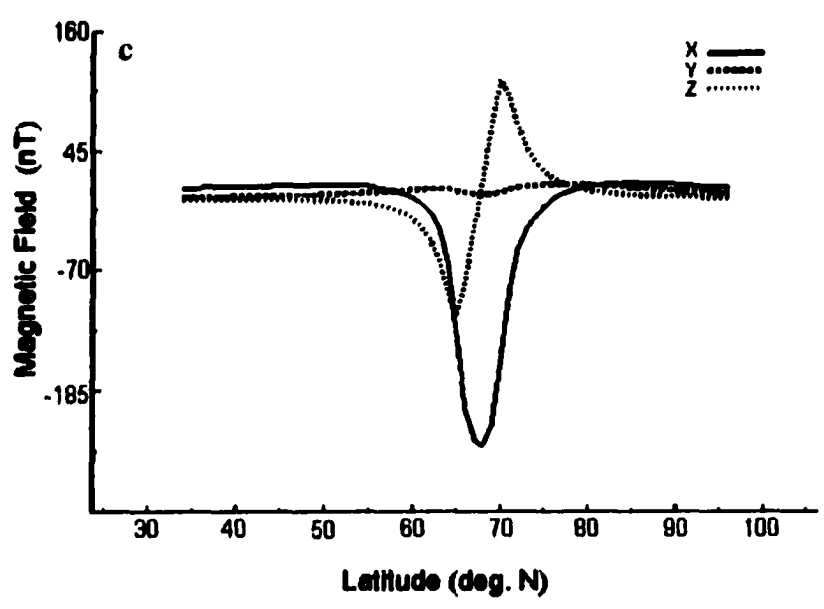
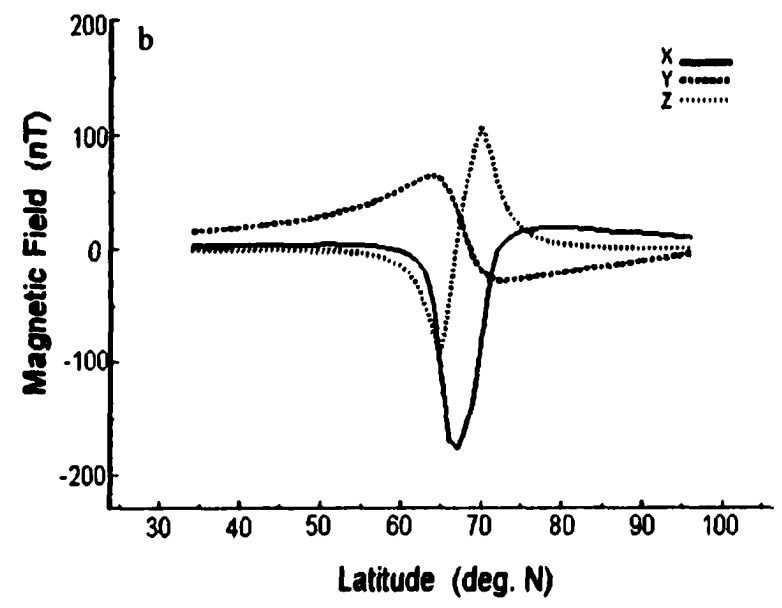
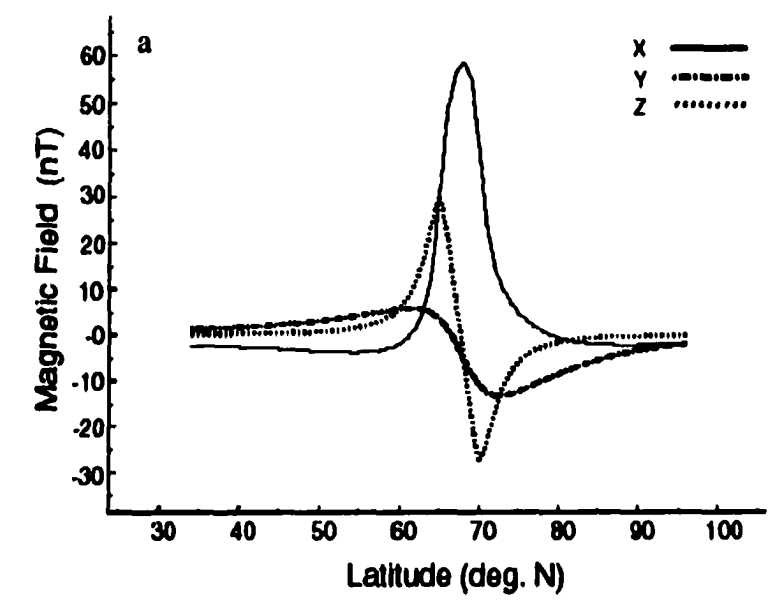


Figure 5.8: Latitude profiles of the post-onset current system showing an eastward electrojet in the dusk sector (a); currents along the midnight meridian (b); and an intensified westward electrojet in the morning sector (c).

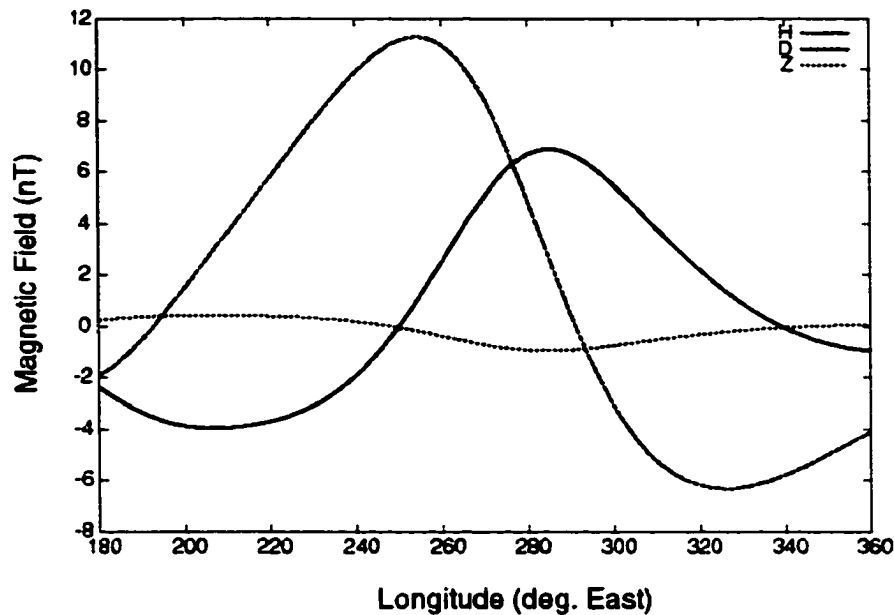


Figure 5.9: Longitude profile of the perturbed directly-driven current system responsible for the substorm current wedge.

5.3 Theory and Observations

The substorm begins with enhanced energy input into the magnetotail, marking the beginning of the growth phase and of enhanced earthward convective flow in the magnetotail. During the growth phase there is an increase in the rate of energy dissipated in the ionosphere by the directly-driven system while, simultaneously, magnetic flux is stored in the tail. The current density in a localized region at the inner edge of the cross-tail current becomes very large prior to expansive phase onset [Kaufmann, 1987]. This intensified region of current flows clockwise through the inner plasma sheet such that it flows parallel to the convective drifting plasma on the dusk side of the Earth, and anti-parallel to the convective flow on the dawn side. These parallel and anti-parallel configurations are consistent with the presence of space charge along the dawn and dusk sides of the near-Earth magnetotail (cf. Figure 5.10). In an MHD context, space charge can be given by

$$\rho = \epsilon_0 \nabla \cdot \vec{E} = -\epsilon_0 \vec{B} \cdot (\nabla \times \vec{v}) + (1/c^2) \vec{J}_\perp \cdot \vec{v} \quad (5.1)$$

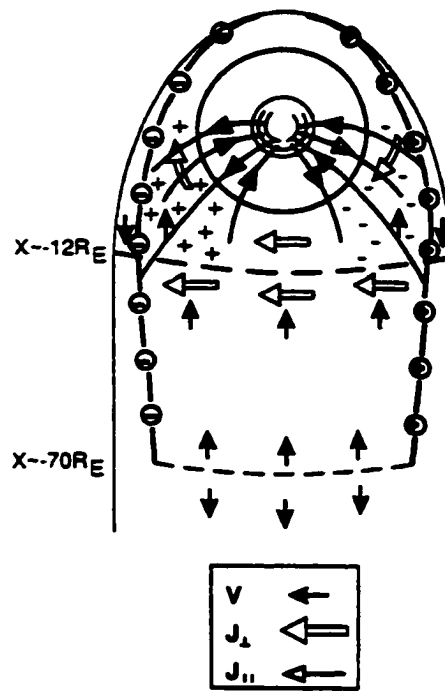


Figure 5.10: A schematic equatorial plane cross-section of the tail illustrating the space charge associated with the Region I and Region II field-aligned currents (from *Rostoker* [1994]).

where \vec{E} is the electric field ($= -\vec{v} \times \vec{B}$, using the MHD assumption), \vec{v} is the plasma drift velocity, c is the speed of light, \vec{B} is the ambient magnetic field, and \vec{J}_{\perp} is the density of current flow normal to the magnetic field. Equation 5.1 shows that there are two terms that can produce space charge. The first relates the velocity shear near the flanks of the magnetosphere with the positive and negative space charge at the LLBL/CPS interfaces. This space charge is consistent in sign and magnitude with being the source of the dawn-to-dusk convection electric field across the plasma sheet [*Rostoker*, 1996]. The second term in Eq. (5.1) is of immediate interest to this model as it shows the parallel (anti-parallel) encounters between the cross-tail current and the convective velocity can produce positive (negative) space charge along the dusk (dawn) sector of the inner plasma sheet. Given cross-tail current densities of ~ 300 mA/m [*Kaufmann*, 1987], a thickness distribution of the space charge of $\sim 5 R_E$, and earthward convective flow velocities of ~ 50 km/s, one can expect volume charge densities of as much as $\sim 5.2 \times 10^{-21}$ Cm $^{-3}$ near the flanks of the magnetotail falling off to zero at the

center of the tail where \bar{J} is perpendicular to \bar{v} [Rostoker, 1996]. The positive and negative space charge produces an electric field that is directed dusk-dawn and has the effect of shielding the dawn-dusk convection electric field from the inner magnetosphere. This electric field is termed the 'shielding' electric field after Rostoker [1994]. The growth phase can now be thought of as an interval during the substorm where the amount of shielding space charge is increased. The maximum charge density calculated above is roughly comparable to that associated with the first term in Eq. (5.1)

($\rho \sim 3.5 \times 10^{-21} \text{ C / m}^3$ [Rostoker, 1996]). Furthermore, it is distributed over a much larger volume of space so that the total shielding charge is considered significant.

At expansive phase onset, the enhanced cross-tail current near the inner edge of the plasma sheet is suddenly and largely reduced, which is equivalent to the reduction of the shielding space charge and, thus, the dusk-dawn electric field. The timescale for building the shielding electric field is of the order of the growth phase timescale (tens of minutes). However, the breakdown of the shielding electric field is expected to be almost immediate as the main component feeding the space charge (namely, J_{\perp}) is suddenly reduced. Unfortunately it is not possible to investigate the timing or the effects of 'overshielding' ($E_{\text{shielding}} > E_{\text{convective}}$), which would occur if the shielding electric field did not register an immediate reduction in magnitude at expansive phase onset. The Surge program is designed only to determine magnetic perturbations due to current systems and not effects due to electric field variations.

The sudden disruption of the cross-tail current is also thought to be the time when the substorm current wedge is formed with the redirection of the cross-tail current as field-aligned currents to and from the ionosphere. However, in this new model it is suggested that the cross-tail current does not redistribute to flow toward the ionosphere, rather it is proposed that the directly-driven current system is enhanced and suddenly reconfigured to form the current wedge. The breakdown of the shielding electric field (which is thought to be immediate after the reduction of the cross-tail current) allows the convection electric field to penetrate closer to the Earth. The convection electric field in the midnight sector maps to the ionosphere as a westward electric field. Already present in the auroral zone is a southward electric field in the midnight and morning sectors (Figure 5.11) [Mozer and Lucht, 1974]. Following the arguments of Kawasaki and

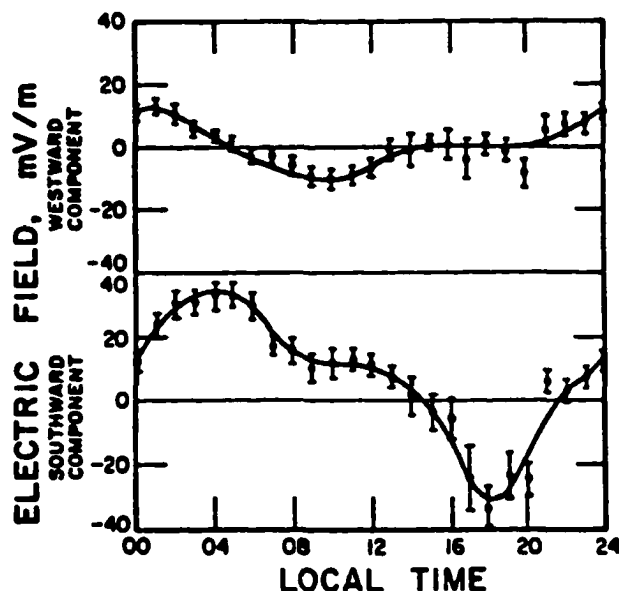


Figure 5.11: One hour averages of meridional and azimuthal electric field components measured in a nonrotating frame of reference on 32 balloons flown in the auroral zone (from *Mozer and Lucht* [1974]).

Rostoker [1979], the westward electric field adds to the primary southward (equatorward) field producing an electric field directed to the southwest (Figure 5.12). A southwestward electric field could also be produced as suggested by *Coroniti and Kennel* [1972] in which the westward convection electric field drives a northward Hall current. The Hall drifts cause the lower ionosphere to polarize leading to a southward electric field. The total field in this case is also southwestward.

A southwestward electric field has been observed frequently in radar data. Studies using the Chatanika incoherent scatter radar, the EISCAT (European Incoherent Scatter) radar, and the Dynamics Explorer satellites have shown reversals in direction of the meridional electric field from northwest to southwest along with an enhancement in the westward electric field at the time of expansive phase onset [*Baumjohann et al.*, 1981; *Kamide and Vickrey*, 1983; *Weimer et al.*, 1994]. Typical magnitudes of the auroral zone electric field during the expansive phase reportedly range from 25 – 50 mV/m. Similarly, when possible to obtain suitable backscatter, the SuperDARN HF radars have shown southwestward-directed electric fields during the expansive phase. Figure 5.13 is an

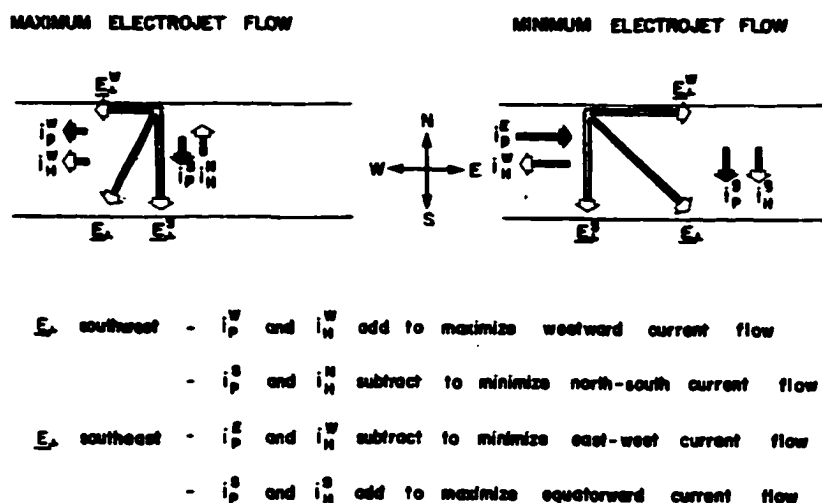


Figure 5.12: Electric field configurations for maximum and minimum electrojet current flow. An intense westward current flows if the auroral zone electric field is directed southwest (from *Kawasaki and Rostoker* [1979]).

example of ionospheric electric field vectors near the time of expansive phase onset (~0603 UT) for an event that occurred on January 11, 1994. Although the number of data points is sparse, they do illustrate the magnitude and direction of the electric field during the expansive phase. The southwestward direction and the 20 - 40 mV/m strength of the electric field vectors agrees well with the observations reported above.

The reconfiguration of the electric field to a southwestwardly direction produces an intense westward Cowling current. In this current wedge model, the Cowling current is the substorm westward electrojet observed at expansive phase onset, and is the ionospheric component of the substorm current wedge. Having the ionospheric wedge currents flow westward within the auroral surge in a Cowling channel of enhanced conductivity has been suggested by *Baumhohann et al.*, [1981], *Inhester et al.*, [1981], *Opgenoorth et al.* [1983], *Weimer et al.*, [1994], and *Lewis et al.*, [1997] although the manner in which the Cowling current is created differs between authors.

Referring to Figure 5.3, the Cowling channel will develop to the west of the western edge of the morning sector Region II upward field-aligned current as the westward electric field becomes more prominent. Along with the Cowling channel and the resulting intense westward electrojet, the Region II field-aligned current is proposed to

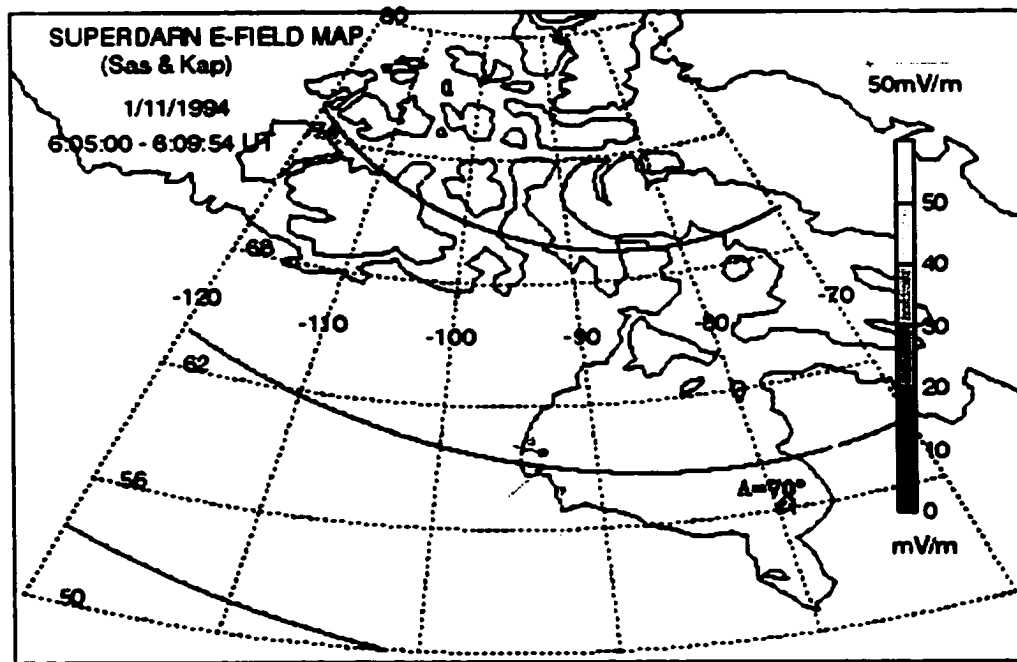


Figure 5.13: An example of the electric field vectors for an event that occurred on January 11, 1994. Expansive phase onset was ~ 0603 UT. The number of vectors is small due to saturation of the E region ionosphere from enhanced particle precipitation.

shift westward to form the substorm current wedge (cf. Figure 5.7). The electrodynamics needed to produce such a shift in field-aligned current is discussed below.

With the southward turning of the electric field, the Hall conductivity is enhanced significantly (e.g. Σ_H has been observed to increase from 6 mhos to 40 mhos at 67° North latitude) [Brekke *et al.*, 1974; Kamide and Vickrey, 1983]. With enhanced particle precipitation along the leading edge of the auroral surge, the westward electrojet expands from the morning sector into the region previously occupied by the evening sector eastward electrojet. The Hall and Pedersen conductivity is enhanced in the pre-midnight sector as the dawnside convection cell associated with the westward electrojet protrudes into the duskside convection cell [Hughes and Rostoker, 1977; Rostoker *et al.*, 1975; Weimer *et al.*, 1994].

The expansion of the enhanced particle precipitation into the midnight and pre-midnight sectors produces gradients in the Hall and Pedersen conductivities in these

regions. As a result, Region II field-aligned current can develop as shown by *Kan* [1987]:

$$J_{\parallel} = \bar{\nabla} \cdot \bar{I}_i = -\Sigma_p \bar{\omega}_i \cdot \bar{B}_i + \bar{V}_i \times \bar{\nabla} \Sigma_p \cdot \bar{B}_i - (\bar{V}_i \cdot \bar{\nabla} \Sigma_H) \bar{B}_i \quad (5.2)$$

where \bar{I}_i is the ionospheric current, \bar{B}_i is the ionospheric magnetic field, \bar{V}_i is the ionospheric convection velocity, $\bar{\omega}_i (= \bar{\nabla} \times \bar{V}_i)$ is the vorticity of the convective flow, and Σ_p, Σ_H are the Pedersen and Hall conductivities, respectively. The expansion of the region of high conductivity into the midnight and pre-midnight sectors will lead to a shift of the western edge of the upward field-aligned current to a new locale further to the west.

In contrast, it is argued that the Region I downward field-aligned current does not shift at substorm onset. Prior to expansive phase onset, the combination of Region I downward and Region II upward field-aligned current, the ionospheric, and magnetospheric closure currents constitute a solenoidal configuration, with some magnetic flux leaking out along the edges (e.g. midnight). At substorm onset, the differential shift of the Region II current with respect to the Region I current effectively opens the solenoid, allowing the magnetic perturbations associated with the Birkeland currents to be detected by ground observatories. The equivalent current system that results has precisely the magnetic perturbation pattern that is attributed to the substorm current wedge (cf. Figure 5.9). As new surges develop further poleward and westward during the expansive phase, new Cowling channels will develop and new portions of Region II field-aligned current will shift westward to form 'wedgelets' [*Wiens and Rostoker, 1975*].

As the substorm recovers, the westward electrojet will recede from the evening sector back to its preonset position. The eastward electrojet will gradually return to its pre-onset evening sector position and the magnetosphere will return to its pre-substorm state.

5.3.1 Magnetospheric Dynamics

The main ionospheric features of this new substorm current wedge model are the development of a Cowling channel, a protrusion of an intense westward electrojet into the

pre-midnight sector, and a shift of the morning sector upward field-aligned current into this same region. With the substantial reconfiguration of the auroral zone electric fields and ionospheric conductivities, the question must be asked as to what changes are taking place in the near-Earth magnetotail in association with these dynamics.

In the discussion above, the interaction between the convection and shielding electric field was outlined for the growth and early expansion phases. During the growth phase and the buildup of the cross-tail current, the shielding electric field effectively shielded the convection electric field from the inner plasma sheet. At expansive phase onset the shielding field suddenly reduced allowing the convection electric field to penetrate closer to the Earth, mapping down to the ionosphere as an enhanced westward electric field. The result is an intense westward electrojet, which is primarily a Cowling current, together with a shift of upward Region II field-aligned current into the pre-midnight quadrant.

All field-aligned current in the ionosphere must have a source region in the magnetosphere, which begs the question as to the source of the Region II field-aligned current as it is expanding westward into the pre-midnight sector. It is believed by many authors that pressure gradients are responsible for generating field-aligned currents in the central plasma sheet [e.g. *Hasegawa and Sato*, 1979; *Vasyliunas*, 1984; *Kan*, 1987]. The most general equation that can be written involving currents and pressure gradients is [*Vasyliunas*, 1984; *Parks*, 1991]:

$$J_{\perp} = \frac{1}{B^2} \left[\bar{B} \times \bar{\nabla} \cdot \bar{P} + \bar{B} \times \rho \frac{d\bar{V}}{dt} \right] \quad (5.3)$$

where the gyrotropic pressure tensor, \bar{P} , is given as:

$$\bar{P} = P_{\perp} \bar{1} + (P_{\parallel} - P_{\perp}) bb \quad (5.4)$$

and ρ and V are the mass density and velocity of the plasma, respectively. However, for an order of magnitude estimate, to first order, one can assume static equilibrium and an isotropic plasma. Under these conditions, the current flow normal to the ambient magnetic field (\bar{B}) can be written as [*Parks*, 1991]:

$$\bar{J}_{\perp} = (1/B^2) \bar{B} \times \bar{\nabla} P_{\perp}, \quad (5.5)$$

Taking the divergence of Equation 5.5 and employing current continuity ($\nabla \cdot \mathbf{J}_\perp = -\nabla \cdot \mathbf{J}_\parallel$) yields an equation for J_\parallel of:

$$J_\parallel = - \int_s \mu_o / B^2 [\bar{\nabla} P_\perp \cdot \bar{\mathbf{J}}_\perp] ds \quad (5.6)$$

Equation 5.6 implies that if there is a cross-tail pressure gradient in the direction of the current flow, field-aligned current will be generated. An extension of the cross-tail pressure gradient toward dusk can account for the shift of the upward field-aligned current at expansive phase onset.

Taking the differential form of Equation 5.6 and using the following values appropriate for the near-Earth plasma sheet at $\sim 8 R_E$ ($B = 50$ nT, $J_\parallel = 2 \times 10^{-2}$ A/m at the equator, $\bar{\mathbf{J}}_\perp = 300$ mA/m, and $L_\parallel = 8 R_E$), we obtain a value for $\bar{\nabla} P_\perp$ of 3.2×10^{-18} N/m³. This value is consistent with the pressure gradients reported by *Liu and Rostoker* [1991], and *Lyons* [1995].

The existence of an azimuthal (dawn-to-dusk) pressure asymmetry was confirmed by the ISEE 1 satellite [*Liu and Rostoker*, 1991]. Statistical studies of plasma data taken in the region $-18 R_E < x < -10 R_E$ and $-20 R_E < y < 10 R_E$ revealed a significant dawn-dusk asymmetry of plasma pressure in the central plasma sheet during relatively undisturbed periods of magnetospheric activity and for periods of growth in the directly driven currents [*Liu and Rostoker*, 1991]. *Liu and Rostoker* [1991] attributed the pressure asymmetry to the gradient/curvature drift of the ions in the central plasma sheet. Under normal conditions (i.e. MHD applies), the duskward drifting ions are at least four times hotter than the dawnward drifting electrons. With most thermal energy imparted to the ions, a positive dP/dy is expected to develop in the central plasma sheet.

To enable the magnetotail to be a source region of Region II field-aligned current in this model, an azimuthally and radially localized region of increased pressure must be created near midnight. Evidence for a pressure gradient with ion pressure peaking near midnight has been observed in geosynchronous measurements [*Spence et al.*, 1989; *Kistler et al.*, 1992; private communication J. Borovsky and M. Thomsen] and from ionospheric observations mapped to the equatorial plane [*Wing and Newell*, 1998]. It has also been found that the normal westward gradient of the ion pressure post-midnight is

actually enhanced with the ion pressure peaking slightly in the pre-midnight region [Korth *et al.*, 1999]. In an MHD context, a localized pressure increase could be generated if the gradient and curvature drift of the heated ions was considerably impeded. The drift of the ions could be considerably slowed if, for example, the ExB drift of the particles was balanced by the gradient and curvature drift. However, the issue of how to generate such a region of pressure speaks to the entire mechanism for substorm onset as a region with a localized pressure gradient (of suitable density) would result in a weak field region (a minimum in the B_z component of the tail magnetic field) near geostationary orbit. The creation of a weak field region leads to the argument of stress balance in the near-Earth magnetotail as the tension of the magnetic field lines would have to be balanced with the magnetic pressure, the anisotropic pressure in the weak field region and the dynamic pressure of the plasma flow. With respect to the anisotropic pressure, the question of which ions (i.e. what portion of the ion energy spectrum) would contribute to the localized pressure region still needs to be addressed. Finally, one must ask the question as to just how large the density of ions needs to be in order to produce a weak field region. Such arguments are outside the scope of this thesis.

5.3.2 Geosynchronous dynamics

One way to determine whether or not this model for the substorm current wedge is physically plausible is to investigate the magnetic tail signatures at geosynchronous orbit [private communication, T. Pulkkinen, 1999]. In order to compare magnetic perturbations associated with the dynamics of our model to those observed at expansive phase onset by the GEOS satellites, the currents from the preonset (Figure 5.3) and the post-onset (Figure 5.7) cases had to be mapped to the equatorial plane.

The mapping was completed using the Kisabeth Surge program by determining the location in the equatorial plane of the closure currents associated with the ionospheric electrojets and field-aligned currents. A simplified picture of where the closure currents are located is shown in Figure 5.14. From the point of view of substorm dynamics, at a time ~ 1 minute prior to expansive phase onset, the cross-tail current is enhanced and the pressure gradients are increasing. Thus, energy is being stored in the two most basic

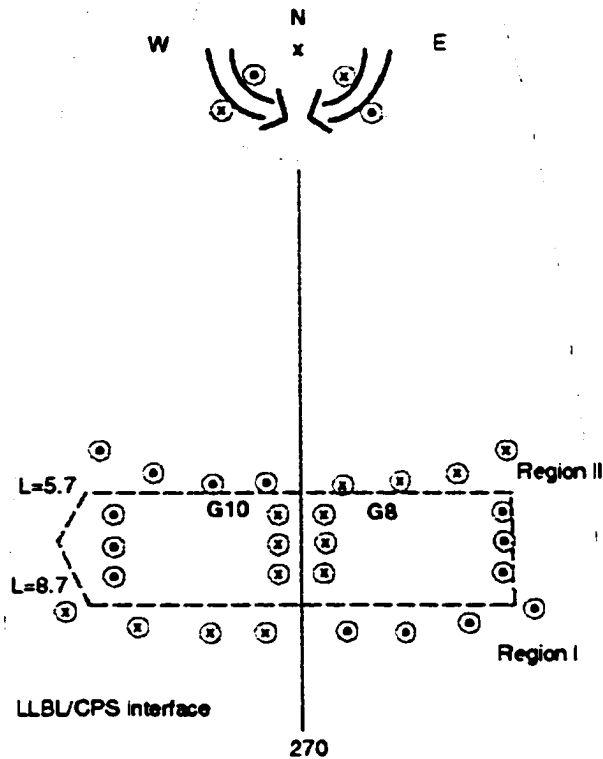


Figure 5.14: Schematic diagram of the closure currents of the preonset current system. The large gray-shaded arrows represent the closure currents associated with the ionospheric electrojets. The gray dashed line represents the cross-tail current and the \odot and \otimes symbols represent upward and downward field-aligned current, respectively.

forms in the magnetotail: pressure gradients in the near-Earth magnetotail (∇P) and parallel sheets of current (∇j_{\parallel}).

For the preonset case, the closure currents are located between L values of 5.7 and 8.7 R_E . The large gray-shaded arrows are the closure currents associated with the ionospheric eastward and westward electrojets. Also included in this model is the cross-tail current, which is represented by a westward flowing current sheet (dashed line in Figure 5.14) that has the same radial width and azimuthal extent as the closure currents. The cross-tail current representation and the closure currents of the electrojets are colocated in the same region of the magnetotail, the end result being a westward flowing

current that is enhanced on the evening side and reduced on the morning side. The strength of the modeled cross-tail current is 3.0 MA.

The closure currents are flanked by upward (near the edge of the central plasma sheet/LLBL) and downward (near midnight) field-aligned currents, which flow into and out of the ionosphere to complete the current circuit. The ionospheric Region I and II field-aligned currents have been represented by one symbol above and below the electrojets, but are understood to be present along the entire length of the large-scale currents. The FACs map into the equatorial plane as azimuthally extended currents along the earthward and tailward edges of the electrojet closure currents. The Region II currents, being further equatorward than the Region I currents in the ionosphere will map to the earthward side of the closure currents. Mapping the closure currents in this manner is not entirely realistic as the program used to determine the magnetic perturbations is written for a strictly dipolar geometry and the latter growth phase is characterized by highly stretched field lines, far distorted from their dipolar shape. We can, however, obtain a qualitative picture of the magnetic perturbations in this region of the plasma sheet and how they compare to what is observed by the GOES satellites.

One important distinction between this current wedge model and other models investigating the dynamics of the current wedge in the equatorial plane is the fact that this model includes a conjugate current wedge. It has long been understood that substorm currents and fields in the Northern Hemisphere are mirrored by similar currents and fields in the Southern Hemisphere, but few studies have actually employed this conjugacy in their modeling. A case in point is the statistical study done by *Nagai* [1991]. Figure 5.15 shows the H (positive northward), V (positive outward), and D (positive eastward) components of the magnetic field observed by the GOES 5 and 6 satellites. These satellites orbited at $+11$ and $+9^\circ$ off the equatorial plane, respectively, and measured variations in the near-Earth magnetic field during substorms. In particular, the GOES satellites observed a noticeable variation in the D-component magnetic field, which was attributed to effects due to substorm-associated field-aligned currents. What was not recognized at the time was the fact that, if the substorm current wedge was a conjugate phenomenon, there would be no D-component in the midplane. Any D-component from the field-aligned currents would come as a result of being off the midplane (for example

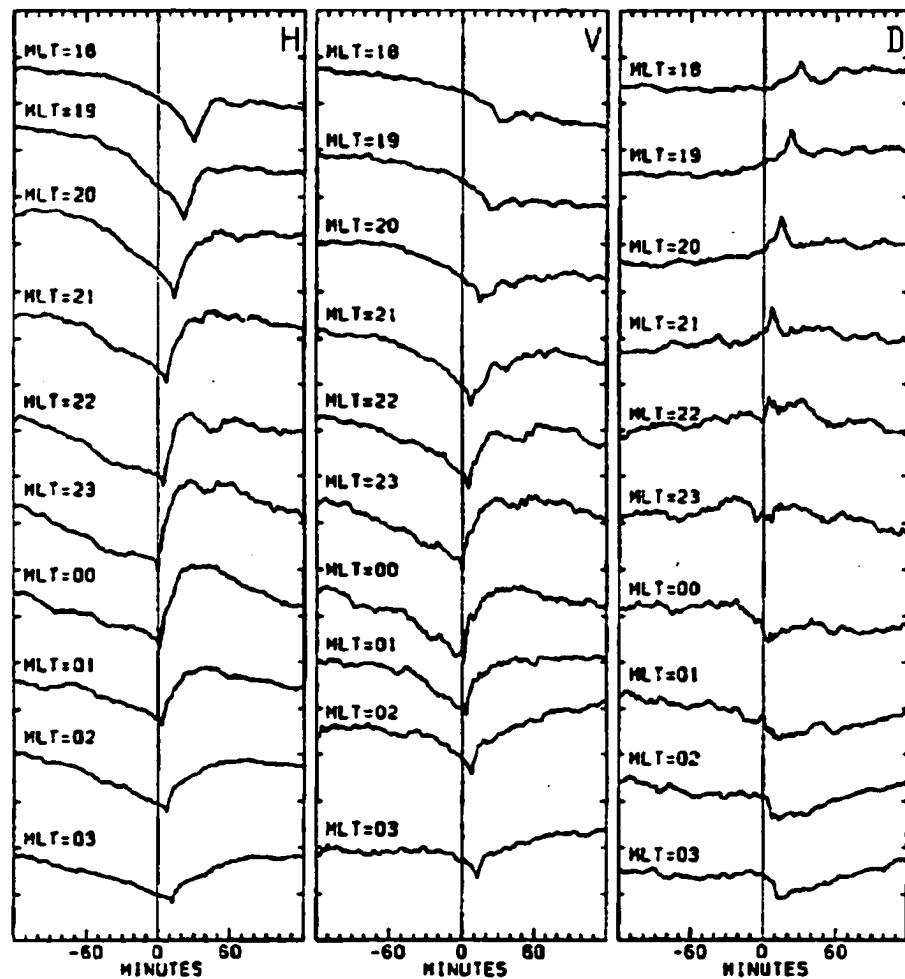


Figure 5.15: Average magnetic field variations during substorms derived from GOES 5 and GOES 6 data. MLT=18 means that the zero time corresponds to the 1800 MLT for the trace (from Nagai [1991]).

in the Northern or Southern Hemispheres) where one set of wedge currents would be closer to the observer than the other. To quantify this point, Figures 5.16 and 5.17 show the magnetic field variations due to a conjugate current wedge system, observed on (Figure 5.16) and $+5^\circ$ off (Figure 5.17) the equatorial plane. At the midplane, the azimuthal (D) and radial (X) components are negligible. The only component observed is the vertical (Z) component, which is twice as large as it would be for a single current wedge since the closure currents associated with each wedge are in the same direction (eastward) across the current sheet and thus double in magnitude. In contrast, observation points a few degrees off the equatorial plane do register azimuthal and radial

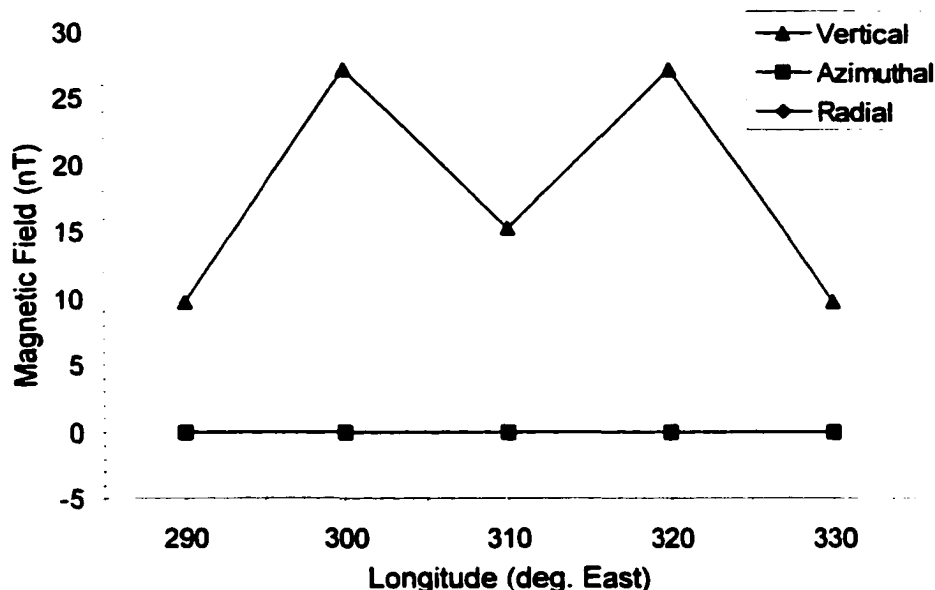


Figure 5.16: Magnetic signatures from a conjugate current wedge system that would be observed on the equatorial plane. Note the radial and azimuthal components are negligible due to the conjugate field-aligned currents.

variations. This is not to say that the study by *Nagai* [1991] is incorrect. His observations were taken $\sim 10^\circ$ off the equatorial plane in the Northern Hemisphere and the D-component variations are expected. However, it should be pointed out that the effects of the conjugate wedge in the Southern Hemisphere, even though they would be small, would be included in these observations.

At this point it is useful to discuss the possible ways in which to produce a D-component disturbance at geosynchronous orbit. The first and most obvious way is by field-aligned currents. Field-aligned currents associated with the substorm current wedge would produce the familiar positive D perturbation in the morning sector and negative perturbation in the evening sector. However, these same perturbation signatures could also be produced in at least two other ways. The first is by radial closure currents between the Region I and Region II currents in the equatorial plane. Looking at Figure 5.14, if the Region I and Region II currents associated with the electrojets were closed in the equatorial plane by radial currents that flowed tailward in the morning sector and

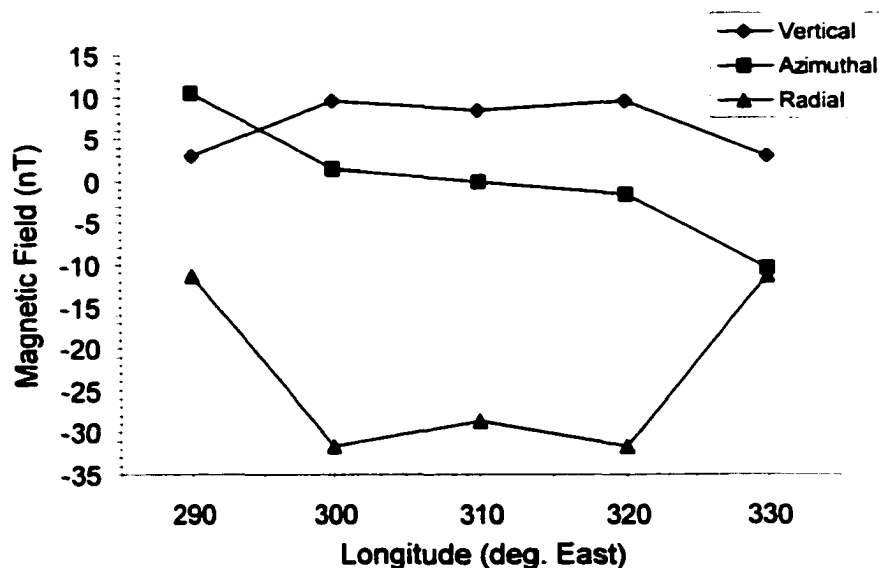


Figure 5.17: Magnetic signatures due to a conjugate wedge current system observed $+5^\circ$ off the equatorial plane. Radial and azimuthal signatures are now observed.

earthward in the evening sector, these currents would produce a positive D perturbation in the morning sector and a negative perturbation in the evening sector. Secondly, these same signatures can be produced simply by currents moving over the satellite. In this case, a satellite moving into or out of a region with Birkeland currents would experience variations in the D-component magnetic field due to the passage of the field-aligned currents.

The consequences of having conjugate current systems could be quite significant in the equatorial plane. To investigate the effects of the conjugate system it was assumed that the same magnitude of current flowed through both hemispheres at the same time during the substorm. It was also assumed that both the Northern and Southern Hemisphere wedges were created at the same time and in the same manner at expansive phase onset.

The magnetic perturbations calculated to be observed at approximately $7.7 R_E$ and 5° above the equatorial plane are shown in Figure 5.18. Seven observation points (238° , 247° , 266° , 274° , 286° , 290° , and 297°) distributed longitudinally throughout the currents

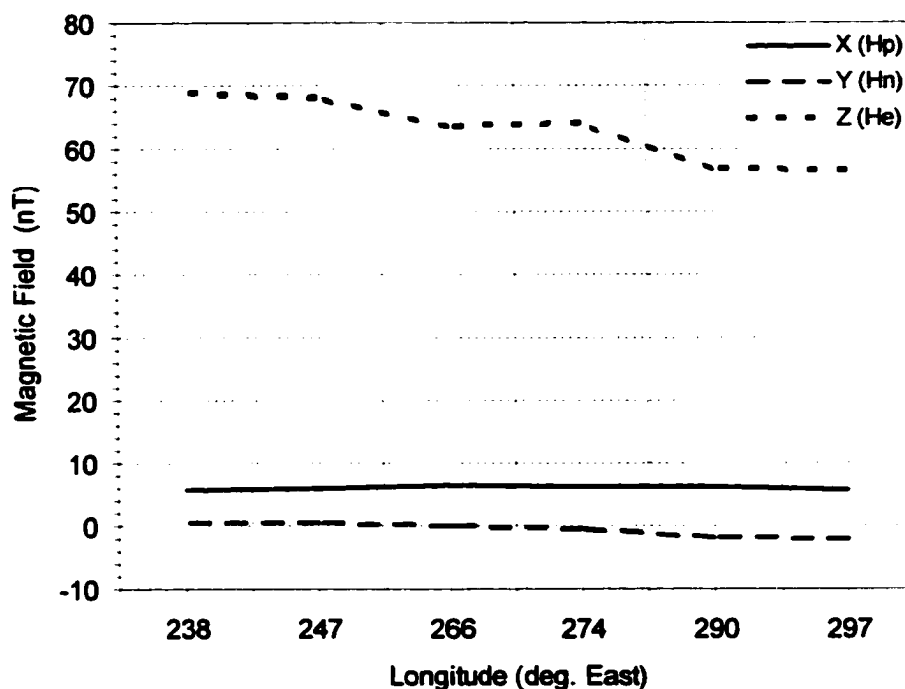


Figure 5.18: Magnetic signatures calculated from the model closure currents in Figure 5.14 and the westward cross-tail/ring current. Observation points are at $L=7.7 R_E$ and 5° above the equatorial plane.

have produced a longitude profile of what one would expect to see from the perturbations of a conjugate current system in a preonset setting. For this model, a large-scale current flowing westward across the plasma sheet (from $L=5.7$ to $L=8.7$) has been included to simulate the near-Earth westward cross-tail/ring current. The total current flowing through this region is 3 MA. The solid line in Figure 5.18 represents the model GSM X-component, which is perpendicular with respect to the equatorial plane and defined positive upwards. Any vertical magnetic perturbation would come from the closure currents associated with the electrojets with maximum magnitudes at the earthward and tailward edges, decreasing steadily to zero at the center of the closure current [Kisabeth and Rostoker, 1971]. Edge effects from the westward cross-tail/ring current would also be included. The location $L=7.7 R_E$ is near the center of the closure currents and westward current and a small X-component is observed as would be expected.

The GSM Y-component is represented by the dashed line in Figure 5.18. In the magnetotail the Y-component is defined positive eastward and is a result of perturbations due to the field-aligned currents. In this model the Y-component will be negligible everywhere except along the edges of the currents due to the fact that the magnetic perturbations from juxtaposed field-aligned currents will cancel.

The dotted line represents the model GSM Z-component, which is aligned radially along the magnetotail and is defined positive earthward. Z-component perturbations will be a result of the westward ring current, electrojet closure currents, and the field-aligned currents in the equatorial plane. Overall, the Z-component is positive due to the westward cross-tail/ring current (recall that our observation point is $+5^\circ$ above the equatorial plane). The slight decrease as one approaches the morning sector is due to the closure currents of the ionospheric electrojets. On the dusk side, the westward closure current increases the cross-tail/ring current. The slight positive rise at 270° is due to the downward field-aligned current associated with the leading edge of the westward electrojet, which has a greater current magnitude than the field-aligned current at the leading edge of the eastward electrojet. The Z-component steeply decreases into the morning sector due to the combined effects of the eastward closure current (which decreases the magnitude of the cross-tail/ring current) and the upward field-aligned current at its eastward edge.

The mapping of the closure currents for the post-onset case is shown in Figure 5.19. At this time, the cross-tail current will have been largely reduced along the inner edge of the plasma sheet and the region of dipolarization will be expanding radially and azimuthally outward, reflected in the ionosphere as the poleward motion of the H β emissions. All the major components of the current systems are the same as those for the preonset case; however now the closure current associated with the substorm westward electrojet has expanded into the pre-midnight sector. It should be noted at this time that polarization currents arising from rapidly varying electric fields (as would be present due to dipolarization of the magnetic field) have not been included in this model. What is presented in this chapter deals mainly with the large-scale ionospheric and Birkeland currents since they are the primary currents affecting the substorm current wedge;

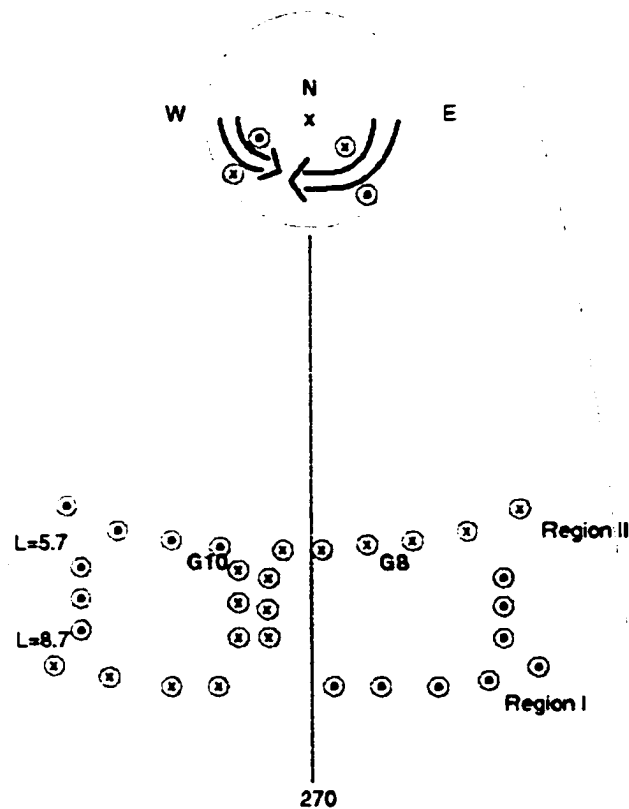


Figure 5.19: Schematic diagram of the closure currents of the post-onset current system. Symbols are the same as described in Figure 5.14.

secondary currents such as the polarization currents should be addressed by future generations of this model.

The expansion of the closure current into the evening sector reflects the formation of the substorm current wedge discussed earlier in Sections 5.2 and 5.3. As the ionospheric westward electrojet intensifies and expands into the pre-midnight sector, and the Region II upward field-aligned currents shift westward to form the current wedge, the closure currents in the equatorial plane reconfigure in a similar manner. The current magnitudes of the electrojet closure currents and the field-aligned currents have also been increased to simulate the expansive phase. Larger magnetic field magnitudes, therefore, can be expected. The magnetic perturbations (observed at $+5^\circ$ off the equatorial plane and at $L=$

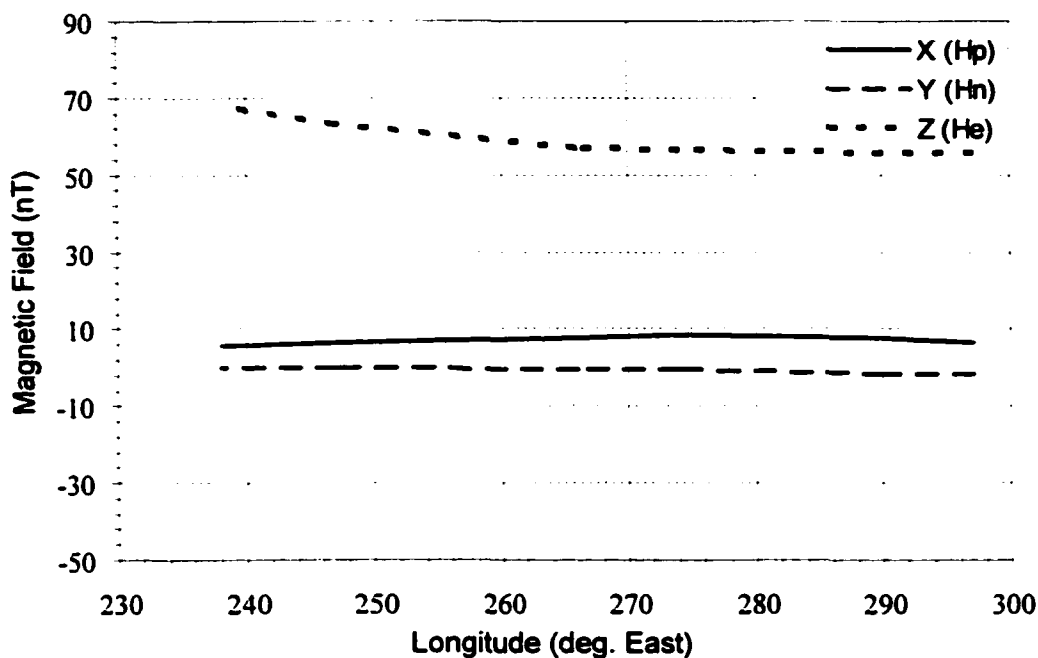


Figure 5.20: Magnetic signatures calculated from the model closure currents in Figure 5.19 and the westward crosstail/ring current. Observation point is 5° above the equatorial plane and at $L=7.7 R_E$.

$7.7 R_E$) due to the post-onset currents are shown in Figure 5.20. The X-component representing the magnetic perturbations perpendicular to the equatorial plane shows the effects of the extended eastward closure current on the westward cross-tail/ring current. The eastward closure current decreases the westward cross-tail/ring current producing a slightly larger vertical component in the morning sector toward midnight. The Y-component demonstrates a slightly more negative bias due to the increase of downward field-aligned current. Again, the magnitude of the perturbation is small due to the location of the observing stations. The Z-component shows the combined effects of the field-aligned currents and the extended eastward closure current. The overall magnitude remains positive, however the enhanced magnetic field of the eastward closure current decreases the magnetic field of the cross-tail/ring current throughout the morning sector. The magnetic field of the enhanced westward closure current adds to the field of the cross-tail/ring current producing the steeper positive field gradient in the evening sector.

Figure 5.21 illustrates the differential longitude profile produced by subtracting the preonset perturbations from the post-onset perturbations. This profile represents the

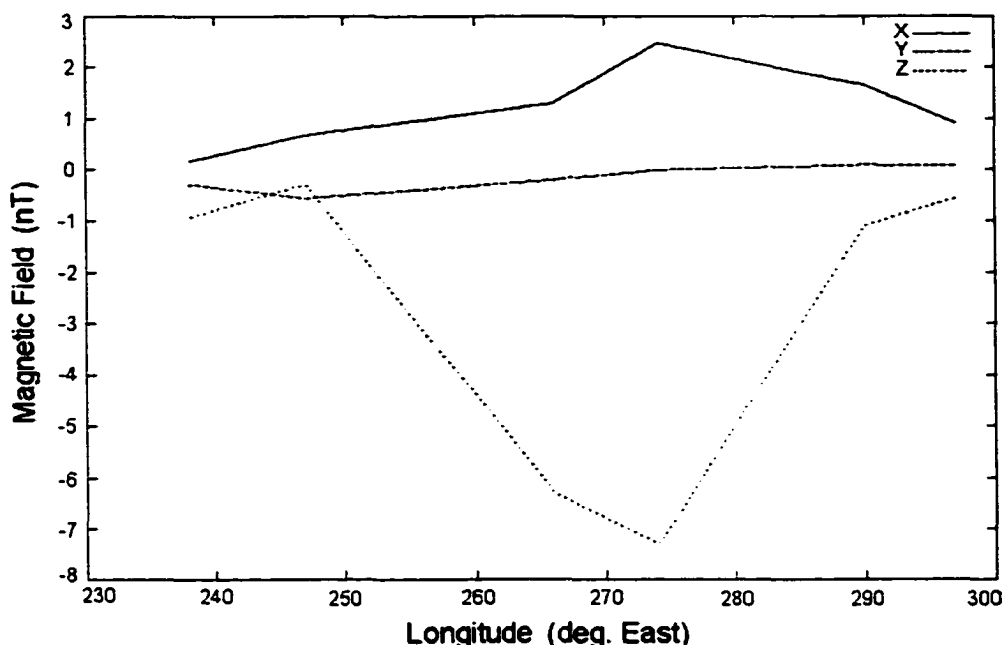


Figure 5.21: A differential longitude profile illustrating the magnetic signatures due to the substorm current wedge.

magnetic perturbations from a conjugate system of current wedge currents, which have been isolated from the background currents in the magnetotail. Figure 5.21 shows that the current system will produce a small positive perturbation perpendicular to the equatorial plane (X component), negligible perturbations in the azimuthal direction (Y component), and a large negative radial perturbation (Z component).

In order to compare the model results with observations from the GOES satellites, we searched for substorm events whose expansive phase onsets occurred within the latitudes of 65° and 70° , and near the Churchill line of magnetometers. These choices place the onset near the earthward edge of the plasma sheet and local midnight between the GOES 8 and GOES 10 satellites. The satellites are situated at 285°W and 225°W geographic longitude, respectively, so the location of onset is biased slightly toward the location of the GOES 8 satellite in order to observe the morning sector dynamics.

Our canonical event occurred on January 1, 1999 as a series of intensifications that began at ~ 0451 UT and continued until 0530 UT (Figure 5.22). For this study, we are primarily interested in the events surrounding the initial breakup at 0451 and the intensification that occurred at 0502 UT.

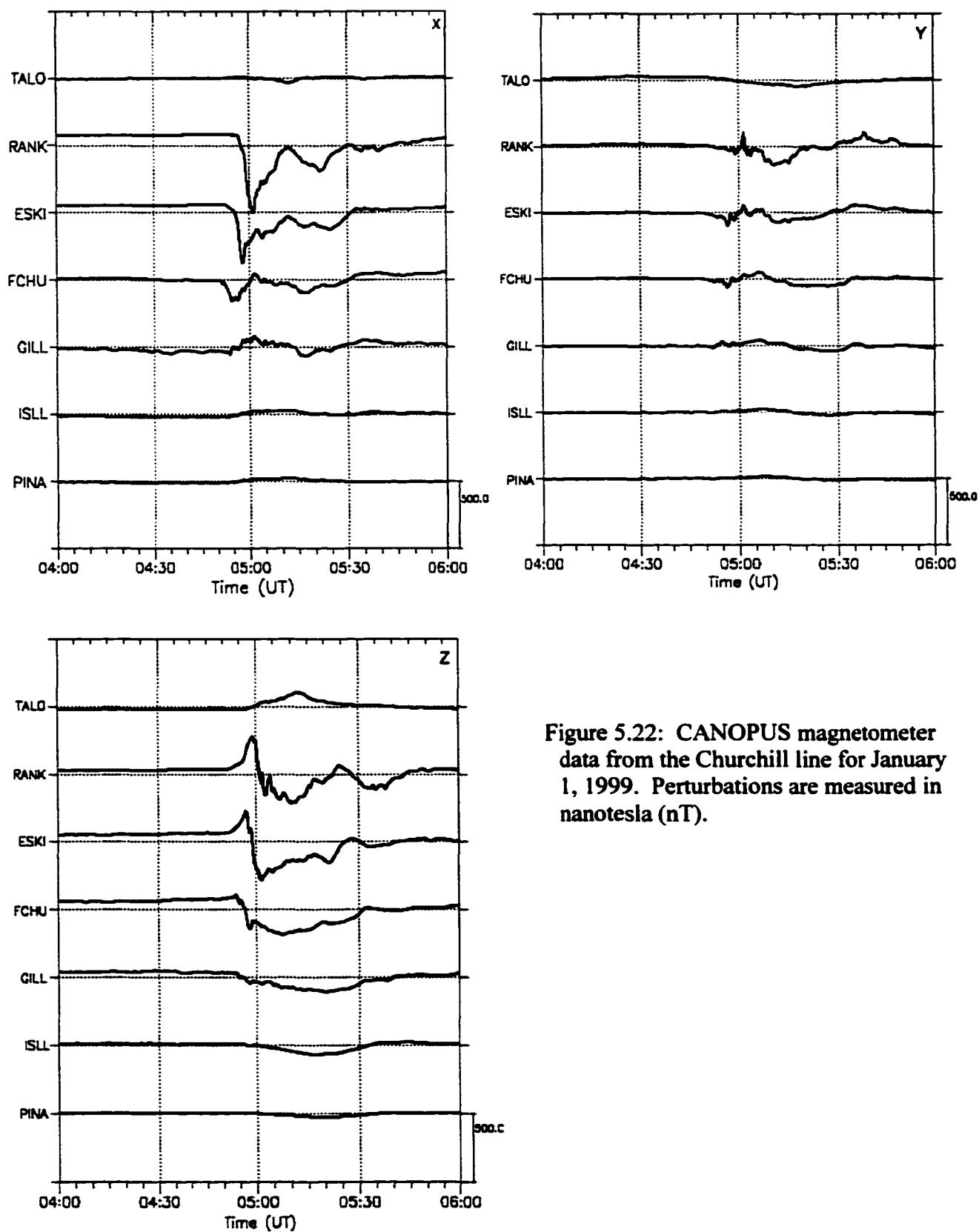


Figure 5.22: CANOPUS magnetometer data from the Churchill line for January 1, 1999. Perturbations are measured in nanotesla (nT).

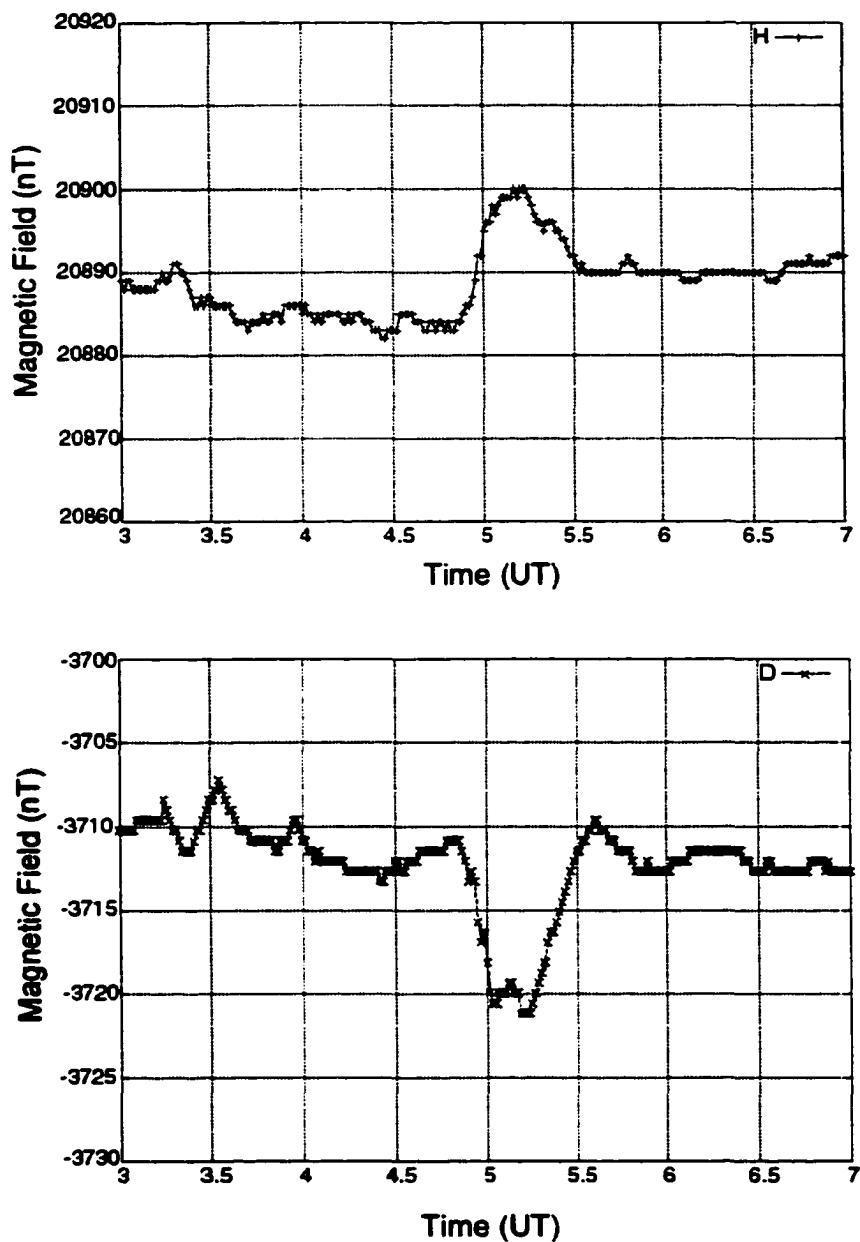


Figure 5.23: Magnetic H and D components from the station of Fredericksburg for January 1, 1999.

The first intensification at 0451 UT was a moderate-sized substorm (magnitude 550 nT) that began at FCHU and quickly moved poleward, reaching latitudes of 73° within ~ 5 minutes (note the magnetic Z-component was positive initially at FCHU and quickly became negative indicating that the currents associated with the breakup moved over that station to higher latitudes). The positive Z-component signatures at ESKI and RANK

indicate that the currents remained at latitudes between FCHU and ESKI for the duration of the intensification. The mid-latitude stations of Victoria (48.5°N , 237°E geographic), Meanook (54.6°N , 247°E geographic) and Ottawa (45.4°N , 285°E geographic) did not seem to observe any activity associated with the substorm current wedge. However the low-latitude stations of Fresno, Newport, Boulder, and Fredericksburg (FRED) did observe the activity. FRED (38°N , 283°E geographic) observed a slight positive northward (H) signature accompanied with a negative eastward (D) component (Figure 5.23). This indicates that it was located in the vicinity of the downward field-aligned current, along the eastern edge of the current wedge. Boulder (40°N , 255°E) observed a positive H component associated with a positive D component indicating that it was located within the wedge but on the western side of the central meridian (data not shown). In agreement with the location of this wedge, Fresno (37°N , 241°E) and Newport (48°N , 243°W) observed no H component signatures and positive D component signatures, placing these stations in the vicinity of the upward field-aligned current along the western edge of the wedge (Figure 5.24).

The intensification at 0502 UT was smaller in comparison ($\sim 100\text{ nT}$ magnitude at PDB) and was observed further west at Rabbit Lake (RABB), Fort McMurray (MCMU) and Fort Smith (FSMI) (Figure 5.25), indicating that a fairly large portion of the cross-tail current sheet was involved in substorm dynamics. Surge signatures were observed along the Churchill line at $\sim 0502\text{ UT}$. The stations RABB, MCMU, and FSMI observed signatures at 0458 UT, which are declining at 0502 but are still strong nonetheless. The mid and low latitude stations of Ottawa (Figure 5.26) and Fredericksburg, observed a negative eastward component associated with no northward signatures, indicating their proximity to the eastern edge of the wedge. The mid-latitude station Meanook observed a large positive eastward component and a small negative northward component, while the low latitude station Newport, observed a large positive eastward component with little or no component northward. These signatures indicate these stations proximity to the western edge of the current wedge.

Figures 5.27 and 5.28 show the magnetic field signatures observed by the GOES 8 and 10 satellites. Figure 5.27 is a differential plot of the magnetic signatures in GSM coordinates observed by GOES 8, which have been baselined to the start of the growth

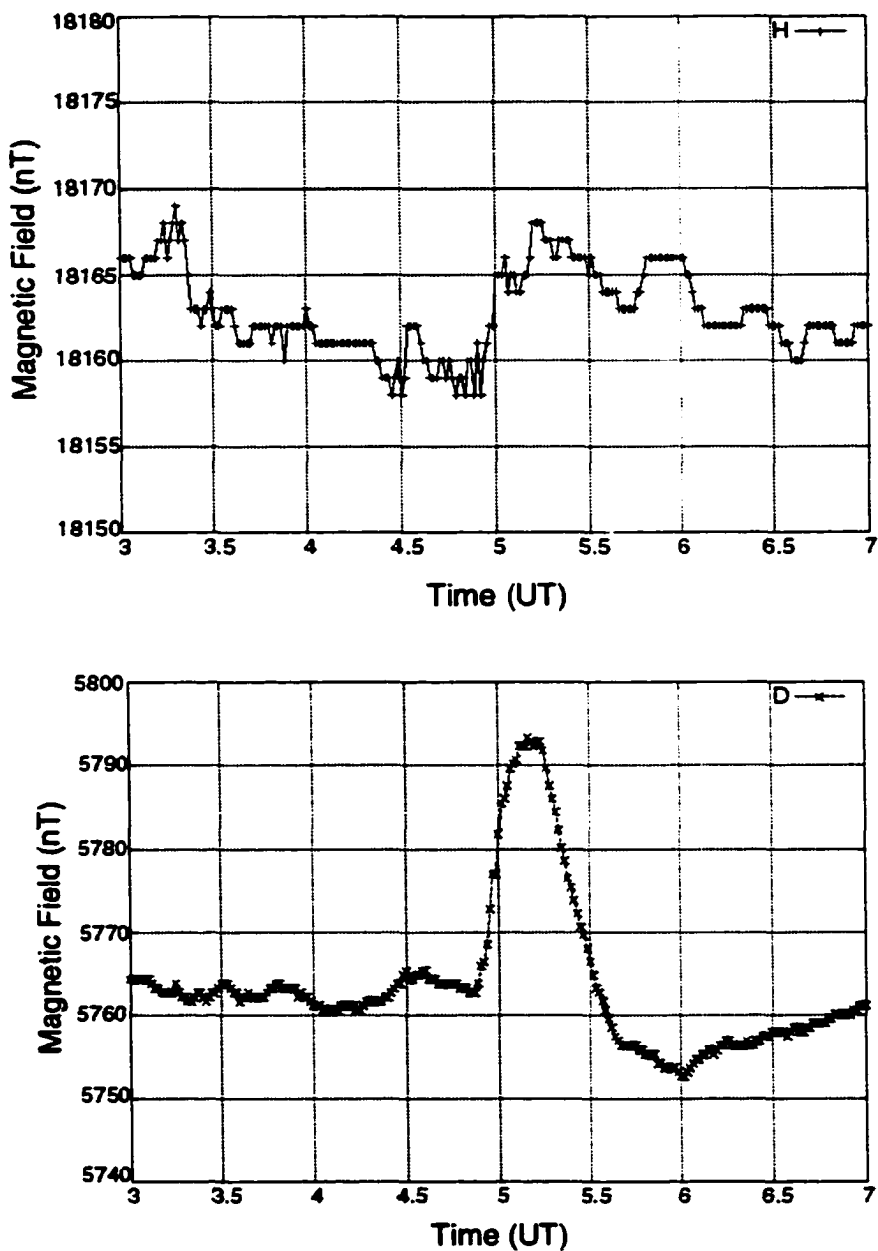


Figure 5.24: Magnetic H and D components from Newport station for January 1, 1999.

phase of the substorm. The GOES 8 satellite is situated along the meridian of Fredericksburg and Poste de la Baleine and therefore is in a good position to view the morning sector dynamics of the current wedge. Unfortunately, GSM data was unavailable for the GOES 10 satellite so we have provided magnetic signatures in

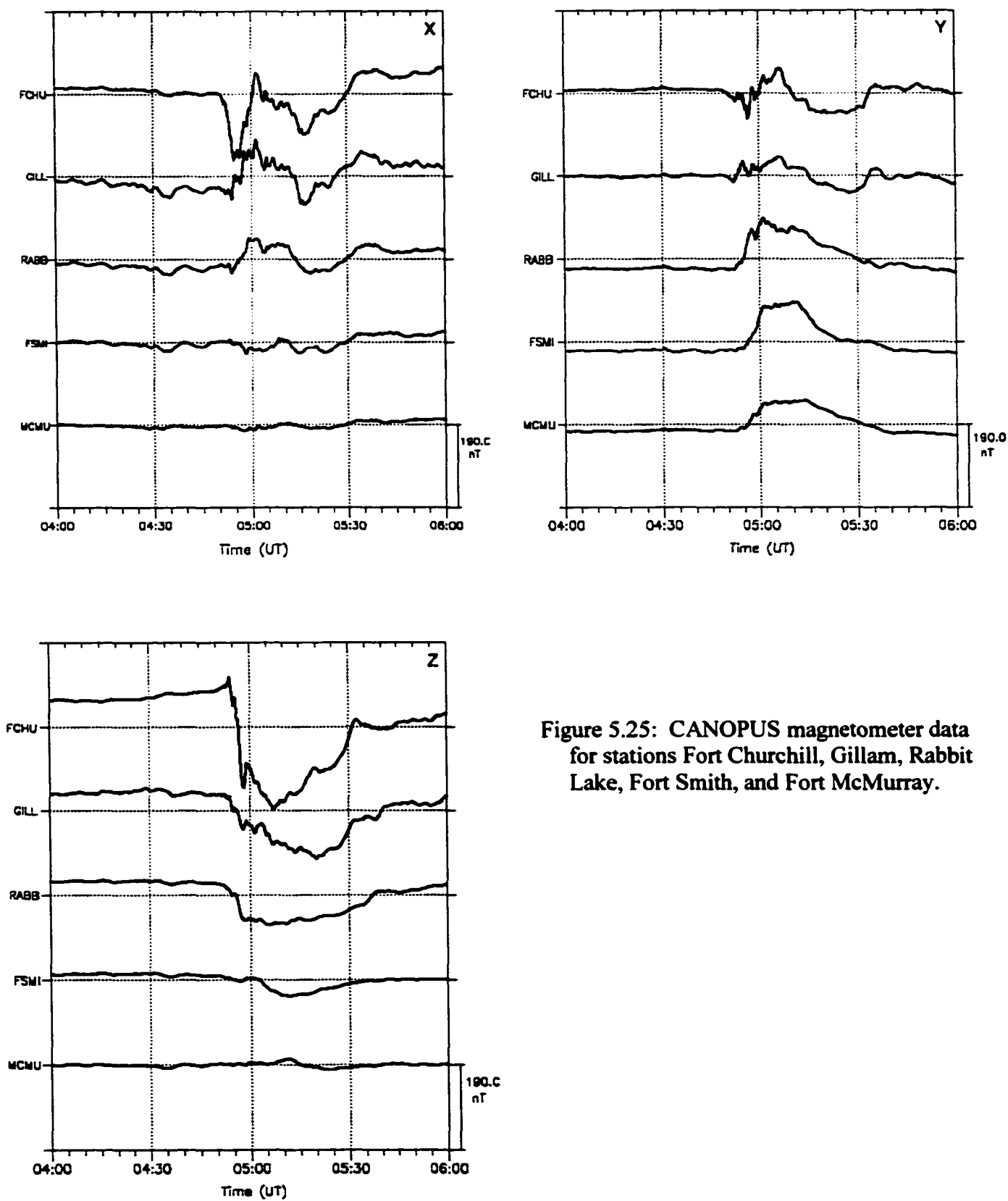


Figure 5.25: CANOPUS magnetometer data for stations Fort Churchill, Gillam, Rabbit Lake, Fort Smith, and Fort McMurray.

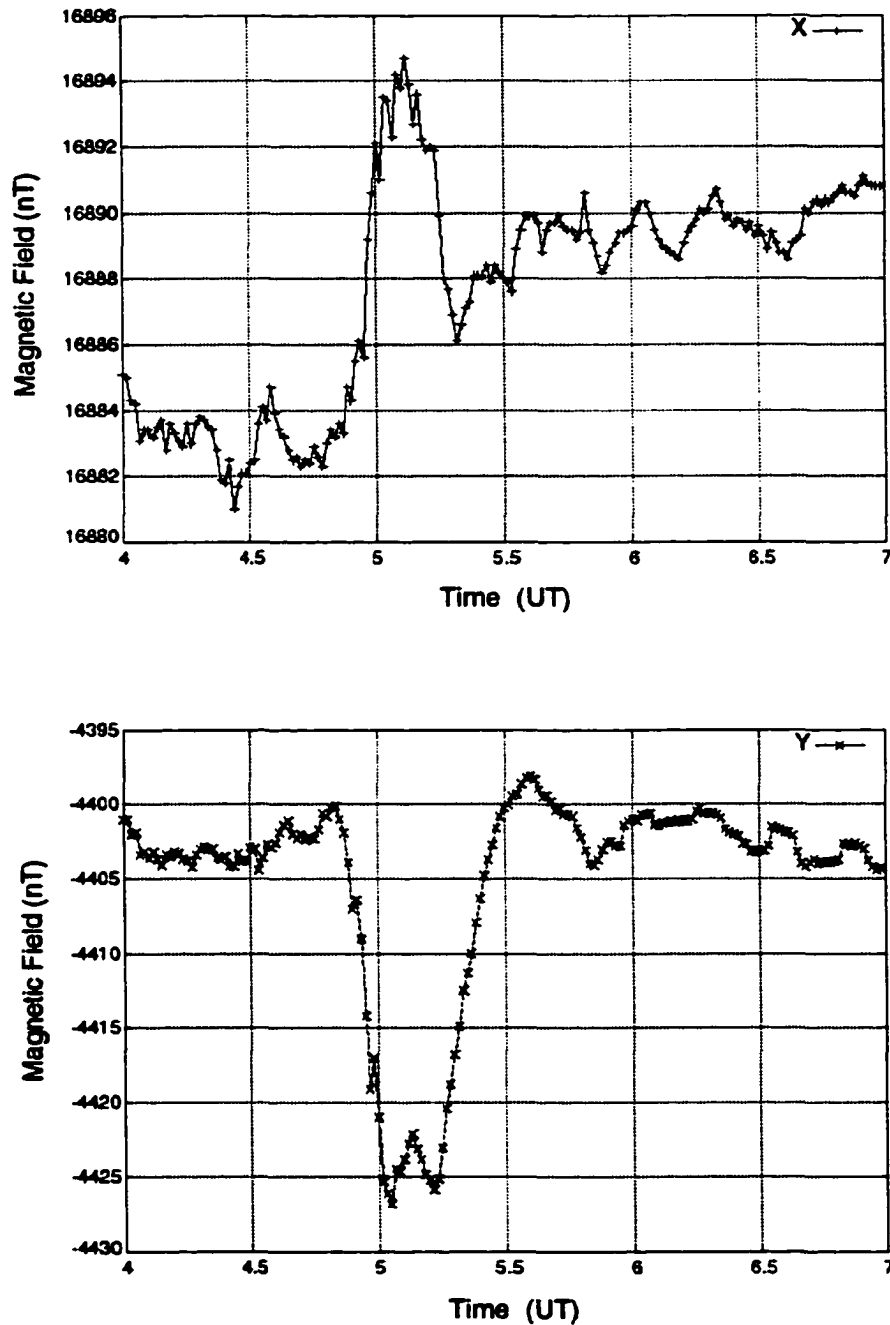


Figure 5.26: Magnetic signatures from the station of Ottawa showing current wedge signatures for the 0502 UT intensifications (courtesy of Larry Newitt at INTERMAGNET).

satellite coordinates to give the reader a sense of what GOES 10 observed during the substorm. The GOES 10 satellite is located along the meridian of the Sitka observing

station, which places it in close proximity to the western edge of the wedge and surge activity. It was somewhat surprising to note that neither satellite observed signatures of dipolarization at the time of the first intensification at 0451 UT. The UV imager data from POLAR (courtesy of G. Parks) provides some insight into this question as the substorm looks to have intensified locally between Rabbit Lake and Gillam and spread azimuthally eastward toward the GOES 8 meridian (Figure 5.29). In Figure 5.29 the Churchill line is situated at ~ 22 MLT and bisects the intensification seen in the 0454:48 UT image. If the onset began west of the Churchill line and expanded eastward, then a delay in observing the signatures at GOES 8 would be expected.

The X-component magnetometer data at PDB (Figure 5.30) and FCHU show further intensifications slightly before and slightly after 05 UT (0458 and ~ 0504 UT, respectively). These intensifications are also seen in the POLAR images. The magnetic signatures at GOES 8 show slight perturbations around 0458 UT that may be associated with dipolarization, although the magnetotail does not succeed in reconfiguring at this time. At 0502 UT there is a large negative perturbation in the B_y component and a large negative perturbation in the B_x component at ~ 0504 UT. The main signature of dipolarization is observed at ~ 0504 UT with a positive perturbation in the B_z component.

The GOES 10 data in satellite coordinates sees very little until ~ 0512 UT when the activity has reached the local times of FSIM. Even at this time the magnitude of the perturbation is small, indicating that GOES 10 is on the periphery of the western edge of the surge activity. The images at POLAR support this claim as the disturbance region is shown to expand to only 21 MLT. From the small ground-based signatures at Newport, it is also clear that GOES 10 is outside the current wedge, but it appears to be close to the western edge as the stations Sitka and Victoria observe positive D-components with small negative H-components and no Z-component signatures.

As mentioned earlier, the POLAR UV images show the auroral activity to expand eastward after onset at 0451 UT. The ground-based signatures at PDB, FCHU, and OTT all show clear intensifications at ~ 0504 UT. The GOES 8 satellite should be in a good position to observe current wedge formation. According to our model results, at expansive phase onset and a few minutes thereafter, the GOES 8 satellite (which is situated roughly between 280° and 290° East in Figure 5.21) should observe a negative

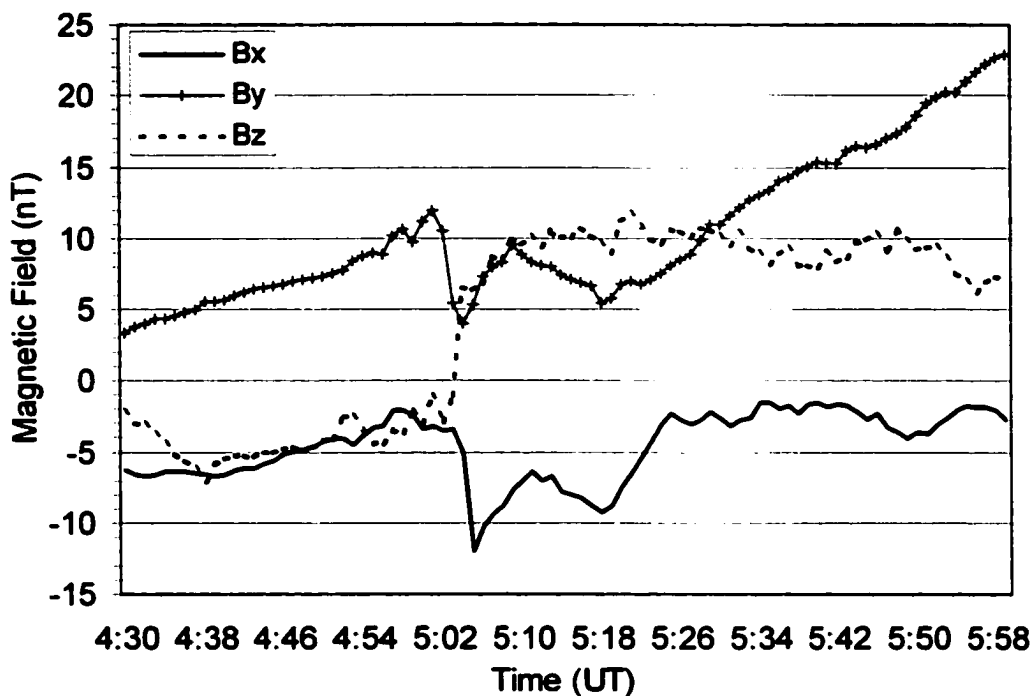


Figure 5.27: Magnetic signatures observed by the GOES 8 satellite for the event that occurred on January 1, 1999. Coordinates are GSM and the data has been baselined to the start of the growth phase (data courtesy of CDAWeb and Howard Singer).

radial component (~ -5.0), a negligible negative eastward component, and a positive vertical component (~ 2.0 nT) in the morning sector of the wedge. Taking magnetic field measurements five minutes before and after ground onset, the preonset values were subtracted from the post-onset values to produce a differential magnetic field at the position of GOES 8. The results showed a negative radial component of -7.05 nT, a small negative eastward component of -1.55 nT, and a positive vertical component of 11.19 nT. With the exception of the large positive vertical component, the model results shown in Figure 5.21 agree quite well with the observations reported by the GOES 8 satellite. It is possible that the large vertical component is due to the dipolarization of stretched field lines, which our model lacks. Similarly, the GOES 10 satellite, situated between 240° and 250° East, showed a differential field of -1.2 nT (radial), 0.5 nT eastward, and $+1.1$ nT (vertical). This agrees fairly well with the model results, which predict the satellite to see a small (~ -0.5 nT) negative radial component, a negligible

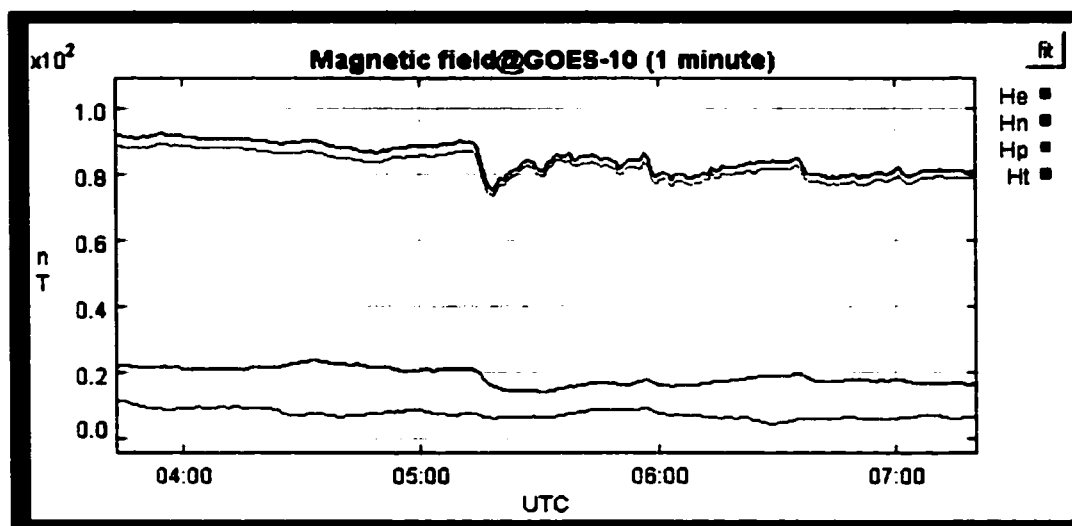


Figure 5.28: Magnetic signatures observed by the GOES 10 satellite. Data are featured here in satellite coordinates (data courtesy of the Space Physics Interactive Data Resource).

eastward component, and a small (~ 0.5 nT) positive vertical component. These results should be taken with caution however, since the data has not been rotated into GSM coordinates.

5.4 Discussion and Conclusions

In this chapter an alternative method for the creation of the substorm current wedge has been proposed that is based on real, rather than equivalent, currents in the magnetosphere-ionosphere system. This new model provides a physical framework in which to create the current wedge that naturally provides the longitudinally extended downward field-aligned current that is not produced in the presently accepted current wedge model. The new model involves the reconfiguration of the ionospheric conductivity and electric fields at midnight to produce a Cowling channel and a shift in the morning sector Region II field-aligned currents. The shift of the Region II currents effectively opens the preonset solenoidal current configuration, exposing the Region I downward field-aligned current. The Cowling channel produces an intense westward electrojet, allowing it to intrude into the evening sector of the auroral oval. In essence, this is the substorm current wedge complete with downward field-aligned current,

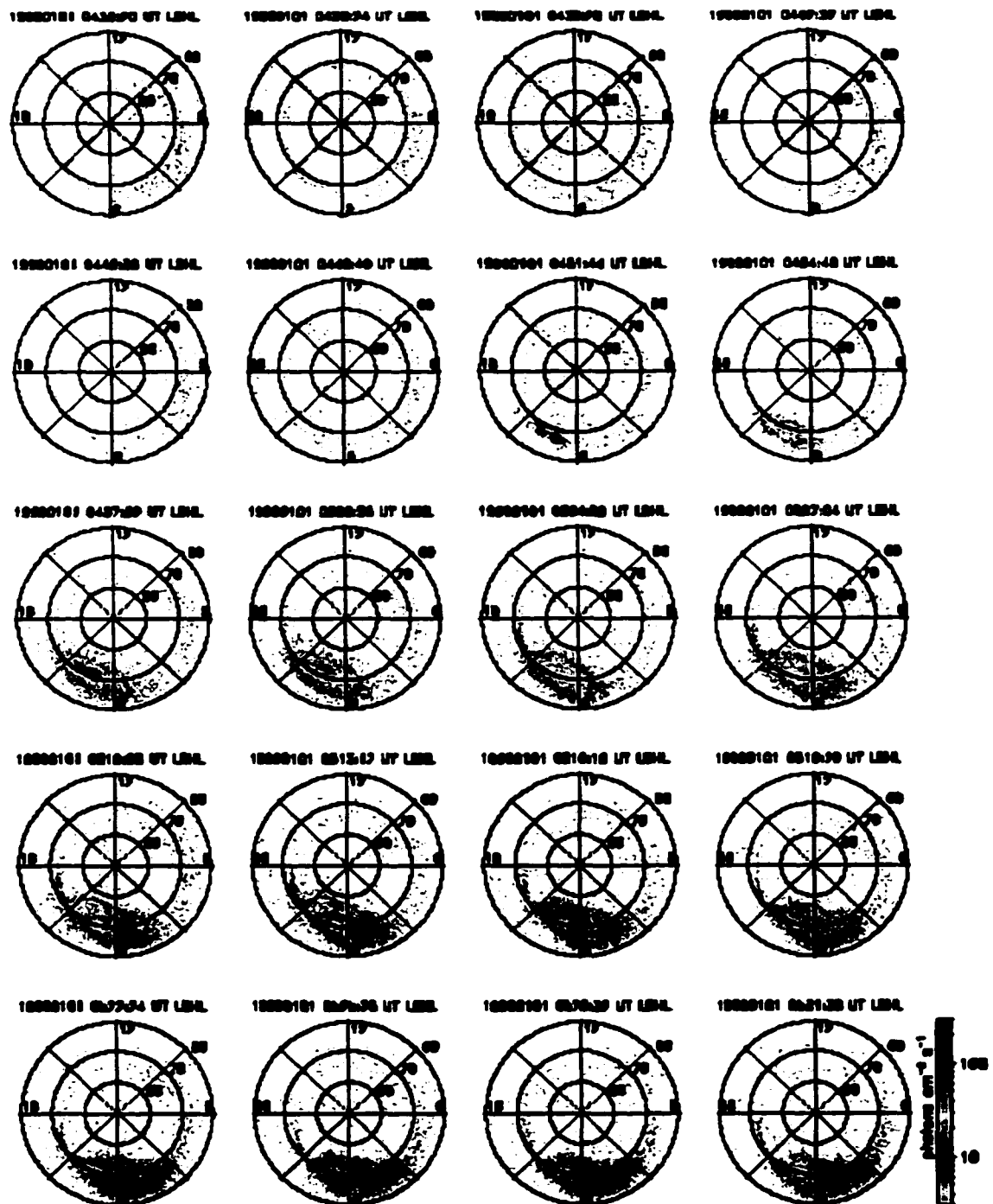


Figure 5.29: POLAR UV images for January 1, 1999 (data courtesy George Parks).

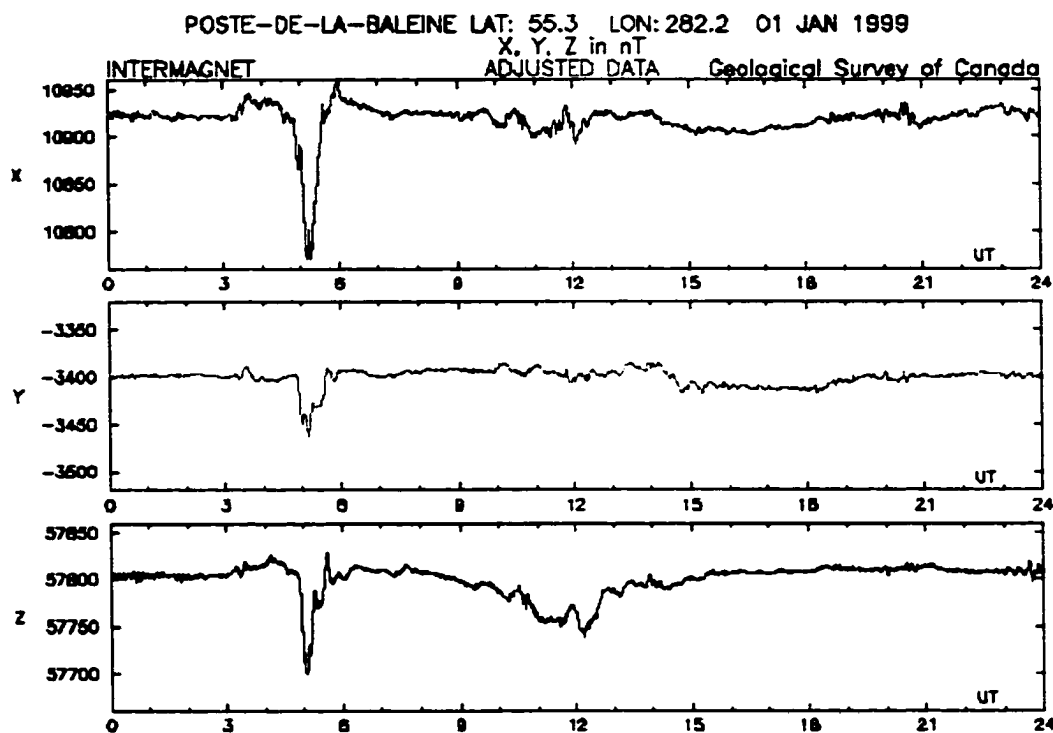


Figure 5.30: Magnetic signatures observed by the station Poste-de-la-Baleine (data courtesy of Larry Newitt at INTERMAGNET).

upward field-aligned current and an intense westward electrojet. A localized region of pressure gradient near the midnight meridian along the earthward edge of the central plasma sheet will provide the source region for the intense upward field-aligned current of the auroral surge. The end result is a magnetic signature of a substorm current wedge that is almost indistinguishable from the magnetic signature of the model by *Clauer and McPherron* [1974].

In the previous chapter it was shown that the beginning of the expansive phase is explosive with timescales of magnetospheric activity of tens of seconds to approximately two minutes. Since the substorm current wedge occurs during the expansive phase of the substorm, it is interesting to consider whether the directly-driven system can reconfigure itself to form the current wedge along these same timescales.

The timescales for such a reconfiguration to take place are expected to be at least of the order of tens of seconds although no quantitative analysis has been done here to confirm this estimate. The timing would depend on a variety of factors. For example, it is not known how quickly the shielding electric field would decrease in magnitude

following the reduction of the cross-tail current, but it is speculated that the 'cause and effect' between the cross-tail current and the shielding electric field would be almost immediate since largely reducing J_{\perp} would largely reduce the magnitude of the second term in Equation 5.1. Secondly, the speed at which the Cowling channel can be created is not known (although the Cowling channel is dependent on the appearance of the convection electric field at auroral latitudes in the ionosphere, and the convection electric field is thought to appear immediately after the reduction of the shielding electric field). Finally, how quickly the conductivity can enhance in a new region northwestward of the previous surge activity (thereby creating gradients in the conductivity) is also speculative. One can postulate a timescale based on observed speeds of surge activity within the intensification region in the ionosphere. Surges have been observed to travel at speeds of 100 km/s within a small region (~ 500 km), giving a travel time of 5 seconds. Thus, qualitatively it is expected that the reconfiguration of the directly-driven current system can be accomplished in quite short timescales, which is consistent with the results of the previous chapter.

With respect to the magnetospheric dynamics, *Shiokawa et al.* [1997,1998], as part of the flow braking model, emphasized the role of the pressure gradient in the midnight sector produced by the slowdown of earthward plasma flow. A radial pressure gradient is associated with reduction of the cross-tail current and dipolarization of the magnetic field and is the initial driver of the upward field-aligned current of the current wedge, while an azimuthal pressure gradient is responsible for maintaining the substorm current system after the high-speed ion flow stops.

From the point of view of computer simulations, *Birn et al.* [1999] have noted that the standard representation of the current wedge as a single current loop represents a simplification that does not account for all of the major field changes. These authors have found that the direct effects of the flow braking via the inertial currents of *Haerendel* [1992] last only as long as the flow burst, approximately a few minutes. In their models however, the effects of the field distortion and the associated pressure gradient changes last longer, leading *Birn et al.* [1999] to assert that the dominant and more permanent contribution to the current wedge stems from the pressure gradients.

In a very detailed examination of observations taken during the growth and expansive phases of the substorm (both auroral and magnetospheric), *Lyons* [1995] proposed a new theory for magnetospheric substorms based on the reduction of the interplanetary large-scale electric field as an external trigger. His model attributes the creation of field-aligned current for the substorm current wedge to gradients in the pressure and flux tube volumes in the central plasma sheet. In particular, a spatial separation near midnight of westward drifting ions produces an azimuthal pressure gradient and variations in proton thermal energy. However, in contrast with the substorm current wedge model presented in this thesis, *Lyons* [1995] proposes that a local minimum in the pressure near midnight (as opposed to a local maximum which is proposed here) will lead to the formation of the field-aligned currents of the current wedge (see Figure 5 of *Lyons* [1995]). Nevertheless, using ideal MHD arguments, *Lyons* [1995] has determined that the time to develop a significant azimuthal gradient from westward drifting ions is roughly four minutes, much shorter than the time it takes growth phase currents to develop. In addition to the pressure gradient arguments, *Lyons* [1995] also reports on the interaction of a significant southward-directed electric field with a westward electric field within the poleward propagating region of active aurora. These electric fields are necessary to maintain current continuity simultaneously in the ionosphere and magnetosphere.

In keeping with the opinion that the directly-driven current system has a more prominent role in substorm dynamics, the renovated Boundary Layer Dynamic (BLDM) [*Rostoker*, 1996] model benefits largely from this new current wedge model. The impetus for development of the BLD model [*Rostoker and Eastman*, 1987] was to address the physics of the directly-driven current system, something that was lacking in the leading substorm model (the NENL model [*Hones*, 1976]) at that time. In its original form, the BLD model provided an explanation for both the directly-driven and storage-release aspects of the substorm. The substorm current wedge was viewed as a perturbation of the directly-driven system as a result of a plasma instability on field lines that mapped out to the LLBL/CPS interface [*de Groot-Hedlin and Rostoker*, 1987]. However, as was discussed in the previous chapter, the seminal work of *Samson* [1992] convinced the scientific community that the location of expansive phase onset was in fact along the inner edge of the central plasma sheet, between 6 and 10 R_E . The BLD model

was revised at this time to account for the new locale of expansive phase onset; however, the plasma instability, which was described as a Kelvin-Helmholtz instability in regions approximately 100 RE downtail [*de Groot-Hedlin and Rostoker, 1987*], was no longer available to produce the substorm current wedge. The current wedge model described in this chapter again uses solely the directly-driven system of currents, but has its locale in the near-Earth magnetosphere between 6 – 10 R_E .

This new model of the substorm current wedge follows naturally from the large role played by the directly-driven system during the growth phase. Since the mechanism for diverting the cross-tail current into the ionosphere is still largely debated, and quite complex from a physical perspective, it leads one to consider whether another physical method for producing the current wedge is possible. Using the directly-driven system to create the substorm current wedge has three distinct advantages: first, the directly-driven system is always present before, during, and after substorms, and reacts to changes in energy in the magnetosphere; second, compared to the physics needed to divert a portion of the cross-tail current and create new field-aligned currents, the physics for this model is simpler; and third, using the directly-driven system produces the longitudinally extended downward field-aligned current that is observed, but not apparent in the presently accepted model. The magnetic perturbation patterns from the wedge model of *McPherron et al. [1973]* and the model presented in this chapter are almost indistinguishable, proving that the substorm current wedge can be produced purely from a reconfiguration of the preexisting directly-driven currents near midnight.

Bibliography

Akasofu, S.-I. and S. Chapman, *Solar Terrestrial Physics*, Oxford University Press, London, 1972.

Akasofu, S.-I. and C.-I. Meng, A study of polar magnetic substorms, *J. Geophys. Res.*, 74, 293, 1969.

Atkinson, G., An approximate flow equation for geomagnetic flux tubes and its application to polar substorms, *J. Geophys. Res.*, 72, 5373, 1967.

Baker, D.N., Reexamination of driven and unloading aspects of magnetospheric substorms, *J. Geophys. Res.*, 102, 7169, 1997.

Baumjohann, W., R.J. Pellinen, H.F. Opgenoorth, and E. Nielsen, Joint two-dimensional observations of ground magnetic and ionospheric electric fields associated with auroral zone currents: Current systems associated with local auroral break-ups, *Planet. Space Sci.*, 29, 431, 1981.

Birn, J., M. Hesse, G. Haerendel, W. Baumjohann, and K. Shiokawa, Flow braking and the substorm current wedge, *J. Geophys. Res.*, 104, 19895, 1999.

Brekke, A., J.R. Doupnik, and P.M. Banks, Incoherent scatter measurements of E region conductivities and currents in the auroral zone, *J. Geophys. Res.*, 79, 3773, 1974.

Clauer, C.R. and R.L. McPherron, Mapping the local time-universal time development of magnetospheric substorms using midlatitude magnetic observations, *J. Geophys. Res.*, 79, 2811, 1974.

Coroniti, F.V., and C.F. Kennel, Polarization of the auroral electrojet, *J. Geophys. Res.*, 77, 2835, 1972.

De Groot-Hedlin, C.D. and G. Rostoker, Magnetic signatures of precursors to substorm expansive phase onset, *J. Geophys. Res.*, 92, 5845, 1987.

Goertz, C.K., L.H. Shan, and R.A. Smith, Prediction of geomagnetic activity, *J. Geophys. Res.*, 98, 7673, 1993.

Haerendel, G., Disruption, ballooning or auroral avalanche: On the cause of substorms, in *Proc. of the International Conference on Substorms (ICS-1)*, Eur. Space Agency Spec. Publ., SP-335, 417, 1992.

Hasegawa, A. and T. Sato, Generation of field-aligned current during substorms, in *Dynamics of the Magnetosphere*, ed. S. -I. Akasofu, D. Reidel Publishing, New York, p. 529, 1979.

- Hones, E.W., Jr., The magnetotail: Its generation and dissipation, in *Physics of solar Planetary Environments*, edited by D.J. Williams, p. 558, AGU, Washington, D.C., 1976.
- Hughes, T.J. and G. Rostoker, Current flow in the magnetosphere and ionosphere during periods of moderate activity, *J. Geophys. Res.*, *82*, 2271, 1977.
- Inhester, B., W. Baumjohann, R.A. Greenwald, and E. Nielson, Joint two-dimensional observations of ground magnetic and ionospheric electric fields associated with auroral zone currents 3, Auroral zone currents during the passage of a westward traveling surge, *J. Geophys. Res.*, *49*, 155, 1981.
- Kamide, Y., and N. Fukushima, Positive geomagnetic bays in evening high latitudes and their possible connection with partial ring current, *Rep. Ionos. Res. Space Res. Jap.*, *26*, 79, 1972.
- Kamide, Y., and J. F. Vickrey, Relative contribution of ionospheric conductivity and electric field to the auroral electrojets, *J. Geophys. Res.*, *88*, 7989, 1983.
- Kan, J.R., L. Zhu, and S.-I. Akasofu, A theory of substorms: Onset and subsidence, *J. Geophys. Res.*, *93*, 17, 263, 1993.
- Kan, J. R., Generation of field-aligned currents in magnetosphere-ionosphere coupling in an MHD plasma, *Planet. Space Sci.*, *35*, (7), p. 903, 1987.
- Kaufmann, R.L., Substorm currents: growth phase and onset, *J. Geophys. Res.*, *92*, 7471, 1987.
- Kawasaki, K, and G. Rostoker, Perturbation magnetic fields and current systems associated with eastward drifting auroral structures, *J. Geophys. Res.*, *84*, 1464, 1979.
- Kisabeth, J.L., and G. Rostoker, Development of the polar electrojet during polar magnetic substorms, *J. Geophys. Res.*, *76*, 6815, 1971.
- Kisabeth, J.L., and G. Rostoker, Modeling of three-dimensional current systems associated with magnetospheric substorms, *Geophys. J. R. Astron. Soc.*, *49*, 655, 1977.
- Kistler, L.M., E. Möbius, W. Baumjohann, G. Paschmann, and D.C. Hamilton, Pressure changes in the plasma sheet during substorm injections, *J. Geophys. Res.*, *97*, 2973, 1992.
- Korth, H., M. Thomsen, J. Borovsky, and D.J. McComas, Plasma sheet access to geosynchronous orbit, *J. Geophys. Res.*, *104*, 25,047, 1999.

- Lester, M., J.A. Davies, and T.S. Virdi, High-latitude Hall and Pedersen conductances during substorm activity in the SUNDIAL-ATLAS campaign, *J. Geophys. Res.*, *101*, 26719, 1996.
- Lewis, R.V., M.P. Freeman, A.S. Rodger, G.D. Reeves, D.K. Milling, The electric field response to the growth phase and expansion phase onset of a small isolated substorm, *Ann. Geophysicae* *15*, 289, 1997.
- Liu, W.W., and G. Rostoker, Effects of dawn-dusk pressure asymmetry on convection in the central plasma sheet, *J. Geophys. Res.*, *96*, 11501, 1991.
- Lui, A.T.Y., A synthesis of magnetospheric substorm models, *J. Geophys. Res.*, *96*, 1849, 1991.
- Lui, A.T.Y., Mechanisms for the substorm current wedge, *Proceedings of the Second International Conference on Substorms*, p. 195, Univ. of Alaska, Fairbanks, 1994.
- Lui, A.T.Y., Current disruption in the Earth's magnetosphere: Observations and models, *J. Geophys. Res.*, *101*, 13067, 1996.
- Lui, A.T.Y., Plasma sheet behavior associated with auroral breakups, in *SUBSTORM-4, International Conference on Substorms-4, Lake Hamana, Japan: March 9-13, 1998*, p. 183, Terra Sci., Tokyo, 1998.
- Lui, A.T.Y., C.-L. Chang, A. Mankofsky, H.-K. Wond, and D. Winske, A cross-field current instability for substorm expansions, *J. Geophys. Res.*, *96*, 11389, 1991.
- Lui, A.T.Y., P.H. Yoon, and C.-L. Chang, Quasi-linear analysis of ion Weibel instability in the Earth's neutral sheet, *J. Geophys. Res.*, *98*, 153, 1993.
- Lyons, L. R., A new theory for magnetospheric substorms, *J. Geophys. Res.*, *100*, 19069, 1995.
- McPherron, R.L., C.T. Russell, and M.P. Aubry, Satellite studies of magnetospheric substorms on August 15, 1968 9. Phenomenological model for substorms, *J. Geophys. Res.*, *78*, 3131, 1973.
- Mozer, F.S., and P. Lucht, The average auroral zone electric field, *J. Geophys. Res.*, *79*, 1001, 1974.
- Mozer, F.S. and R. Serlin, Magnetospheric electric field measurements with balloons, *J. Geophys. Res.*, *74*, 4739.
- Nagai, T., An empirical model of substorm-related magnetic field variations at synchronous orbit, in *Magnetospheric Substorms*, eds. J. Kan, T.A. Potemra, S.

- Kokubun, and T. Iijima, *Geophys. Monograph 64*, AGU, Washington, D.C., pp. 91-95, 1991.
- Ohtani, S., K. Takahashi, L.J. Zanetti, T.A. Potemra, R.W. McEntire, and T. Iijima, Initial signatures of magnetic field and energetic particle fluxes at tail reconfiguration: Explosive growth phase, *J. Geophys. Res.*, *97*, 19311, 1992.
- Opgenoorth, H.J., R.J. Pellinen, W. Baumjohann, E. Nielsen, G. Marklund, and L. Eliasson, Three-dimensional current flow and particle precipitation in a westward traveling surge (Observed during the Barium-GOES rocket experiment), *J. Geophys. Res.*, *88*, 3138, 1983.
- Opgenoorth, H.J., M.A.L. Persson, T.I. Pulkkinen, and R.J. Pellinen, Recovery phase of magnetospheric substorms and its association with morning-sector aurora, *J. Geophys. Res.*, *99*, 4115, 1994.
- Parks, G. K., *Physics of Space Plasmas: An Introduction*, Addison-Wesley Publishing, New York, © 1991.
- Paterson, W.R. and L.A. Frank, Survey of plasma parameters in Earth's distant magnetotail with the Geotail spacecraft, *Geophys. Res. Lett.*, *21*, 2971, 1994.
- Robinson, R.M., F. Rich, and R.R. Vondrak, Chatanika radar and S3-2 measurements of auroral zone electrodynamics in the midnight sector, *J. Geophys. Res.*, *90*, 8487, 1985.
- Rostoker, G., Current flow in the magnetosphere during magnetospheric substorms, *J. Geophys. Res.*, *79*, 1994, 1974.
- Rostoker, G., A renovated boundary layer dynamics model for magnetospheric substorms, in *Proceedings of the Second International Conference on Substorms*, eds. J.R. Kan, J.D. Craven and S.-I. Akasofu, Fairbanks, Alaska, USA, p. 189, 1994.
- Rostoker, G., Phenomenology and physics of magnetospheric substorms, *J. Geophys. Res.*, *101*, 12955, 1996.
- Rostoker, G., On the place of the pseudo-breakup in a magnetospheric substorm, *Geophys. Res. Lett.*, *25*, 217, 1998.
- Rostoker, G. and T. Eastman, A boundary layer model for magnetospheric substorms, *J. Geophys. Res.*, *92*, 12187, 1987.
- Rostoker, G., J.C. Armstrong, and A.J. Zmuda, Field-aligned current flow associated with intrusion of the substorm-intensified westward electrojet into the evening sector, *J. Geophys. Res.*, *80*, 3571, 1975.

- Rostoker, G., S. -I. Akasofu, W. Baumjohann, Y. Kamide, and R. L. McPherron, The roles of direct input of energy from the solar wind and unloading of stored magnetotail energy in driving magnetospheric substorms, *Space Sci. Rev.*, *46*, 93, 1987.
- Rothwell, P.L., L.P. Block, M.B. Silevitch, C.-G. Falthammar, A new model for substorm onsets: The pre-breakup and triggering regimes, *Geophys. Res. Lett.*, *15*, 1279, 1988.
- Roux, A., S. Perraut, P. Robert, A. Morane, A. Pedersen, A. Korth, G. Kremser, B. Aparicio, D. Rodgers, and R. Pellinen, Plasma sheet instability related to the westward traveling surge, *J. Geophys. Res.*, *96*, 17697, 1991.
- Samson, J.C., L.R. Lyons, P.T. Newell, F. Creutzberg, and B. Xu, Proton aurora and substorm intensifications, *J. Geophys. Res.*, *97*, 8495, 1992.
- Shiokawa, K., G. Haerendel, W. Baumjohann, Azimuthal pressure gradient as a driving force of substorm currents, *Geophys. Res. Lett.*, *25*, 959, 1998.
- Shiokawa, K., W. Baumjohann, and G. Haerendel, Braking of high-speed flows in the near-Earth tail, *Geophys. Res. Lett.*, *24*, 1179, 1997.
- Spence, H.E., M.G. Kivelson, and R.J. Walker, Magnetospheric plasma pressures in the midnight meridian: Observations from 2.5 to 35 RE, *J. Geophys. Res.*, *94*, 5264, 1989.
- Untiedt, J. and W. Baumjohann, Studies of polar current systems using the IMS Scandinavian magnetometer array, *Space Sci. Rev.*, *63*, 247, 1993.
- Vasyliunas, V. M., Fundamentals of current description, in *Magnetospheric Currents*, ed. T. A. Potemra, Geophys. Monograph 28, AGU, Washington, D.C., p. 63, 1984.
- Voronkov, I., E. Friedrich, and J.C. Samson, Dynamics of the substorm growth phase as observed using CANOPUS and SuperDARN instruments, *J. Geophys. Res.*, *104*, 28491, 1999.
- Voronkov, I., E.F. Donovan, B.J. Jackal, and J.C. Samson, Large scale vortex dynamics in the evening and midnight auroral zone: Observations and simulations, *J. Geophys. Res.*, *105*, 18505, 2000.
- Wallis, D. D. and E. E. Budzinski, Empirical models of height integrated conductivities, *J. Geophys. Res.*, *86*, 125, 1981.
- Weimer, D.R., J.D. Craven, L.A. Frank, W.B. Hanson, N.C. Maynard, R.A. Hoffman, and J.A. Slavin, Satellite measurements through the center of a substorm surge, *J. Geophys. Res.*, *99*, 23639, 1994.

Wiens, R. G. and G. Rostoker, Characteristics of the development of the westward electrojet during the expansive phase of magnetospheric substorms, *J. Geophys. Res.*, *80*, 2109, 1975.

Wing, S., and P.T. Newell, Central plasma sheet ion properties as inferred from ionospheric observations, *J. Geophys. Res.*, *103*, 6785, 1998.

Chapter 6: Conclusions and Future Work

This thesis has presented a detailed look into the dynamics of the substorm expansive phase using the instruments from the CANOPUS ground-based array. Two main aspects of the expansive phase were studied: the temporal dynamics of expansive phase onset, and the substorm current wedge.

Analysis of the CANOPUS meridian scanning photometer data was completed using a new technique of fitting the auroral emissions to a Gaussian distribution. It was found that a Gaussian profile fit the data extremely well during the growth phase of the substorm due to the definite peak of the emissions at auroral latitudes against the lower intensity background. During the expansive phase the Gaussian technique continued to fit the 486.1 nm emissions, but it was found that for some events the 557.7 nm and 630.0 nm emissions needed a step function to fit ~ 1% - 20% of the data cross-sections (depending on the event) in order to determine the emission borders. When determining the equatorward borders of the emissions, the Gaussian technique was always used.

Based on analysis of the MSP data set, this thesis has provided the following observational constraints:

- The expansive phase is a rapid duration of dipolarization involving three stages: explosive onset (10s of seconds), rapid poleward expansion of 557.7 nm emissions (2 - 3 minutes), and subsequent slower poleward expansion (tens of minutes) of 630.0 nm emissions.
- The expansive phase begins close to the Earth (~ 6-10 R_E), within the proton aurora region, with the plasma sheet boundary layers and magnetotail lobes becoming active approximately two to three minutes later.
- The instability causing onset expands rapidly downtail, perhaps energizing plasma sheet electrons.
- The instability creates favourable conditions for, or initiates, lobe flux reconnection.

These observations place serious constraints on substorm models as the timescales are very rapid and the sequence of events, from inner plasma sheet tailward, are consistently

defined. A few of the more debated substorm models are the near-Earth Current Disruption (NECD) model, the near-Earth Neutral Line (NENL) model, the Boundary Layer Dynamics model (BLDM), the Electric Field model, and the Flow Braking model. Using the constraints above, it is possible to look at the pros and cons of these models to better understand which one(s) accurately describe the substorm. Table 6.1 summarizes some of the main aspects of each model as they pertain to the results found in this thesis (EP = Expansive Phase):

Table 6.1: Pros and Cons of Substorm Models based on Observational Constraints

Substorm Model	Pros	Cons
NECD	<ul style="list-style-type: none"> - has B field fluctuation on timescales of minutes - begins EP onset near Earth, $\sim 6-7 R_E$ - EP onset precedes lobe flux reconnection - dipolarization (current disruption) can expand rapidly downtail - instability may lead to reconnection 	<ul style="list-style-type: none"> - tailward expansion speeds of current disruption are much slower than suggested in this thesis
BLDM	<ul style="list-style-type: none"> - begins EP onset near Earth along earthward edge of plasma sheet - EP onset occurs prior to lobe field line reconnection - plasma wave travels downtail to site of reconnection - plasma wave may enhance reconnection 	<ul style="list-style-type: none"> - timescales of expansion downtail (7-24 minutes) are longer than calculated in this thesis (2-3 minutes)
E-Field	<ul style="list-style-type: none"> - source region of intensification arc located in region of highest particle pressure, $\sim 6-10 R_E$ - dipolarization expands downtail 	<ul style="list-style-type: none"> - this thesis cannot evaluate external influences on onset such as changes in IMF and large-scale electric field - affects on lobe flux reconnection not addressed - timing of dipolarization downtail not addressed

<p>NENL/Flow Braking</p>	<ul style="list-style-type: none"> - EP onset occurs near Earth in region of strong cross-tail current - dipolarization travels downtail 	<ul style="list-style-type: none"> - EP onset occurs after mid-tail reconnection (no evidence of reconnection prior to onset found in this thesis) - tries to lower energy state of the inner plasma sheet while continuing to add energy to it - timescale between EP onset and lobe flux reconnection is much longer (~ 45 minutes) than determined in this thesis
------------------------------	--	---

From Table 6.1 there are two substorm models that stand out as having most of the observational constraints accounted for in their conception: the BLDM and the NECD model. The one main point that stands out as an issue for all substorm models is the rapid timing of the poleward motion of the 557.7 nm emissions. The issue of how an instability could travel downtail in 2-3 minutes and influence lobe flux reconnection still needs to be addressed.

From the second study in this thesis it has been shown that the magnetic signatures associated with the substorm current wedge can indeed be produced using solely the directly-driven system of currents. The combination of ionospheric electric fields and conductivities allows for the formation of a Cowling current and the westward shift of the Region II field-aligned current. By calling on azimuthal pressure gradients in the magnetotail, the source region for the upward field-aligned current of the auroral surge can be produced. The natural appearance of an extended region of downward field-aligned current on the eastern edge of the wedge, which is consistent with ionospheric observations, serve to make this an appealing model for the substorm current wedge.

There is the potential to create a substorm model that involves both the shear flow ballooning instability, which might be the trigger of expansive phase onset, and the model for the substorm current wedge; although some caution should be used on this point as the shear flow ballooning model is a physical model based on non-ideal magnetohydrodynamic theory and the current wedge model presented here is a

parametric model with numerous adjustable parameters. Nevertheless, the similarities between these two models include the location of onset (between 7 – 10 R_E), the need for pressure gradients in the near-Earth plasma sheet (albeit the shear flow ballooning model calls for earthward gradients as opposed to azimuthal gradients), and radial electric fields. The sequence of events for such a model might be as follows: The first stage of the expansive phase might be appropriately labeled the “instability phase” wherein the instability (possibly shear flow ballooning) evolves and expands down the magnetotail in the observed 2.5 minutes. (It should be stated, however, that the shear flow ballooning instability has not yet been proven to expand downtail.) Pressure gradients that have developed during the growth phase would allow for the reconfiguration of the directly-driven currents to produce the substorm current wedge during this first stage. A qualitative analysis shows the timescales required for the reconfiguration to take place could be of the order of tens of seconds at least. The second stage of the expansive phase would then be spent by the magnetosphere returning to its pre-substorm configuration, with the beginning of reconnection of lobe flux taking place as the latter part of the expansive phase, and the substorm current wedge expanding downtail and azimuthally. The poleward motion of the 630.0 nm emissions is of the order of tens of minutes, which is consistent with the time-scale of the lifetime of the substorm current wedge observed to be of the order of 15 minutes.

If one believes that a substorm model should explain both the directly-driven and storage-release processes of the substorm, then it should be noted that the renovated Boundary Layer Dynamic model seems to have all the requisite components. The model begins with a near-Earth expansive phase onset and proposes an instability that would travel downtail to perhaps initiate enhanced reconnection. The timescales are slightly longer than what has been observed in the photometer and POLAR data, but are of the order of minutes nonetheless. With further development of the new current wedge model discussed in this thesis (including the physics of how to sustain an enhanced region of pressure gradient in the midnight and pre-midnight sectors of the magnetotail, narrowing the latitudinal extent of the electrojets so that they better reflect the localized region of expansive phase onset, and quantitative analysis of timescales for the reconfiguration of the directly-driven currents and electric fields), the BLDM could effectively explain all

aspects of the substorm at least from a phenomenological, if not completely physical, point of view.

It has been said that Theses are never finished- they are abandoned. Such is the case for the work presented here. With respect to the substorm current wedge model, a thorough investigation of the pressure gradients, electric fields and ion densities in the midnight region along the near-Earth ($\sim 8 R_E$) plasma sheet is warranted. This thesis has provided a cursory look into the dynamics of the near-Earth magnetotail during the creation of the substorm current wedge and shown that it is possible for the magnetotail to provide the pressure gradients necessary to facilitate the shift of the Region II field-aligned currents. However, a more indepth look into the size and magnitude of the region of pressure gradient, the magnitude of the radial electric field, and the density of ions needed to create a weak field region near midnight is needed before this model can be considered complete. In addition, a more robust look at the GOES satellite signatures and their agreement, or disagreement with the current wedge model presented here would be useful.

With respect to the instability at expansive phase onset, the nature of the mechanism that allows the instability to travel so rapidly downtail is unknown. However, *Koskinen et al.* [1990] showed that the source of the auroral horn propagates at speeds greater than a reasonable expansion speed of a current disruption region in the current sheet. The authors suggested that a natural fast propagation mode could be a magnetosonic wave. If it is proven that an instability can travel downtail and influence reconnection, the kinetic processes involved in initiating reconnection would be a necessary subject of study. Determining how the instability travels downtail will require complex simulations, perhaps incorporating non-linear dynamics. Such an endeavour is beyond the scope of this thesis; however, the timing and the dynamics discovered in Chapter 4 will hopefully be useful in constraining any future models that attempt to investigate this problem.

Although only one event was investigated in detail, the high correlation between the motion and location of the electrojet boundaries with the photometer data is very intriguing. Future work investigating whether the electrojets indeed mirror the activity of the photometer data will be useful with respect to interests surrounding ionospheric/magnetospheric convection and substorm processes. Incorporating all sky imager data into

this study could also provide clues as to the position of the auroral arc during the substorm. The correlation between the arc position determined by the ASI data and the location of the electrojets and the auroral emissions could point to the source location of the auroral arc and the physics involved in its creation. This would indeed be an important asset to auroral arc simulation models and to the overall study of the substorm itself.

Appendix I: Upper Atmospheric Chemistry

As mentioned in the Introduction, energy input into the ionosphere comes not only from solar UV radiation, but also in the form of precipitating particles that have been energized due to physical processes in the magnetosphere related to the aurora. Figure A1.1 illustrates the electron and proton aurora over the southern polar regions of the Earth as inferred from optical observations [*Fukunishi, 1975*]. The diagram on the left illustrates the aurora seen at quiet times, while the aurora associated with the expansive phase is shown on the right. One can see from this figure that the precipitation of particles into the ionosphere occurs along the auroral oval.

From Figure A1.1a we can see that there is always a diffuse proton aurora present from local evening to local morning that is situated equatorward of the electron aurora. The proton aurora is produced by H β (Hydrogen Balmer β line) emissions that, in turn, are produced by protons (H $^+$) precipitating into the E region of the ionosphere. During quiet times the magnitude of the H β emissions is approximately 10-30 Rayleighs (R) [*Fukunishi, 1975*].

The quiet time electron auroras are produced by OI (neutral oxygen) 5577 Å emissions (5577 Å = 557.7 nm) with magnitudes between 200-1000 R. In the local evening sector, the intensity ratio $I(5577\text{Å})/I(\text{H}\beta)$ is approximately 10 suggesting that both the OI 5577Å and the H β emissions are excited by precipitating protons. This was also evident in Figure 1.7 of Chapter 1 where the growth phase 5577Å and H β emissions were collocated along the same latitude. Diffuse-type electron auroras are not observed in this sector. In the midnight to morning sector however, the ratio is ~20-30 indicating that electron auroras are present and are collocated with the hydrogen emissions.

In contrast, the location of the proton and electron aurora changes dramatically during activity associated with an auroral substorm. The key signatures, shown in Figure A1.1b, are the rapid poleward expansion of the regions of proton and electron auroras. The changes in location of auroral activity are due to changes in the precipitation of the electrons and protons. During a substorm, the processes taking place in the central plasma sheet energize the particles. Primary auroral electron intensities are large (from

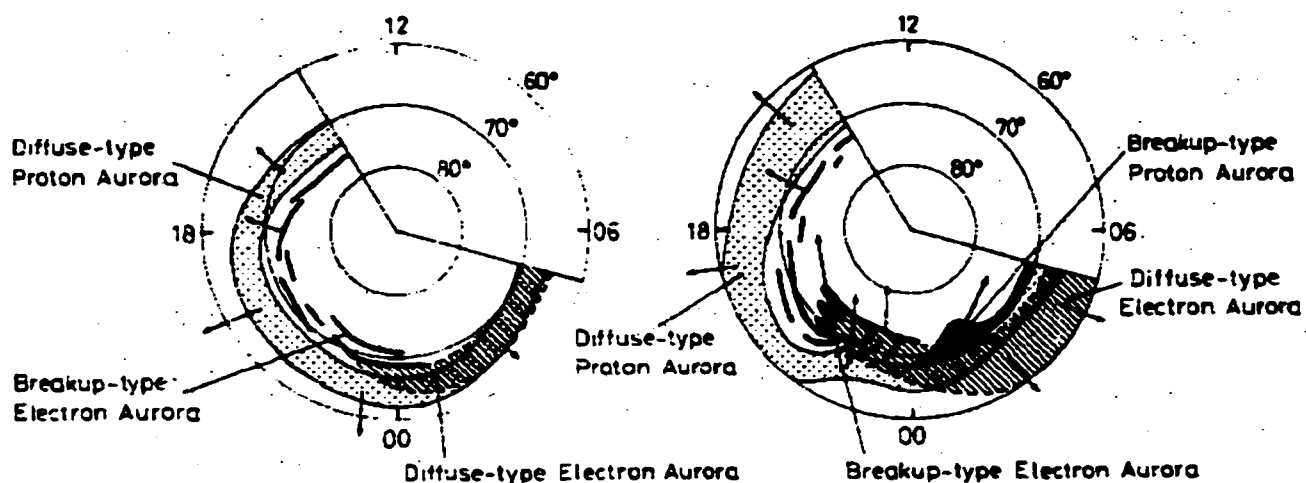


Figure A.1: Electron and proton precipitation patterns over the Northern polar regions of the Earth. The term 'breakup-type' aurora refers to auroras characterized by a sudden brightening and a rapid poleward motion. 'Diffuse-type' auroras are characterized by a gradual equatorward movement with less variation in luminosity (from Fukunishi [1975]).

100s of eV to a few keV) allowing them to precipitate to lower altitudes in the ionosphere. In the E region, electrons collide with O_2^+ ions producing excited states and secondary electrons. It is the secondary electrons that are of importance to producing the aurora, as many auroral spectral features peak at energies less than 20 eV [Rees, Ch. 3]. The secondary electrons are most numerous at energies much lower than the primary electrons and have the added advantage of being emitted in all directions.

Collisions between primary and secondary electrons with atmospheric constituents are inelastic, changing the internal energy of the target molecules. In the E and F regions, collisions involving atoms and molecules in excited states are rare, allowing the excitation energy to be released via radiation [Kivelson and Russell, 1995]. For the purposes of this thesis we are interested in emission lines at 5577\AA (E region at 110km altitude) and 6300\AA (F region at 250km altitude), both transitions of OI produced by electron impact. Both emission lines involve forbidden transitions (due to the parity of the momentum states being equal at ground state) with the auroral green line (5577\AA) being produced by the transition from $^1S_0 - ^1D_2$, and the nebular red line (6300\AA) being produced by the transition from $^1D_2 - ^3P_{2,1}$. The terms 1S_0 , 1D_2 , and $^3P_{2,1}$ refer to

momentum states of the OI species with the superscripts corresponding to the spin angular momentum of the electrons ($2s + 1$), the letters S, D, and P referring to the orbital angular momentum (S=sharp ($l=0$), D=diffuse ($l=2$), and P=principal ($l=1$)), and the subscripts corresponding to the addition of the spin and orbital angular momenta.

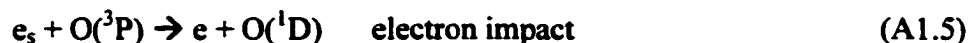
Several excitation sources for the O(1S) electronic state are possible. The reactions that involve electron impact are:



where e_s and e_p represent secondary and primary electrons, respectively. The importance of each reaction with respect to the other is investigated by model computations. Once the O(1S) atom has been produced, it takes roughly 0.91 seconds (Figure A1.2) for it to radiate a photon at 5577Å.



Equations A1.1 to A1.4 also represent collisions producing the excited O(1D) state needed for the production of the 6300Å emissions. The exception is Eq. A1.2, which becomes:



After a rather long radiative lifetime (~110 seconds), the excited O(1D) state emits a photon at the wavelength of 6300Å:



Finally, the Hydrogen Balmer β line is produced by energetic protons precipitating into the E region of the ionosphere (~110 km altitude). The protons have energies of tens

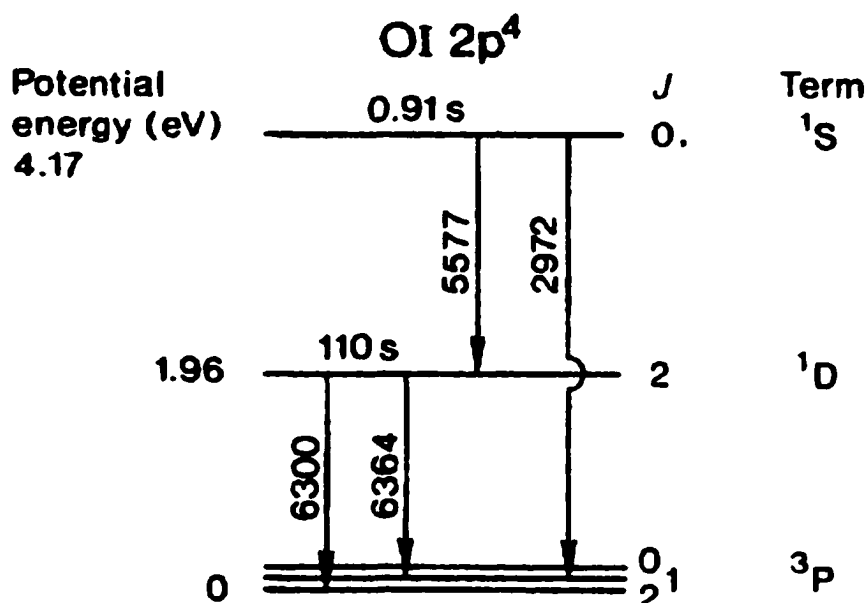


Figure A.2: Partial energy level diagrams for atomic oxygen showing excited and ground state configurations (from Rees [1989]).

of keV gained by convecting earthward from the magnetotail into the more dipolar regions of the magnetosphere during the substorm growth phase [Fukunishi, 1975; Samson, 1994]. It has been suggested that the protons are accelerated towards the atmosphere by a downward parallel electric field [Fukunishi, 1975]. Proton fluxes with highly anisotropic pitch angle distributions, peaked near 0° , have been observed at ~ 0440 magnetic local time by Réme and Bosqued [1971]. The protons enter the atmosphere and undergo inelastic collisions with molecules and atoms.

The protons then undergo charge changing, or charge exchange, collisions via electron capture:



where M represents any E region molecule or atom. If the H^+ ion is left in an excited state, it will jump to ground state by emission of $H\alpha$ or $H\beta$.

The process of charge exchange tends to produce a 'spread' in the initially narrow proton beam as it penetrates the atmosphere. The spread is observable in meridian scanning photometer data as a 'fuzzy' extension, latitudinally, of the maximum intensity

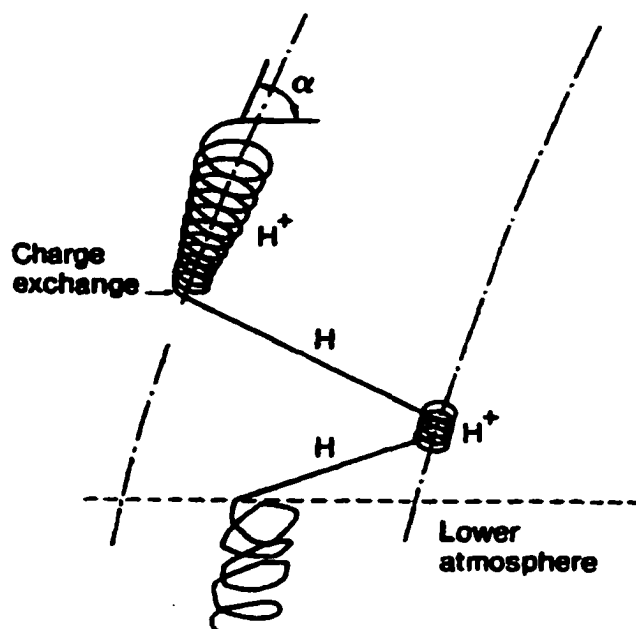


Figure A.3: Proton (H^+) and H atom trajectories in the ionosphere (from Rees [1989]).

emissions. The spread is due to the trajectories of H^+ and H atoms in the vicinity of the geomagnetic field and where the excited atom is when it decays back to its ground state. As the proton enters the atmosphere, its motion is confined to a helical trajectory around the magnetic field (Figure A1.3). On the other hand, the H atom is free to move in a direction dictated by the collision illustrated in Eq. A1.7. The extent of the spreading depends upon the length of time the proton spends as a charged particle (H^+) and as a neutral atom (H).

Bibliography

Fukunishi, H., Dynamic relationship between proton and electron auroral substorms, *J. Geophys. Res.*, 80, 553, 1975.

Kivelson, M. G. and C. T. Russell, *Introduction to Space Physics*, Cambridge University Press, New York, © 1995.

Rees, M. H., *Physics and Chemistry of the Upper Atmosphere*, Cambridge University Press, New York, © 1989.

Reme, H., and J. M. Bosqued, Evidence near the auroral ionosphere of a parallel electric field deduced from energy and angular distributions of low-energy particles, *J. Geophys. Res.*, 76, 7683, 1971.

Samson, J. C., Mapping substorm intensifications from the ionosphere to the magnetosphere, in *Proceedings of the ICS-2 International Conference on Substorms*, eds. J. R. Kan, J. D. Craven, and S.-I. Akasofu, Fairbanks, Alaska, USA, p. 237, 1994.